



**HAL**  
open science

# Microstructure and durability of praseodymium-doped lanthanum nickelate for solid oxide cells

Nur Istiqomah Khamidy

► **To cite this version:**

Nur Istiqomah Khamidy. Microstructure and durability of praseodymium-doped lanthanum nickelate for solid oxide cells. Mechanics of materials [physics.class-ph]. Université Grenoble Alpes [2020-..], 2020. English. NNT: 2020GRALI020 . tel-02894862

**HAL Id: tel-02894862**

**<https://theses.hal.science/tel-02894862>**

Submitted on 9 Jul 2020

**HAL** is a multi-disciplinary open access archive for the deposit and dissemination of scientific research documents, whether they are published or not. The documents may come from teaching and research institutions in France or abroad, or from public or private research centers.

L'archive ouverte pluridisciplinaire **HAL**, est destinée au dépôt et à la diffusion de documents scientifiques de niveau recherche, publiés ou non, émanant des établissements d'enseignement et de recherche français ou étrangers, des laboratoires publics ou privés.



## THÈSE

Pour obtenir le grade de

## DOCTEUR DE L'UNIVERSITÉ GRENOBLE ALPES

Spécialité : 2MGE : Matériaux, Mécanique, Génie civil,  
Electrochimie

Arrêté ministériel : 25 mai 2016

Présentée par

**Nur Istiqomah KHAMIDY**

Thèse dirigée par **Elisabeth DJURADO**, Professeur  
et codirigée par **Jérôme LAURENCIN**, Ingénieur de recherche,  
CEA

et **David JAUFFRES**, Grenoble INP

préparée au sein du **Laboratoire Laboratoire d'Electrochimie et  
de Physico-Chimie des Matériaux et des Interfaces**,  
dans l'**École Doctorale I-MEP2 - Ingénierie - Matériaux,  
Mécanique, Environnement, Energétique, Procédés,  
Production**

**Microstructure et durabilité de nickélate de  
lanthane dopé au praséodyme pour cellules  
à oxydes solides**

**Microstructure and durability of  
praseodymium-doped lanthanum nickelate  
for solid oxide cells**

Thèse soutenue publiquement le **13 mai 2020**,  
devant le jury composé de :

**Madame ELISABETH DJURADO**

PROFESSEUR DES UNIVERSITES, GRENOBLE INP, Directeur de  
thèse

**Monsieur CHRISTOPHE MARTIN**

DIRECTEUR DE RECHERCHE, CNRS DELEGATION ALPES, Président

**Madame PAOLA COSTAMAGNA**

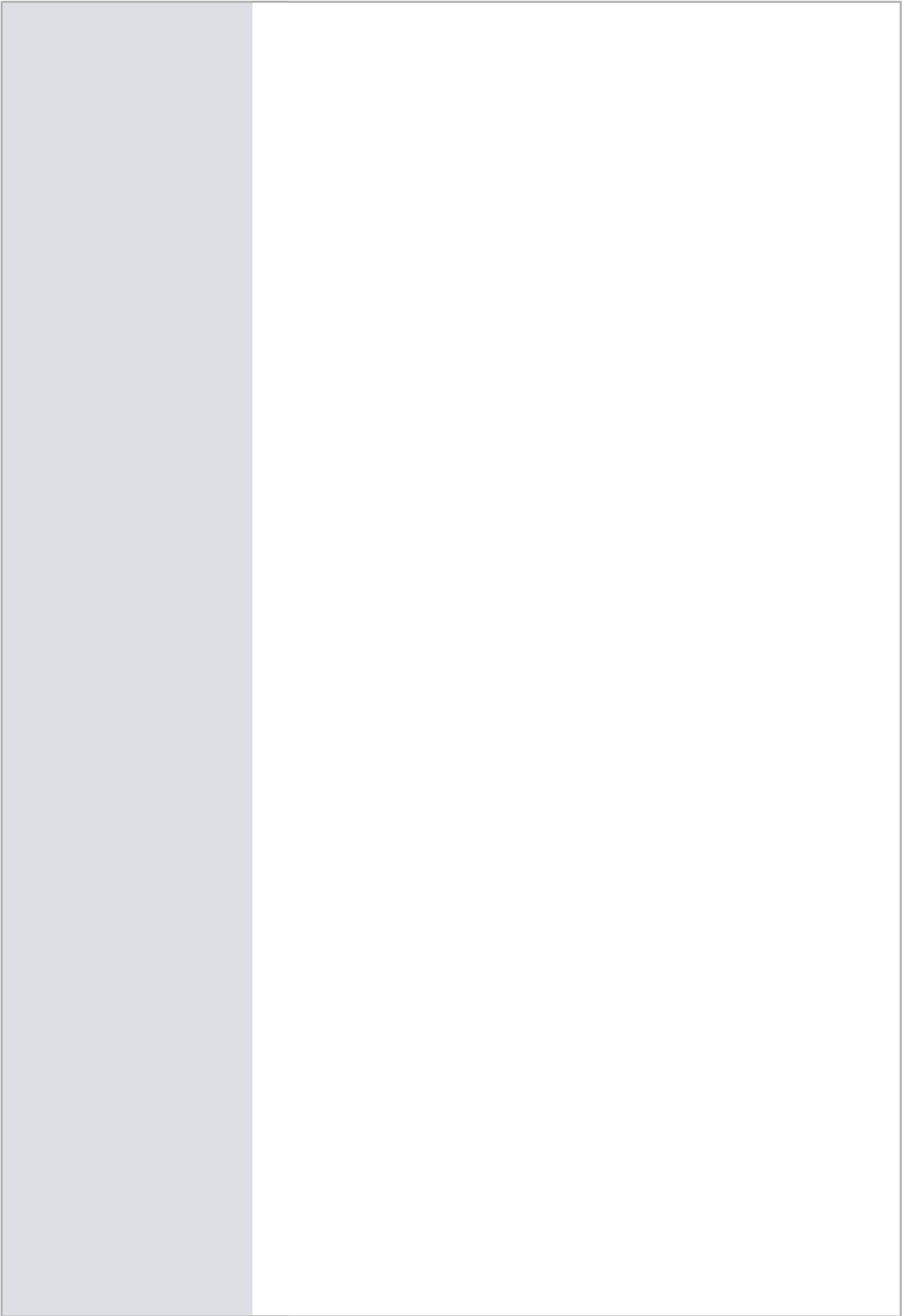
PROFESSEUR ASSOCIE, UNIVERSITE DE GENES - ITALIE,  
Rapporteur

**Monsieur NORBERT H MENZLER**

DOCTEUR-INGENIEUR, CENTRE DE RECHERCHE JÜLICH -  
ALLEMAGNE, Rapporteur

**Monsieur JEROME CHEVALIER**

PROFESSEUR DES UNIVERSITES, INSA LYON, Examineur



---

## ACKNOWLEDGMENTS

First and foremost, all praises and thanks be to God.

I would like to convey my enormous gratitude for my thesis director Prof. Elisabeth Djurado. Thank you for believing in me since the beginning when you offer me this project. I am forever indebted for your guidance and support throughout my PhD life. I learned a great deal from you, especially regarding your love for research and teaching, your astounding attention to details, and your kindness. This thesis would not be possible without your persistence, and I can proudly say that you are one of the people I look up to.

I would like to express my deep gratitude to my thesis co-director Dr. Jérôme Laurencin who show me how a good researcher should be. Thank you for your continued encouragement and for helping me to believe in myself when I could not do it myself. You are one of the most brilliant people I know, and I am glad to have the opportunity to work with you.

I would also like to pass on my sincere gratitude to my thesis co-supervisor Dr. David Jauffrès. I am thankful for your expert guidance especially regarding the image processing, and also for your support during my thesis.

My sincere thanks to all the jury members Dr. Christophe L. Martin, Dr. Paola Costamagna, Dr. Norbert H. Menzler, and Prof. Jérôme Chevalier for your willingness to be the jury for my thesis and to read my thesis manuscript.

I would also like to thank Prof. Elisabeth Siebert and Prof. Laurent Dessemond for the valuable discussion on electrochemistry and impedance spectroscopy.

I am extremely thankful to all researchers and technicians mentioned hereafter for their tremendous help for the sample preparations and characterizations: Thierry Encinas and Stéphane Coindeau for XRD in CMTC, Grenoble INP, France; Frédéric Charlot, Joëlle Calabro, and Rachel Martin for SEM and its sample preparation in CMTC, Grenoble INP, France; Dr. Marlu César Steil, Etienne Omnès-Sabardak, and Franck Fournet-Fayard for the manufacturing of the GDC electrolyte pellets and for the screen printing equipment in M2E, Grenoble INP, France; Bertrand Morel, Karine Couturier, Marie Petitjean, Olivier Stamenoff, and Pascal for the experiments on the test bench in CEA-Liten, Grenoble, France; Dario Ferreira Sanchez for synchrotron X-ray  $\mu$ -XRD and  $\mu$ -XRF in Swiss Light Source (SLS), Paul Scherrer Institut (PSI),

---

Switzerland; Laure Lavernot and Vincent Martin for the experiments in LEPMI, Grenoble INP, France; and Pierre-Henri Jouneau and Nanoscience foundation for FIB-SEM analysis in CEA, Grenoble, France.

This work will not be possible without the funding by the project Mimosa from “Institut Carnot Energies du Futur”. In addition, the work in Swiss Light Source (SLS), Paul Scherrer Institut (PSI), Switzerland, is based on the proposal ID of 20180976.

Thank you also for all my friends, for being a second family for me: Kathina Aninditya who show me how a good friend should be; the members of un-faedah group who are now scattered everywhere, let’s meet again over a barbeque!; my office-mates in LEPMI (Veronica Müller, Lydia Yefsah, Özden Çelikbilek, Rakesh Sharma, Hoang Phuong Khanh Ngo, Thi Khanh Ly Nguyen, Vladyslav Tezyk) and my office-mates in CEA-Liten (Federico Monaco, Hamza Moussaoui, Elisa Effori, Amira Abaza) with whom I share smiles, laughter, problems, and even tears; Xiaohong Chen for the sporadic long chats over meals we have from time to time, I am going to miss it for sure; and the amazing crew of PPI Grenoble that I cannot mention here one by one.

Last but not least, thank you to my family for the endless support. For my parents, Bapak Djati Soepangkat and Ibu Chumaidah Baroroh, who allow me to leave their side to follow my dreams, thank you for your endless prayers. For my brother Nur Iman Khamidy who is also working hard for his dreams and to build his life with my sister-in-law Masturoh; I will always cheer you on. For my sister Nur Maritsa Khamidy, thank you for all the nonsense talks we have that always cheer me up from miles away without fail. I dedicate this thesis for my late grandmother who left before I could show her off my degree; thank you for always believed in me and reminded me to be humble.

---

## RÉSUMÉ (FRANÇAIS)

Dans le cadre du déploiement des énergies renouvelables par nature intermittentes, le couplage des technologies de piles à combustibles et d'électrolyseurs offre une solution innovante pour absorber les pics de production ou de consommation électrique. Dans ce cadre, la technologie basée sur des "cellules à oxydes solides" (SOCs) apparaît comme une solution attractive permettant de remplir les deux fonctions avec le même objet. Ces convertisseurs électrochimiques spécifiques sont constitués d'un électrolyte céramique oxyde fonctionnant à haute température (800 – 1000 °C) permettant d'atteindre des rendements très importants. Néanmoins, la durabilité des SOCs reste à ce jour insuffisante. Dans ce cadre, un des verrous technologiques important est la déstabilisation chimique et mécanique de l'électrode à oxygène ainsi que sa réactivité chimique avec l'électrolyte en fonctionnement. De plus, la température de fonctionnement élevée des SOFC entraîne des contraintes sévères sur l'assemblage des matériaux et sur les processus de fabrication.

Les objectifs de cette thèse sont de mieux comprendre les mécanismes réactionnels et le rôle de la microstructure des électrodes à oxygène dans les cellules à oxydes solides fonctionnant à température intermédiaire (650 - 750 °C) et d'étudier le vieillissement à travers une approche couplant caractérisations électrochimiques, physico-chimiques et de modélisation. Dans ce travail, l'électrode à oxygène architecturée  $\text{LaPrNiO}_{4+\delta}$ , nommée LPNO, a été déposée sur l'électrolyte  $\text{Ce}_{0.9}\text{Gd}_{0.1}\text{O}_{2-\delta}$  en vue de tirer parti des propriétés complémentaires des phases extrêmes, à savoir  $\text{La}_2\text{NiO}_{4+\delta}$  de plus grande stabilité chimique et  $\text{Pr}_2\text{NiO}_{4+\delta}$ , de plus grande activité électrochimique. Par ailleurs, les performances des SOCs dépendent non seulement des propriétés intrinsèques des matériaux mais aussi de l'association des matériaux fonctionnels et des propriétés de leurs interfaces. Par conséquent, de nouvelles architectures d'électrodes, à base d'une couche fonctionnelle active (AFL) fabriquée par atomisation électrostatique (ESD) et surmontée d'une couche de collecteur de courant optimisée (CCL) déposée par sérigraphie (SP), ont été optimisées pour diminuer la température de fonctionnement afin d'améliorer les performances et la durée de vie des cellules. Une couche fonctionnelle active nanostructurée avec une microstructure unique de type corail présentant une grande porosité et une bonne adhérence sur l'électrolyte s'est avérée d'une grande importance dans les réactions des électrodes à oxygène. Les performances et la durabilité des électrodes dans les SOC symétriques et dans une cellule d'électrolyse complète ont été étudiées en détail en

---

vieillessement thermique et en mode galvanostatique. Ces données ont été discutées en relation avec l'évolution structurale et microstructurale de l'électrode à oxygène LPNO grâce à des caractérisations post-mortem utilisant la microscopie électronique à balayage, la reconstruction 3D par faisceau d'ions focalisés MEB, la diffraction des rayons X en laboratoire et la  $\mu$ -diffraction et  $\mu$ -fluorescence par rayonnement X synchrotron.

---

## ABSTRACT (ENGLISH)

Coupling fuel cell and electrolysis technologies provide an attractive solution to absorb the fluctuations induced by the deployment of the intermittent renewable energy sources. In this frame, the technology based on the "Solid Oxide Cells" (SOCs) appears as a promising solution as the same device can be alternatively used in both the electrolysis and fuel cell modes. The SOCs are based on an oxide ceramic electrolyte operating at a high temperature (800-1000 °C) allowing to reach very good efficiency. However, their durability is still insufficient to envisage their economic deployment. An important issue limiting the SOCs lifetime is the chemical and mechanical destabilizations of the oxygen electrode, as well as its chemical reactivity with the electrolyte upon operation. Moreover, the high operating temperature of SOCs leads to severe constraints on materials assembling and on fabrication processes.

The objectives of this PhD thesis are to better understand the role of microstructure and the reaction mechanisms of oxygen electrode in SOCs operating in intermediate temperature (650-800 °C) and to investigate the aging in electrolysis and fuel cell modes through an integrated approach coupling electrochemical and physicochemical characterizations with modeling. In this work, architecturally designed  $\text{LaPrNiO}_{4+\delta}$ , referred to as LPNO, oxygen electrode has been prepared on  $\text{Ce}_{0.9}\text{Gd}_{0.1}\text{O}_{2-\delta}$  electrolyte by taking advantage of the complementary properties of  $\text{La}_2\text{NiO}_{4+\delta}$  and  $\text{Pr}_2\text{NiO}_{4+\delta}$  extremes, i.e. larger chemical stability of  $\text{La}_2\text{NiO}_{4+\delta}$  and larger electrochemical activity of  $\text{Pr}_2\text{NiO}_{4+\delta}$ . The performances of SOCs not only depend on the intrinsic properties of materials, but also to the association of functional structured materials and the properties of their interfaces. In this frame, novel architectures based on an active functional layer (AFL) fabricated by electrostatic spray deposition (ESD) and topped by an optimized current collecting layer (CCL) deposited by screen-printing (SP) have been optimized aiming to decrease the operating temperature in order to improve the performances and the lifetime. A unique coral-like nanostructured AFL with large porosity and good adhesion on the electrolyte has been proved to be of great importance in the oxygen electrode reactions. The electrode performance and durability in symmetrical SOCs and in a complete electrolysis cell have been investigated in detail in thermal aging and in galvanostatic mode. These data have been thoroughly discussed in relationships with structural and microstructural evolution of LPNO oxygen electrode thanks to post-mortem characterizations using scanning

---

electron microscopy, 3D reconstruction by focused ion beam-SEM, laboratory X-ray diffraction, and synchrotron X-ray  $\mu$ -diffraction and  $\mu$ -fluorescence.

---

## CONTENTS

<b>ACKNOWLEDGMENTS</b> .....	i
<b>RÉSUMÉ (FRANÇAIS)</b> .....	iii
<b>ABSTRACT (ENGLISH)</b> .....	v
<b>CONTENTS</b> .....	vii
<b>LIST OF FIGURES</b> .....	x
<b>LIST OF TABLES</b> .....	xv
<b>NOMENCLATURE</b> .....	xvi
<b>INTRODUCTION</b> .....	1
<b>Objectives</b> .....	6
<b>Structure of the thesis</b> .....	6
<b>CHAPTER 1: LITERATURE STUDY</b> .....	9
<b>1.1 Fundamentals of solid oxide cell (SOC)</b> .....	10
1.1.1 Electrolyte .....	11
1.1.2 Air/oxygen electrode .....	12
1.1.3 Fuel/hydrogen electrode .....	14
1.1.4 Sealing materials and interconnects .....	14
<b>1.2 Oxygen reduction/evolution reaction</b> .....	15
1.2.1 Triple-phase boundary (TPB) .....	15
1.2.2 Factors affecting oxygen reduction/evolution reaction (ORR and OER) .....	16
<b>1.3 Ruddlesden-Popper phase: rare-earth nickelates</b> .....	22
<b>1.4 Degradation of several MIEC oxygen electrode materials for SOC</b> .....	25
1.4.1 Degradation mechanism of LSCF oxygen electrode .....	27
1.4.2 Degradation mechanism of rare-earth nickelates .....	28
<b>CHAPTER 2: FABRICATION AND CHARACTERIZATION TECHNIQUES</b> .....	30
<b>2.1 Electrolytes for symmetrical and complete cells</b> .....	31
<b>2.2 Fabrication techniques</b> .....	31
2.2.1 Sol-gel auto-combustion to prepare LPNO powder for screen printing .....	31
2.2.2 Screen printing (SP) .....	32
2.2.3 Electrostatic spray deposition (ESD) .....	34
2.2.4 Design of the LPNO oxygen electrode .....	38
<b>2.3 Microstructural characterization techniques</b> .....	39
2.3.1 Scanning electron microscopy (SEM) .....	39
2.3.2 Focused ion beam-scanning electron microscopy (FIB-SEM) tomography .....	40
<b>2.4 Structural characterization techniques</b> .....	45
2.4.1 Laboratory X-ray diffraction (XRD): room temperature and <i>in-situ</i> XRD .....	45

2.4.2 Synchrotron-based X-ray: Lamellae preparation by plasma-FIB, micro-X-ray diffraction ( $\mu$ -XRD), and micro-X-ray fluorescence ( $\mu$ -XRF).....	45
<b>2.5 Electrochemical characterization technique: Electrochemical impedance spectroscopy (EIS) .....</b>	<b>47</b>
<b>2.6 Long-term durability tests.....</b>	<b>52</b>
2.6.1 Long-term test on the symmetrical cell.....	52
2.6.2 Long-term test on the complete cell.....	53
<b>CHAPTER 3: IMPROVING THE ELECTRODE PERFORMANCE OF RARE-EARTH NICKELATES BY IMPROVING THE MICROSTRUCTURE AND ARCHITECTURAL DESIGN .....</b>	<b>55</b>
<b>3.1 Introduction.....</b>	<b>56</b>
<b>3.2 Preliminary experiments .....</b>	<b>57</b>
3.2.1 Optimized deposition parameters by SP and ESD.....	57
3.2.1.1 SP layer: binder for the ink .....	57
3.2.1.2 ESD layer: solution stabilization, deposition time, and hierarchical microstructure .....	58
3.2.2 Electrochemical performance of coral-type $\text{La}_{2-x}\text{Pr}_x\text{NiO}_{4+\delta}$ ( $x = 0, 1, 2$ ).....	63
3.2.3 Reproducibility .....	64
<b>3.3 Structural characterization of LPNO as a powder, SP layer, and ESD layers .....</b>	<b>65</b>
<b>3.4 Equivalent electrical circuit model for EIS data fitting .....</b>	<b>69</b>
<b>3.5 Influence of the electrode/electrolyte interface quality on the performance of the LPNO electrode .....</b>	<b>71</b>
<b>3.6 Influence of the secondary higher-order phase on the electrochemical performance of the ESD layer .....</b>	<b>77</b>
<b>3.7 Influence of the CCL microstructure on the performance of the electrode .....</b>	<b>82</b>
<b>3.8 Influence of the various architectural designs on the performance of the electrode .....</b>	<b>87</b>
<b>3.9 Summary and conclusions.....</b>	<b>90</b>
<b>CHAPTER 4: DURABILITY STUDY ON THE SYMMETRICAL AND COMPLETE CELLS .....</b>	<b>94</b>
<b>4.1 Introduction.....</b>	<b>95</b>
<b>4.2 Durability study on the symmetrical cell .....</b>	<b>96</b>
4.2.1 Pre-test measurements.....	96
4.2.2 Long-term measurement in electrolysis and fuel cell modes ( $i_{dc} = \pm 300 \text{ mA cm}^{-2}$ ) .....	98
<b>4.3 Preliminary durability study on the complete cell .....</b>	<b>102</b>
4.3.1 Preliminary durability test on CCell 1: GDC barrier layer by screen printing.....	103
4.3.2 Preliminary test on CCell 2: GDC barrier layer by RF magnetron sputtering.....	106
<b>4.4 Summary and conclusions.....</b>	<b>108</b>
<b>CHAPTER 5: POST-MORTEM STRUCTURAL AND MICROSTRUCTURAL CHARACTERIZATIONS .....</b>	<b>110</b>
<b>5.1 Introduction.....</b>	<b>111</b>

---

<b>5.2 Post-mortem microstructural characterization: SEM and 3D reconstruction by FIB-SEM</b>	114
5.2.1 Characterization of the samples operated in the electrolysis mode	114
5.2.2 Characterization of the sample operated in fuel cell mode	116
<b>5.3 Post-mortem structural characterization: synchrotron-based <math>\mu</math>-XRD and <math>\mu</math>-XRF</b>	116
5.3.1 Pristine cell	117
5.3.1.1 Laboratory XRD characterizations for ESD and SP layers	118
5.3.1.2 Synchrotron-based $\mu$ -XRD and $\mu$ -XRF characterizations for ESD-SP double-layer electrode	118
5.3.2 Thermally-aged cell	122
5.3.3 Long-term test in electrolysis mode (anodic polarization): symmetrical and complete cells	124
5.3.3.1 Anodic side of the symmetrical cell (sample 3 or SCell-anodic)	124
5.3.3.2 Anodically-aged oxygen electrode of the complete cell (sample 4 or CCell 1)	126
5.3.4 Long-term test in fuel cell mode (cathodic polarization): symmetrical cell	127
<b>5.4 Summary and conclusions</b>	129
<b>GLOBAL CONCLUSIONS AND PERSPECTIVES</b>	131
Conclusions	132
Perspectives	136
<b>REFERENCES</b>	138
<b>APPENDIX A: Scanning electron microscopy</b>	149
<b>APPENDIX B: Laboratory X-ray diffraction (XRD): room temperature and <i>in-situ</i> XRD</b>	152
<b>APPENDIX C: Electrochemical characterization technique: Electrochemical impedance spectroscopy (EIS)</b>	156

---

## LIST OF FIGURES

<b>Fig. i</b> Efficiency potential of various power generation technologies (Stambouli, 2011) [10]. CCPP refers to a combined cycle power plant. ....	5
<b>Fig. 1. 1</b> The illustrations of solid oxide cells (a) operating as a fuel cell (SOFC) and (b) operating as electrolysis cell (SOEC).....	10
<b>Fig. 1. 2</b> The illustration of possible reaction steps for oxygen reduction reaction (ORR) in a mixed ionic and electronic conductor (MIEC) oxygen electrode (remade with modification from Takeda, et al. [24]). ....	16
<b>Fig. 1. 3</b> The illustration of electrical potential at each interface across the cell (Laurencin [25]).....	17
<b>Fig. 1. 4</b> (a) Polyhedral view of a Ruddlesden-Popper structure of general formula $A_{n+1}B_nO_{3n+1}$ consisting of $nABO_3$ perovskite layers sandwiched between two AO rock-salt layers. Oxygen in equatorial ( $O_{eq}$ ), apical ( $O_{ap}$ ), and interstitial ( $O_i$ ) sites have been highlighted (Tarancón, et al. [32]). (b) The illustrations showing the $ABO_3$ layers for $n = 1, 2,$ and $3$ (Amow, et al. [34]). ....	23
<b>Fig. 1. 5</b> The cell parameters as a function of Pr content in $La_{2-x}Pr_xNiO_{4+\delta}$ ( $0 \leq x \leq 2$ ) (Nishimoto, et al. [38]). ....	25
<b>Fig. 1. 6</b> Degradation rate under SOFC and SOEC operations in (a) $V\% kh^{-1}$ and (b) $m\Omega cm^2 kh^{-1}$ , as well as (c) the estimated lifetime, of various stacks versus the start date of the test taken from published articles. (d) The degradation rate of stacks versus operating temperature for various oxygen electrode materials. All graphs are taken from Skafte, et al. [46]. ....	27
<b>Fig. 1. 7</b> The evolution of polarization resistance during operation in (a) SOFC mode and (b) SOEC mode for $La_{2-x}Pr_xNiO_{4+\delta}$ ( $x = 0, 0.5, 2$ ). The test is carried out in air at $700^\circ C$ and current density ( $i_{dc}$ ) of $\pm 300 mA cm^{-2}$ (Vibhu [36])......	29
<b>Fig. 2. 1</b> (a) GDC electrolyte, (b) Ni-YSZ supported half-cell, and (c) the sketch of the cross-section of the half-cell. ....	31
<b>Fig. 2. 2</b> Flowchart of the sol-gel auto-combustion procedure for the preparation of LPNO powder..	32
<b>Fig. 2. 3</b> Illustration of screen printing. ....	33
<b>Fig. 2. 4</b> (a) Schematic diagram of electrostatic spray deposition (ESD) and (b) sketch of the stages of spray formation as a function of the applied voltage. ....	35
<b>Fig. 2. 5</b> Schematic diagrams of different architectural designs of LPNO electrode: single-layer (SL) LPNO deposited by (a) SP and (b) ESD, (c) double-layer (DL) of LPNO AFL deposited by ESD topped by LPNO CCL deposited by SP, and (d) triple-layer electrode (TL) in which the AFL is a GDC interlayer deposited by SP topped by LPNO deposited by ESD and the CCL is LPNO deposited by SP. ....	38
<b>Fig. 2. 6</b> (a) The schematic illustration of FIB set-up (Gierak, 2014) [65] and (b) FIB-SEM tomography configuration. ....	41
<b>Fig. 2. 7</b> The schematic representation of step-by-step FIB-SEM tomography: (a) protective Pt deposition on the region of interest (ROI) – (b) FIB milling to create a trench close to the ROI – (c) the view of the ROI – (d) an example of a slice of image acquired by SEM using the in-lens detector with the black parts indicating the resin-filled pores. ....	42
<b>Fig. 2. 8</b> (a) The raw, unprocessed SEM image – (b) the image after Bleach Correction to reduce the shadowing effect – (c) the segmented image which shows the solid phase in white and the porosity in black. ....	43
<b>Fig. 2. 9</b> The schematic representation of the lamella preparation by p-FIB: (a) protective Pt deposition on ROI – (b) FIB milling around the ROI – (c) isolated lamella – (d) sample extraction from the cell –	

(e) sample mounted on the Al pin. (f) The schematic diagram of $\mu$ -XRD and $\mu$ -XRF characterization at $\mu$ XAS beamline, SLS, PSI, Switzerland. ....	46
<b>Fig. 2. 10</b> The graphical representation of impedance $Z$ (Barsoukov & Macdonald (Eds.), 2005) [76]. ....	49
<b>Fig. 2. 11</b> (a) Nyquist and (b) Bode representation of EIS data. The numbers on the Nyquist plot indicates the logarithmic of the frequency. ....	49
<b>Fig. 2. 12</b> (a) 2-electrode and (b) 3-electrode configurations for EIS measurement. CE is a counter electrode, WE is a working electrode, and RE is a reference electrode. ....	52
<b>Fig. 2. 13</b> The illustration of the test bench configuration for the durability test on the complete cell. ....	53
<b>Fig. 3. 1</b> The Arrhenius plots of single-layer deposited by SP using either PVP or PVB as the binder for the ink. ....	58
<b>Fig. 3. 2</b> The LPNO precursor solution (a) right after the preparation and (b) 1.5 h later without $\text{HNO}_3$ addition which showed that the solution became opaque due to the formation of precipitates, (c) the precipitates blocked the opening of the tube which prevented the solution of precursors to continue to flow to the needle and thus stopped the spray production. The SEM images of (d) the surface and (e)-(f) the cross-section of the ESD layer prepared from solution without $\text{HNO}_3$ . The SEM images of (g) the surface and (h)-(i) the cross-section of the ESD layer prepared from solution with the addition of $\text{HNO}_3$ . Both layers were deposited by ESD for 3 h of deposition time. ....	60
<b>Fig. 3. 3</b> The cross-section SEM images of ESD layer deposited for (a) 3 h 45', (b) 4 h 30', and (c) 6 h; (d) the thickness of the ESD layer versus time. ....	61
<b>Fig. 3. 4</b> The Arrhenius plots of double-layer symmetrical cells with different ESD deposition time: 3 h 45', 4 h 30', and 6 h. ....	62
<b>Fig. 3. 5</b> The SEM images of the LPNO columnar electrode: (a) the surface view, (b) the cross-section, and (c) a larger magnification at the electrode/electrolyte interface which show the uniform deposition at the electrode/electrolyte interface. ....	63
<b>Fig. 3. 6</b> The Arrhenius plots of LNO, LPNO, and PNO double-layer symmetrical cells. ....	64
<b>Fig. 3. 7</b> The Arrhenius plots of three identical double-layer symmetrical cells for reproducibility test. ....	65
<b>Fig. 3. 8</b> XRD of (a) LPNO powder prepared by auto-combustion and calcined at 1050 $^\circ\text{C}/2$ h + 1100 $^\circ\text{C}/0.5$ h in air and (b) screen-printed layers of LPNO on GDC thermally treated in air at (i) 450 $^\circ\text{C}/2$ h + 800 $^\circ\text{C}/2$ h, (ii) 450 $^\circ\text{C}/2$ h + 900 $^\circ\text{C}/2$ h, (iii) 450 $^\circ\text{C}/2$ h + 1050 $^\circ\text{C}/2$ h + 1100 $^\circ\text{C}/0.5$ h, and (iv) 450 $^\circ\text{C}/2$ h + 1200 $^\circ\text{C}/2$ h; (c) In-situ high temperature XRD from 25 to 1200 $^\circ\text{C}$ of the as-deposited SL LPNO electrode by ESD. ....	66
<b>Fig. 3. 9</b> The diffractogram of the ESD layer after sintering in the air at 960 $^\circ\text{C}$ for 6 h. ....	67
<b>Fig. 3. 10</b> SEM images of cross-sections of (a), (b) SL SP sintered at 1100 $^\circ\text{C}$ (sample 2) and (c), (d) SL ESD sintered at 960 $^\circ\text{C}$ (sample 3) on two different magnifications. The electrode/electrolyte interfaces are indicated by the dashed white lines. ....	68
<b>Fig. 3. 11</b> The schematic diagram of the equivalent circuit model which is used to fit the experimental EIS data. ....	69
<b>Fig. 3. 12</b> (a)-(c) Nyquist plots and (d)-(f) Bode plots of samples 1, 2, and 3 at 500, 600, and 700 $^\circ\text{C}$ , respectively. The Nyquist plots are plotted by subtracting the contribution of the series resistance and the numbers on the Nyquist plots indicate the logarithmic of the frequencies. ....	74
<b>Fig. 3. 13</b> The Arrhenius plots of (a) series resistance ( $R_s$ ) and (b) polarization resistance ( $R_{\text{pol}}$ ). The deconvolution of (c) resistance ( $R$ ) and (d) capacitance ( $C$ ) associated with P1 (half-filled markers), P2 (filled markers), and P3 (empty markers) processes, as well as chemical capacitance ( $C_{\text{chem}}$ , empty with plus sign markers). All plots are for sample 1 (black square), 2 (blue circle), and 3 (triangle red). ....	75

<b>Fig. 3. 14</b> XRD patterns of the ESD layer (i) as-sintered at 960 °C for 6 h in air and after second heat-treatment in air at (ii) 450 °C/2 h + 800 °C/2 h, (iii) 450 °C/2 h + 900 °C/2 h, and (iv) 450 °C/2 h + 1050 °C/2 h + 1100 °C/0.5 h.....	78
<b>Fig. 3. 15</b> (a)-(c) Nyquist plots and (d)-(f) Bode plots of samples 4, 5, and 6 at 500, 600, and 700 °C, respectively. The Nyquist plots are plotted by subtracting the contribution of the series resistance and the numbers on the Nyquist plots indicate the logarithmic of the frequencies. ....	80
<b>Fig. 3. 16</b> The Arrhenius plots of (a) series resistance ( $R_s$ ) and (b) polarization resistance ( $R_{pol}$ ). The deconvolution of (c) resistance ( $R$ ) and (d) capacitance ( $C$ ) associated with P2 (filled markers) and P3 (empty markers) processes, as well as chemical capacitance ( $C_{chem}$ , empty with plus sign markers). All plots are for sample 4 (black square), 5 (blue circle), and 6 (triangle red). ....	81
<b>Fig. 3. 17</b> The cross-section images of (a), (b) ESD layer after second heat-treatment at 450 °C/2 h + 900 °C/2 h and (c), (d) ESD layer after second heat-treatment at 450 °C/2 h + 1050 °C/2 h + 1100 °C/0.5 h at two different magnifications. The dashed white line indicates the electrode/electrolyte interface. ....	82
<b>Fig. 3. 18</b> SEM images of (a), (b) LPNO powder before ball-milling; (c), (d) LPNO powder after ball-milling; the cross-section of the double-layer electrodes (e) with non-ball-milled LPNO powder and (f) with ball-milled LPNO powder as the CCL; and (g), (h) the cross-section of the triple-layer electrode at two different magnifications. The dashed white line indicates the interfaces. ....	83
<b>Fig. 3. 19</b> The elements distribution observed at three different regions across the screen-printed GDC: at the LPNO ESD/GDC SP interface (black), at 3 $\mu$ m from this interface (blue), and at 5 $\mu$ m from this interface (red). ....	84
<b>Fig. 3. 20</b> (a)-(c) Nyquist plots and (d)-(f) Bode plots of samples 4, 7, 8, and 9 at 500, 600, and 700 °C, respectively. The Nyquist plots are plotted by subtracting the contribution of the series resistance and the numbers on the Nyquist plots indicate the logarithmic of the frequencies. ....	86
<b>Fig. 3. 21</b> The Arrhenius plots of (a) series resistance ( $R_s$ ) and (b) polarization resistance ( $R_{pol}$ ). The deconvolution of (c) resistance ( $R$ ) and (d) capacitance ( $C$ ) associated with P1 (half-filled markers), P2 (filled markers), and P3 (empty markers) processes, as well as chemical capacitance ( $C_{chem}$ , empty with plus sign markers). All plots are for sample 4 (black square), 7 (blue circle), 8 (triangle red), and 9 (inverted-triangle olive). ....	87
<b>Fig. 3. 22</b> (a)-(c) Nyquist plots and (d)-(f) Bode plots of samples 3, 7, and 9 at 500, 600, and 700 °C, respectively. The Nyquist plots are plotted by subtracting the contribution of the series resistance and the numbers on the Nyquist plots indicate the logarithmic of the frequency. ....	89
<b>Fig. 3. 23</b> The Arrhenius plots of (a) series resistance ( $R_s$ ) and (b) polarization resistance ( $R_{pol}$ ). Several $R_{pol}$ values of LPNO with similar configuration are also given for comparison [22], [35]. The deconvolution of (c) resistance ( $R$ ) and (d) capacitance ( $C$ ) associated with P1 (half-filled markers), P2 (filled markers), and P3 (empty markers) processes, as well as chemical capacitance ( $C_{chem}$ , empty with plus sign markers). All plots are for sample 3 (magenta diamond), 7 (blue circle), and 9 (inverted-triangle olive). ....	90
<b>Fig. 4. 1</b> (a),(c) Nyquist plots and (b),(d) Bode plots of SCell at 550-700 °C taken at OCP for the bottom and top electrodes, respectively. The Nyquist plots are plotted by subtracting the contribution of the series resistance and the numbers on the Nyquist plots indicate the logarithmic of the frequency. The inset graphs indicating the magnification of the plots taken at 650 and 700 °C for clarity. ....	97
<b>Fig. 4. 2</b> The Arrhenius plots of (a) series resistance ( $R_s$ ) and (b) polarization resistance ( $R_{pol}$ ) for the bottom (black square) and top (blue circle) electrodes of SCell. ....	98
<b>Fig. 4. 3</b> Voltage between the working and the reference electrodes as a function of time for SCell operating in fuel cell mode. ....	99
<b>Fig. 4. 4</b> (a),(c) Nyquist plots and (b),(d) Bode plots of SCell at 700 °C which are taken before and after a long-term test for cathodic and anodic sides, respectively. The Nyquist plots are plotted by subtracting	

the contribution of the series resistance and the numbers on the Nyquist plots indicate the logarithmic of the frequency. ....	101
<b>Fig. 4. 5</b> (a) The series resistance ( $R_s$ ) and (b) the polarization resistance ( $R_{pol}$ ) before and after a long-term test for the cathodic (black square) and anodic (blue circle) sides of SCell. ....	101
<b>Fig. 4. 6</b> The iV curve of CCell 1 at 700 °C taken at various times during the test for (a) fuel cell operation with $D_{tot,SOFC}$ 9 and (b) electrolysis operation with $D_{tot,SOEC}$ 9. ....	103
<b>Fig. 4. 7</b> The Nyquist and Bode plots of CCell 1 at 700 °C taken at OCV before the long-term test ( $t = 0$ h) for $D_{tot,SOEC}$ 9 and $D_{tot,SOEC}$ 20. The numbers indicate the logarithm of the measuring frequency. ....	104
<b>Fig. 4. 8</b> Cell voltage as a function of time for CCell 1 operating in the electrolysis mode. The spikes show the timestamps when the applied current is stopped for either system check or measuring the iV curve and impedance of the cell. ....	105
<b>Fig. 4. 9</b> The Nyquist and Bode plots of CCell 1 at 700 °C taken at OCV before, during, and after the long-term test for $D_{tot,SOEC}$ 9. The numbers indicate the logarithm of the measuring frequency. ....	106
<b>Fig. 4. 10</b> (a) The series resistance ( $R_s$ ) and (b) the polarization resistance ( $R_{pol}$ ) measured at various times during the long-term test of CCell 1. ....	106
<b>Fig. 4. 11</b> The iV curve of CCell 1 and CCell 2 at 700 °C taken before the long-term test for (a) fuel cell operation with $D_{tot,SOFC}$ 9 and (b) electrolysis operation with $D_{tot,SOEC}$ 9. ....	108
<b>Fig. 4. 12</b> The Nyquist and Bode plots of CCell 1 and CCell 2 at 700 °C taken at OCV before, and during the long-term test for $D_{tot,SOEC}$ 9. The numbers indicate the logarithm of the measuring frequency. ....	108
<b>Fig. 5. 1</b> The cross-section SEM images of (a) pristine cell (sample 1), (b) anodically-aged symmetrical cell (sample 3 or SCell-anodic), (c) anodically-aged complete cell (sample 4 or CCell 1), and (d) cathodically-aged symmetrical cell (sample 5 or SCell-cathodic). The dashed white line indicates the LPNO electrode/electrolyte interface. The surface of sample 4 is slightly damaged during the removal of the cells from the test bench after electrolysis operation by sandblasting. ....	114
<b>Fig. 5. 2</b> The 3D reconstruction visualization of (a) pristine cell (sample 1) and (b) anodically-aged symmetrical cell (sample 3 or SCell-anodic). ....	115
<b>Fig. 5. 3</b> SEM micrographs of the lamella of (a) pristine cell (sample 1), (b) thermally-aged cell (sample 2), (c) anodically-aged symmetrical cell (sample 3 or SCell-anodic), and (d) anodically-aged complete cell (sample 4 or CCell 1). ....	117
<b>Fig. 5. 4</b> (a) The average XRD patterns on several Y-positions and (b)-(c) refinement of the peaks at two different Y-positions, i. e. 18 and 4 $\mu\text{m}$ above the electrode/GDC, respectively, for the pristine cell (sample 1). ....	120
<b>Fig. 5. 5</b> 2D maps of the XRD which shows the distribution of the phases, namely GDC, LPNO, (LP)3N2, Pr6O11, and (LP)4N3, in (a) pristine cell (sample 1), (b) thermally-aged cell (sample 2), (c) anodically-aged symmetrical cell (sample 3 or SCell-anodic), and (d) anodically-aged complete cell (sample 4 or CCell 1). The brighter color indicates the higher local intensity of the corresponding compound. ....	121
<b>Fig. 5. 6</b> 2D maps of the XRF which shows the distribution of the elements, namely Ce, Gd, La, Ni, Pr, and Pt, in (a) pristine cell (sample 1), (b) thermally-aged cell (sample 2), (c) anodically-aged symmetrical cell (sample 3 or SCell-anodic), and (d) anodically-aged complete cell (sample 4 or CCell 1). The brighter color indicates the higher local intensity of the corresponding element. ....	122
<b>Fig. 5. 7</b> (a) The average XRD patterns on several Y-positions and (b)-(c) refinement of the peaks at two different Y-positions, i. e. 4.5 and 1.5 $\mu\text{m}$ above the electrode/GDC interface, respectively, for the thermally-aged cell (sample 2). ....	123
<b>Fig. 5. 8</b> The quantitative comparison of (LP)3N2, Pr6O11, and (LP)4N3 to LPNO in the LPNO electrode as the function of distance from electrode/GDC interface for (a) pristine cell (sample 1), (b)	

---

thermally-aged cell (sample 2), (c) anodically-aged symmetrical cell (sample 3 or SCell-anodic), and (d) anodically-aged complete cell (sample 4 or CCell 1). .....	124
<b>Fig. 5. 9</b> (a) The average XRD patterns on several Y-positions and (b)-(c) refinement of the peaks at two different Y-positions, i. e. 14 and 4 $\mu\text{m}$ above the electrode/GDC interface, respectively, for the anodically-aged symmetrical cell (sample 3 or SCell-anodic).....	125
<b>Fig. 5. 10</b> (a) The average XRD patterns on several Y-positions and (b)-(c) refinement of the peaks at two different Y-positions, i. e. 10 and 4 $\mu\text{m}$ above the electrode/GDC interface, respectively, for the anodically-aged complete cell (sample 4 or CCell 1). .....	127
<b>Fig. 5. 11</b> The lab XRD of (a) pristine cell (sample 1) and (b) cathodically-aged symmetrical cell (sample 5 or SCell-cathodic). The symbol ‘C’ indicated the carbon phase which is originating from the carbon tape used for sample preparation by p-FIB. ....	129

---

## LIST OF TABLES

<b>Table i</b> Typical reactions on the cathode and anode of fuel cells with either cationic or anionic conductor electrolyte operating as both fuel cell and electrolyzer cell. ....	4
<b>Table 1. 1</b> The ionic conductivity ( $\sigma$ ) and thermal expansion coefficient (TEC) of several electrolyte materials. ....	12
<b>Table 1. 2</b> The electronic conductivity ( $\sigma_e$ ), ionic conductivity ( $\sigma_{io}$ ), thermal expansion coefficient (TEC), oxygen diffusion coefficient ( $D^*$ ), and surface exchange coefficient ( $k^*$ ) of several oxygen electrode materials. ....	13
<b>Table 1. 3</b> The oxygen over-stoichiometry ( $\delta$ ), polarization resistance ( $R_{pol}$ ) at 600 °C, and thermal decomposition of $La_{2-x}Pr_xNiO_{4+\delta}$ ( $0 \leq x \leq 2$ ) after heat treatment at 700 °C for 30 days taken from two literature. ....	24
<b>Table 1. 4</b> The final phases after operation in SOFC and SOEC modes for $La_{2-x}Pr_xNiO_{4+\delta}$ ( $x = 0, 0.5, 2$ ). The test is carried out in air at 700 °C for 1800 h and current density ( $i_{dc}$ ) of $\pm 300 \text{ mA cm}^{-2}$ (Vibhu [36]). ....	29
<b>Table 2. 1</b> Deposition parameters by ESD to obtain a coral-like microstructure. ....	37
<b>Table 2. 2</b> The diameter (in mm) of the deposition size for symmetrical and complete cells. ....	39
<b>Table 2. 3</b> The NiO reduction steps at 800 °C from 5 to 15 minutes. ....	54
<b>Table 3. 1</b> List of samples discussed in this chapter with the sintering program. As described in §2.2.4, SL = single-layer, DL = double-layer, and TL = triple-layer. ....	56
<b>Table 3. 2</b> Architectural design, thickness, and particle size for all the samples mentioned in this chapter. ....	92
<b>Table 3. 3</b> The summary of the electrochemical data at 500, 600, and 700 °C for all samples mentioned in this chapter. ....	93
<b>Table 4. 1</b> The list of samples and the detailed long-term test parameters for each. ....	96
<b>Table 4. 2</b> The details on the gas composition and flow rates of each gas for measurements of complete cell in both fuel cell and electrolysis modes. The steam conversion rates (SC) are given for a current density of $0.2 \text{ A cm}^{-2}$ . ....	102
<b>Table 5. 1</b> The list of samples and the summary of the characterization results. ....	113
<b>Table 5. 2</b> The values of several microstructural properties of the pristine cell and anodic side of the symmetrical cell calculated based on the 3D reconstruction by FIB-SEM. ....	116

---

## NOMENCLATURE

### *Abbreviations*

(LP)3N2	(La,Pr) <sub>3</sub> Ni <sub>2</sub> O <sub>7-δ</sub> , a Ruddlesden-Popper phase ( $A_{n+1}B_nX_{3n+1}$ ) with n = 2
(LP)4N3	(La,Pr) <sub>4</sub> Ni <sub>3</sub> O <sub>10-δ</sub> , a Ruddlesden-Popper phase ( $A_{n+1}B_nX_{3n+1}$ ) with n = 3
AC	Alternating current
ALS	Adler-Lane-Steele model
AFC	Alkaline fuel cell
AFL	Active functional layer
BM	Ball milling
BSE	Back-scattered electrons
CCL	Current collector layer
CHP	Combined heat and power
CL	Cathodoluminescence
CPE	Constant phase element
DC	Direct current
DCFC	Direct carbon fuel cell
DL	Double-layer electrode, which consists of a layer of LPNO deposited by ESD and then topped by a layer of LPNO deposited by SP (see: LPNO, ESD, SP, SL, TL)
DMFC	Direct methanol fuel cell
EDX	Energy-dispersive X-ray spectroscopy
EHT	Electron high tension
EIS	Electrochemical impedance spectroscopy
ESD	Electrostatic spray deposition

---

FIB	Focused-ion beam
FLW	Finite-length Warburg
G	Gerischer
GDC	$Ce_{1-y}Gd_yO_{2-y/2}$ . In this manuscript, the term GDC is exclusively used for the material chosen as the electrolyte for the symmetrical cell with $y = 0.1$ ( $Ce_{0.9}Gd_{0.1}O_{2-\delta}$ ) unless indicated otherwise
IT-SOC	Intermediate temperature solid oxide cells
LPG	Liquefied petroleum gas
LPNO	$LaPrNiO_{4+\delta}$ , a Ruddlesden-Popper phase ( $A_{n+1}B_nX_{3n+1}$ ) with $n = 1$ , the main material studied in this thesis
LSCF	$La_{1-x}Sr_xCo_{1-y}Fe_yO_{3-\delta}$ , one of the vastly used materials for oxygen electrode
MCFC	Molten carbonate fuel cell
OCP	Open circuit potential
OCV	Open circuit voltage
OER	Oxygen evolution reaction
ORR	Oxygen reduction reaction
PAFC	Phosphoric acid fuel cell
PCFC	Protonic ceramic fuel cell
PEMFC	Proton-exchange membrane fuel cell
PVB	Polyvinyl butyral, $(C_8H_{14}O_2)_n$
PVP	Polyvinylpyrrolidone, $(C_6H_9NO)_n$
RE	Renewable energy
ROI	Region of interest
RP	Ruddlesden-Popper phase
SC	Steam conversion rates

---

---

SE	Secondary electrons
SEM	Scanning electron microscope
SL	Single-layer electrode, which consists of a layer of LPNO deposited by ESD or SP (see: LPNO, ESD, SP, DL, TL)
SOC	Solid oxide cell
SOEC	Solid oxide electrolysis cell
SOFC	Solid oxide fuel cell
SP	Screen printing
TL	Triple-layer electrode, which consists of a layer of GDC deposited by SP, topped by a layer of LPNO deposited by ESD, and then coated by a layer of LPNO deposited by SP (see: GDC, LPNO, ESD, SP, DL, SL)
TPB	Triple-phase boundary
XRD	X-ray diffraction
XRF	X-ray fluorescence
YSZ	Yttria-stabilized zirconia

### ***Symbols***

Symbol	Meaning	Usual dimensions (values)
<i>Roman symbols</i>		
A	Area of the electrode	cm <sup>2</sup>
a	Specific surface area	cm <sup>-1</sup>
a, b, c	lattice parameter	Å
C	Capacitance	F cm <sup>-2</sup>
D	Diffusion coefficient	m <sup>2</sup> s <sup>-1</sup>
d	Needle-substrate distance (ESD)	mm
E or U	Voltage or potential	V

---

$E_0$	Standard potential	V
F	Faraday constant	96485 C mol <sup>-1</sup>
f	Frequency	Hz
$f_{\text{thermo}}$	Thermodynamic factor	none
I	Current	A
i	Current density	A cm <sup>-2</sup>
j	Complex number	
k	Surface exchange coefficient	m s <sup>-1</sup>
L	Inductance	H
n	(i) The number of consecutive perovskite layers in an RP compound	none
	(ii) the unknown partial charge state of adsorbed oxygen	none
Q	(i) Solution flow rate	mL h <sup>-1</sup>
	(ii) Factor of proportionality (CPE element)	S s <sup>-<math>\alpha</math></sup>
R	(i) Resistance	$\Omega$ or $\Omega$ cm <sup>2</sup> (area-specific)
	(ii) the Boltzmann constant	8.314 J mol <sup>-1</sup> K <sup>-1</sup>
T	Temperature	°C or K (K = 273 + °C)
t	(i) time	s
	(ii) ESD deposition time	h
$V_m$	Molar volume	cm <sup>3</sup> mol <sup>-1</sup>
Z	Impedance	$\Omega$ or $\Omega$ cm <sup>2</sup> (area-specific)

*Greek symbols*

$\alpha$	The exponential for circuit elements	none
$\alpha, \beta, \gamma$	Unit cell angular parameters	degrees (°)
$\gamma$	Solution surface tension	N m <sup>-1</sup>
$\delta$	Oxygen over-/under-stoichiometry	none
$\epsilon_0$	Vacuum permittivity	8.85 x 10 <sup>-12</sup> F m <sup>-1</sup>
$\eta$	Overpotential	V
$\theta$	(i) Diffraction angle	degrees (°)
	(ii) Phase angle	degrees (°)
$\lambda$	Wavelength	nm

---

---

$\rho$	(i) Solution density	$\text{g cm}^{-3}$
	(ii) Resistivity	$\Omega \text{ m}$
$\sigma$	Conductivity	$\text{S m}^{-1}$
$\tau$	Time constant	s
$\omega$	Angular frequency	$\text{rad s}^{-1}$

*Subscripts*

act	activation
ads	adsorbed
ACC	Anode current collector
AFL	Anode functional layer
CCC	Cathode current collector
CFL	Cathode functional layer
conc	concentration
chem	Chemical
dc	Direct current
e <sup>-</sup>	electrical
f	fractal (for Gerischer circuit)
io	ionic
pol	polarization
rev	reversible
s	series

---

# INTRODUCTION

The global warming inducing the climate change is becoming a very important issue to be addressed since it is not only environmentally urgent, but it also affects social and economic development, human welfare, and health [1]. Several studies have been carried out to model the possible future scenarios on global warming with various mitigation efforts. In this context, it is accepted by the community that the global temperature rise should not exceed more than 2 °C above the pre-industrial levels to avoid dangerous risks of climate change [2]. The Paris Agreement, signed in 2016 within the United Nations Framework Convention on Climate Change (UNFCCC), has a long-term goal to limit the temperature increase to 1.5 °C. To achieve this goal, various mitigation efforts, especially from policy-makers, are necessary.

To find the best mitigation pathways, it is important to understand the causes of global warming. The rise on the global surface temperature is more likely to be dominantly caused by human influence (anthropogenic) as reported by the Fifth Assessment Report of the Intergovernmental Panel on Climate Change (IPCC) [1]. The anthropogenic emission of greenhouses gases (GHG) has a significant contribution to the increase of the atmospheric GHG concentrations which causes the global temperature to increase. GHGs, such as carbon dioxide, methane, and nitrous oxide, are produced from deforestation, agriculture, soil erosion, and, most important of all, the combustion of fossil fuels. The emission of carbon dioxide from the combustion of fossil fuel itself evidently contributed to 78% of the total GHG emission increase from 1970 and 2010 and the same percentage was observed between 2000 to 2010 [1]. Several strategies to reduce the emission from fossil fuel use have been proposed such as energy conservation and efficiency, fossil fuel switching, renewable energy (RE), nuclear, and carbon capture and storage (CCS) [1].

Replacing the use of direct combustion of fossil fuels to low-carbon, clean energy systems such as RE (e.g. biomass, geothermal, solar heat, hydropower, wind power), nuclear, and hydrogen and fuel cells technology is on the top priority to reduce GHG emission, especially for the electricity sector. Besides the aforementioned environmental reasons, the transition to low-carbon energy systems is also motivated by the limited amount of non-renewable fossil fuel resource which is predicted to become scarce in the near future.

One of the challenges in the utilization of RE technologies is their intermittency, especially for solar and wind energy. Thus, to ensure the reliability of clean energy systems, the current research interest in the energy sector is to develop energy systems by utilizing RE technologies and integrating energy vectors such as hydrogen in the system [3]. Hydrogen is considered to

---

be a promising energy carrier due to its abundance. As one of the most widespread elements on earth, hydrogen can be obtained from various sources, either renewable or non-renewable. Hydrogen can also be produced in numerous ways through electrical, thermal, biochemical, and photonic means [4]. Until recently, more than 90% of hydrogen is produced from the thermal dissociation of hydrocarbons such as steam reforming of natural gas, oil reforming, and coal gasification, while the small fraction is produced from water electrolysis and other sources [5], [6].

Hydrogen is vastly used in many industrial processes. In energy-related applications, it is commonly used as fuel for the fuel cell system. A fuel cell is an electrochemical energy conversion device that converts the chemical energy from the fuels into electricity and thermal energy [7]–[10]. It consists of two highly catalytic electrodes which are separated by an electrolyte. Unlike a battery, fuel cell requires an external supply of fuels and oxidants on either side of the electrodes where a set of electrochemical reactions occurs to produce direct current without the expense of the electrodes [9].

One of the key advantages of fuel cells, as compared to the conventional power generation systems, is its high efficiency which can reach 40-50% of electrical efficiency, 65-70% for combined cycle solid oxide fuel cell (SOFC) / gas turbine, and even up to more than 90% for the combined heat and power (CHP system) [7], [11], [12]. The fuel that is used to power fuel cells is normally hydrogen. However, other fuels such as solid carbon and hydrocarbon fuels (natural gas, liquefied petroleum gas (LPG), biogas) can also be utilized. Even when carbon-containing fuels are used, the emission of the fuel cell is still lower as compared to the conventional energy system due to its high efficiency [10]. A fuel cell is also quiet in operation, highly reliable, and requires low operating and maintenance costs. Fuel cell setup can operate in a reversible mode as electrolyzer cells for hydrogen production, although normally the setups are designed for one purpose only.

Notwithstanding all the mentioned advantages, several issues inhibit the wide applications of hydrogen and fuel cell technology. The main issues are the relatively short lifetime of fuel cell systems and the high capital cost. The high cost is especially related to the materials used for the construction of the device, the current limited number of hydrogen and fuel cell facilities, and the transport and storage of hydrogen.

A fuel cell consists of an electrolyte that separates two electrodes; one works as the cathode and the other one as the anode. The electrolyte can be either cationic (e.g.  $H^+$ ) or anionic (e.g.  $O^{2-}$ ,  $OH^-$ ,  $CO_3^{2-}$ ) conductor. On the fuel cells with cationic conductor electrolytes, the hydrogen from the fuel is oxidized into hydrogen ions and produced electrons on the anode. The hydrogen ions then pass through the electrolyte while the electrons pass through the external circuit. The hydrogen ions and electrons combine with oxygen from the oxidants on the cathode to produce water and heat. The flow of electrons induces the production of electric current. Meanwhile, on the fuel cells with anionic conductor electrolytes, the oxidants (e.g. oxygen) are reduced on the cathode. Then, the resulting anions pass through the electrolyte, which then combined with hydrogen from the fuel on the anode, produces water, heat, and electrons.

In electrolyzer cells, the opposite reactions occur on each electrode and the global reaction is the electrolysis of water to produce hydrogen and oxygen. Note that the cathode of fuel cell operates as the anode in the electrolyzer cell and vice versa. Thus, to avoid confusion, the electrode exposed to the oxygen is normally referred to as the oxygen or air electrode while the one exposed to the hydrogen as the hydrogen electrode. The typical reactions occurring on each electrode for both fuel cell and electrolyzer cell for the two different electrolytes are summarized in **Table i**.

**Table i** Typical reactions on the cathode and anode of fuel cells with either cationic or anionic conductor electrolyte operating as both fuel cell and electrolyzer cell.

	Cationic conductor electrolyte		Anionic conductor electrolyte	
	Fuel cell mode	Electrolysis mode	Fuel cell mode	Electrolysis mode
Oxygen electrode	$\frac{1}{2} O_2 + 2 H^+ + 2 e^- \rightarrow H_2O$ (cathode)	$H_2O \rightarrow \frac{1}{2} O_2 + 2 H^+ + 2 e^-$ (anode)	$\frac{1}{2} O_2 + 2 e^- \rightarrow O^{2-}$ (cathode)	$O^{2-} \rightarrow \frac{1}{2} O_2 + 2 e^-$ (anode)
Hydrogen electrode	$H_2 \rightarrow 2 H^+ + 2 e^-$ (anode)	$2 H^+ + 2 e^- \rightarrow H_2$ (cathode)	$H_2 + O^{2-} \rightarrow H_2O + 2 e^-$ (anode)	$H_2O + 2 e^- \rightarrow H_2 + O^{2-}$ (cathode)
Overall reaction	$\frac{1}{2} O_2 + H_2 \rightarrow H_2O$	$H_2O \rightarrow \frac{1}{2} O_2 + H_2$	$\frac{1}{2} O_2 + H_2 \rightarrow H_2O$	$H_2O \rightarrow \frac{1}{2} O_2 + H_2$

Fuel cells can be classified according to the type of electrolyte used in the system determining the operating temperature and the types of fuel [7], [10], [11]. Alkaline fuel cell (AFC), proton-exchange membrane fuel cell (PEMFC), and direct methanol fuel cell (DMFC) are among fuel cells operate at a temperature lower than 100 °C. These fuel cells have found a place on portable and mobile applications such as cars. Phosphoric acid fuel cell (PAFC) operates at a temperature between 160-210 °C and is typically used for stationary applications. Intermediate temperature fuel cells such as molten carbonate fuel cell (MCFC) and protonic ceramic fuel

cell (PCFC) operate at 600-750 °C. Lastly, the high-temperature fuel cells operate at a temperature as high as 1000 °C such as direct carbon fuel cell (DCFC) and solid oxide fuel cell (SOFC). The higher operating temperature fuel cells have higher efficiency due to faster kinetic even without the use of expensive catalysts. Moreover, the high operating temperature provides internal reforming capability which means that a wide range of fuels can be used without utilizing an external reformer. The high-temperature fuel cells are most suited for stationary power generation applications. Among fuel cells, SOFC has the highest efficiency which can reach up to 90% with the CHP system. The comparison of the electrical efficiency of several types of fuel cells and conventional power generation systems is presented in **Fig. i**.

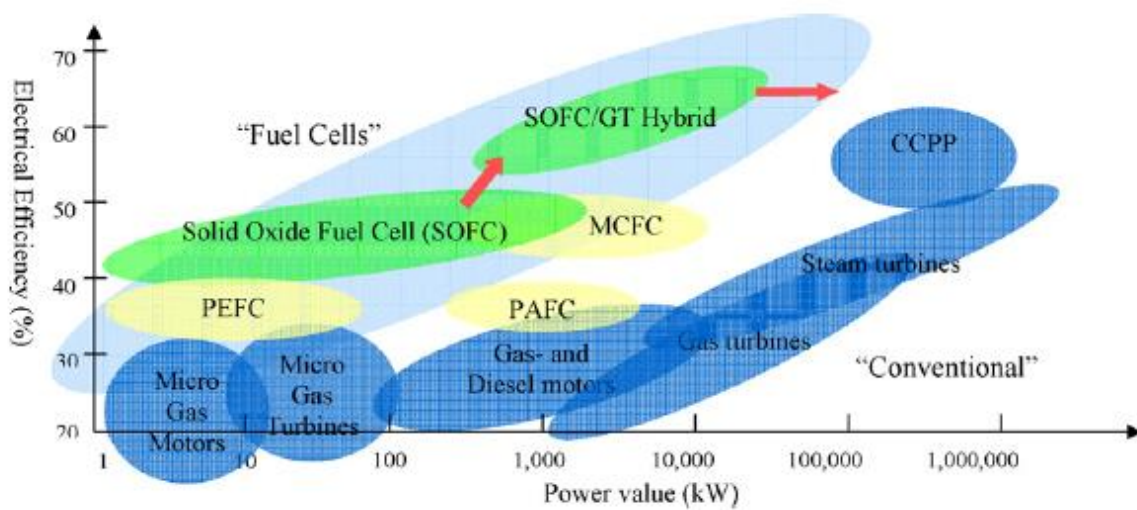


**Fig. i** Efficiency potential of various power generation technologies (Stambouli, 2011) [10]. CCPP refers to a combined cycle power plant.

The share of clean energy as energy sources increases as the year goes by. The growing market is driven by the rising demand for clean energy from the policy-makers to achieve the carbon emission reduction target. The swift technological developments which able to optimize the performance and lowering the cost of the new energy system also plays an important role. In the field of hydrogen and fuel cell technology, various research and development efforts are also being conducted to increase the availability of these systems, especially to address the issues regarding the durability and to bring down the cost. Several examples on the current research interest are efficiently and cleanly produce hydrogen from renewable sources by using renewable energy, developing systems with the internal reforming capability to tackle the problems on hydrogen transport and storage, and lowering the operating temperature of the systems while maintaining the performance and efficiency to increase the lifetime and avoid

the use of expensive materials. The main objective of this thesis is focused on the study of a material suitable for oxygen electrode of solid oxide fuel/electrolyzer cell (SOFC/SOEC) operating at a lower temperature with certain durability.

### Objectives

Solid oxide cells (SOCs), which cover both SOFC and SOEC, operate at a high temperature around 800-1000 °C. While there are several advantages, there are also several issues due to this high operating temperature which will be detailed in **Chapter 1.1**. Therefore, it is of current interest to decrease the operating temperature to around 650-750 °C. Such a system is called an intermediate temperature SOC (IT-SOC). The main challenge on the development of IT-SOC is the large overpotential of the oxygen electrode influenced by slower oxygen reduction/evolution reaction (ORR/OER) as operating temperature goes down. To overcome this challenge, it is hence important to work with materials which have good intrinsic properties at lower temperature and also to vary the microstructures of the electrode as both factors are important to determine the kinetics of ORR/OER (see **Chapter 1.2**). In this work, LaPrNiO<sub>4+δ</sub> (LPNO) is chosen as the material for the oxygen electrode due to its intrinsic properties and chemical stability in the range of the operating temperature (see **Chapter 1.3**). The durability of the materials under polarization, temperature, and time is also important to be understood since one of the issues on the development of fuel cell, in general, is their relatively short lifetime. Thus, based on these facts, the objectives of this thesis are as follow:

- To improve the LPNO oxygen performance by improving the microstructure and varying the architectural designs of the electrode.
- To do a comprehensive study on the durability of LPNO as an oxygen electrode material under polarization, temperature, and time in symmetrical fuel and electrolysis cells.
- To do preliminary durability investigation in real electrolysis cells.

### Structure of the thesis

Besides the front pages and the introduction of the thesis, this manuscript is divided into 5 chapters. The details of each chapter are as follow:

- Chapter 1: Literature Study – This chapter is dedicated to providing the basic knowledge on the core topics of the thesis which covers the sub-chapters on solid oxide cells (SOCs), oxygen reduction/evolution reaction (ORR/OER), Ruddlesden-Popper phase materials with
-

---

more focus on the rare-earth nickelates, and the degradation mechanisms on two types of MIEC (mixed ionic and electronic conductor) oxygen electrode materials: the under-stoichiometric and over-stoichiometric ones.

- Chapter 2: Fabrication and Characterization Techniques – In this chapter, the detailed explanation of the fabrication and characterizations of the electrodes is provided. The chapter starts with an explanation of the electrolyte materials that were used in the study, followed by a presentation of the basic principles and detailed parameters of screen printing (SP) and electrostatic spray deposition (ESD) as the fabrication techniques. The microstructural characterization techniques by scanning electron microscopy (SEM) and focused ion beam-scanning electron microscopy (FIB-SEM) tomography follow next. Afterwards, the description of several structural characterizations such as laboratory X-ray diffraction (XRD) in both room temperature and high temperature, and synchrotron-based X-ray diffraction and fluorescence (including the preparation procedures of the lamellae by plasma-focused ion beam (p-FIB)) are given. The last parts of this chapter include the electrochemical characterization by electrochemical impedance spectroscopy (EIS) as well as the details on the long-term durability tests.
- Chapter 3: Improving the Electrode Performance by Improving the Microstructure and Electrode Designs – This chapter explains in detail the experimental results on the improvement of the LPNO electrode performance in various ways. After the introduction of the chapter, several preliminary results on the sample preparation by SP and ESD are described. It is then followed by the results of structural characterization on LPNO powder as well as ESD and SP layers. Afterwards, a brief explanation of the equivalent circuit model for the EIS data fitting is provided. The following sub-chapters consist of the four main results on the correlation between the electrode performance to the electrode/electrolyte interface, the presence of secondary higher-order nickelate phase in the ESD layer, the current collector layer (CCL) microstructure, and the architectural designs. The summary and conclusions of this chapter are then given at the end. Large parts of this chapter have been published in the Journal of Electroanalytical Chemistry (<https://doi.org/10.1016/j.jelechem.2019.113373>).
- Chapter 4: Durability Study on the Symmetrical and Complete Cells – In this chapter, the results of a long-term durability test in fuel cell and electrolysis modes in a symmetrical configuration are presented. A preliminary study of the durability of the LPNO electrode in two complete cells using different GDC barrier layers operating in electrolysis mode is

described afterwards. Parts of this chapter have been published in the Journal of Power Sources (<https://doi.org/10.1016/j.jpowsour.2020.227724>).

- Chapter 5: Post-mortem Structural and Microstructural Characterizations – This last chapter is dedicated to the post-mortem analysis of the samples after durability tests. The chapter is divided into two sub-chapters: (i) microstructural characterizations by SEM and FIB-SEM and (ii) structural characterizations by XRD,  $\mu$ -XRD, and  $\mu$ -XRF. A comparison between the aged samples and the pristine electrode is also performed here. Large parts of this chapter have been published in the Journal of Power Sources (<https://doi.org/10.1016/j.jpowsour.2020.227724>).

In the last part of the manuscript, global conclusions and perspectives based on this work are given. Some classical techniques are described in appendices.

---

# CHAPTER 1: LITERATURE STUDY

This chapter is dedicated to providing the basic knowledge on the core topics of the thesis which covers the sub-chapters on solid oxide cells (SOCs), oxygen reduction/evolution reaction (ORR/OER), Ruddlesden-Popper phase materials with more focus on the rare-earth nickelates, and the degradation mechanisms on two types of MIEC (mixed ionic and electronic conductor) oxygen electrode materials: the under-stoichiometric and over-stoichiometric ones.

### 1.1 Fundamentals of solid oxide cell (SOC)

Solid oxide cell (SOC) is an electrochemical energy-conversion system which can operate reversibly as a fuel cell for power generation (solid oxide fuel cell or SOFC) and an electrolysis cell for hydrogen production (solid oxide electrolysis cell or SOEC). It is characterized by a solid, oxygen-ion conducting ceramic as its electrolyte which is sandwiched in between air/oxygen electrode and fuel/hydrogen electrode [8], [11], [13]. The use of all solid materials resulting in the compact and flexible cell configuration (e.g. planar, tubular, corrugated) [13]. In addition, no corrosive liquids are involved in the system. SOC is mainly used for stationary applications [14]. The illustrations of SOC and its basic operating principle as both SOFC and SOEC are shown in **Fig. 1.1a-b**.

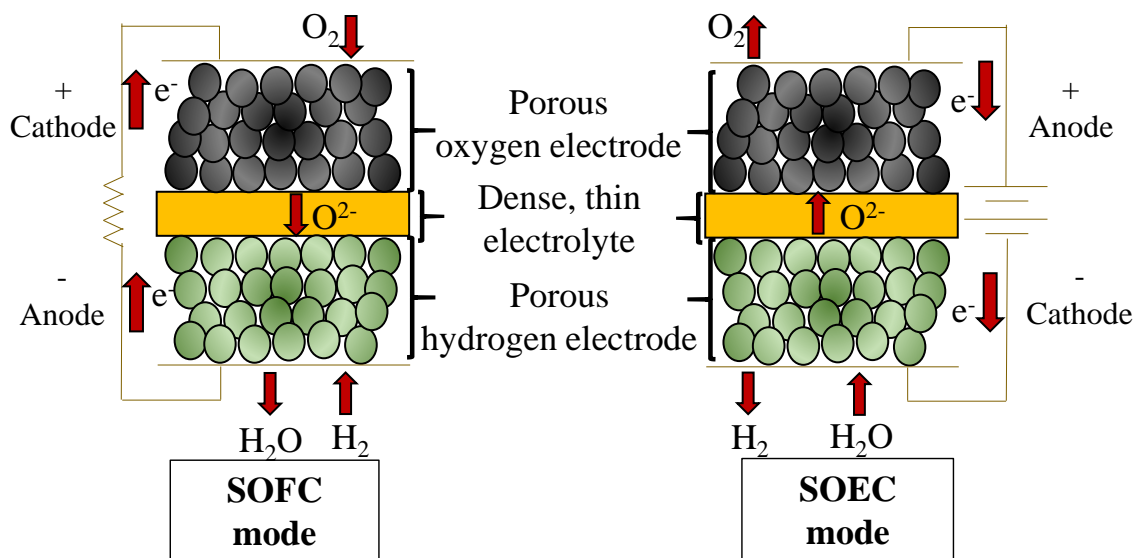


**Fig. 1. 1** The illustrations of solid oxide cells (a) operating as a fuel cell (SOFC) and (b) operating as electrolysis cell (SOEC).

As a fuel cell, the oxygen, either pure or containing in air, is reduced to oxygen ions in a process called oxygen reduction reaction (ORR) at the oxygen electrode. The oxygen ions are then transported through the ionic conducting electrolyte to the hydrogen electrode where they react with the fuel (normally hydrogen but can also be carbon monoxide (CO), hydrocarbons, or alcohols) to produce either water or carbon dioxide ( $CO_2$ ). The reduction-oxidation (redox) reaction on each electrode resulting in the flow of electrons from the hydrogen electrode to the oxygen electrode that produces direct-current (DC) electricity. On the other hand, DC electricity is required for the electrolysis of water at the hydrogen electrode, producing hydrogen and oxygen ions. The oxygen ions are then transported through the electrolyte and

oxidized into oxygen gas at the oxygen electrode through a process called oxygen evolution reaction (OER). The overall reaction in SOFC and SOEC can be found in the two last columns in **Table i** in the Introduction part of this manuscript.

SOC normally operates at high temperatures between 800 to 1000 °C [11], [14]. Compared to the other types of fuel/electrolysis cells, SOC has the highest efficiency, especially in a combined heat and power (CHP) system, thanks to the high operating temperature. Moreover, an expensive catalyst (e.g. platinum) to assist the reaction is not necessary. An SOFC also has the capability for internal reforming, leading to flexibility on the choice of fuel [13], [14]. However, the high operating temperature means that the materials should not only exhibit excellent electrical and electrochemical properties, but also good chemical, thermal, and mechanical stability to ensure a longer lifetime of the system in operation. At the same time, from the techno-economic point of view, the cost of materials should also be low and they should be able to be fabricated with ease at low fabrication cost [11]. SOC also has an issue regarding the slow start-up and shutdown cycles which limits its portability. Thus, it is of current interest to reduce the operating temperature down to 650-750 °C (intermediate temperature SOC, IT-SOC) and even lower to below 650 °C (low-temperature SOC, LT-SOC) [15]. Indeed, lowering the operating temperature brings down the cost of materials and prolongs the lifetime of the system. However, it also reduces the kinetics of the reactions taking place in the system because of the higher polarization losses from the electrolyte and electrodes at lower temperature, as will be explained in more detail in §1.2. Hence, new materials developments have been extensively studied as an effort to address this issue.

The detailed explanations on each component in an SOC are given hereafter.

### 1.1.1 Electrolyte

As previously mentioned, the electrolyte of an SOC should be able to conduct only oxygen ions, hence, high ionic conductivity and low electronic conductivity are required for this purpose. The oxygen ions are transported through the electrolyte via an oxygen vacancy hopping mechanism which is a thermally-activated process [8]. Moreover, it should also be fully dense with no open porosity to avoid any cross-diffusion of the fuel and oxidant compounds. Since the electrolyte is in contact with both oxygen and hydrogen electrodes, it should be chemically inert, have a similar thermal expansion coefficient (TEC), and have good mechanical properties with respect to the electrode materials. The electrolyte should also be chemically and structurally stable under both oxidizing and reducing environments. Reliable

---

mechanical properties (i.e. high tensile strength and toughness) are also necessary to be able to withstand thermal and mechanical stresses during cell fabrication and operation [8], [11].

Several common materials for SOC are the fluorite structure oxides (e.g. stabilized zirconia  $\text{ZrO}_2$ , doped ceria  $\text{CeO}_2$ , doped  $\text{Bi}_2\text{O}_3$ ) and perovskites (e.g. doped  $\text{LaGaO}_3$ ) [8], [11]. The dopant enhances the ionic conductivity and phase stability of the electrolyte materials. The material that has been widely used in practice is 3-10 mol% yttria-stabilized zirconia ( $\text{Y}_2\text{O}_3\text{-ZrO}_2$ , YSZ) due to its excellent stability. Among this family of material, 8 mol% YSZ (8YSZ) with cubic structure has the highest ionic conductivity. However, compared to other ceramics, the ionic conductivity of 8YSZ is far from the best and it is not good enough for operation at intermediate and lower temperature as indicated in **Table 1.1**. Moreover, there is also an issue of reactivity when lanthanum-based material is used for the electrode, such as the commonly used  $\text{La}_{1-x}\text{Sr}_x\text{Co}_{1-y}\text{Fe}_y\text{O}_{3-\delta}$  (LSCF), forming an insulating phase  $\text{La}_2\text{Zr}_2\text{O}_7$ . For these reasons, another electrolyte material is preferred especially for the development of IT-SOC and LT-SOC. One such material is the gadolinium-doped ceria ( $\text{Ce}_{1-y}\text{Gd}_y\text{O}_{2-y/2}$ , GDC). The GDC with the addition of 10 mol% gadolinium as a dopant has been found to be a good candidate for electrolyte due to its sufficiently high ionic conductivity, around 4-5 times higher than YSZ [16], [17]. Moreover, GDC is also chemically stable in operation and compatible with various electrode materials. The main drawback of GDC is the reduction of  $\text{Ce}^{4+}$  to  $\text{Ce}^{3+}$  in a highly reducing environment especially at a temperature above 600 °C, which leads to the lattice expansion, mechanical instability, and internal short-circuit due to high electronic conductivity.

**Table 1. 1** The ionic conductivity ( $\sigma$ ) and thermal expansion coefficient (TEC) of several electrolyte materials.

Electrolyte material	$\sigma$ , $\text{S cm}^{-1}$ (T, °C)	TEC, $1 \times 10^{-6} \text{ K}^{-1}$
8 mol% $\text{Y}_2\text{O}_3\text{-ZrO}_2$ (8YSZ)	0.052 (800), 0.178 (1000) [11]	10.5 [18]
$\text{Ce}_{0.9}\text{Gd}_{0.1}\text{O}_{2-\delta}$ (GDC)	0.0095 (500), 0.0253 (600), 0.0544 (700) [16]	12.4 [8]
$(\text{La}_{0.9}\text{Sr}_{0.1})\text{Ga}_{0.8}\text{Mg}_{0.2}\text{O}_{3-\delta}$	0.121 (800), 0.316 (1000) [11]	10.4 [8]
$(\text{La}_{0.9}\text{Sr}_{0.1})\text{Ga}_{0.83}\text{Mg}_{0.17}\text{O}_{3-\delta}$	0.17 (800) [11]	-
25 mol% $\text{Er}_2\text{O}_3\text{-Bi}_2\text{O}_3$	0.37 (700) [11]	-

### 1.1.2 Air/oxygen electrode

The air/oxygen electrode is where the ORR/OER takes place. As will be explained in more detail in §1.2, the reactions involve three different species which are gas, electrons, and ions at

reaction sites called triple-phase boundary (TPB). Thus, the material for the oxygen electrode should be porous to allow gas transport. The ORR/OER is considered to be responsible for the majority of cell voltage losses, thus the choice of material for oxygen electrode with high electrocatalytic activity is important to enhance the cell performance and efficiency. The electrode should also have high electronic conductivity to ensure the electron flows to/from the reaction sites from/to the external electrical circuit. High oxygen ion conductivity is not compulsory, but its presence can significantly extend the reaction sites and, as a consequence, increased the kinetics of reactions and electrode performance. The oxygen electrode should also have similar TEC with the electrolyte to ensure compatibility. Good chemical stability during fabrication and operation is also important. The properties, i.e. electronic and ionic conductivities, thermal expansion coefficient, oxygen diffusion coefficient, and surface exchange coefficient, of several oxygen electrode materials are listed in **Table 1.2**.

**Table 1. 2** The electronic conductivity ( $\sigma_e$ ), ionic conductivity ( $\sigma_{io}$ ), thermal expansion coefficient (TEC), oxygen diffusion coefficient ( $D^*$ ), and surface exchange coefficient ( $k^*$ ) of several oxygen electrode materials.

O <sub>2</sub> electrode material	$\sigma_e$ , S cm <sup>-1</sup> (T, °C)	$\sigma_{io}$ , S cm <sup>-1</sup> (T, °C)	TEC, 1 x 10 <sup>-6</sup> K <sup>-1</sup>	$D^*$ , cm <sup>2</sup> s <sup>-1</sup> (T, °C)	$k^*$ , cm s <sup>-1</sup> (T, °C)
La <sub>0.65</sub> Sr <sub>0.35</sub> MnO <sub>3</sub> (LSM)	102 (800) [17]	1.7 x 10 <sup>-8</sup> (800) [17]	12.3 [17]	4 x 10 <sup>-14</sup> (900) [17]	5 x 10 <sup>-8</sup> (900) [17]
La <sub>0.6</sub> Sr <sub>0.4</sub> Co <sub>0.2</sub> Fe <sub>0.8</sub> O <sub>3-<math>\delta</math></sub> (LSCF)	302 (800) [17]	8 x 10 <sup>-3</sup> (800) [17]	17.5 [17]	2.5 x 10 <sup>-8</sup> (800) [17]	5.6 x 10 <sup>-6</sup> (800) [17]
La <sub>2</sub> NiO <sub>4+<math>\delta</math></sub> (LNO)	70 (700) [19]	1.8 x 10 <sup>-2</sup> (700) [20]	13.8 [21]	3 x 10 <sup>-8</sup> (700) [22]	0.5 x 10 <sup>-6</sup> (700) [22]
Pr <sub>2</sub> NiO <sub>4+<math>\delta</math></sub> (PNO)	100 (700) [22]	-	-	5 x 10 <sup>-8</sup> (700) [22]	2 x 10 <sup>-6</sup> (800) [22]
La <sub>3</sub> Ni <sub>2</sub> O <sub>7-<math>\delta</math></sub> (L3N2)	90 (700) [19]	-	13.2 [21]	-	-
La <sub>4</sub> Ni <sub>3</sub> O <sub>10-<math>\delta</math></sub> (L4N3)	170 (700) [19]	-	13.2 [21]	-	-

A pure electronic conductor that is used the most as oxygen electrode material is strontium-doped lanthanum manganite, La<sub>1-x</sub>Sr<sub>x</sub>MnO<sub>3</sub> (LSM). It has a perovskite-type structure, high electronic conductivity, and negligible ionic conductivity. Thus, the TPB where the reactions

take place is restricted only at the electrode/electrolyte interface where the gas, electrons, and ions can be present at the same time. To extend the reaction site beyond the electrode/electrolyte interface, a composite of pure electronic conductor, i.e. LSM, and pure ionic conductor, i.e. YSZ, can be used as the oxygen electrode material. Another option is by using mixed ionic and electronic conductor (MIEC) such as  $\text{La}_{1-x}\text{Sr}_x\text{Co}_{1-y}\text{Fe}_y\text{O}_{3-\delta}$  (LSCF) or rare-earth nickelates  $\text{Ln}_2\text{NiO}_{4+\delta}$  ( $\text{Ln} = \text{La, Pr, Nd}$ ). The mixed conducting properties of MIEC arise from the presence of either oxygen vacancy (oxygen under-stoichiometry such as for LSCF) or interstitial (oxygen over-stoichiometry such as for rare-earth nickelates) resulting in high oxygen ion conductivity in addition to the high electronic conductivity.

### 1.13 Fuel/hydrogen electrode

Similar to the air/oxygen electrode, three species are also involved in the reactions to produce either water or hydrogen at the fuel/hydrogen electrode. Thus, similar requirements also apply for hydrogen electrode, i.e. it should be porous, highly catalytic for water or hydrogen production reactions, has high electronic conductivity and preferably also has high ionic conductivity, has similar TEC with the electrolyte, and is chemically stable. If hydrocarbon is used as the fuel in SOFC, the material should also possess high catalytic activity for hydrocarbon cracking, sulfur tolerance, and resistance to coking [11].

The most common material used for the hydrogen electrode is Ni-YSZ cermet. Normally, it is fabricated by mixing NiO with YSZ and reduction treatment is required before cell operation. Ni metal exhibits high catalytic activity and high electronic conductivity ( $2 \times 10^4 \text{ S cm}^{-1}$ ) [11]. The addition of YSZ, which is a pure ionic conductor, not only extends the reaction sites but also prevents Ni coarsening during operation.

### 1.1.4 Sealing materials and interconnects

The seal is necessary to prevent the mixing between gases in the oxygen and hydrogen electrodes. It is normally applied on the electrolyte, thus similar TEC between the sealant and electrolyte is important. Moreover, it should also be chemically inert with respect to the other cell materials and chemically stable under operating conditions. The sealing material is normally made of glasses or glass-ceramic composites.

Interconnects are mainly used to provide an electrical connection between the stack of cells. It should have high electronic and thermal conductivities, high creep resistance, good mechanical properties, similar TEC with the other components, and structural and chemical stability under operating conditions. In a high-temperature SOC, ceramic materials are normally used for interconnections. However, the electronic and thermal conductivities of ceramic materials are low and they are also expensive. Hence, this is also one reason to lower the operating temperature to allow the use of cheaper metallic interconnects.

## 1.2 Oxygen reduction/evolution reaction

### 1.2.1 Triple-phase boundary (TPB)

The processes that occur at the oxygen electrode of SOC involve three different species: electrons, oxygen ions, and oxygen gas. In the simplest configuration, a porous electronic-conducting oxygen electrode is in contact with an ionic-conducting electrolyte and both phases are exposed to the oxygen-containing gas phase. The electrode is connected to an electrical circuit at some distance away from the electrode-electrolyte interface. For the oxygen electrode of SOC, the electrical circuit plays a role to conduct electrons to (for SOFC) or from (for SOEC) this interface. The electrolyte provides the sink for the oxygen ions from the oxygen reduction reaction (ORR for SOFC operation) or the source of oxygen ions for oxygen evolution reaction (OER for SOEC operation). Thus, the ORR/OER should take place in the vicinity of the electrode-electrolyte-gas phases interface. Since three phases are involved, these active regions where the reactions take place are called the triple-phase boundary (TPB).

To increase the contact area between electronic and ionic conducting phases, hence, extend the TPBs, a composite consisting of pure electronic (i.e. LSM) and pure ionic (i.e. YSZ) conducting phases is used as the electrode instead of a pure electronic conductor. Another approach is to use a single-phase mixed ionic- and electronic-conducting (MIEC) materials (i.e. rare-earth nickelates) which can significantly extend the active regions since the ORR/OER can take place on large parts of the electrode.

The mechanisms of ORR/OER itself are quite complex and involving several possible reaction steps which are illustrated in **Fig. 1.2** for a MIEC electrode [23]. The illustration is given for ORR, thus, equivalent reactions in reverse direction should apply for OER. The explanation for each step is given hereafter:

- (i) direct reduction of oxygen and incorporation of oxygen ions into the bulk of the electrode,
- (ii) adsorption and/or partial reduction of oxygen on the surface of the electrode phase. The partial reduction is driven by catalytic and/or electrocatalytic reactions and produces the so-called electroactive species  $O^{n-}$  where  $n$  is the unknown partial charge state of adsorbed oxygen,
- (iii) direct reduction of  $O^{n-}$  into oxygen ions which are then incorporated into the bulk of electrode,
- (iv) surface transport of the  $O^{n-}$  into TPB regions where it is fully reduced into oxygen ions, and
- (v) the charge transfer of  $O^{2-}$  from the electrode to the electrolyte.

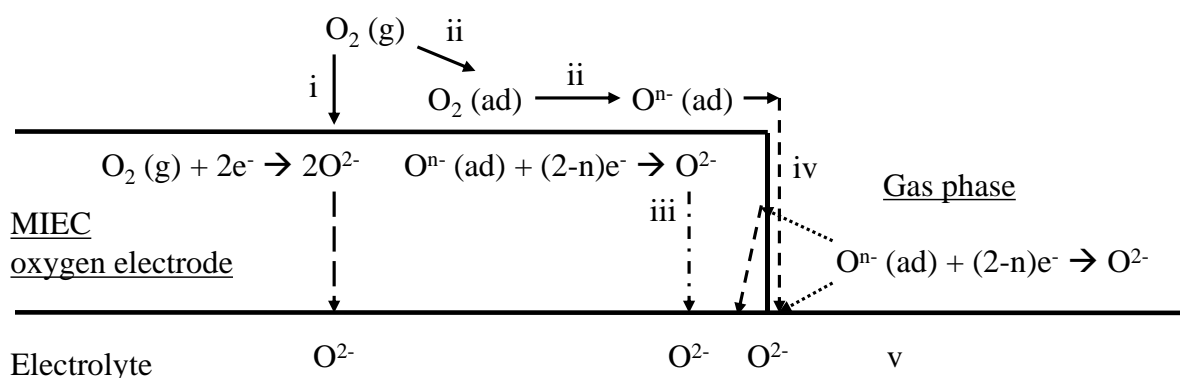


**Fig. 1. 2** The illustration of possible reaction steps for oxygen reduction reaction (ORR) in a mixed ionic and electronic conductor (MIEC) oxygen electrode (remade with modification from Takeda, *et al.* [24]).

### 1.2.2 Factors affecting oxygen reduction/evolution reaction (ORR and OER)

To start the explanation on factors affecting the ORR and OER, it is important to first understand the basic concept of the electrochemical response given by cell voltage,  $U$ , measured as a function of current density,  $i$ . The  $U$ - $i$  relation is normally presented in the polarization curve. The cell voltage itself is the sum of various electrical potential differences across the cell as current flows through the cell. The partition of each contribution is illustrated in **Fig. 1.3**.

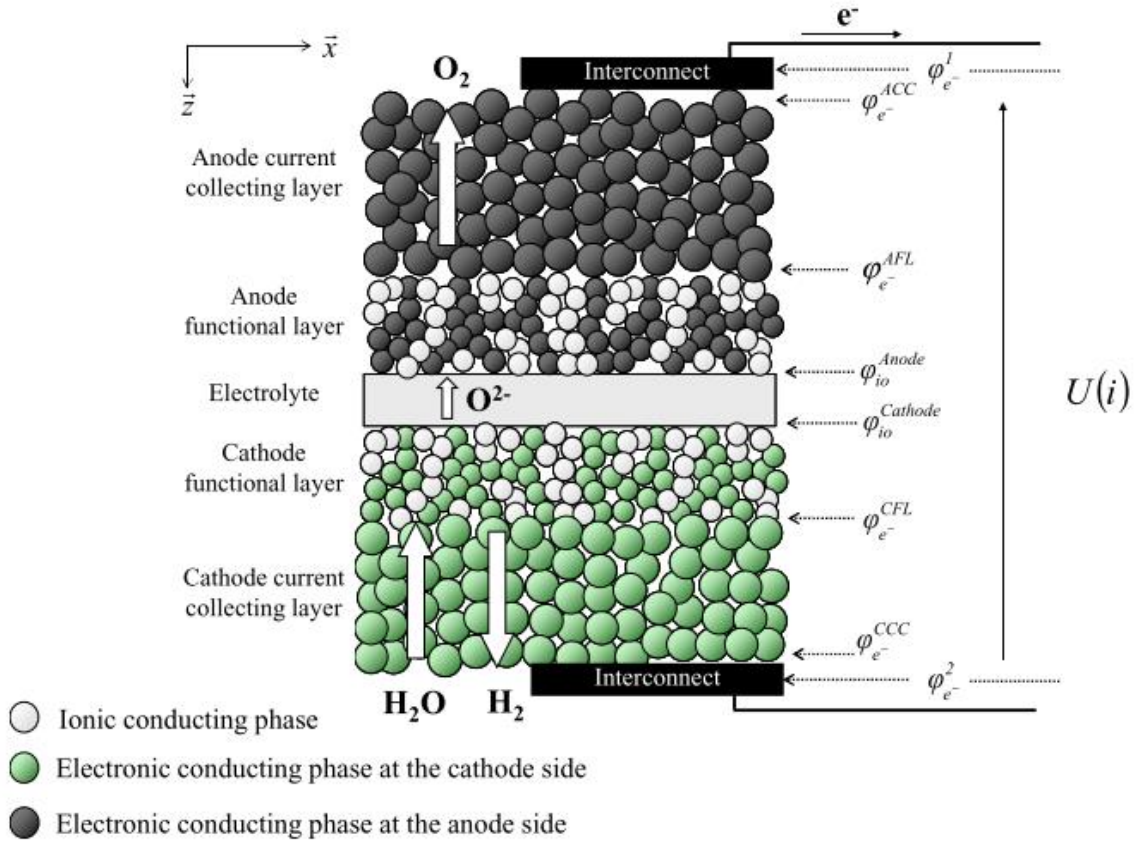


**Fig. 1.3** The illustration of electrical potential at each interface across the cell (Laurencin [25]).

Notwithstanding that this illustration represents the SOEC system, the same contributions can be applied also for the SOFC system. The differences lie on the convention of the current density signs (here, the convention is taken as  $i < 0$  for SOEC and  $i > 0$  for SOFC) and the role of each electrode (the oxygen/air electrode is always the positive electrode and operates as the anode in SOEC and as the cathode in SOFC, vice versa for the hydrogen/fuel electrode). In this illustration, the cell consists of (i) an ionic conducting electrolyte, (ii) electrodes (anode and cathode) which consist of active functional layers, which is a composite of ionic and electronic conductors, where the reactions take place and electronic-conducting current collector layer, and (iii) metallic interconnects on the side of both electrodes. The cell voltage,  $U(i)$ , can be written as following [25]:

$$\begin{aligned}
 U(i) = & (\varphi_{e^-}^1 - \varphi_{e^-}^{ACC}) + (\varphi_{e^-}^{ACC} - \varphi_{e^-}^{AFL}) + (\varphi_{e^-}^{AFL} - \varphi_{io}^{Anode}) \\
 & + (\varphi_{io}^{Anode} - \varphi_{io}^{Cathode}) + (\varphi_{io}^{Cathode} - \varphi_{e^-}^{CFL}) \\
 & + (\varphi_{e^-}^{CFL} - \varphi_{e^-}^{CCC}) + (\varphi_{e^-}^{CCC} - \varphi_{e^-}^2) = \varphi_{e^-}^1 - \varphi_{e^-}^2 \quad (\text{Eq. 1.1})
 \end{aligned}$$

Thus, it can be seen that the measured cell voltage is the electrical potential difference between the cell terminals. By considering all contributions above, the cell voltage can be decomposed as followed for both SOEC (+ sign) and SOFC (- sign) operations:

$$U = U_{rev}(x) \pm |\eta_{ohmic}(x)| \pm |\eta_{act}^{Cell}(x)| \pm |\eta_{conc}^{Cell}(x)| \quad (\text{Eq. 1.2})$$

In this equation, the cell voltage is considered to be constant along the cell length ( $x$ -direction indicated in the illustration above) which means that at a certain cell voltage, the current density is distributed along the cell length (and referred to as  $i(x)$  which is the local current density as a function of the cell length) so that Eq. 1.2 is verified at each position  $x$ . The explanation for each contribution is as follow [25]–[28]:

- The reversible voltage,  $U_{rev}$ , is the thermodynamic contribution that corresponds to the behavior of an ideal electrode. This term follows the Nernst equation and consists of the contribution at open circuit potential (OCP,  $i = 0$ ),  $E_{OCP}^{Cell}$ , and under the current ( $i \neq 0$ ),  $\Delta V_{rev}^{Cell}$ , for both anode and cathode (Eq. 1.3).

$$\begin{aligned} U_{rev} &= E_{rev}^{O_2\text{electrode}} - E_{rev}^{H_2\text{electrode}} \\ &= (E_{OCP}^{O_2\text{electrode}} + \Delta V_{rev}^{O_2\text{electrode}}) - (E_{OCP}^{H_2\text{electrode}} + \Delta V_{rev}^{H_2\text{electrode}}) \\ &= E_{OCP}^{Cell} + \Delta V_{rev}^{Cell} \end{aligned} \quad (\text{Eq. 1.3})$$

As indicated by Eq. 1.4-1.7, the reversible potential depends on the partial pressure,  $p$ , of the gases involved in the reaction on each side of the electrode. In these equations,  $R$  is the gas constant ( $8.314 \text{ J K}^{-1} \text{ mol}^{-1}$ ),  $T$  is the temperature (K), and  $F$  is the Faraday constant ( $96485 \text{ C mol}^{-1}$ ).

$$E_{OCP}^{O_2\text{electrode}} = E_0^{O_2\text{electrode}} + \frac{RT}{4F} \ln(pO_{2,i=0}) \quad (\text{Eq. 1.4})$$

$$E_{OCP}^{H_2\text{electrode}} = E_0^{H_2\text{electrode}} + \frac{RT}{2F} \ln\left(\frac{pH_{2O,i=0}}{pH_{2,i=0}}\right) \quad (\text{Eq. 1.5})$$

$$\Delta V_{rev}^{O_2\text{electrode}} = \frac{RT}{4F} \ln\left(\frac{pO_{2,i \neq 0}}{pO_{2,i=0}}\right) \quad (\text{Eq. 1.6})$$

$$\Delta V_{rev}^{H_2\text{electrode}} = \frac{RT}{2F} \ln\left(\frac{pH_{2O,i \neq 0} \times pH_{2,i=0}}{pH_{2,i \neq 0} \times pH_{2O,i=0}}\right) \quad (\text{Eq. 1.7})$$

The contribution under current arises from the polarization due to changes in the gas composition. In SOEC operation, O<sub>2</sub> is produced on the oxygen electrode (anode) and thus increases the O<sub>2</sub> partial pressure and, in consequence,  $\Delta V_{rev}^{O_2\_electrode} > 0$ . Meanwhile, steam is consumed and H<sub>2</sub> is produced on the hydrogen electrode (cathode) leading to  $\Delta V_{rev}^{H_2\_electrode} < 0$ . The changes in both electrodes resulting in an increase in the overall cell voltage. The opposite explanations are true for SOFC operation which leads to the decrease of the cell voltage.

This term is the theoretical voltage for the cell to operate. However, in real operation, the voltage deviates from this theoretical value due to the polarization arises from the operating condition and the nature of the materials involved. Moreover, since it only considers the thermodynamics, it cannot predict the rate or kinetics. The polarization, which is also called overpotentials ( $\eta$ ), consists of several terms which will be explained in the next bullet points.

- The ohmic overpotentials,  $\eta_{ohmic}$ , originating from the polarization due to the ionic resistances of the electrolyte ( $R_{electrolyte}$ ), electronic resistance of the current collector layer ( $R_{ACC}^{eff}$  and  $R_{CCC}^{eff}$ ), and contact resistance of the interconnect/electrode ( $R_c^{Anode}$  and  $R_c^{Cathode}$ ) under the flow of current. This polarization is ohmic which means that it describes the opposition of each material to the flow of electric current. It follows Ohm's law and it is described by Eq. 1.8. The electrolyte and current collector layer resistances are proportional to the ratio between its thickness ( $l$ ) and its ionic or electrical conductivity ( $\sigma_{io}$  or  $\sigma_{e^{-}^{eff-CC}}$ ) (Eq. 1.9 and 1.10).

$$\eta_{ohmic} = (R_{electrolyte} + R_{ACC}^{eff} + R_{CCC}^{eff} + R_c^{Anode} + R_c^{Cathode}) \times |i(x)| \quad (\text{Eq. 1.8})$$

$$R_{electrolyte} = \frac{l_{electrolyte}}{\sigma_{io}} \quad (\text{Eq. 1.9})$$

$$R_{CC}^{eff} = \frac{l_{CC}}{\sigma_{e^{-}^{eff-CC}}} \quad (\text{Eq. 1.10})$$

The term 'effective' electrical conductivity of the current collector layer refers to the combination of the intrinsic properties of the material and the microstructure of the layer.

Since the current collector layer normally exhibits high electrical conductivity, its contribution to the loss can be considered to be negligible. The electrolyte resistance can be minimized by choosing materials exhibiting high ionic conductivity and/or by reducing its thickness. The interconnect/electrode contact resistance is relevant mainly for the stack of cells and arises due to various causes such as the properties of the material, the contact load, and the contact geometry. As indicated by Eq. 1.2, the ohmic polarization causes the voltage gain in SOEC and voltage drop in SOFC.

- The activation overpotential,  $\eta_{act}$ , is predominantly related to the kinetics of the reactions at the electrodes. As mentioned in §1.2.1, several steps are involved in the reaction in the oxygen electrode only while another set of reaction steps take place in the hydrogen electrode. Each step in both electrodes may have its contribution to the activation polarization.

The rate of the reaction is proportional to the current density. The polarization at a certain value of current density or vice versa is used to quantify the rate. The relation between the polarization and the current density for a simple charge transfer can be expressed in the widely known polarization equation called the Butler-Volmer equation. Activation polarization depends on the nature of the reaction and it is more pronounced at lower current density. By considering this factor, Eq. 1.11 shows the Butler-Volmer equation derived for activation polarization.

$$i(x) = i_0 \left[ \exp \left( \frac{(1 - \alpha^{Anode}) 2F(\eta_{act}^{Cell}(x))}{RT} \right) - \exp \left( \frac{-\alpha^{Cathode} 2F(\eta_{act}^{Cell}(x))}{RT} \right) \right] \quad (\text{Eq. 1.11})$$

In this equation,  $\alpha$  is the symmetrical factor which is usually taken as 0.5 and  $i_0$  is the current exchange density which depends on the temperature, atmosphere, and the electrochemical activity of the materials.

In a simple redox reaction, the kinetics of the reaction is limited by the charge transfer. However, in a complex system like SOC, this is not the case because non-charge-transfer processes, such as solid-state diffusion and chemical reaction, are also involved which

might limit the reaction kinetics. Hence, the Butler-Volmer equation cannot fully explain the kinetics for this system.

The activation overpotential of the oxygen electrode is considered to be more important because OER and ORR are considered to be more difficult than the reactions on the hydrogen electrode. One way to reduce the contribution of activation overpotential is by using MIEC for the electrode material. As explained in §1.2.1, the reactions in MIEC are extended to the whole electrode instead of restricted on the vicinity of TPB lines, thus lowering the activation overpotential as a result. For the IT-SOC system, lower operating temperature means that the activation polarization increases due to the higher activation energy for the reaction to occur. Thus, for this system, the choice of materials with high electrochemical activity even at intermediate temperature is important.

- The concentration overpotential,  $\eta_{conc}$ , arises from the gas transport between the bulk gas phase and the surface of the electrode as well as inside the porous electrode. The gradient of partial pressure exists between the reaction sites (i.e. electrode surface) and the bulk gas phase which arises from the supply or depletion of gas due to reactions and diffusion. This effect is more significant at a higher current density where the reaction rate is faster. From the derivation of the Butler-Volmer equation, the gradient of partial pressure induces electrode polarization.

As the current density increases, the reaction rate becomes faster up to a certain value of current density, called limiting current density  $i_{lim}$ , at which the reaction diverges due to the lack of available gas for reaction (for reduction reactions). The limiting current depends on the surface area and thickness of the electrode, as well as diffusion coefficient and the bulk concentration of the gas (in SOEC: steam on hydrogen electrode, in SOFC: O<sub>2</sub> on oxygen electrode and H<sub>2</sub> on hydrogen electrode).

From the explanations above, the cell voltage shows the deviation from the ideal behavior of the electrode due to the ohmic losses, and activation and concentration overpotentials. This deviation is directly related to the efficiency of the cell and is proportional to the current density. In SOFC, the polarization results in the decrease of the cell voltage which means that the work/energy that can be recovered from the processes is less than the theoretical calculation. Meanwhile, the increase of the cell voltage due to the polarization in SOEC means that more energy than the thermodynamic prediction is required for the reactions to take place.

A model developed by Adler-Lane-Steele (ALS model) explains the electrode kinetics specifically for porous MIEC oxygen electrode and takes into account the polarization due to ohmic losses, charge transfer processes, and non-charge-transfer processes [29]. From this model, the mechanism of the ORR and OER seems to be governed by O<sub>2</sub> exchange at electrode/gas interface and transport of O<sup>2-</sup> across the electrode through solid-state diffusion. The electrode kinetics related to the non-charge-transfer processes, which is expressed as its impedance  $R_{chem}$ , is proportional to the intrinsic transport properties of the electrode material and the microstructural properties of the electrode through the equation below:

$$R_{chem} = \frac{RT}{2F^2} \sqrt{\frac{\tau}{(1-\varepsilon)ak_oD_o c_o^2}} \quad (\text{Eq. 1.11})$$

Thus, the kinetics of the reaction on the oxygen electrode depends mainly on two factors: (i) the intrinsic properties of the electrode materials such as the oxygen concentration in the lattice ( $c_o$ ) and the transport properties (oxygen surface exchange ( $k_o$ ) and oxygen diffusion coefficient ( $D_o$ )); (ii) the microstructure of the electrodes (porosity ( $\varepsilon$ ), specific surface area ( $a$ ), tortuosity factor ( $\tau$ )).

### 1.3 Ruddlesden-Popper phase: rare-earth nickelates

Ruddlesden-Popper (RP) phase, which was named after Ruddlesden and Popper who previously reported the series of titanates  $\text{Sr}_{n+1}\text{Ti}_n\text{O}_{3n+1}$  [30], is a homologous series of compounds which are structurally similar to the titanates. These compounds are based on  $\text{K}_2\text{NiF}_4$  structure and have a general formula of  $\text{A}_{n+1}\text{B}_n\text{X}_{3n+1}$ , where A is an alkaline-earth or rare-earth metal cation (e.g. Ca, Sr, Ba, La-Lu), B is a transition metal cation (e.g. Ti, Ni, Mn, Fe), X is an anion (e.g. O), and  $n = 1, 2, 3, \infty$  [31]. The compound consists of alternating  $n$  numbers of perovskite layers  $(\text{ABO}_3)_n$  with a rock-salt AO intergrowth along the crystallographic  $c$  direction as shown in **Fig. 1.4a-b** [21], [31], [32]. The relatively open structural framework of the RP structure provides the over-stoichiometry ( $\delta$ ) of oxide ions at the interstitial sites on the rock-salt layers, resulting in high ionic conductivity. The oxygen over-stoichiometry also resulting in B cation oxidation and generating electron-hole charge carriers which contribute to the electronic conductivity [33]. Both ionic and electronic conducting properties indicating that RP phase is a MIEC.

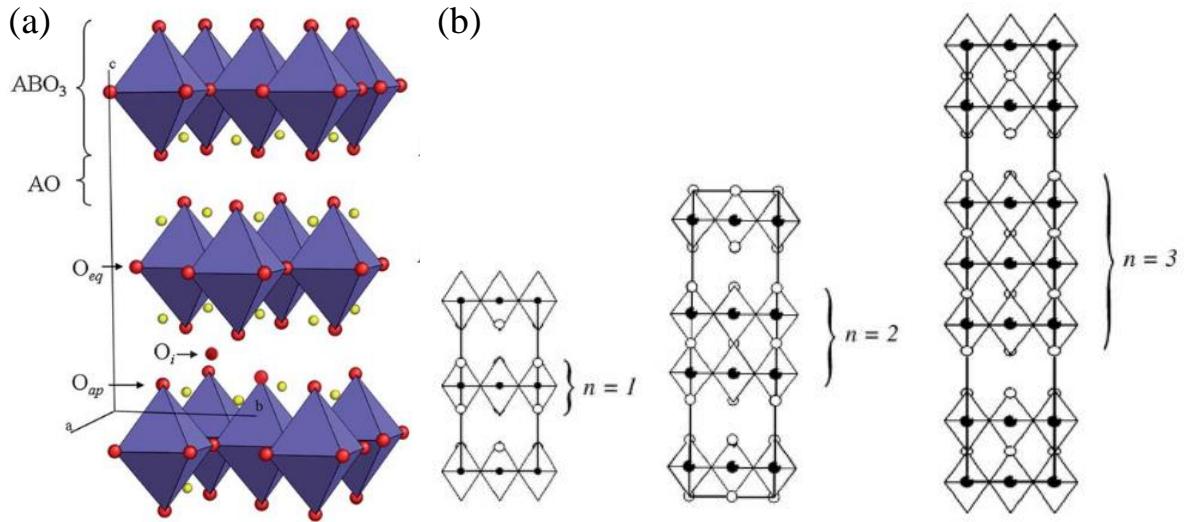


**Fig. 1. 4** (a) Polyhedral view of a Ruddlesden-Popper structure of general formula  $A_{n+1}B_nO_{3n+1}$  consisting of  $nABO_3$  perovskite layers sandwiched between two  $AO$  rock-salt layers. Oxygen in equatorial ( $O_{eq}$ ), apical ( $O_{ap}$ ), and interstitial ( $O_i$ ) sites have been highlighted (Taranc3n, *et al.* [32]). (b) The illustrations showing the  $ABO_3$  layers for  $n = 1, 2,$  and  $3$  (Amow, *et al.* [34]).

Among the family of RP phases, the first-order ( $n = 1$ ) rare-earth nickelates  $Ln_2NiO_{4+\delta}$  ( $Ln = La, Pr, Nd$ ) has been gained interest as a material suitable for the oxygen electrode of IT-SOC. There have been several studies on the solid solution of lanthanum-praseodymium nickelate,  $La_{2-x}Pr_xNiO_{4+\delta}$  ( $0 \leq x \leq 2$ ), which shows a promising electronic and ionic conductivity as well as oxygen transport properties (oxygen diffusion coefficient and surface exchange coefficient) even at an intermediate temperature as indicated in **Table 1.2** in §1.1.2. Moreover, the TECs of these compounds are close to those of YSZ and GDC electrolytes. The conductivities and the transport properties of the La-Pr nickelates improve as the Pr content in the compound increases. The improvement in the transport properties for Pr-rich compound can be attributed to the smaller size of Pr ions as compared to La ions which resulting in higher overstoichiometry of oxide ions ( $\delta$ ) as seen in **Table 1.3**. However, higher Pr contents in the compound lead to a less chemically stable compound [35]–[37]. The decomposition of  $La_{2-x}Pr_xNiO_{4+\delta}$  ( $0 \leq x \leq 2$ ) after heat treatment at 700 °C for 30 days as reported in the literature is given in **Table 1.3**. In this table, the electrochemical performance of the electrode, which is expressed as the polarization resistance ( $R_{pol}$ ), taken from one of the references is also given and shows a decrease of the value as Pr content increases. The thermal decomposition of La-Pr nickelates might be different depending on the fabrication technique and the microstructure

of the powder or film. However, it is well accepted that higher Pr contents resulting in a more unstable compound.

**Table 1. 3** The oxygen over-stoichiometry ( $\delta$ ), polarization resistance ( $R_{\text{pol}}$ ) at 600 °C, and thermal decomposition of  $\text{La}_{2-x}\text{Pr}_x\text{NiO}_{4+\delta}$  ( $0 \leq x \leq 2$ ) after heat treatment at 700 °C for 30 days taken from two literature.

Compound	Configuration	$\delta$	$R_{\text{pol}}$ at 600 °C ( $\Omega \text{ cm}^2$ )	Final phases	Ref.
$\text{La}_2\text{NiO}_{4+\delta}$ (LNO)	ESD layer on GDC electrolyte	0.16	3.33	Stable	[35]
	Powder	0.16		Stable	[36]
$\text{La}_{1.5}\text{Pr}_{0.5}\text{NiO}_{4+\delta}$	ESD layer on GDC electrolyte	0.18	2.37	Stable	[35]
	Powder	0.17		Stable	[36]
$\text{LaPrNiO}_{4+\delta}$ (LPNO)	ESD layer on GDC electrolyte	0.22	1.63	Stable	[35]
	Powder	0.19		$\text{LaPrNiO}_{4+\delta} + (\text{La,Pr})\text{NiO}_{3-\delta} +$ $(\text{La,Pr})_4\text{Ni}_3\text{O}_{10-\delta} + \text{Pr}_6\text{O}_{11}$	[36]
$\text{Pr}_2\text{NiO}_{4+\delta}$ (PNO)	ESD layer on GDC electrolyte	0.24	0.83	$\text{Pr}_2\text{NiO}_{4+\delta} + \text{PrNiO}_{3-\delta} + \text{NiO} +$ $\text{Pr}_6\text{O}_{11}$	[35]
	Powder	0.25		$\text{PrNiO}_{3-\delta} + \text{Pr}_4\text{Ni}_3\text{O}_{10-\delta} +$ $\text{Pr}_6\text{O}_{11}$	[36]

The crystal structures of La-Pr nickelates have been identified as orthorhombic. However, a phase transition from *Fmmm* to *Bmab* space group depending on the Pr content have been reported by Nishimoto, *et al.*, Vibhu, *et al.*, and Jacobson [22], [38], [39]. The cell parameters as a function of Pr content is shown in **Fig. 1.5** which shows that the compound with  $x \geq 1$  belongs to *Bmab* space group.

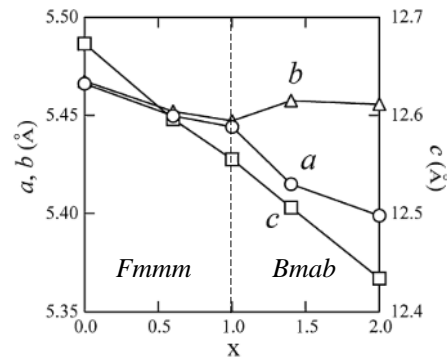


**Fig. 1.5** The cell parameters as a function of Pr content in  $\text{La}_{2-x}\text{Pr}_x\text{NiO}_{4+\delta}$  ( $0 \leq x \leq 2$ ) (Nishimoto, *et al.* [38]).

Montenegro-Hernández, *et al.* conducted a study on the reactivity of LNO and PNO with YSZ and GDC electrolyte by mixing nickelate and electrolyte powders and then heating the mixture to 900 °C for 72 h [37]. The study suggested a minor reactivity between LNO and PNO with both YSZ and GDC electrolyte. However, they also showed that the reactivity depends on the microstructure of the powder as indicated by a stronger reactivity for smaller particle size.

Besides the first-order phase, the higher-order RP phases such as  $\text{Ln}_3\text{Ni}_2\text{O}_{7-\delta}$  ( $n = 2$ ) and  $\text{Ln}_4\text{Ni}_3\text{O}_{10-\delta}$  ( $n = 3$ ) also show excellent electrochemical properties. The electrical conductivity increases with the increase of  $n$ , as seen in **Table 1.2** in §1.1.2 [19], [21], [34]. Moreover, the TECs are found to be similar to the first-order phase. The good electrochemical properties are also reflected in the electrode performance which is found to be comparable or even better than the first-order phase [40]–[43]. In terms of thermal stability, the higher-order phases are more stable as shown by no detected decomposition after heat treatment at 900 °C for 2 weeks in air, unlike for the first-order phase [34]. It is expected due to the increase of  $\text{Ni}^{3+}$  which is more stable at lower temperatures.

#### 1.4 Degradation of several MIEC oxygen electrode materials for SOC

Degradation or destabilization of the oxygen electrode is influenced by the material, its fabrication technique and microstructure, and the operating conditions [37], [44]. The cell operating conditions include the temperature, the electrode polarization, the current densities, and gas composition. Thus, it is expected that the degradation of the same material might be different in either fuel cell or electrolysis operations. It has been, for example, shown that the LSCF decomposition is higher under electrolysis current compared to fuel cell condition [45].

As a general matter, it has been suggested that the major factor on the degradation of oxygen electrode could be the oxygen partial pressure ( $p_{O_2}$ ) or the oxygen chemical potential ( $\mu_{O_2}$ ) in the material across the electrode, especially at electrode/electrolyte interface [44], [45]. The  $p_{O_2}$  or  $\mu_{O_2}$  indeed plays a key role on the catalytic activity and phase stability of the materials. It affects the electronic and ionic conductivities of the material. Besides, the phase decomposition results in passivation film and/or insulating secondary phases that can hinder or even block the electrochemical reactions [44].

In a complete cell operating as an SOEC, the degradation of the oxygen electrode becomes especially important in a high current density ( $> 0.25 \text{ A cm}^{-2}$ ). In addition to the decomposition, the cell degradation also originates from many other phenomena such as the Ni coarsening of the hydrogen electrode microstructure upon operation or the chromium poisoning of the oxygen electrode by the interconnect materials.

The degradation rate of a cell is indicated by the difference in either the cell voltage or the polarization resistance before and after the long-term test and expressed in  $\text{mV kh}^{-1}$  or  $\text{V\% kh}^{-1}$  or  $\text{m}\Omega \text{ cm}^2 \text{ kh}^{-1}$  or  $\Omega\% \text{ kh}^{-1}$ . With the developments in the SOC technology over the years, it is expected that the degradation rate of a stack in operation to be  $0.11 \text{ V\% kh}^{-1}$  by 2019 [46]. The evolutions of the degradation rate and lifetime of SOC stacks over the years are given in **Fig.1.6a-d**. For example, Jülich research center (Germany) have reported durability experiments on a two-layer short stack in fuel cell mode with degradation rates of  $0.5 \text{ V\% kh}^{-1}$  and  $2.5 \Omega\% \text{ kh}^{-1}$  for the operation of more than 100,000 hours at  $700 \text{ }^\circ\text{C}$  and  $0.5 \text{ A cm}^{-2}$  [47].

The degradation mechanism of one of the most used MIEC for oxygen electrode, LSCF, will be given in the following sub-chapter. A brief explanation of the degradation of rare-earth nickelates will be subsequently given in §1.4.2.

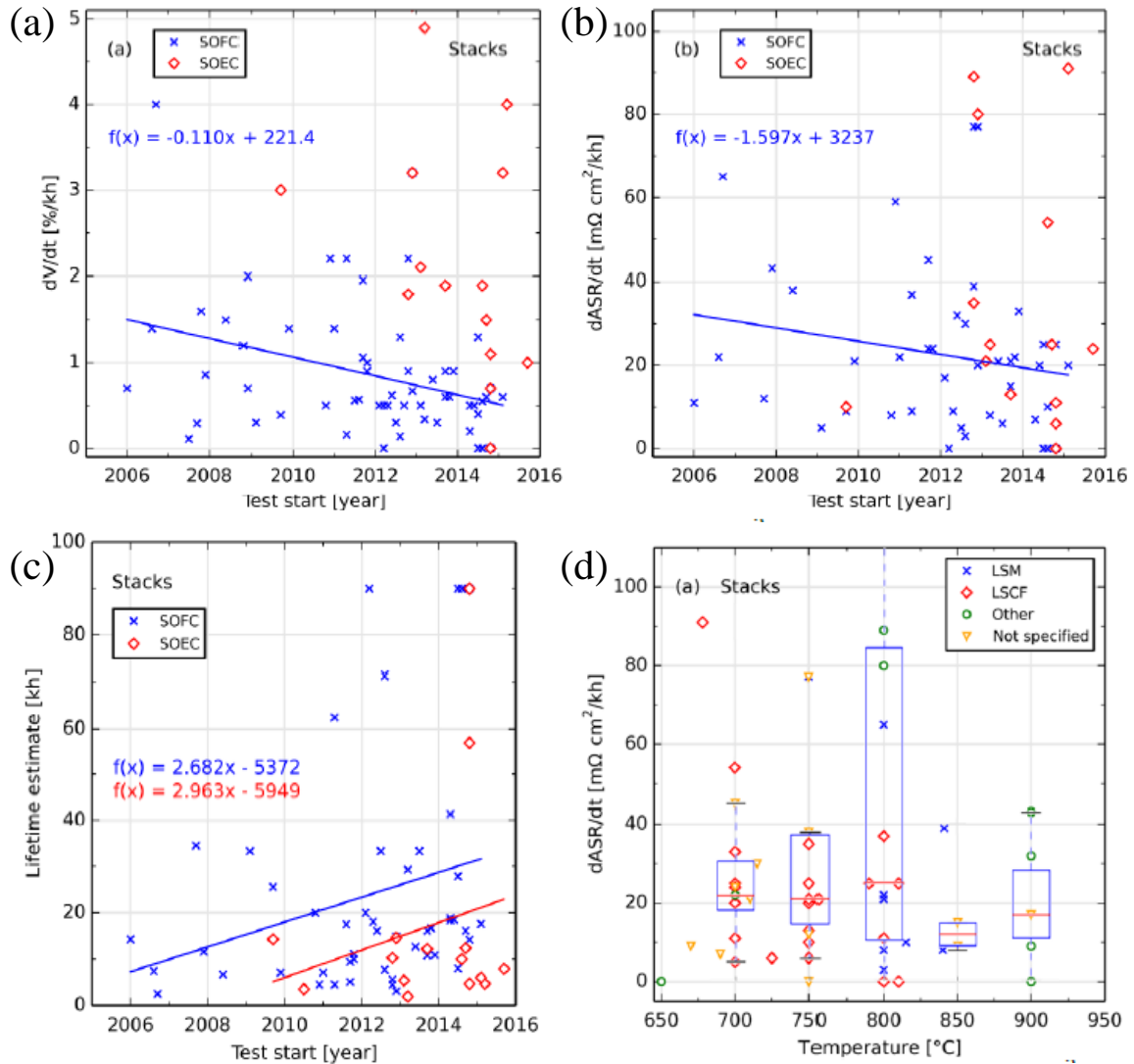


**Fig. 1. 6** Degradation rate under SOFC and SOEC operations in (a)  $\text{V\% kh}^{-1}$  and (b)  $\text{m}\Omega \text{ cm}^2 \text{ kh}^{-1}$ , as well as (c) the estimated lifetime, of various stacks versus the start date of the test taken from published articles. (d) The degradation rate of stacks versus operating temperature for various oxygen electrode materials. All graphs are taken from Skafte, *et al.* [46].

#### 1.4.1 Degradation mechanism of LSCF oxygen electrode

As one of the most vastly used oxygen material, extensive studies on the degradation of LSCF are available in the literature. It has been well understood that the strong segregation of Sr in LSCF to both electrode surface and electrode/electrolyte interface upon operation is the main cause of LSCF degradation. Moreover, LSCF reacts with YSZ electrolyte forming insulating phases such as  $\text{SrZrO}_3$  and  $\text{La}_2\text{Zr}_2\text{O}_7$ . Thus, in practice, a thin GDC barrier layer is usually

inserted in between LSCF and YSZ electrolyte. However, strong Sr diffusion is still found even with the barrier layer as indicated by the formation of  $\text{SrZrO}_3$  at the GDC/YSZ interface, especially in SOEC operating conditions. Indeed, it has been demonstrated that Sr and Co diffusions to GDC/YSZ interface are observed after an operation in electrolysis mode while such diffusion is not observed after fuel cell operation, resulting in the higher degradation rate of LSCF in SOEC operating condition. Since LSCF is characterized by its oxygen under-stoichiometry, it is suggested that the high oxygen chemical activity in SOEC operation is resulting in the decrease of the oxygen vacancy content in LSCF and driving the Sr segregation from the structure [45].

#### 1.4.2 Degradation mechanism of rare-earth nickelates

Rare-earth nickelates are one of the newly-developed materials for oxygen electrode, thus, unlike LSCF, the study on its degradation is still very limited. However, it has been shown that in contrast to LSCF, the degradation rate of these compounds is slower in electrolysis operation than in fuel cells [36], [48]. Indeed, rare-earth nickelates exhibit oxygen over-stoichiometry instead of the under-stoichiometry of LSCF, thus different behaviors are expected. For instance, Kim, *et al.* reported that the LSCF electrode deposited on GDC/YSZNi-YSZ degrades much faster than the one of LNO under the same SOEC conditions [48]. The post-mortem analyses on the aged LNO have revealed that there is no reactivity with the electrolyte. Only a decomposition of LNO into a deficient-perovskite  $\text{LaNiO}_{2.5}$  is detected, suggesting the reason why the degradation rate is slow.

Meanwhile, Vibhu, *et al.* studied the effect of La/Pr ratio on the degradation of  $\text{La}_{2-x}\text{Pr}_x\text{NiO}_{4+\delta}$  ( $x = 0, 0.5, 2$ ) symmetrical cells deposited on GDC/YSZ electrolyte in both SOFC and SOEC operating conditions [36]. It has been shown that the degradation rate is slower in electrolysis operation for all compositions while strong degradation is observed after fuel cell operation (**Fig. 1.7**). After the test in fuel cell mode, the polarization resistances increase 9, 4, and 35 times the initial values for  $x = 0, 0.5,$  and  $2,$  respectively. The post-mortem structural characterization shows that similar decomposition is observed after both operations in SOEC and SOFC for  $x = 0$  and  $0.5,$  while different phases are observed for  $x = 2$  (**Table 1.4**). It is suggested that the fast degradation in fuel cell operation is stemmed from the stronger La or Pr diffusion to the electrode/GDC interface under cathodic polarization and resulting in the formation of La-doped or Pr-doped ceria at the interface.

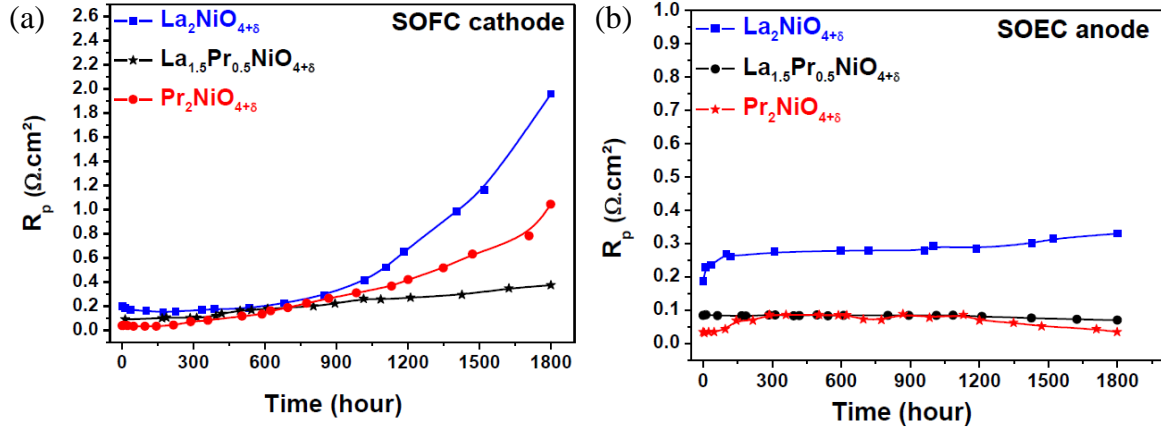


**Fig. 1. 7** The evolution of polarization resistance during operation in (a) SOFC mode and (b) SOEC mode for  $\text{La}_{2-x}\text{Pr}_x\text{NiO}_{4+\delta}$  ( $x = 0, 0.5, 2$ ). The test is carried out in air at  $700\text{ }^\circ\text{C}$  and current density ( $i_{dc}$ ) of  $\pm 300\text{ mA cm}^{-2}$  (Vibhu [36]).

**Table 1. 4** The final phases after operation in SOFC and SOEC modes for  $\text{La}_{2-x}\text{Pr}_x\text{NiO}_{4+\delta}$  ( $x = 0, 0.5, 2$ ). The test is carried out in air at  $700\text{ }^\circ\text{C}$  for 1800 h and current density ( $i_{dc}$ ) of  $\pm 300\text{ mA cm}^{-2}$  (Vibhu [36]).

$x$	SOFC	SOEC
0 ( $\text{La}_2\text{NiO}_{4+\delta}$ )	$\text{La}_2\text{NiO}_{4+\delta} + \text{La}_4\text{Ni}_3\text{O}_{10-\delta} + \text{La}_2\text{O}_3$	$\text{La}_2\text{NiO}_{4+\delta} + \text{La}_4\text{Ni}_3\text{O}_{10-\delta} + \text{La}_2\text{O}_3$
0.5 ( $\text{La}_{1.5}\text{Pr}_{0.5}\text{NiO}_{4+\delta}$ )	$\text{La}_{1.5}\text{Pr}_{0.5}\text{NiO}_{4+\delta} + (\text{La,Pr})_4\text{Ni}_3\text{O}_{10-\delta} + \text{La}_2\text{O}_3 + \text{PrO}_x$	$\text{La}_{1.5}\text{Pr}_{0.5}\text{NiO}_{4+\delta} + (\text{La,Pr})_4\text{Ni}_3\text{O}_{10-\delta} + \text{La}_2\text{O}_3 + \text{PrO}_x$
2 ( $\text{Pr}_2\text{NiO}_{4+\delta}$ )	$\text{Pr}_2\text{NiO}_{4+\delta} + \text{Pr}_4\text{Ni}_3\text{O}_{10-\delta} + \text{Pr}_6\text{O}_{11} + \text{NiO}$	$\text{Pr}_2\text{NiO}_{4+\delta} + \text{PrNiO}_{3-\delta} + \text{Pr}_6\text{O}_{11}$

---

# CHAPTER 2: FABRICATION AND CHARACTERIZATION TECHNIQUES

In this chapter, the detailed explanation of the fabrication and characterizations of the electrodes is provided. The chapter starts with an explanation of the electrolyte materials that were used in the study, followed by a presentation of the basic principles and detailed parameters of screen printing (SP) and electrostatic spray deposition (ESD) as the fabrication techniques. The microstructural characterization techniques by scanning electron microscopy (SEM) and focused ion beam-scanning electron microscopy (FIB-SEM) tomography follow next. Afterwards, the description of several structural characterizations such as laboratory X-ray diffraction (XRD) in both room temperature and high temperature, and synchrotron-based X-ray diffraction and fluorescence (including the preparation procedures of the lamellae by plasma-focused ion beam (p-FIB)) are given. The last parts of this chapter include the electrochemical characterization by electrochemical impedance spectroscopy (EIS) as well as the details on the long-term durability tests.

## 2.1 Electrolytes for symmetrical and complete cells

Both symmetrical and complete cells are studied in this work. The symmetrical cells were prepared by depositing LPNO as the oxygen electrode on both sides of the gadolinium-doped ceria ( $\text{Ce}_{0.9}\text{Gd}_{0.1}\text{O}_{2-\delta}$ ; GDC) pellet as the electrolyte. The dense GDC pellets, 1.1 mm thick and 19.6 mm in diameter, were prepared by pressing commercial powder (Praxair) followed by sintering at 1400 °C for 4 h in the air (**Fig. 2.1a**).

Meanwhile, the complete cells were prepared by depositing the LPNO electrode on top of commercial Ni-YSZ-supported half-cell (**Fig. 2.1b**). The half-cell, which is 50 mm in diameter and 250  $\mu\text{m}$ -thick, consisted of a thin ( $\sim 8 \mu\text{m}$ ) 8 mol% yttria-stabilized zirconia (8YSZ) electrolyte deposited on top of thick cermet Ni-YSZ as the hydrogen electrode. A thin GDC barrier layer was deposited on top of the YSZ electrolyte to prevent a reaction between LPNO electrode and YSZ electrolyte. The sketch of the cross-section of a half-cell is given in **Fig. 2.1c**. Two different complete cells were studied in this work, which will be explained in details in Chapter 4. The difference lies in the deposition technique of the GDC barrier layer; for CCell 1, it was deposited by screen printing and has a thickness of 4  $\mu\text{m}$ , while for CCell 2, the 400-nm thick barrier layer was deposited by RF magnetron sputtering [49].

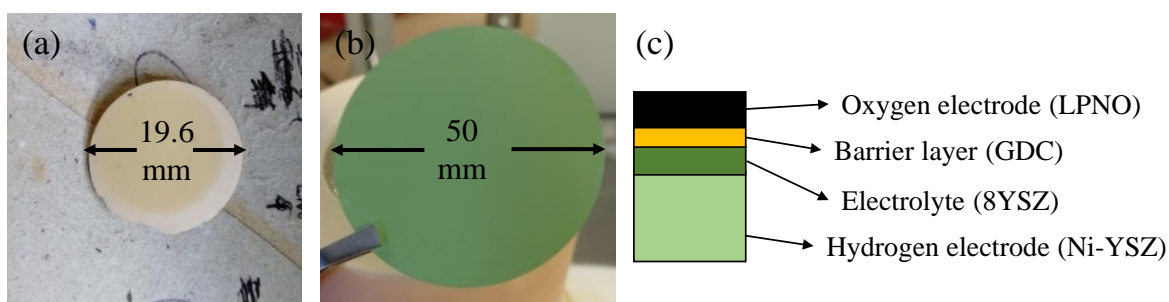


**Fig. 2. 1** (a) GDC electrolyte, (b) Ni-YSZ supported half-cell, and (c) the sketch of the cross-section of the half-cell.

## 2.2 Fabrication techniques

### 2.2.1 Sol-gel auto-combustion to prepare LPNO powder for screen printing

LPNO powder was prepared in the lab by the sol-gel auto-combustion technique. This technique is one of the most widely used methods to prepare oxide powders or nanoparticles because it is able to produce a high-purity homogeneous crystalline powder with a small particle size distribution [50]. The principle of this technique is based on propellant chemistry

and involves a combination of chemical sol-gel and subsequent combustion processes [51]. The aqueous mixture of metal salts and organic complexing agent/fuel (e.g. glycine, urea, citric acid) is stirred to ensure that the organic compound is well chelated with the metal ions. The gel is then formed from this aqueous mixture through the sol-gel process followed by the ignition of the gel to induce self-propagating combustion between the metal salts and the organic fuel. The combustion resulting in the voluminous product with a large surface area which is then ground to obtain powders.

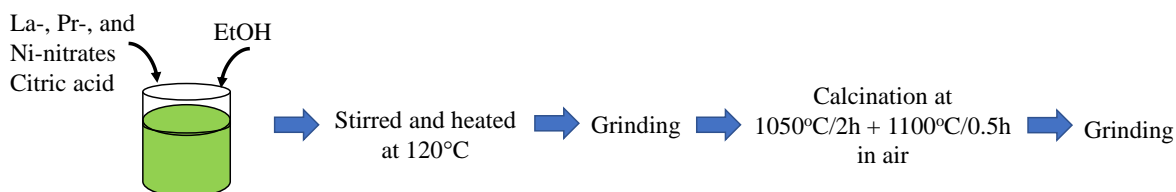


**Fig. 2. 2** Flowchart of the sol-gel auto-combustion procedure for the preparation of LPNO powder.

The procedure of sol-gel auto-combustion to prepare LPNO powder is schematically shown in **Fig. 2.2**. Firstly, the precursor powders  $\text{La}(\text{NO}_3)_3 \cdot 6\text{H}_2\text{O}$  (Acros Organic, 98.00 %),  $\text{Pr}(\text{NO}_3)_3 \cdot 6\text{H}_2\text{O}$  (Sigma-Aldrich 99.90 %), and  $\text{Ni}(\text{NO}_3)_2 \cdot 6\text{H}_2\text{O}$  (Fischer Scientific, 99.00 %) in stoichiometric ratio, as well as 30 mol. % excess of citric acid  $\text{C}_6\text{H}_8\text{O}_7$  (Acros Organic, 99.5 %) as the organic chelating agent, were dissolved in absolute ethanol ( $\text{C}_2\text{H}_5\text{OH}$  or EtOH, VWR Chemical, 99.95%) in 0.02 M (total cation concentration). This aqueous solution was then heated at around 120 °C while maintaining the stirring to evaporate the solvent to form a gel. The gel would be self-ignited to combust with the citric acid which leads to the formation of voluminous green product. The obtained product was then manually ground and calcined in air subsequently at 1050 °C for 2 h and at 1100 °C for 0.5 h. The post-calcined powder was then manually ground. In some experiments, the LPNO powder was then ball-milled in dry condition using a planetary ball mill for 2 h.

### 2.2.2 Screen printing (SP)

Screen printing (SP) is a versatile printing technique that has been vastly used in various areas from garment printing to circuit board printing. It is also one of the most widely used techniques for the deposition of electrodes for SOC due to its simplicity and flexibility. It is fast, easy to adjust the microstructure of the deposited film, and can be used for a wide range of materials.

The deposition by SP is carried out by transferring the ink containing the material that is intended to be deposited onto the substrate through a screen, as illustrated in **Fig. 2.3**. The screen is a mesh (inox 18/0 mesh 90°, JFP Microtechnic, mesh size 20  $\mu\text{m}$ ) that is made impermeable for the ink except on the area where the deposition is intended. The ink is transferred onto the substrate by passing a squeegee to spread the ink across this permeable area. The dimension and shape of the deposited film depend on the size and shape of the permeable area itself, thus SP can be adapted for the deposition of a film of any size and shape just by using a screen with a suitable permeable area. The density and thickness of the deposited film depend on the size of the mesh aperture, the viscosity of the ink, and the speed and force of the passing squeegee.

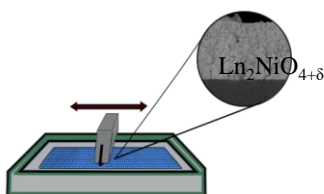


**Fig. 2. 3** Illustration of screen printing.

In this work, SP was used to deposit both GDC and LPNO. The SP inks were prepared by mixing powder (GDC or LPNO) and organic solvent (KD2921, Zschimmer, and Schwarz) with the mass ratio of 1:1 for LPNO ink and 2:3 for GDC ink, with an addition of 1 wt. % polyvinyl butyral ( $\text{C}_8\text{H}_{14}\text{O}_2$ )<sub>n</sub>, Aldrich) as a binder. The GDC powder for the ink was a commercial powder (Solvay) while the LPNO powder was prepared in the laboratory by the sol-gel auto-combustion method as described in §2.2.1. The ink mixture was stirred and then passed through the three-roll mill to further blend and homogenize the ink. The ink was then screen-printed on the substrate. The GDC SP layer was deposited by passing the squeegee onto the substrate once to obtain a film with 6  $\mu\text{m}$  in thickness. The deposited film is then thermally treated in the air at 450 °C for 2 h to remove the organic solvent and followed by further sintering at 1200 °C for 2 h to obtain good adhesion between the film and the substrate. On the other hand, the squeegee was passed twice to prepare the LPNO SP layer with a drying step at 100 °C for 10 minutes in between each SP deposition to obtain 30  $\mu\text{m}$ -thick of film. The subsequent thermal removal of the organic solvent was carried out in air at 450 °C for 2 h followed by sintering at temperature  $\geq 800$  °C depending on the type of the samples and the experiments which will be detailed in each chapter regarding the experimental results.

### 2.2.3 Electrostatic spray deposition (ESD)

Electrostatic spray deposition (ESD), schematically shown in **Fig. 2.4a**, is a film deposition technique, based on the electro-hydrodynamic laws, that is able to coat films from tenth of nanometers to tenth of micrometers [52]–[54]. The electrically conductive precursor solution is injected through a needle/nozzle on which electrical voltage is applied. When the small volume of precursor droplet on the tip of the needle is exposed to a small electric field, it is slightly deformed in shape due to the force from the solution surface tension alone. The electric field force becomes more important as the electric potential increases and when both forces reach a similar magnitude, a cone-like shape is formed on the tip of the needle. When the applied potential reaches a certain critical value (several kV), the jet of liquid is emitted from the vertex of the cone. The critical voltage depends on the physical-chemistry of the precursor solution. The jet then breaks up into spray containing small and uniform electrostatically charged droplets which will be attracted to the grounded and heated substrate by a Coulombic force, and then spread and dry on the substrate leaving the solute in the precursor solution to form a film [52]. When the flow rate of solution feeding the droplets on the tip of needle equals the flow rate of the emitted jet, a steady-state condition is achieved and the conical meniscus is usually referred to as the Taylor cone [55]. To obtain a stable cone-jet, the applied voltage should be slightly higher than the critical value. The voltage should not be too high either because it leads to the formation of multiple jets from the inside of the needle [56]. The jet breakup into spray is also more disordered because of large lateral instability [52]. The stages of the spray formation as a function of the applied voltage is illustrated in **Fig.2.4b**. To avoid dripping of solution in the beginning and at the end of the deposition, there are only two possible directions of the spray which are either upwards or horizontally.

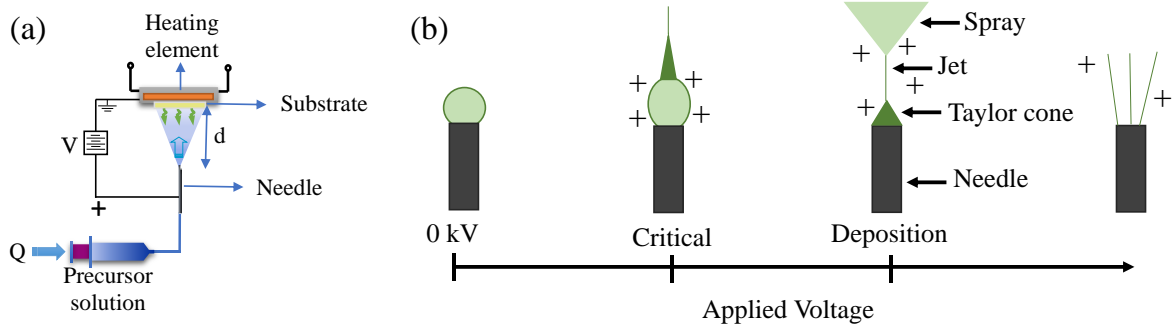


**Fig. 2. 4** (a) Schematic diagram of electrostatic spray deposition (ESD) and (b) sketch of the stages of spray formation as a function of the applied voltage.

The microstructure of the deposited film is greatly dependent on the arriving droplet size on the surface of the substrate. This arriving droplet size can be estimated by Gañán-Calvo equation (Eq. 2.1) [57].

$$d_{size} \propto \left( \frac{\rho \varepsilon_0 Q^3}{\gamma \sigma} \right)^{1/6} \quad (\text{Eq. 2.1})$$

In this equation,  $\rho$  is the solution density ( $\text{g cm}^{-3}$ ),  $\varepsilon_0$  is the vacuum permittivity ( $8.85 \times 10^{-12} \text{ F m}^{-1}$ ),  $Q$  is the solution flow rate ( $\text{mL h}^{-1}$ ),  $\gamma$  is the solution surface tension ( $\text{N m}^{-1}$ ), and  $\sigma$  is the solution electrical conductivity ( $\text{S m}^{-1}$ ). This equation shows that the microstructure is especially influenced by the physical-chemistry properties of the precursor solution, i.e. the surface tension ( $\gamma$ ), the electrical conductivity ( $\sigma$ ), and the density of the solution ( $\rho$ ). The boiling point of the solvent in the precursor solution is also significant because it determines the evaporation rate of the solvent. Besides these factors, the technical deposition parameters such as the flow rate of the precursor solution ( $Q$ ), the distance between the needle and the substrate ( $d$ ), and the temperature of the substrate ( $T$ ) are also important to determine the microstructure of the deposited film. Flow rate determines the arriving droplet size as indicated in Eq. 1, while both needle-substrate distance and substrate temperature determine the evolution of the droplets during transport [58]. The substrate temperature is also especially important in the spreading and drying of the droplets as they arrive on the surface of the substrate. Larger needle-substrate distance resulting in longer transport time of the droplets and consequently, the solvent in the droplets has more time to evaporate and resulting in drier and smaller arriving droplets. A larger substrate temperature induces also a higher evaporation rate of the solvent and consequently leads to the formation of smaller droplets.

The variations of the film morphology controlled by the parameters mentioned above can be explained by the different spreading and drying processes affected especially by the size of the arriving droplets on the substrate. Several studies have been done to observe the morphology of the film by varying the solvent in the precursor solution and the deposition parameters [53], [58]–[62]. Larger droplet size indicates that the droplets are wetter and contain a larger amount of solvent. As they impact the substrate, the droplets will spread on the surface. If the boiling point of the solvent is sufficiently high, the evaporation of the remaining solvent is slow and a thin dense film is formed. However, intermediate to low solvent boiling point leads to simultaneous spreading and drying on the surface of the substrate leading to cracked or reticulated coatings, resembling columnar or reticular structure. Meanwhile, smaller droplet size is drier and, consequently, presenting little spreading when impacting the heated substrate. Instead, a mechanism called “preferential landing” becomes more important [52]. This mechanism arises from the presence of induced charge on the surface of the grounded substrate with an opposite sign from the arriving droplets in the strong electrostatic field. The induced charge concentrates more on the parts of the substrate with larger local curvature resulting in a larger electric field in these regions. Thus, the charged droplets are more attracted to these areas leading to the formation of particle agglomerations. The morphology of the film resembles a coral or tree-like microstructure.

ESD is a great alternative for the deposition of films due to its simple set-up and inexpensive and non-toxic precursor. The low-temperature deposition, which is usually not more than 450 °C, is also beneficial to obtain small particle size in the nanometric scale. In the applications for electrodes of fuel cells and batteries, the easy adjustment to vary the microstructure is especially interesting because different morphologies are evidently able to affect the electrochemical performance [53], [63]. Moreover, the adhesion of the ESD films is usually very good even after sintering at low temperatures.

**Table 2. 1** Deposition parameters by ESD to obtain a coral-like microstructure.

Physical-chemistry properties of the solution	
Solvent	EtOH: H <sub>2</sub> O 1:2 + 8 drops of HNO <sub>3</sub> as a stabilizer
Conductivity (S m <sup>-1</sup> )	≈12 mS cm <sup>-1</sup> at 25 °C
Technical deposition parameters	
Distance between needle and substrate ( <i>d</i> )	50 mm
Solution flow rate ( <i>Q</i> )	1.5 mL h <sup>-1</sup>
Temperature of the substrate ( <i>T</i> )	350 °C
Applied voltage ( <i>V</i> )	12-14 kV
Deposition time ( <i>t</i> )	216 min for symmetrical cell for a durability test 270 min for the other samples
Scan speed	2 mm/s
Step size	2 mm

In this work, the microstructure of the ESD layer is focused only on the coral-like microstructure based on previous studies on La<sub>2-x</sub>Pr<sub>x</sub>NiO<sub>4+δ</sub> by Sharma [35], [61], [63]. The precursor solution for ESD was prepared in the same way as the precursor solution for the preparation of LPNO powder by sol-gel auto-combustion (§2.2.1), but the solvent was a mixture of EtOH and H<sub>2</sub>O (1:2). The addition of water slightly increased the boiling point of the solution as compared to pure ethanol so that in the beginning step of the deposition, the droplets slightly spread on the surface of the substrate before preferential landing mechanism became more important. In this way, a coral-like microstructure with a very thin layer that uniformly covered the surface of the substrate was obtained. To stabilize the solution and prevent the formation of precipitates in the solution, 8 drops of nitric acid (HNO<sub>3</sub>, Chem-Lab, 65% vol.) were also added for every 30 mL of solution. The deposition was then carried out at a temperature of 350 °C, a nozzle-to-substrate distance of 50 mm, a solution flow rate of 1.5 mL/h, and a long deposition time of 4.5 hours (except for symmetrical cell for durability test which was deposited for only 216 minutes since smaller electrodes are required due to the measurement setup). During the ESD deposition, the voltage was fixed to approximately 12-14 kV. Since the size of the spray was limited to a certain value, the sample holder was moved on horizontal directions (X and Y directions) to ensure that the spray covered every part of the substrate irrespective of the size of the substrate. In this work, the speed of the movement of the sample holder (scan speed) was 2 mm/s. A step size, which indicates the step taken to

change the direction of the movement after each deposition in a direction, of 2 mm was chosen. All the ESD deposition parameters are listed in **Table 2.1**. The sintering after ESD deposition was carried out at 960 °C for 6 hours in the air to promote crystallization and phase formation.

#### 2.2.4 Design of the LPNO oxygen electrode

By combining SP and ESD, four electrode designs were prepared and studied. **Fig. 2.5** shows the sketches of the four investigated architectures of the LPNO oxygen electrode which are described hereafter:

(i) and (ii) the single-layer electrode (SL) in which LPNO was deposited on the electrolyte by either SP (**Fig. 2.5a**) or ESD (**Fig. 2.5b**);

(iii) the double-layer electrode (DL) of LPNO which consisted of the active functional layer (AFL) deposited by ESD coated by the current collecting layer (CCL) deposited by SP (**Fig. 2.5c**);

(iv) the triple-layer electrode (TL) in which the AFL was composed of a porous SP interlayer of GDC sandwiched between the dense electrolyte and the ESD layer of LPNO. The AFL was topped by the CCL of LPNO deposited by SP (**Fig. 2.5d**).

The thickness in which the reactions extend within the electrode from the electrolyte interface is estimated to be only several microns [29]. From this point of view, the LPNO ESD layer on the DL electrode and both GDC SP and LPNO ESD layers on the TL electrode were referred to as the active functional layer while the LPNO SP layer acted as the current collecting layer. The deposition size varies depending on the purpose of the prepared electrode. The details on the deposition size in diameter is given in **Table 2.2**.

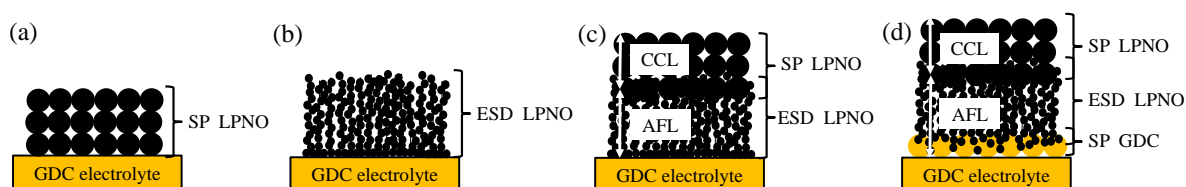


**Fig. 2. 5** Schematic diagrams of different architectural designs of LPNO electrode: single-layer (SL) LPNO deposited by (a) SP and (b) ESD, (c) double-layer (DL) of LPNO AFL deposited by ESD topped by LPNO CCL deposited by SP, and (d) triple-layer electrode (TL) in which

the AFL is a GDC interlayer deposited by SP topped by LPNO deposited by ESD and the CCL is LPNO deposited by SP.

**Table 2. 2** The diameter (in mm) of the deposition size for symmetrical and complete cells.

	Symmetrical cell		Complete cell
	All, except for the durability test	For durability test	
GDC SP	14	N/A	N/A
LPNO ESD	15.6	10	20
LPNO SP	14	10	20

## 2.3 Microstructural characterization techniques

### 2.3.1 Scanning electron microscopy (SEM)

In this work, SEM is used to observe the morphology of the films by using ZEISS Ultra 55 instrument equipped with a FEG Schottky gun and equipped by a Bruker EDX system for composition analysis. The EDX detector is an SDD detector with a 30 mm<sup>2</sup> of collecting surface. This kind of detector works at around -20°C, thus, it is not necessary to use liquid nitrogen to cool the SDD detector. The observation was carried out both on the surface and the cross-section of the prepared electrode. To observe the cross-section, the sample was cut by a diamond pen. The samples were prepared for the characterization by placing them on small aluminum blocks. Electrically conducting carbon tape was used to fix the samples in place. The silver paste was then applied to connect the samples with the aluminum blocks and left to completely dry at least for several hours to prevent outgassing inside the sample chamber of SEM. Since the electrolyte was not electrically conducting, 1 nm-thin Au/Pd was deposited by vacuum metallization on the surface/cross-section of the samples to obtain a conducting surface. The images were mainly acquired by secondary electron imaging using an in-lens detector which is located inside the electronic column above the objective lens. The electron accelerating voltage (electron high tension or EHT) was 20 kV for the imaging of the surface and 3 kV for the imaging of the cross-section. The measurements from the SEM images such

as average particle size and thickness were estimated by using ImageJ software. The basic principle of SEM can be found in **Appendix A**.

### 2.3.2 Focused ion beam-scanning electron microscopy (FIB-SEM) tomography

The focused ion beam (FIB) is a technique vastly used especially in material science for site-specific analysis, deposition, and ablation. Its set-up is similar to SEM as shown in **Fig. 2.6a**, but a focused beam of ions is used instead of electrons. In the conventional FIB, liquid metal ion source (LMIS) is used as the source of the ions. The most common LMIS is Ga source as it has a low melting point and it can be focused on a very fine probe size (<10 nm in diameter) [64]. The ion beam is produced by placing a reservoir of Ga in contact with a tungsten needle. Liquid Ga reaches down to the tip of the needle and upon application of high electric potential, a sharp cone is formed. Ions are then emitted from this cone due to field ionization and accelerated down to the FIB column. The ion beam is then focused by a series of electrostatic lenses before it reaches the sample chamber.

Contrary to the electron beam in SEM, the ion beam is destructive for the sample. As the ion beam reaches the sample, the atoms in the sample surface are sputtered into either secondary ions, neutral atoms, and secondary electrons. Thus, imaging by FIB is possible especially at lower beam currents through the secondary ions. The sputtering is, however, also resulting in the implantation of  $\text{Ga}^+$  into the samples.

The milling capability of FIB is widely used to prepare thin lamella or pillar for transmission electron microscope (TEM) or synchrotron-based characterizations. FIB can also be coupled with SEM and used for FIB-SEM tomography with the configuration shown in **Fig.2.6b**. For this application, the SEM and FIB columns are separated by an angle of around  $50^\circ$ . The sample stage is tilted so that the surface of the sample which is going to be milled is perpendicular to the primary ion beam. The sample is then milled line-by-line by the ion beam followed by image acquisition by SEM on the newly exposed surface. In this way, image slices correspond to each SEM image are obtained. The slices of images are then stacked together and processed to obtain a 3D reconstruction of the sample.

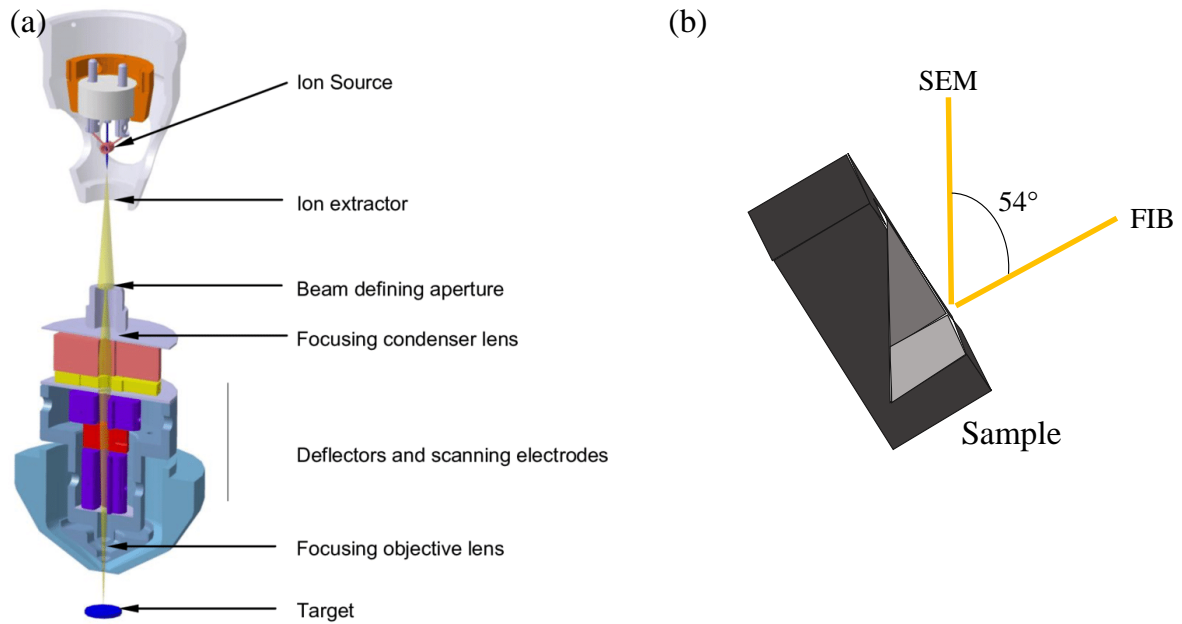


**Fig. 2. 6** (a) The schematic illustration of FIB set-up (Gierak, 2014) [65] and (b) FIB-SEM tomography configuration.

Usually, the sample for FIB-SEM tomography is prepared by infiltrating the sample with resin under vacuum. The purpose is to fill the porosity and to avoid the contrast due to the depth of field within the pores which makes the segmentation between the solid phase and the pores impossible. Moreover, it is also to avoid a common artifact in FIB-SEM tomography called ion mill curtaining. One of the causes of this artifact is different milling rates of the phases in the sample such as between the solid phase and pores. The curtaining resulting in an irregular milled surface appears as lines on the acquired images and is undesirable for quantitative analysis. The dry sample-containing resin is then mechanically polished to obtain the flat and parallel top and bottom surfaces as well as to decrease the thickness down to 7 mm or less. A thin coating of carbon on the surface of the sample is necessary to reduce the charging of the insulating materials.

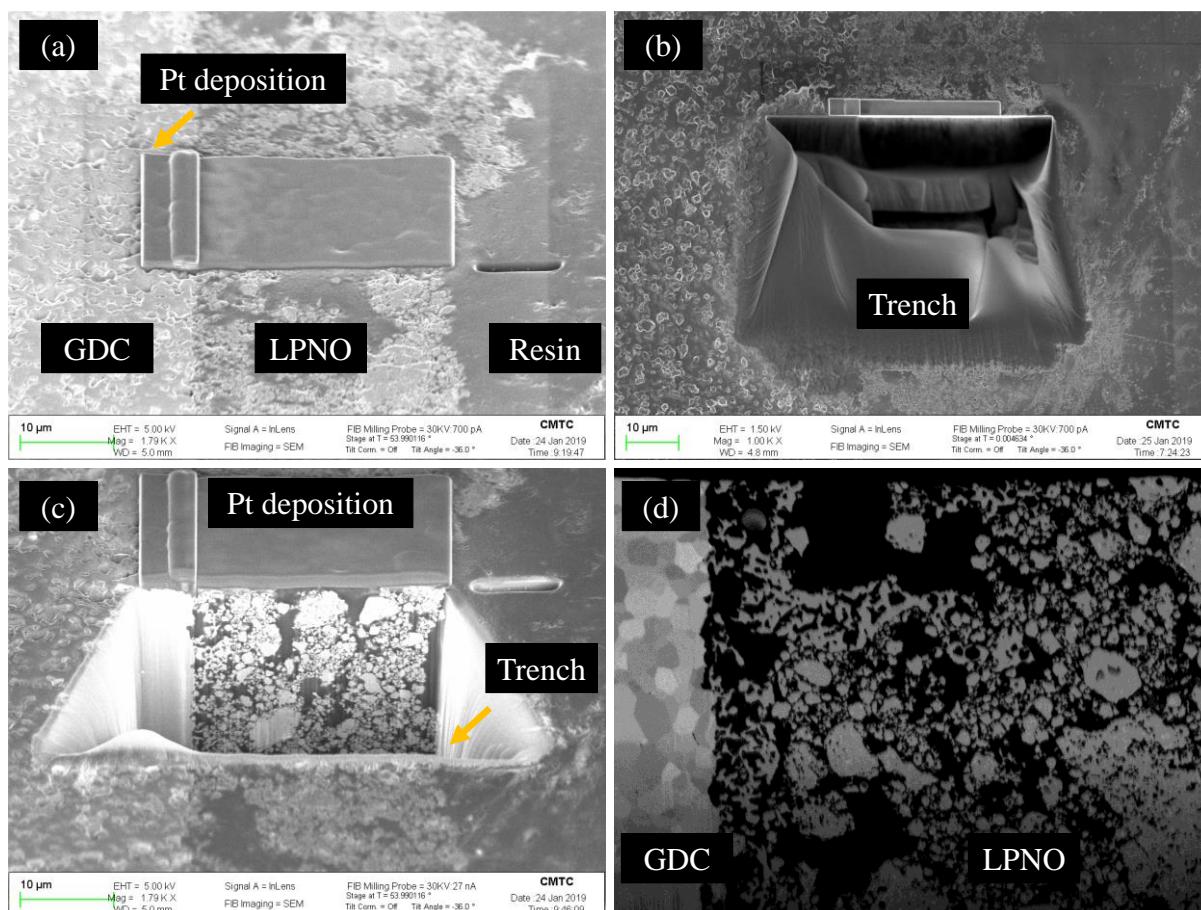


**Fig. 2. 7** The schematic representation of step-by-step FIB-SEM tomography: (a) protective Pt deposition on the region of interest (ROI) – (b) FIB milling to create a trench close to the ROI – (c) the view of the ROI – (d) an example of a slice of image acquired by SEM using the in-lens detector with the black parts indicating the resin-filled pores.

The FIB-SEM tomography on the prepared samples was carried out using either Crossbeam 550 (ZEISS) and Crossbeam NVision 40 (ZEISS, with a specific FIB column from SEYCO SII) machines. Gallium source was used to produce  $\text{Ga}^+$  ions for the milling. The process began with the deposition of platinum on the region of interest (ROI) to protect the top of the surface from unintended sputtering (**Fig. 2.7a**). The rapid milling by the ion beam was then started from an area outside the ROI to create a 25  $\mu\text{m}$ -depth trench (**Fig. 2.7b**) and open the field of view for the SEM (**Fig. 2.7c**). Afterwards, ion milling proceeded with a small current of 1.5 nA and a step size of 15 nm. The step size indicates the distance between each slice of the image taken by SEM. An example of the SEM images was shown in **Fig. 2.7d**. The images are acquired by SEM with an EHT of 1.5 kV and a pixel size of 15 nm x 15 nm. Both secondary

electron and back-scattered electron imaging can be obtained. However, in this work, the processed images were taken by secondary electron using the in-lens detector.

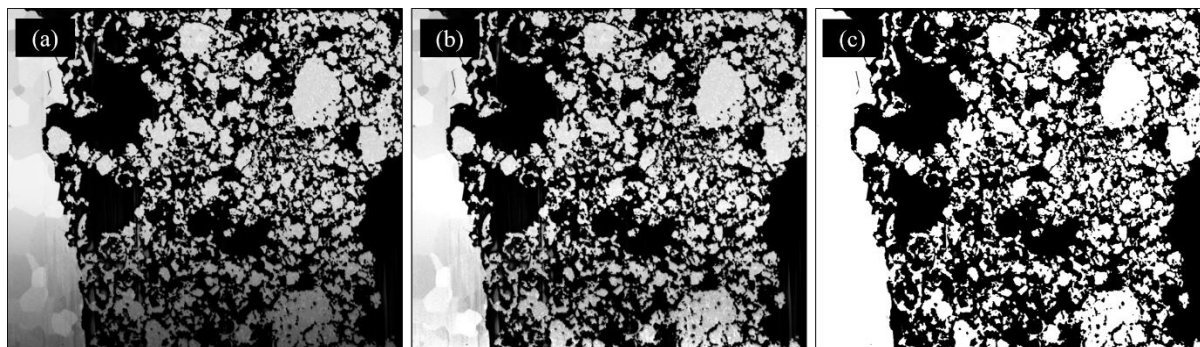


**Fig. 2. 8** (a) The raw, unprocessed SEM image – (b) the image after *Bleach Correction* to reduce the shadowing effect – (c) the segmented image which shows the solid phase in white and the porosity in black.

A few hundreds of image slices were necessary to obtain a sufficient size of a 3D volume. The 3D reconstructions and image processing were carried out by using Atlas3D (Fibics) and Fiji (ImageJ) software in collaboration with the SIMAP laboratory. The first step was to put together the slices of the images to create a 3D stack of images. Since there might be a slight drift between each slice of the image, the alignment of the images was necessary. In Fiji (ImageJ), the alignment was carried out by using a plugin called *StackReg* in which each slice of image is used as the template to align the next slice. After the stack was perfectly aligned, the next step was to do various image corrections such as to reduce the shadowing effect and removing the artifacts if present (e.g. air bubble or curtaining due to imperfect resin impregnation and other noises during image acquisition). The shadowing effect is an inevitable effect that arises from the shadow cast by the walls of the trench resulting in the uneven gray level distribution in which the bottom part of the image was several shades darker than the top part, as seen in **Fig. 2.7d** and **Fig.2.8a**. The correction of this effect on every image in the stack can be done by the *Bleach Correction* plugin in Fiji. The corrected stack, which was shown in **Fig. 2.8b**, was then segmented. Image segmentation is a process of dividing a digital image into multiple sets of pixels or segments. Each set of pixels is assigned to a label and each pixel in the same label shares the same characteristics. In this work, the labels were given to identify the solid phase and porosity. One way to do image segmentation is by thresholding method in which a threshold grayscale value is chosen and every pixel less than that value is assigned to a label while the pixels greater than that value are referred to another label. The thresholding

method resulting in the transformation of the grayscale image to the binary image as seen in **Fig. 2.8c**.

The microstructural properties of the sample were then computed from the segmented stack. The computation was carried out by using in-house codes written in MATLAB which has been detailed in literature [66]–[68]. The computed properties were as follow:

(i) The phase volume fraction ( $\varepsilon_i$ ) is obtained by calculating the percentage of voxels assigned to phase  $i$  ( $i$  = solid phase or pores) over the total voxels of the 3D volume.

(ii) The phase connectivity ( $\delta_i$ ) is calculated from the percentage of connecting phase from one side of the volume to the other.

(iii) The mean phase diameter ( $\mu\text{m}$ ) is taken from the particle size distribution (PSD or granulometry). The PSD is obtained by using a morphological opening method. A spherical structuring element B is used with increasing size after each sequence. It starts with the opening of the image with small B resulting in the disappearance of small particles. As the size of B increases, the larger particles start to disappear. The obtained PSD is then fitted by Weibull distribution. The mean phase diameter is obtained from the fitted parameter.

(iv) Specific surface area (SSA,  $S_p^i$ ,  $\mu\text{m}^{-1}$ ) is defined as the total surface area of a material per unit of bulk volume. It calculates the total surface area which is the contact area between both phases (solid and pores) by using covariance function. The calculated total surface area is then normalized to the total volume of the 3D volume.

(v) Microstructure-factor ( $M_i$ ) shows the microstructural influence on the effective transport property [69]. It is defined as the ratio between the effective conductivity  $\sigma_i^{eff}$  and the intrinsic conductivity for the dense, bulk material  $\sigma_i^{bulk}$ . This factor is also related to various microstructural properties which are important for the diffusional properties such as the phase volume fraction  $\varepsilon_i$ , percolation  $P$ , constrictivity (bottleneck effect)  $\beta_i$ , and geometrical tortuosity  $\tau_i^{geo}$ . In this work,  $M_i$  is used to compute the “apparent” tortuosity factor through this equation:

$$M_i = \varepsilon_i / \tau_i \quad (\text{Eq. 2.2})$$

## 2.4 Structural characterization techniques

### 2.4.1 Laboratory X-ray diffraction (XRD): room temperature and *in-situ* XRD

The structural characterization of the powders and films by laboratory XRD for this work was carried out with a PANalytical X'pert Pro MPD. The X-ray beam is generated by copper source (Cu-K $\alpha$  radiation) with the wavelength ( $\lambda$ ) of 1.5419 Å in Bragg-Brentano geometry. An *in-situ* high-temperature XRD was also performed from 25 to 1200 °C using the same instrument equipped with a high-temperature chamber (Anton Paar HTK1200N). The dwelling time at each temperature before the measurement is 30 minutes. The phases were identified based on the powder diffraction file (PDF) from International Centre for Diffraction Data (ICDD) and the cell parameters were obtained by Rietveld refinement using Fullprof software [70]. The basic principle of XRD is given in **Appendix B**.

### 2.4.2 Synchrotron-based X-ray: Lamellae preparation by plasma-FIB, micro-X-ray diffraction ( $\mu$ -XRD), and micro-X-ray fluorescence ( $\mu$ -XRF)

For characterization by  $\mu$ -X-ray diffraction and  $\mu$ -X-ray fluorescence, thin lamellae were extracted from the samples by using a plasma-focused ion beam (p-FIB) Vion (FEITM) machine working with an inductively coupled plasma ions source. It is similar to the conventional FIB described in §2.3.2 but Xe<sup>+</sup> ions are used for milling instead of Ga<sup>+</sup>. The use of Xe<sup>+</sup> ions allowing higher maximum currents and milling rates about 60 times faster than classical Ga<sup>+</sup> FIB [71]. The lamellae were prepared by firstly positioning the samples in the vacuum chamber of the plasma-FIB machine on a five-axial motorized stage. After the identification of the eucentric height, the region of interest (ROI) was covered with a Platinum (Pt) deposition (~3-4  $\mu$ m) to protect the samples surfaces (**Fig. 2.9a**) using a low current of 15 nA [72]. Subsequently, the two sides of the ROI were milled to obtain the lamella (**Fig. 2.9b**). This step was the longest of all procedure and was done at two currents, 180 nA and 59 nA, far and close to the ROI, respectively. Once the lamella milling was completed (**Fig. 2.9c**), a small Pt deposition was used to fix it on a specific micromanipulator and the sample was detached from the cell using a low ion current of 59 nA (**Fig. 2.9d**). Finally, the last Pt deposition was used to glue the lamella detached from the cell to an aluminum pin compatible with the sample holder of the beamline (**Fig. 2.9e**). The extracted sample dimensions were approximately 100 x 80 x 20  $\mu$ m<sup>3</sup> (for width, height and depth, respectively) and all the procedures took around 10-11 hours per sample.

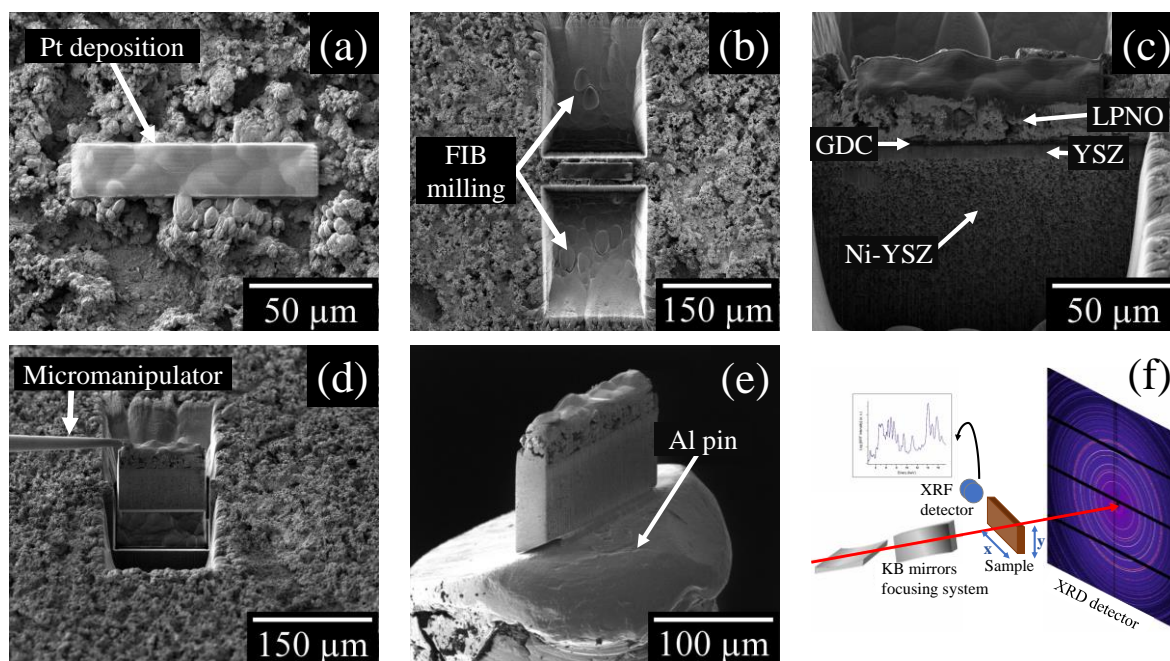


**Fig. 2. 9** The schematic representation of the lamella preparation by p-FIB: (a) protective Pt deposition on ROI – (b) FIB milling around the ROI – (c) isolated lamella – (d) sample extraction from the cell – (e) sample mounted on the Al pin. (f) The schematic diagram of  $\mu$ -XRD and  $\mu$ -XRF characterization at  $\mu$ XAS beamline, SLS, PSI, Switzerland.

The lamellae prepared from all the samples were characterized by  $\mu$ -X-ray diffraction ( $\mu$ -XRD) and  $\mu$ -X-ray fluorescence ( $\mu$ -XRF) at  $\mu$ XAS beamline on the Swiss Light Source (SLS), Paul Scherrer Institut (PSI), Switzerland. The measurement setup is schematically shown in **Fig. 2.9f**. A synchrotron-based X-ray beam with a high energy of 17.2 keV is passed through the Kirkpatrick-Baez (KB) mirror which is able to focus the beam to a spot size smaller than  $1 \mu\text{m}^2$  ( $1 \mu\text{m}$  horizontally by  $0.5 \mu\text{m}$  vertically). The lamella of the sample was then positioned at the focal plane and two-dimensional (2D) raster scans on X (horizontal) and Y (vertical) directions were performed all over the lamella using the step size of 500 nm. Since the energy was high, the X-ray was able to transmit through the thin lamella. An area detector positioned behind the lamella and perpendicular to the incident beam was used to record the 2D projection of the diffracted beam. Apart from it, a fluorescence detector was positioned at  $90^\circ$  from the incident beam. Thus, both the local diffraction pattern and fluorescence spectrum can be recorded simultaneously. The fluorescence refers to the re-emission of the X-ray beam with different energy due to the absorption of the incident beam by the atoms in the sample which is the basic principle of XRF. The incident beam ejects the electrons in the atom and as a result, the electrons at higher energy levels fill-up the electron holes, and energy is released. The amount

of the released energy depends on the orbitals of the atom involved, thus this technique can be used for the identification of the chemical elements in the sample. By obtaining the data for both XRD and XRF, the distribution of both compounds/phases and chemical elements can be obtained.

The high energy X-ray beam is obtained from the synchrotron source. A synchrotron is a cyclic particle accelerator. The particle, such as an electron, is accelerated by the magnetic field in a large (288 m in circumference for SLS) circular path called the storage ring. The particle moves at very high speed close to the speed of light. The direction of the accelerated particle is changed periodically towards the beamlines located in several locations around the storage ring. Since the energy of the accelerated particle is high, the change in the direction results in the release of energy at X-ray wavelength. The emitted X-ray is then used for various experiments in the beamlines.

The following step after the characterization was to do data reduction for both diffraction patterns and fluorescence spectra. The diffraction ring of each measured point was azimuthally integrated by utilizing pyFAI, a Python library, to obtain the traditional 1D diffractograms [73]. A series of data conversion was then performed with scripts developed using Python. The 1D diffractograms were then integrated along the horizontal direction parallel to the electrolyte (X-direction in **Fig. 2.9f**) for each vertical position in the electrode thickness (Y-direction in **Fig. 2.9f**). Therefore, a set of 1D diffractograms is obtained so that the distribution of the phases across the thickness of the samples can be examined. The Rietveld refinement and fitting of the diffractograms were carried out by XRDU software [74], [75]. For the quantitative analysis of the phases, batch line fitting was carried out also with the same software. The identification of the elements from the fluorescence spectra was performed by PyMCA, another Python library [74]. The 2D maps were generated by using Fiji software.

### **2.5 Electrochemical characterization technique: Electrochemical impedance spectroscopy (EIS)**

Electrochemical impedance spectroscopy (EIS) is a powerful technique that is used to characterize and evaluate the behavior of electrochemical systems/cells. This technique is able to measure the response of the cell under controlled variables such as temperature and oxygen

partial pressure. It has been widely used in various applications, e.g. fuel cell and battery systems, corrosion, coating, etc.

Measurements by EIS are carried out by applying a small perturbation to the system in the form of sine waves of either voltage ( $v(t) = V_m \sin(\omega t)$ ) or current ( $i(t) = I_m \sin(\omega t)$ ), and then measuring the response in the current evolution ( $i(t) = I_m \sin(\omega t + \theta)$ ) or voltage ( $v(t) = V_m \sin(\omega t + \theta)$ ). In a linear system, the response will be sinusoidal and has the same frequency ( $f = \omega/2\pi$ ) as the input waves but different phase ( $\theta$ ) and amplitude ( $V_m$  or  $I_m$ ). The amplitude of the perturbation should be sufficiently small to ensure the linearity of the system. With the use of Fourier transformation, the voltage and current can be expressed as complex quantity  $V(j\omega)$  and  $I(j\omega)$  where  $j$  is an imaginary number ( $j = \sqrt{-1}$ ). Thus, the ratio between voltage and current at a specific frequency is similar to Ohm's law for the DC circuit as indicated by Eq. 2.3 [27], [76], [77].

$$Z(j\omega) = \frac{V(j\omega)}{I(j\omega)} \quad (\text{Eq. 2.3})$$

The term  $Z(j\omega)$ , or normally written as  $Z(\omega)$ , is the impedance function and its frequency-specific value is the impedance of the system. As in resistance for DC circuit, impedance is defined as the opposite of the materials to electrical current flow. However, there is no phase shift between voltage and current for a pure resistance, which is not the case for real electrodes. Thus, impedance is the more general term to be used. The impedance function is expressed as complex number  $Z(\omega) = Z' + jZ''$  where  $Z'$  is the real part ( $Re(Z)$ ) and  $Z''$  is the imaginary part ( $Im(Z)$ ). By definition,  $j$  equals to  $exp(j\pi/2)$ , hence the impedance can be graphically represented in a planar vector consisting of the real part along the  $x$ -axis and the imaginary part along the  $y$ -axis ( $90^\circ$  rotation in reference to  $x$ -axis), as shown in **Fig. 2.10**. The planar vector has a magnitude of  $|Z|$  and a phase angle relative to  $x$ -axis of  $\theta$ , which is the phase difference between the voltage and current. By applying simple trigonometric relations ( $Re(Z) = |Z| \cos \theta$  and  $Im(Z) = |Z| \sin \theta$ ) and Euler relation ( $exp(j\theta) = \cos \theta + j \sin \theta$ ), the impedance can be expressed in polar form as indicated by Eq. 2.4.

$$Z(\omega) = |Z|(\cos \theta + j \sin \theta) = |Z|exp(j\theta) \quad (\text{Eq. 2.4})$$

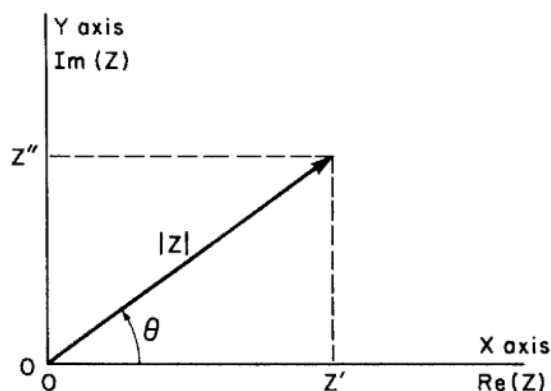


**Fig. 2. 10** The graphical representation of impedance  $Z$  (Barsoukov & Macdonald (Eds.), 2005) [76].

Characterization by EIS is carried out by measuring the impedance of the system by varying the frequency. The obtained data can be graphically presented in Nyquist and Bode plots shown in **Fig 2.11**.

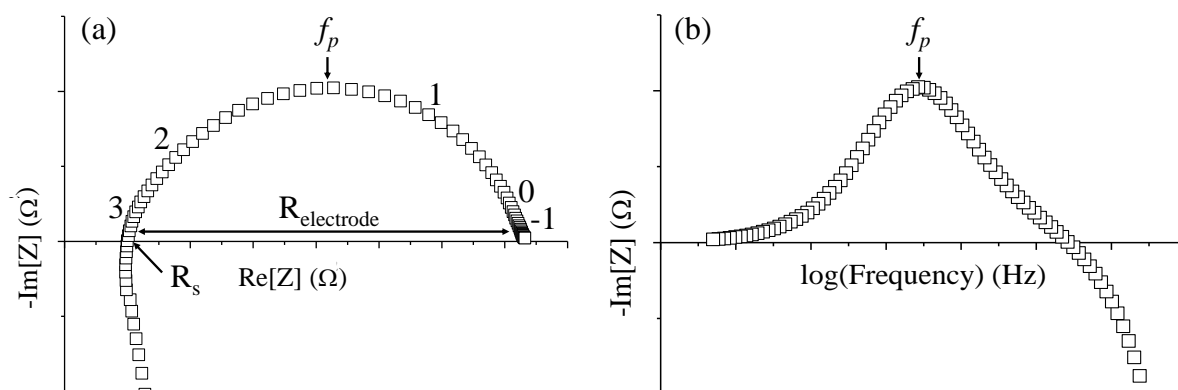


**Fig. 2. 11** (a) Nyquist and (b) Bode representation of EIS data. The numbers on the Nyquist plot indicates the logarithmic of the frequency.

A Nyquist plot maps the real part,  $Re(Z)$ , of the impedance on the  $x$ -axis and the imaginary part (normally in negative values,  $-Im(Z)$ ) on the  $y$ -axis for each measured frequency. The features of this plot are very useful to obtain the first interpretation of the electrochemical performance of a system. For example, the shape of the plot may give an initial prediction on the processes that take place on the system. The noises on the measurement points may show a sign of irregularity on the system or the test bench. Moreover, several important points, which are listed below, can be used to obtain the quantitative values of the measured system.

- (i) The intercept of the plot on the  $x$ -axis at high frequency is called the series resistance ( $R_s$ ). It is related to the ohmic resistance originating mainly from the electrolyte.
- (ii) The difference between the intercept on the  $x$ -axis at low ( $\omega \rightarrow 0$ ) and high frequency ( $R_s$ ) shows the total resistance of the electrode. This resistance is the sum of the resistances for each process that takes place on the system. A more detailed explanation will be given later in this section. The polarization resistance ( $R_{pol}$ ) of the electrode is calculated from this resistance.
- (iii) The frequency on the peak,  $f_p$ , can be used to calculate the time constant,  $\tau$ , through the equation  $\omega_p \tau = constant$ . The value of the constant depends on the electrical element, which will be explained later in this section. In a simple RC circuit, the value of the time constant equals the resistance multiplied by the capacitance ( $\tau = RC$ ), thus this relation can be used to calculate the capacitance of a process.

On the other hand, a Bode plot maps the frequency on the  $x$ -axis and either phase angle  $\theta$  or  $-Im(Z)$  as the  $y$ -axis. This plot is especially useful for easier visualization of the frequency distribution versus the response of the system. Each peak present on the plot can be correlated to a specific process that takes place in the system.

The frequency-dependent impedance of the system is related directly to the kinetics of various reaction steps that take place on that system. Since an electrochemical system is analogous to an electrical circuit, the interpretation of EIS data can be done by building a mathematical model based on an equivalent electrical circuit consisting of the electrical element(s). Each electrical element is equivalent to a specific physical process on the electrode. The electrical circuit is then used to fit the experimental data. However, this data interpretation can be complicated and uncertain by the fact that several different combinations of electrical elements may yield the same impedance. Thus, it is important to have a rough idea of the possible processes on the electrode and choose the suitable equivalent electrical element(s). A careful interpretation of the modeling results is also important to ensure that the obtained properties from the model are theoretically correct. By establishing a suitable model, the impedance response of the system can be deconvoluted and assigned to a specific reaction(s), hence the electrochemical behavior of the system can be explained.

The equivalent electrical circuit can be built from a simple element or a complex element. A complex element consists of the combination of simple elements and/or other complex elements in series and/or parallel. The simple elements can be divided into lumped elements,

---

which are taken from electrical elements, and frequency-dependent elements, which have a correlation to a specific electrochemical process. The explanations on each element are given in **Appendix C**.

There are several configurations to measure a cell by EIS based on the number of the connections, namely 2-, 3-, and 4-electrode configurations (also called 2-, 3-, and 4-terminal). In general, the measurement requires a counter electrode (CE) which provides current to the cell and a working electrode (WE) from which the current through the cell is measured. In 3-electrode configuration, a reference electrode (RE) is placed within the cell, while two REs are necessary for 4-electrode configuration. The reference electrode is used for voltage measurement. The illustrations of 2- and 3-electrode configurations for a symmetrical cell are given in **Fig. 2.12**. A symmetrical cell consists of two identical electrodes which are prepared on both sides of the electrolyte. Gold grids are placed on both electrodes for the current collection. In 2-electrode configuration, the measured cell response corresponds to the response of both electrodes, thus, the polarization resistance of the electrode ( $R_{pol}$ ) is calculated by divided the total electrode resistance (**Fig. 2.11a**) by two as indicated by Eq. 2.5. In this equation,  $A$  is the electrode area which is necessary on the calculation to normalize the resistance. This normalized resistance is called the area-specific resistance. All the resistance presented in this work refers to the area-specific resistance.

$$R_{pol} = R_{electrode} \cdot \frac{A}{2} \quad (\text{Eq. 2.5})$$

For the 3-electrode configuration, a silver wire is placed in the middle of the side part of the electrolyte as the reference electrode (**Fig. 2.12b**). By placing the RE, the response of the working electrode can be separated from the counter electrode.

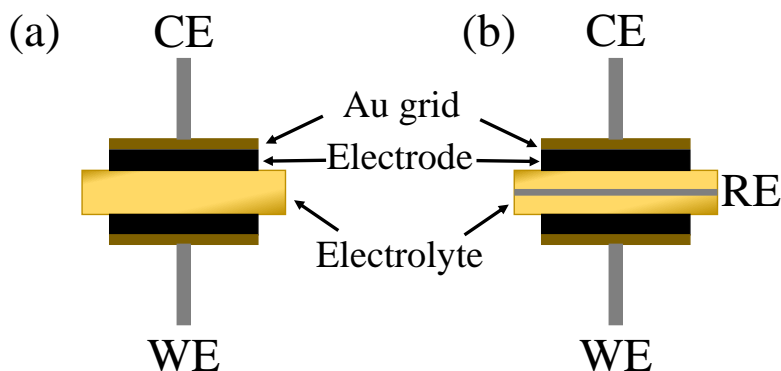


**Fig. 2. 12** (a) 2-electrode and (b) 3-electrode configurations for EIS measurement. CE is a counter electrode, WE is a working electrode, and RE is a reference electrode.

In this work, the electrochemical characterization of the symmetrical cell was carried out by electrochemical impedance spectroscopy (EIS) technique using autolab potentiostat-galvanostat (PGSTAT 302N). All measurements were carried out by using 2-electrode configuration, except for the long-term test which will be detailed in §2.6.1. The measurements were performed in a potentiostatic mode with a small sinusoidal amplitude of 0.02 V in the 0.01 Hz – 1 MHz frequency range. The tests were conducted in ambient air at the open circuit potential (OCP) for a temperature ranging from 450 to 700 °C. The measurements were taken for every 50 °C with dwell time before the measurement at each temperature of 2 h to ensure the stabilization of the temperature. Gold grids (Heraeus, 1024 meshes  $\text{cm}^{-2}$  woven from 0.06 mm in diameter wire) were used as current collectors. The impedance spectra were analyzed in terms of equivalent circuits with the EC-Lab® software.

## 2.6 Long-term durability tests

### 2.6.1 Long-term test on the symmetrical cell

In this work, a symmetrical cell is subjected to be investigated under current and temperature. The double-layer LPNO, 10 mm in diameter, was deposited on both sides of the GDC pellet. For the purpose of electrochemical measurement by a 3-electrode configuration, a silver wire was placed approximately in the middle of the side of the GDC electrolyte pellet as the reference electrode (see **Fig. 2.12b** for the configuration). Gold grids (Heraeus, 1024 meshes  $\text{cm}^{-2}$  woven from 0.06 mm in diameter wire) were used as current collectors. This sample was then subjected to a long-term electrochemical characterization at 700 °C for 960 h in the air

using autolab potentiostat-galvanostat (PGSTAT 302N). During the long-term experiment, DC polarization currents ( $i_{dc}$ ) of  $+300 \text{ mA cm}^{-2}$  and  $-300 \text{ mA cm}^{-2}$  (current of  $\pm 235 \text{ mA}$ ) were applied on the upper and lower electrode, respectively. It means that the upper electrode was subjected to an anodic polarization and worked in the electrolysis mode, while the lower electrode was under a cathodic polarization and fuel cell mode. Before and after the long-term study, EIS measurements were carried out on each side of the electrode both at the open circuit potential (OCP) and under applied direct current in galvanostatic mode with a sinusoidal amplitude of  $10 \text{ mA}$  in the  $0.01 \text{ Hz} - 1 \text{ MHz}$  frequency range.

### 2.6.2 Long-term test on the complete cell

The durability test on the complete cell is performed on a test bench, illustrated in **Fig. 2.13**, in CEA-Liten Grenoble. The complete cell was prepared by depositing double-layer LPNO on top of the GDC barrier layer on the YSZ electrolyte. Nickel grid (50 mm in diameter) and gold grid (34 mm in diameter) were used as the current collector on the hydrogen electrode and oxygen electrode, respectively.

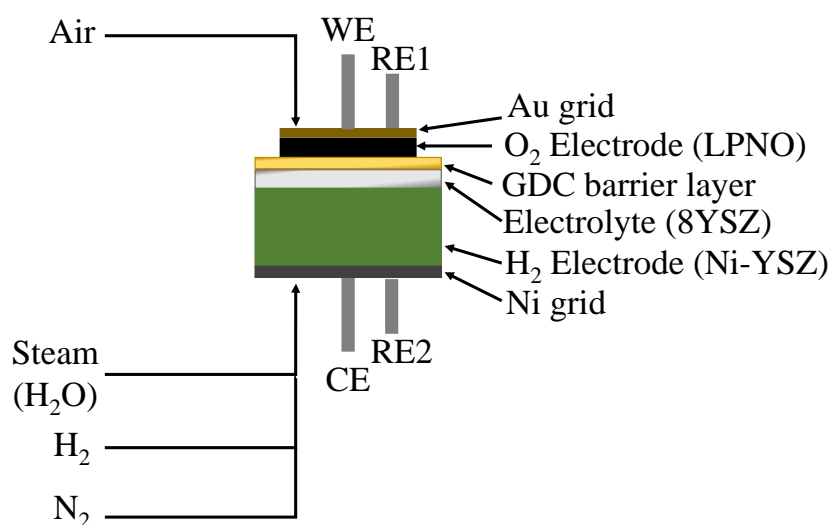


**Fig. 2. 13** The illustration of the test bench configuration for the durability test on the complete cell.

To ensure gas tightness between both sides of the cell, glass sealing was carried out at only  $860 \text{ }^\circ\text{C}$  for  $1.5 \text{ h}$  to avoid any grain growth of the oxygen electrode. During gas sealing, air and nitrogen with the flow rate of  $0.5 \text{ NI h}^{-1}$  were passed through the oxygen and hydrogen electrode, respectively. A load of  $3.38 \text{ kg}$  ( $\approx 0.37 \text{ kg cm}^{-2}$ ) was applied to ensure good contact between

the cell and current collector grids. Before the electrochemical measurement, NiO on the hydrogen electrode was first reduced to Ni. The NiO reduction was carried out at 800 °C from 5 to 15 minutes by passing a mixture of N<sub>2</sub> and H<sub>2</sub> gases with a total flow rate of 4 NI h<sup>-1</sup> to the hydrogen electrode side; the reduction started with pure N<sub>2</sub>, followed by increasing the amount of H<sub>2</sub>, and the last step was performed with pure H<sub>2</sub>. Air was passed on the oxygen electrode side with a flow rate of 4 NI h<sup>-1</sup> during the reduction. The reduction steps are detailed in **Table 2.3**.

**Table 2. 3** The NiO reduction steps at 800 °C from 5 to 15 minutes.

O <sub>2</sub> electrode	H <sub>2</sub> electrode		Duration (minutes)
Air flow rate (NI h <sup>-1</sup> )	N <sub>2</sub> flow rate (NI h <sup>-1</sup> )	H <sub>2</sub> flow rate (NI h <sup>-1</sup> )	
4	4	0	5
4	3.8	0.2	25
4	3.6	0.4	15
4	3.2	0.8	15
4	2.4	1.6	15
4	1.6	2.4	15
4	0	4	30

The cell was then operated in electrolysis mode under the current density of -200 mA cm<sup>-2</sup> (current of 0.63 A). During the test, air (O<sub>2</sub>/N<sub>2</sub> = 0.21/0.79) was passed on the oxygen electrode side. Meanwhile, a mixture of steam (H<sub>2</sub>O) and hydrogen (H<sub>2</sub>) with a ratio of 90/10 and the steam conversion rate of 20% was supplied on the hydrogen electrode. The electrochemical characterization was carried out at 700 °C for 900 h and the potential was recorded over time. As in the symmetrical cell previously discussed, EIS was also performed before and after the long-term aging both at the open circuit voltage (OCV) and under applied direct current in galvanostatic mode.

---

# **CHAPTER 3: IMPROVING THE ELECTRODE PERFORMANCE OF RARE-EARTH NICKELATES BY IMPROVING THE MICROSTRUCTURE AND ARCHITECTURAL DESIGN**

This chapter explains in detail the experimental results on the improvement of the LPNO electrode performance in various ways. After the introduction of the chapter, several preliminary results on the sample preparation by SP and ESD are described. It is then followed by the results of structural characterization on LPNO powder as well as ESD and SP layers. Afterwards, a brief explanation of the equivalent circuit model for the EIS data fitting is provided. The following sub-chapters consist of the four main results on the correlation between the electrode performance to the electrode/electrolyte interface, the presence of secondary higher-order nickelate phase in the ESD layer, the current collector layer (CCL) microstructure, and the architectural designs. The summary and conclusions of this chapter are then given at the end. Large parts of this chapter have been published in the Journal of Electroanalytical Chemistry (<https://doi.org/10.1016/j.jelechem.2019.113373>).

### 3.1 Introduction

As described in §1.2, the microstructure of the oxygen electrode and its interface with the electrolyte plays a key role in its electrochemical activity. Thus, this chapter describes in detail the experimental results of the effect of several microstructure-related variations on the electrode performances. Nine symmetrical cells with various electrode designs and thermal treatments of LPNO were prepared on gadolinium-doped ceria ( $\text{Ce}_{0.9}\text{Gd}_{0.1}\text{O}_{2-\delta}$ ; GDC) electrolyte. The samples are listed in **Table 3.1**. The electrochemical performances of all samples were then characterized by EIS at the OCP. Structural and microstructural characterizations by XRD and SEM were also carried out to provide supporting explanations on the electrochemical responses of the oxygen electrodes.

**Table 3. 1** List of samples discussed in this chapter with the heat treatment program. As described in §2.2.4, SL = single-layer, DL = double-layer, and TL = triple-layer.

Sample #	Architectural design	Heat treatment in air	Note
Sample 1	SL LPNO SP	450 °C / 2h + 800 °C / 2h	
Sample 2	SL LPNO SP	450 °C / 2h + 1050 °C / 2h + 1100 °C / 0.5h	
Sample 3	SL LPNO ESD	960 °C / 6h	
Sample 4	DL LPNO (ESD + SP)	960 °C / 6h (ESD) 450 °C / 2h + 800 °C / 2h (SP)	
Sample 5	DL LPNO (ESD + SP)	960 °C / 6h (ESD) 450 °C / 2h + 900 °C / 2h (SP)	
Sample 6	DL LPNO (ESD + SP)	960 °C / 6h (ESD) 450 °C / 2h + 1050 °C / 2h + 1100 °C / 0.5h (SP)	
Sample 7	DL (LPNO ESD + LPNO SP)	960 °C / 6h (ESD) 450 °C / 2h + 800 °C / 2h (SP)	Ball milling of LPNO powder
Sample 8	TL (GDC SP + LPNO ESD + LPNO SP)	450 °C / 2h + 1200 °C / 2h (GDC SP) 960 °C / 6h (ESD) 450 °C / 2h + 800 °C / 2h (SP)	
Sample 9	TL (GDC SP + LPNO ESD + LPNO SP)	450 °C / 2h + 1200 °C / 2h (GDC SP) 960 °C / 6h (ESD) 450 °C / 2h + 800 °C / 2h (SP)	Ball milling of LPNO powder

Preliminary experiments are first reported to determine the optimized deposition parameters by both SP and ESD. Various compositions belonging to the solid solution  $\text{La}_{2-x}\text{Pr}_x\text{NiO}_{4+\delta}$  (with  $x = 0, 1, 2$ ) have also been prepared to investigate the effect of the La/Pr ratio on the electrochemical behavior of La-Pr nickelates. These results have been compared with those of the literature. Lastly, the reproducibility of the sample fabrication by SP and ESD has also been tested by comparing the electrochemical responses of three identical symmetrical cells.

## 3.2 Preliminary experiments

### 3.2.1 Optimized deposition parameters by SP and ESD

#### 3.2.1.1 SP layer: binder for the ink

A binder is required for the preparation of ink for SP to obtain a well-mixed ink paste. It is also important for the texture and consistency of the ink. Binder plays a key role to ensure particle network strength and has been shown to affect the microstructure and electrochemical performance of the electrode [78]. The addition of binder increases the viscosity of the ink which, in turn, improves the particle network strength. However, there is a maximum amount of binder that can be added before the ink becomes too tacky and difficult to be printed. Normally, 1 wt% of the binder is sufficient to obtain the ideal ink for screen printing.

There are two available options for the binder in our laboratory: polyvinylpyrrolidone (PVP,  $(\text{C}_6\text{H}_9\text{NO})_n$ ) and polyvinyl butyral (PVB,  $(\text{C}_8\text{H}_{14}\text{O}_2)_n$ ). Both are polymer-based resin. To determine which binder to use, two symmetrical cells of single-layer SP were prepared by using either PVP or PVB. The other deposition parameters and the subsequent heat treatments were identical for both cells following the procedures explained in §2.2.2. The electrochemical measurement results by EIS of both samples from 450 to 700 °C in the air at OCP are presented in the Arrhenius plots in **Fig. 3.1**. The activation energies are 1.23 and 1.20 eV for the samples prepared by PVP and PVB, respectively. The similar values show that the same processes occur at both electrodes. However, the  $R_{\text{pol}}$  of PVB cell is lower by around 30% at all temperatures as compared to the PVP cell. Since there were no other characterizations carried out on these samples, it is difficult to pinpoint the explanation behind the improvement of the PVB cell. However, it is stated in the literature that the addition of PVB increases the viscosity of the ink more significantly as compared to PVP of the same molecular weight [79]. Thus, it can be suggested that PVB improved the connection between particles in the ink which results in a

better electrode microstructure. Based on this result, PVB is then chosen for the binder for SP ink.

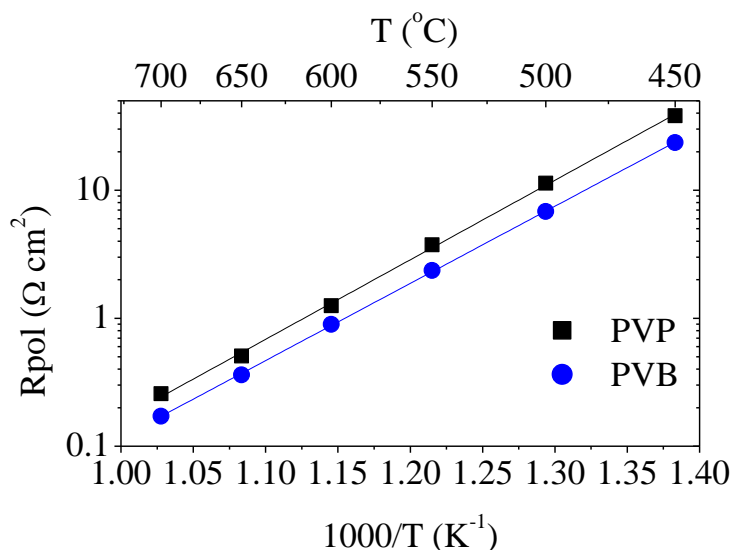


**Fig. 3. 1** The Arrhenius plots of single-layer deposited by SP using either PVP or PVB as the binder for the ink.

### 3.2.1.2 ESD layer: solution stabilization, deposition time, and hierarchical microstructure

The precursor solution for ESD which is composed of nitrates and citric acid (as a chelating agent) powders is proven to be chemically unstable when a mixture of water and ethanol is used as the solvent. The choice of the solvent is crucial to obtain an ESD layer with a coral-like microstructure, which is the microstructure-of-interest for this work. The instability is shown by the formation of precipitates in the solution just 1.5 h after the solution preparation (**Fig. 3.2a** and **b**). Since the deposition time required to obtain sufficient thickness of the electrode is more than 1.5 h, the precipitates blocked the flow of the solution to feeding the needle during the deposition as shown by the picture in **Fig. 3.2c**. In consequence, the formation of the spray to the surface of the substrate is hindered and it is impossible to complete the deposition without intervention in the middle of the process (i.e. stop the deposition, clean the tube, change the needle, and refill the tube with fresh solution). Moreover, some instabilities of the spray impacting the substrate can occur if precipitates are formed and, consequently, the morphology of the deposit is no longer homogeneous and the reproducibility of the electrode cannot be guaranteed.

The origin of the formation of precipitates is probably linked to a closed limit of solubility, but it is still not well understood. The precipitates are not formed when the same precursor powders are dissolved in pure ethanol, nor when only La- and Pr-nitrates are dissolved in the mixture of ethanol and water. Moreover, all powders are supposed to be highly soluble in both water and ethanol. Constant stirring and heating do not solve the problem as well. However, a test carried out by adding several droplets of nitric acid ( $\text{HNO}_3$ ) is proven to stabilize the precursor solution and prevent the precipitation. After several trials, it is found that 8 droplets of nitric acid in 30 mL of solution is sufficient for this purpose.

At first glance, the addition of nitric acid seems to not greatly affecting the properties of the solution since only small amounts of nitric acid are necessary. However, the measurement by electrical conductivity meter shows that the solution conductivity increases by 4 times when  $\text{HNO}_3$  is added ( $3 \text{ mS cm}^{-1}$  without  $\text{HNO}_3$  and  $12 \text{ mS cm}^{-1}$  with  $\text{HNO}_3$  at  $20 \text{ }^\circ\text{C}$ ). From the Gañán-Calvo equation (Eq. 2.1, §2.2.3), solution conductivity is one of the factors which determine the arriving droplet size on the surface of the substrate. Since the droplet size is inversely related to the solution conductivity, the arriving droplet size is estimated to be smaller for the electrode prepared from solution with nitric acid. Thus, to see if there are any changes in the microstructure due to nitric acid addition, two ESD layers were prepared by using the precursor solution without and with nitric acid. The deposition time for both samples is 3 h, and the subsequent sintering is carried out in air at  $960 \text{ }^\circ\text{C}$  for 6 h. The surfaces and cross-sections of both samples were then observed by SEM.

The surface of the sample without  $\text{HNO}_3$  (**Fig. 3.2d**) shows larger blocks of a deposition while for the sample with  $\text{HNO}_3$  (**Fig. 3.2g**) the deposition is more separated. Moreover, from the cross-section images, the coral-like microstructure is more defined for the sample with  $\text{HNO}_3$  (**Fig. 3.2h**) as compared to the one without  $\text{HNO}_3$  (**Fig. 3.2e**). A decrease in the average particle size is also observed when  $\text{HNO}_3$  is added ( $310 \text{ nm}$  without  $\text{HNO}_3$  vs  $190 \text{ nm}$  with  $\text{HNO}_3$ ). Thus, it can be concluded that the addition of nitric acid is overall very important for solution stability as well as to reduce the particle size.

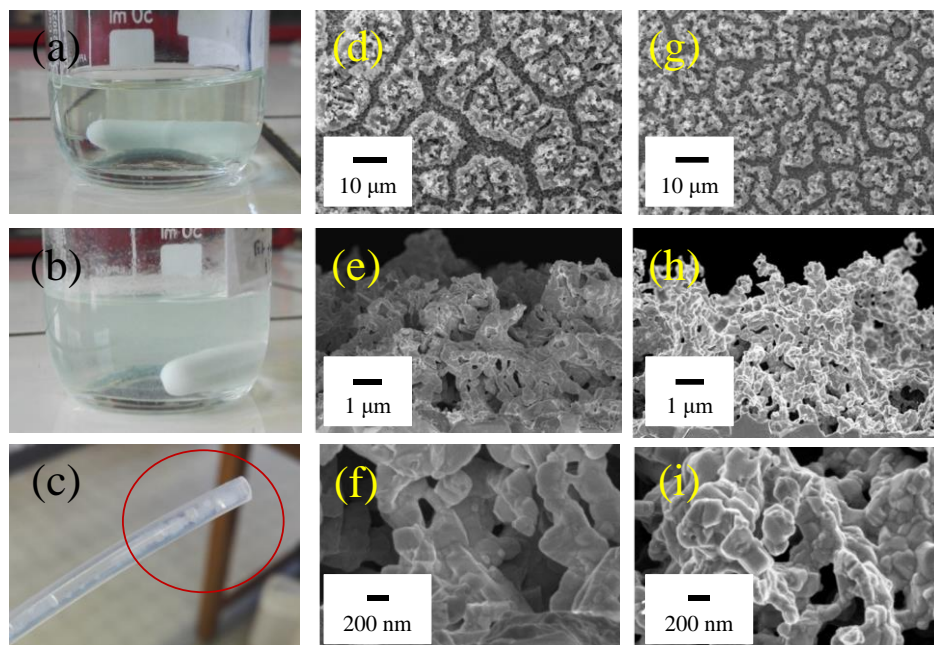


**Fig. 3. 2** The LPNO precursor solution (a) right after the preparation and (b) 1.5 h later without  $\text{HNO}_3$  addition which showed that the solution became opaque due to the formation of precipitates, (c) the precipitates blocked the opening of the tube which prevented the solution of precursors to continue to flow to the needle and thus stopped the spray production. The SEM images of (d) the surface and (e)-(f) the cross-section of the ESD layer prepared from solution without  $\text{HNO}_3$ . The SEM images of (g) the surface and (h)-(i) the cross-section of the ESD layer prepared from solution with the addition of  $\text{HNO}_3$ . Both layers were deposited by ESD for 3 h of deposition time.

A set of preliminary tests, varying ESD deposition time, has also been conducted to optimize the thickness of the active functional layer (AFL). Sufficient thickness of the AFL is required to not limit the extension of the reaction in the electrode as it has been shown by Çelikkilek in the case of a  $\text{La}_{0.6}\text{Sr}_{0.4}\text{Co}_{0.2}\text{Fe}_{0.8}\text{O}_{3-\delta}$  (LSCF) columnar microstructure prepared by ESD in which a minimum thickness of  $2.5 \mu\text{m}$  is necessary [60]. For this purpose, three LPNO electrodes with different ESD deposition times (3 h 45', 4 h 30', and 6 h) were prepared. All samples were then sintered at  $960 \text{ }^\circ\text{C}$  for 6 h in air. The cross-sections of the three samples were then observed by SEM (**Fig. 3.3a-c**). As expected, the thickness of the ESD layer was increased from  $21 \mu\text{m}$ ,  $31 \mu\text{m}$ , to  $43 \mu\text{m}$  for sample deposited for 3 h 45', 4 h 30', and 6 h, respectively. The film growth is not linear to the deposition time as shown in **Fig. 3.3d**. The coral-like microstructure is observed for all samples. However, the one deposited for 4 h 30'

seems to be the most uniform. Some spots with less deposition are observed after deposition for 3 h 45' while the rougher surface is observed after deposition for 6 h which can be attributed to a more concentrated preferential landing over time.

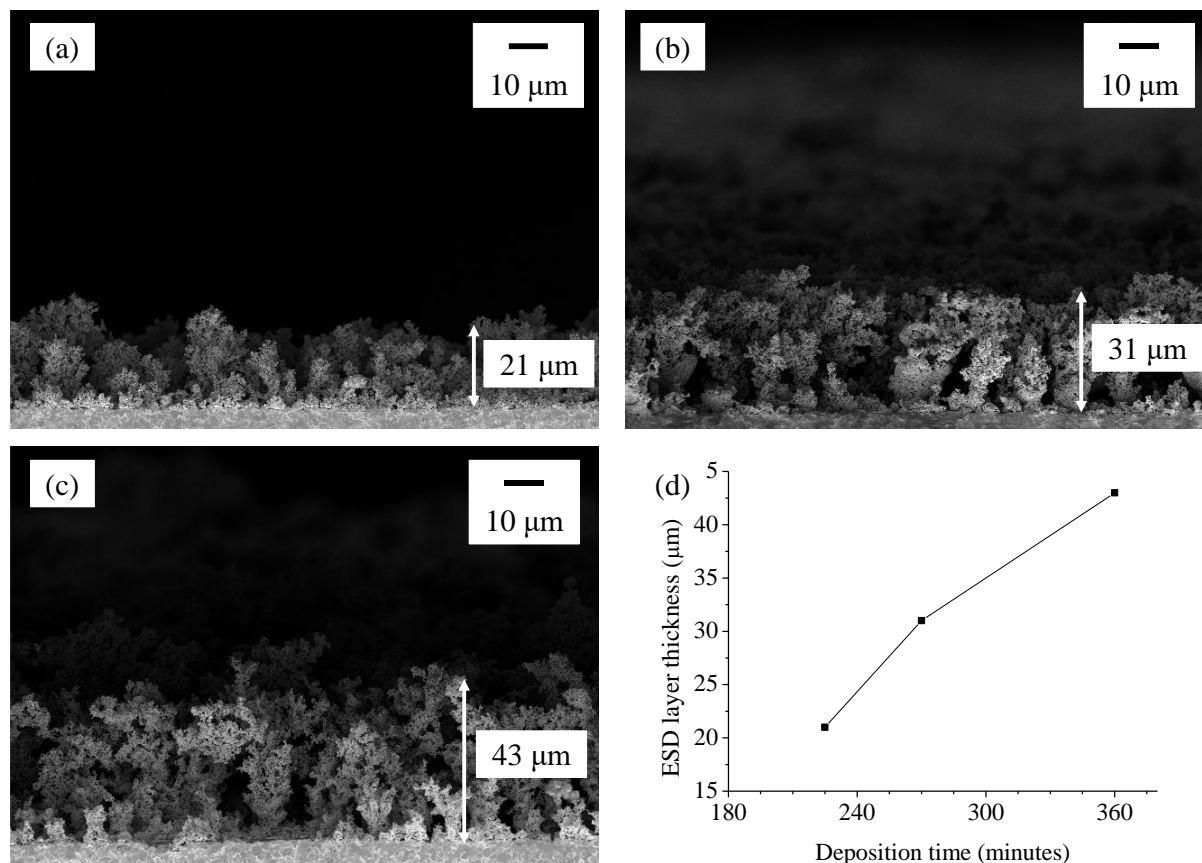


**Fig. 3. 3** The cross-section SEM images of ESD layer deposited for (a) 3 h 45', (b) 4 h 30', and (c) 6 h; (d) the thickness of the ESD layer versus time.

To study the effect of ESD AFL thickness on the electrode performance, three symmetrical cells were measured by EIS in the air at OCP from 450 to 700 °C. The three cells were first prepared on GDC electrolyte by using ESD with three different deposition times (3 h 45', 4 h 30', and 6 h) and sintered at 960 °C for 6 h in air. Afterwards, LPNO was screen-printed on top of the ESD layer followed by two steps of heat treatments in the air: at 450 °C for 2 h to remove the organic solvent in the SP ink and then sintering at 800 °C for 2 h. The thickness of the SP layers for all these cells was around 30 μm. The electrochemical responses are presented in the Arrhenius plots in **Fig. 3.4**. The  $R_{pol}$  of all samples are similar and in the same range, especially for the cells with ESD deposition time of 3 h 45' and 6 h. The  $R_{pol}$  of the cell with ESD deposition time of 4 h 30' is slightly lower at the lower measurement temperature. Thus,

the SEM and EIS results show that the AFL thickness is already sufficient when the deposition time is only 3 h 45', but the microstructure and the electrochemical behavior are optimized when the ESD layer is deposited for 4 h 30'.

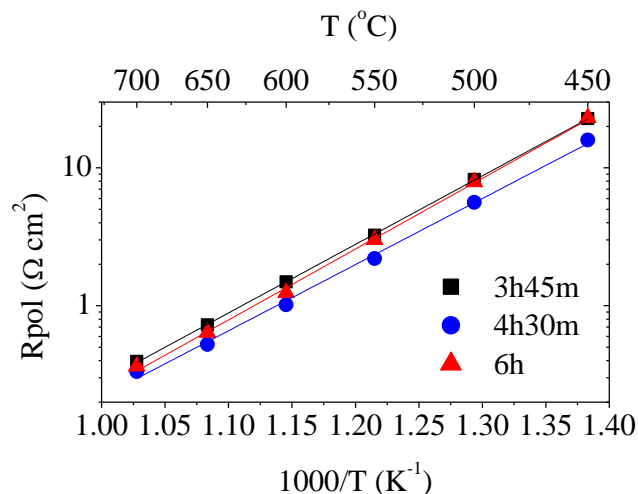


**Fig. 3. 4** The Arrhenius plots of double-layer symmetrical cells with different ESD deposition time: 3 h 45', 4 h 30', and 6 h.

Besides the coral-like microstructure, an attempt to study the electrochemical performance of the ESD layer with a hierarchical microstructure was carried out. It has been shown previously from our group, that the columnar microstructure of LSCF prepared by ESD has better electrochemical performance as compared to the coral microstructure [80]–[82]. The better performance of the columnar film is attributed to the presence of nano-scaled porosity instead of macroscopic porosity observed in the coral film, resulting in the larger specific surface area of the former. Thus, in this work, the columnar LPNO electrode was prepared on the GDC electrolyte by following the same procedure as the ones developed in Çelikkbilek's PhD thesis [81]. To obtain the columnar microstructure, the precursor powders (La-, Pr-, and Ni-nitrates, as well as citric acid) were dissolved in a mixture of ethanol and butyl carbitol, ( $\text{C}_4\text{H}_9(\text{OCH}_2\text{CH}_2)_2\text{OH}$ , Acros Organics, 99+%) (1:2 vol. ratio). The needle-substrate distance was 22 mm, the solution flow rate was  $0.5 \text{ mL h}^{-1}$ , the substrate temperature was  $300 \text{ }^{\circ}\text{C}$ , and the deposition time was 3.5 h. The subsequent sintering in the air was carried out at  $960 \text{ }^{\circ}\text{C}$  for 6 h. Afterwards, the prepared sample was observed by SEM (**Fig. 3.5a-c**). From the SEM image, it can be seen that there is a uniform thin layer of deposition at the electrode/electrolyte interface. The columns, around  $4 \mu\text{m}$ -width, can also be observed. However, the surface view shows that there is a lot of space between the columns which means that the columns are not

uniformly formed. The columns also seem to not be well-attached to the GDC electrolyte revealing a rather poor adhesion. As a consequence, the further EIS measurement has been unsuccessfully attempted since the electrode was severely delaminated from the electrolyte. Thus, an optimization of the deposition parameters and sintering is still required for any future works on the LPNO of columnar-type.

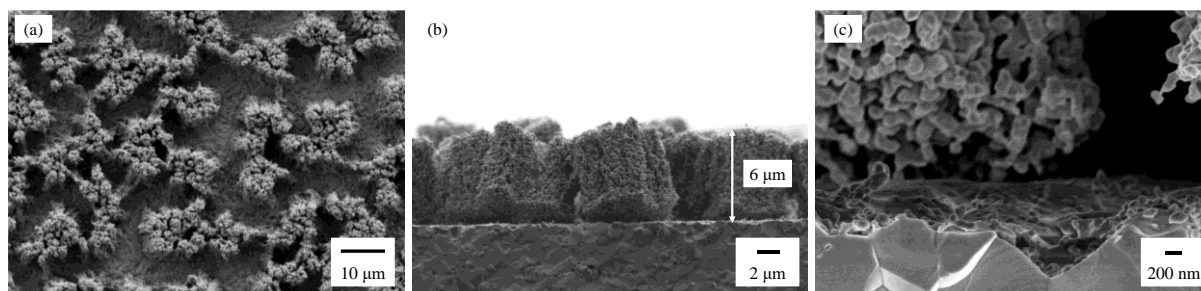


**Fig. 3. 5** The SEM images of the LPNO columnar electrode: (a) the surface view, (b) the cross-section, and (c) a larger magnification at the electrode/electrolyte interface which show the uniform deposition at the electrode/electrolyte interface.

### 3.2.2 Electrochemical performance of coral-type $\text{La}_{2-x}\text{Pr}_x\text{NiO}_{4+\delta}$ ( $x = 0, 1, 2$ )

It has been mentioned in §1.2 that the transport properties of  $\text{La}_{2-x}\text{Pr}_x\text{NiO}_{4+\delta}$  are better as the praseodymium content ( $x$ ) increases, which is evidently shown on the electrochemical response as well. To confirm that, three La-Pr nickelates double-layer symmetrical cells were prepared based on a ‘coral-type’ AFL. The chosen compositions were  $x = 0$  ( $\text{La}_2\text{NiO}_{4+\delta}$ , LNO),  $x = 1$  ( $\text{LaPrNiO}_{4+\delta}$ , LPNO), and  $x = 2$  ( $\text{Pr}_2\text{NiO}_{4+\delta}$ , PNO). All three electrodes were deposited on the GDC electrolyte by ESD for 3 h followed by SP deposition. The sintering in the air after ESD was carried out at 960 °C for 6 h for both for LNO and LPNO, while higher temperatures (1050 °C for 2 h followed by 1100 °C for 0.5 h) were necessary to obtain pure PNO. After SP, all three electrodes were thermally treated in the air at 450 °C for 2 h to remove the organic solvent followed by sintering at 900 °C for 2 h (for LNO and LPNO) or at 1000 °C for 2 h + 1050 °C for 0.5 h (for PNO). The electrochemical performances of the three cells were then measured by EIS at OCP and the results are shown in **Fig. 3.6**. From 450 to 700 °C, the lowest  $R_{\text{pol}}$  values are the ones of PNO and the highest are the ones of LNO. This is in agreement with

our previous studies, where the electrochemical performance of  $\text{La}_{2-x}\text{Pr}_x\text{NiO}_{4+\delta}$  is increased with the increase of praseodymium content [35].

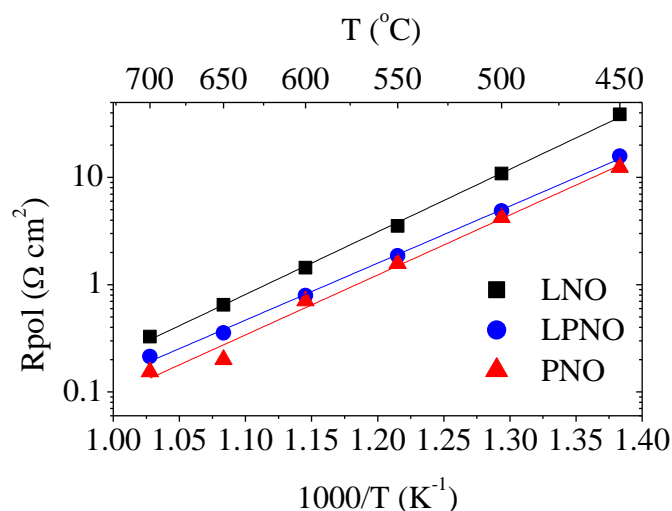


**Fig. 3. 6** The Arrhenius plots of LNO, LPNO, and PNO double-layer symmetrical cells.

### 3.2.3 Reproducibility

To ensure the reproducibility of the electrodes fabricated by both SP and ESD, three identical double-layer symmetrical cells (DL1, DL2, and DL3) were prepared. These electrodes were deposited by ESD on both sides of the GDC electrolyte for 4.5 h followed by a sintering step in the air at 960 °C for 6 h. After the subsequent SP deposition, the three electrodes were again heated in air at 450 °C for 2 h to remove the organic solvent and then sintered at 900 °C for 2 h. The prepared symmetrical cells were then characterized by EIS at OCP. The  $R_{\text{pol}}$  of each cell was extracted from the Nyquist diagrams and plotted in Arrhenius plots which are presented in **Fig. 3.7**. It can be seen that the three cells show similar  $R_{\text{pol}}$  at all temperatures with a deviation of less than 15%, which can be considered within the error range of the measurement. Thus, it can be claimed that the reproducibility of the sample preparation by ESD and SP is confirmed.

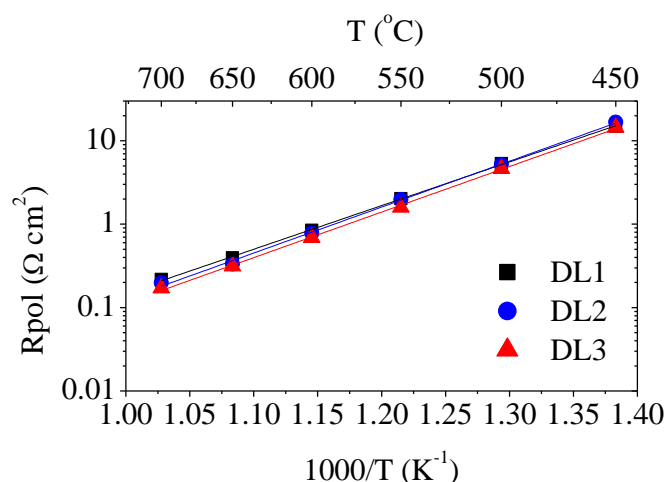


**Fig. 3. 7** The Arrhenius plots of three identical double-layer symmetrical cells for reproducibility test.

### 3.3 Structural characterization of LPNO as a powder, SP layer, and ESD layers

Crystallization of pure  $\text{LaPrNiO}_{4+\delta}$  (LPNO) powder prepared by auto-combustion (§2.2.1) for SP layer was obtained after calcination at 1050 °C for 2 h and at 1100 °C for 0.5 h in air, as shown by XRD (**Fig. 3.8a**). The LPNO phase was indexed to an orthorhombic unit cell with the  $Bmab$  space group (N° 64). The cell lattice parameters deduced from the Rietveld refinement ( $a = 5.432(2) \text{ \AA}$ ,  $b = 5.475(8) \text{ \AA}$ , and  $c = 12.586(9) \text{ \AA}$ ) are also in a good agreement with literature data [22], [35].

The LPNO powder was then screen-printed on several GDC electrolytes. The SP layers were firstly heated in air at 450 °C for 2 h to remove the organic solvent used for the ink and then sintered at different temperatures from 800 °C to 1200 °C to check the thermal stability of the SP layer (**Fig. 3.8b**). Up to 900 °C, there is no presence of secondary phases detected in the XRD patterns. After sintering at 1100 °C, however, a minor contribution of a higher-order nickelate phase  $(\text{La,Pr})_3\text{Ni}_2\text{O}_{7-\delta}$ , referred to as (LP)3N2, can be detected. It appears that sintering at 1200 °C leads to a decrease of the (LP)3N2 content to some traces only.

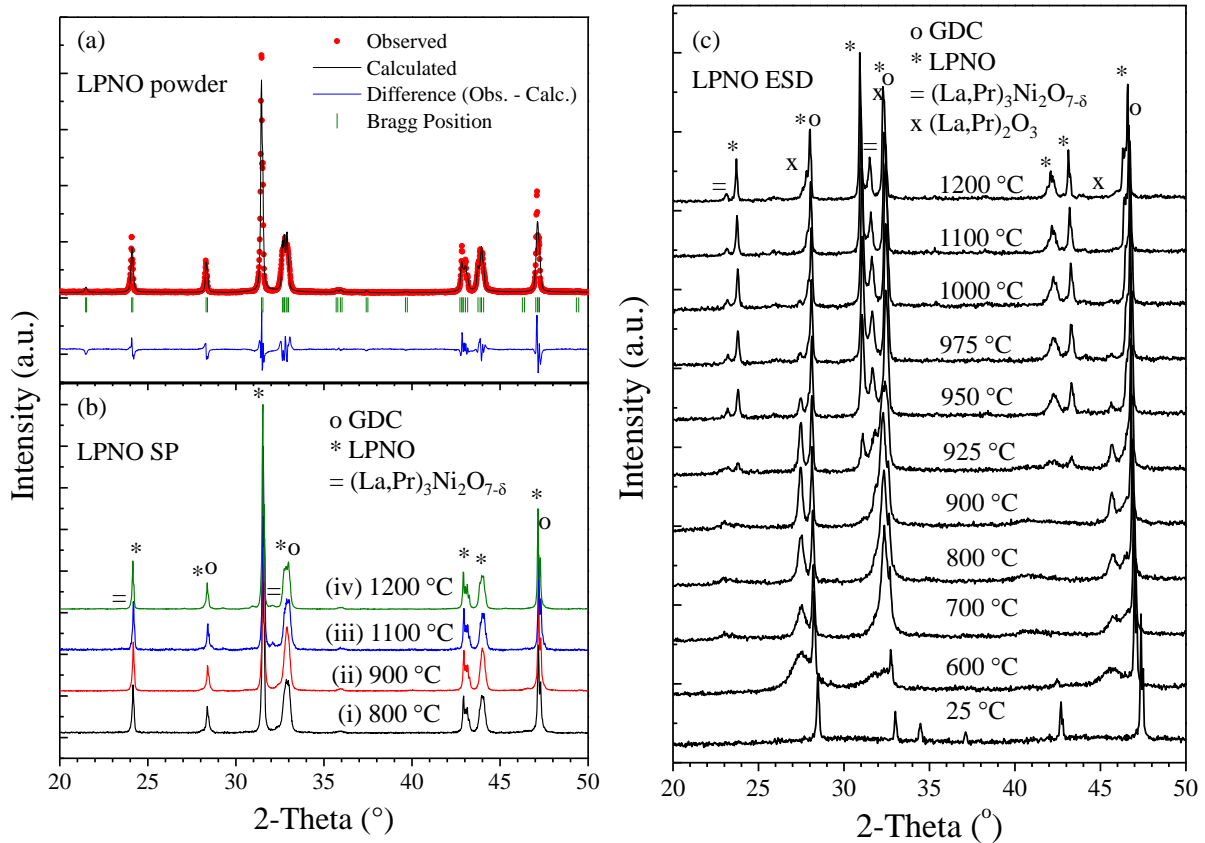


**Fig. 3. 8** XRD of (a) LPNO powder prepared by auto-combustion and calcined at 1050 °C/2 h + 1100 °C/0.5 h in air and (b) screen-printed layers of LPNO on GDC thermally treated in air at (i) 450 °C/2 h + 800 °C/2 h, (ii) 450 °C/2 h + 900 °C/2 h, (iii) 450 °C/2 h + 1050 °C/2 h + 1100 °C/0.5 h, and (iv) 450 °C/2 h + 1200 °C/2 h; (c) In-situ high temperature XRD from 25 to 1200 °C of the as-deposited SL LPNO electrode by ESD.

The structural properties of as-deposited LPNO ESD electrode on GDC electrolyte were investigated using *in-situ* high-temperature XRD at a variable temperature from 25 °C to 1200 °C. The purpose of the *in-situ* measurement is to follow the phase evolution of ESD LPNO layer versus temperature and to identify an optimum in the sintering temperature allowing the LPNO crystallization and partial densification without its decomposition. The XRD pattern at each measurement temperature is shown in **Fig. 3.8c**. Initially, at 25 °C, only GDC peaks are detected from the amorphous fresh film. The evolution of the XRD patterns reveals that the crystallization of the film starts at 600 °C with the appearance of broad peaks which are quite difficult to index since there are a lot of possible phases in this  $2\theta$  range. From 700 to 900 °C, the broad peaks become sharper and can be assigned more than likely to lanthanum-praseodymium oxide,  $(\text{La,Pr})_2\text{O}_3$ . The oxide starts to transform into an LPNO

structure at 925 °C, but at the same time, there is also the formation of a higher-order nickelate which is identified as (LP)3N2. At 950 °C, the signature of both LPNO and the higher-order phase significantly increases, while the initial phase of lanthanum-praseodymium oxide tends to vanish. Above 950 and up to 1200 °C, the two phases of LPNO and higher-order coexist and are quite stable, while the initial (La,Pr)<sub>2</sub>O<sub>3</sub> phase has completely disappeared.

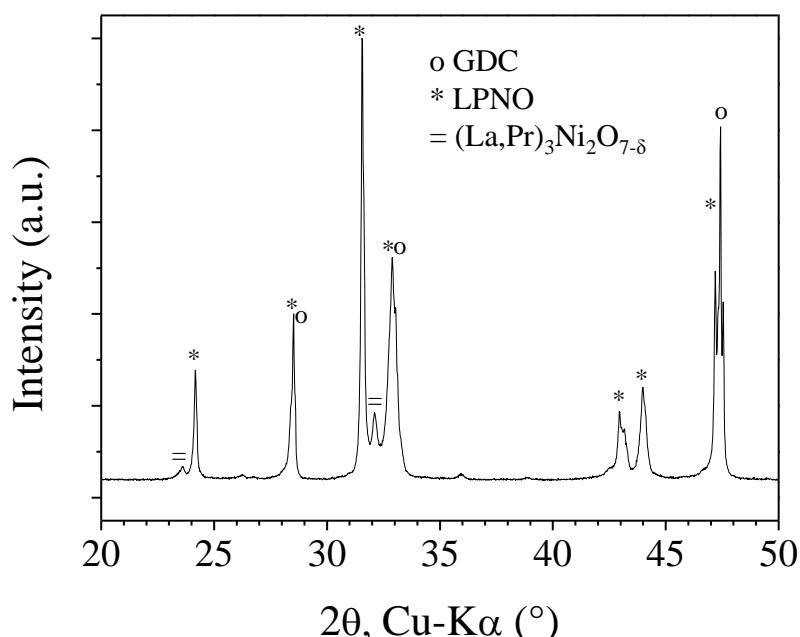


**Fig. 3. 9** The diffractogram of the ESD layer after sintering in the air at 960 °C for 6 h.

The results of *in-situ* high-temperature XRD give a rough estimation of the phase evolution because the diffractogram is taken just 30 minutes after the furnace temperature reaches the setting point. Based on this result, the sintering condition of the ESD layer is determined to be at 960 °C for 6 h. At this sintering condition, the lanthanum-praseodymium oxide is no longer present and the temperature is sufficiently low to preserve the small particle size of the ESD layer. A scratch test of LPNO on GDC electrolyte also reveals a good electrode/electrolyte adhesion after sintering at only 960 °C. However, in line with the *in-situ* high-temperature XRD, a small amount of higher-order nickelate (LP)3N2 is also present as a secondary phase as shown in the XRD pattern in **Fig. 3.9**. This phase, which is also a Ruddlesden-Popper phase with  $n = 2$ , has been reported to be an electrochemically active material [19], [40], [41]. The effect of the presence of this secondary phase on the electrochemical performance of the LPNO electrode will be explained in more detail in §3.6. The durability study of the electrode in order

to see whether the presence of the secondary phase affects the degradation is reported in Chapters 4 and 5.

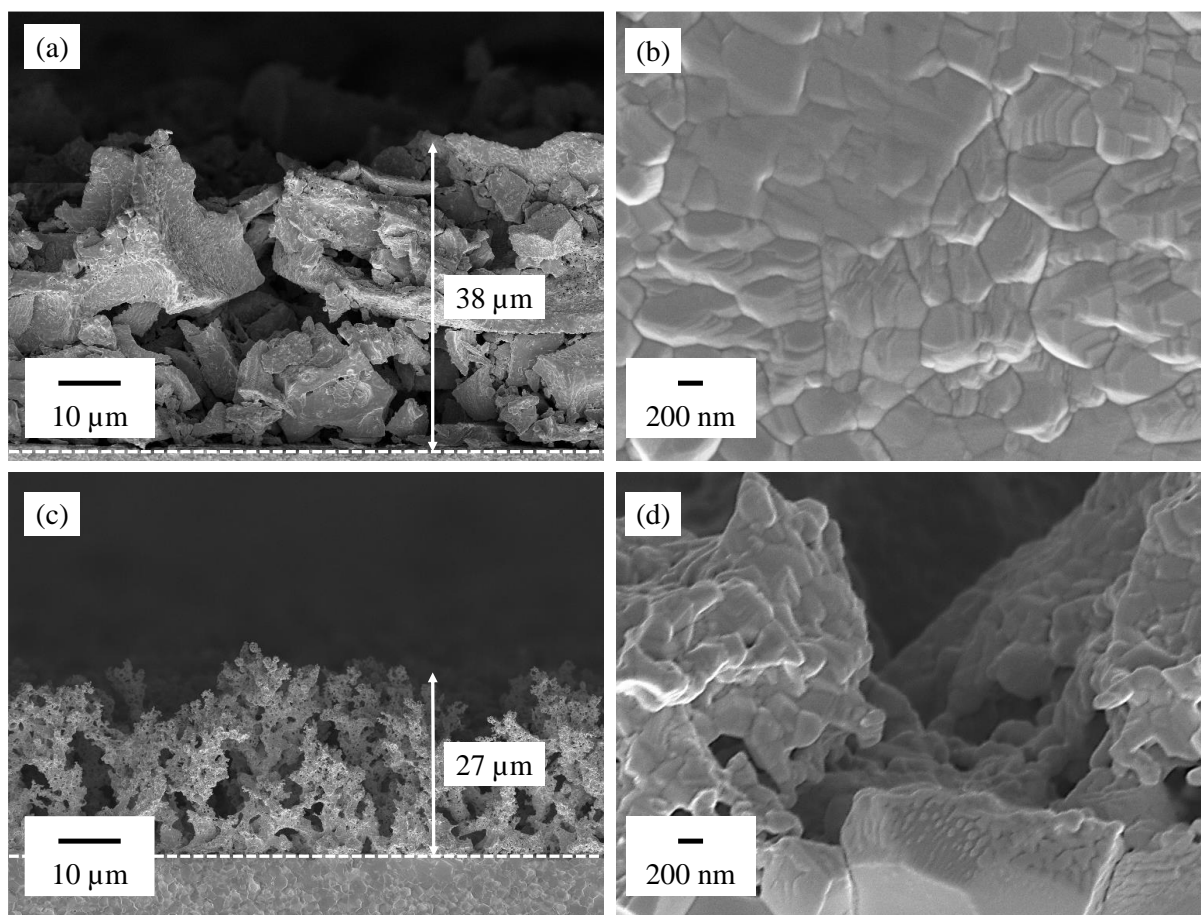


**Fig. 3.10** SEM images of cross-sections of (a), (b) SL SP sintered at 1100 °C (sample 2) and (c), (d) SL ESD sintered at 960 °C (sample 3) on two different magnifications. The electrode/electrolyte interfaces are indicated by the dashed white lines.

The difficulty to obtain single-phase LPNO deposited by ESD might be explained by its fine microstructure resulting in a more reactive material compared to the coarse SP microstructure. From the SEM images (**Fig. 3.10a-d**), the average particle size of the ESD layer is estimated to be 130 nm while the SP layer is 500 nm. Indeed, a study by Montenegro-Hernández *et al.* has shown that both lanthanum and praseodymium nickelates are very chemically active if the particle size is submicronic [37]. Also, the microstructure of the ESD layer is more ‘open’ with larger porosity than the SP one which may also explain the chemical reactivity. A more detailed explanation of the microstructure, especially the electrode/electrolyte interface, of both SP and ESD layers will be given in §3.5.

### 3.4 Equivalent electrical circuit model for EIS data fitting

As previously mentioned in §2.5, the EIS data fitting with an equivalent electrical circuit is necessary for the accurate determination of the series and electrode polarization resistances [83]. Besides, the EIS fitting can be also used to interpret the electrode reaction mechanism associated with the electrochemical performances. Indeed, under the assumption that each element of the electrical circuit can be associated with a physical process with a given time constant, the analyses of the fitting results can be helpful to identify the co-limiting steps of the reaction pathway [84]. In this work, an equivalent circuit, which is schematically shown in **Fig. 3.11**, was used to fit the EIS data of all the samples.

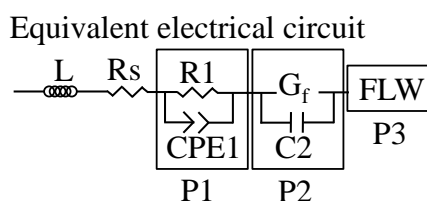


**Fig. 3. 11** The schematic diagram of the equivalent circuit model which is used to fit the experimental EIS data.

The circuit consists of several elements in series and is composed of:

- (1) an inductor ( $L$ ) to take into account the contribution from the wire and interconnection,
- (2) a resistor ( $R_s$ ) corresponding to the pure ohmic contribution of the electrolyte (also called the series resistance) which is shown as the intercept with the  $x$ -axis at high frequency in Nyquist plot (**Fig. 2.13** in §2.5),
- (3) a resistor in parallel to a constant phase element ( $R1//CPE$ ) to account for the high frequencies process (more than  $10^2$  Hz) ascribed to the ionic transfer at the electrode/electrolyte interface (this process is assigned as P1). This process is also indicated by a low capacitance values ( $10^{-5}$ - $10^{-4}$  F/cm<sup>2</sup>) [23]. The values of the resistance will be referred to as  $R1$  while the capacitance, which is calculated by using **Eq. C.16** in **Appendix C**, will be called  $C1$ ,
- (4) a fractal Gerischer element ( $G_f$ ) in parallel with a capacitor ( $C2$ ) for the process arising at medium frequencies (1-100 Hz, assigned as P2) and associated with a large capacitance value ( $10^{-3}$ - $10$  F/cm<sup>2</sup>) [23], [29]. This capacitance is called the ‘chemical capacitance’ or ‘pseudo-

capacitance'. Chemical capacitance is related to the change on the oxygen stoichiometry of MIEC within the active regions where the ORR/OER takes place. Since the active regions of MIEC are usually extended to a few micrometers from the electrolyte, the chemical capacitance is larger than the interfacial capacitance (i.e.  $C_1$ ) which is confined only at the interface. The fractal Gerischer element, which takes into account for a deviation from the ideal Gerischer, represents the solid-state diffusion in the bulk convoluted with the charge transfer reaction taking place at the surface of the LPNO particles [29]. It was shown in a previous study that the capacitor element allows improving the global quality of fitting for this medium frequency contribution [85]. However, the underlying physical process associated with this capacitor is still unclear. It could be due to the presence of oxygen ions attached on the surface of LPNO involving a surface double-layer characterized by its capacitance. In this view, the rate of oxygen incorporation/excorporation from LPNO would not be purely chemical but described by a Butler-Volmer electrochemical reaction as proposed by Fleig for mixed conducting electrodes [86].

The obtained resistance extracted from the fitting for this process P2 will be called as R2. There are two capacitance values obtained: (i) the chemical capacitance ( $C_{chem}$ ) which is calculated from the time constant of fractal Gerischer element ( $\tau_{G_f}$ ) divided by R2, both of the values are obtained from the fitting ( $C_{chem} = \tau_{G_f}/R_2$ ) and (ii) the capacitance obtained from the capacitor element which is called C2,

(5) a finite-length Warburg element (FLW) to account for the gas transfer that appears at low frequencies (less than 1 Hz, assigned as P3) [87], [88]. As this gas diffusional process is not thermally activated, this contribution starts to be detectable especially at a temperature higher than 600 °C. Indeed, the rate of oxygen incorporation/excorporation step strongly improves with increasing the temperature leading to the reduction of the contribution of P2 and resulting in the appearance of P3. The resistance related to this process is called R3 while the capacitance, calculated by **Eq. C.8** in **Appendix C**, is called C3.

The presented series resistances ( $R_s$ ) are normalized by multiplying the fitted values with the surface area of the electrode (i.e.  $R_s = R_{s\_fitted} \times A$ ). The polarization resistance ( $R_{pol}$ ) is obtained by either calculating the difference on the intercept with  $x$ -axis at low and high frequency on the Nyquist plot or by the summation of R1, R2, and R3. The presented values

of  $R_{pol}$  are normalized according to Eq. 2.5 in §2.5 (i.e.  $R_{pol} = R_{electrode\_fitted} \times A/2$ ). All the capacitance values are also expressed by the electrode surface area.

### 3.5 Influence of the electrode/electrolyte interface quality on the performance of the LPNO electrode

Three different single-layers (SL) have been deposited by either SP or ESD on GDC electrolyte (i.e. samples 1-3 in **Table 3.1**) with the purpose to observe the effect of electrode/electrolyte interface quality on the electrochemical performance of the electrode. As detailed in **Table 3.1**, two SL electrodes have been deposited by SP and then thermally treated at two different temperatures in the air: 450 °C for 2 h + 800 °C for 2 h (sample 1) and 450 °C for 2 h + 1050 °C for 2 h + 1100 °C for 0.5 h (sample 2). In both samples, the powder used for SP is manually ground. Another single-layer electrode is prepared by ESD and sintered at 960 °C for 6 h in the air (sample 3).

The electrodes microstructure has been characterized by SEM. For sample 1, the observations have revealed that the layer is poorly bonded to the substrate, thus it is difficult to obtain a clear SEM image. This issue is probably due to the final sintering temperature of 800 °C which is lower than the required temperature to achieve good adhesion between LPNO and GDC electrolyte for the SP layer. A sintering temperature of at least 1100 °C is required to obtain good contact and avoid any delamination between the electrode and the electrolyte as shown for sample 2 in **Fig. 3.10a-b**. The thickness and average particle size of sample 2 are around 38 μm and 500 nm, respectively. It is worth noting the presence of large agglomerates which are certainly the consequence of a manual and heterogeneous grinding of the SP powder. Meanwhile, the thickness and average particle size of sample 3 are 27 μm and 130 nm, respectively (**Fig. 3.10c-d**). As expected from the previous work in our group using the same ESD conditions, the ‘coral-like’ microstructure is clearly observed [35]. This unique microstructure is obtained due to the deposition parameters described in §2.2.3, resulting in small and drier arriving droplets on the substrate and promote the preferential landing of these droplets [89]. Close observation on the electrode/electrolyte interface shows that the LPNO is continuously deposited along the interface. It is also clear that the ESD layer is more porous than the SP layer, especially close to the surface. That means that the ESD layer has a more ‘open’ surface.

To study the impact of the electrode/electrolyte interface quality on the electrode response, electrochemical characterizations by EIS have been performed on the symmetrical cells for the three samples at a temperature range of 450 to 700 °C. The Nyquist and Bode representations of the measurement results for these cells at 500, 600, and 700 °C are plotted in **Fig. 3.12a-f** after subtracting the series resistances for the sake of clarity and easier comparison. It is clear that the shape and size of the Nyquist plots for sample 1 are different as compared to the other two samples at all temperatures. The frequency distribution shown in the Bode plots is shifted toward higher values as temperature increases which can be attributed to the faster oxygen exchange at the surface [90], [91]. The Bode plots also show that the peaks related to P2 are strongly dominant for all samples at all temperatures. Meanwhile, the contribution of P1 is significant at all temperatures for sample 1, and it is slightly present up to 600 °C for sample 2. However, the contribution of P1 is not detected for sample 3 at all temperatures. The P3 becomes important at 700 °C for all samples, except for sample 3 which shows that P3 contribution starts to appear at 600 °C. Based on this observation, each sample is fitted with a suitable circuit according to **Fig. 3.11** in the previous section.

The values of series resistance ( $R_s$ ), which were subtracted from the Nyquist plots in **Fig. 3.12a-c**, are plotted versus temperature in **Fig. 3.13a**. Meanwhile, the polarization resistances ( $R_{pol}$ ) are shown in the Arrhenius plots in **Fig. 3.13b**. As expected, both the  $R_s$  and  $R_{pol}$  values decrease when the temperature is increased for all samples. The values of both resistances are the highest for sample 1 as compared to the other samples. As has been already mentioned in the previous section,  $R_s$  is directly related to the ohmic resistance from the electrolyte which is proportional to the ratio between its thickness and conductivity (Eq. 1.9 in §1.2.2). Moreover, it also depends on the contact between the electrode/electrolyte. Since all samples were prepared on the same electrolyte with similar thickness, one may suggest that the series resistance is higher for sample 1 because of poor contact between the electrode and the grid for this sample and/or some interfacial cracks at the electrode/electrolyte interface due to the poor electrode adhesion. This argument is further supported by the  $R_{pol}$  values. A significant improvement in the electrode performance is clearly observed for sample 2 as compared to sample 1 despite the fact that both electrodes are deposited by SP. From the fitting with the equivalent circuit, the polarization resistance can be deconvoluted to the resistance related to the corresponding processes. The deconvolution of the resistance is shown in **Fig. 3.13c**. As previously mentioned from the Bode plots, the contribution of P1 is apparent for both samples

1 and 2. However, it is clear that  $R_1$  of the sample 1 is very large and it contributes to almost 50% of the polarization resistance as compared to only 4% for sample 2. As mentioned in §3.4, this process is attributed to the ionic transfer across the electrode/electrolyte interface and is thus enlarged for the delaminated layer of sample 1. Therefore, the high  $R_{pol}$  of sample 1 can be attributed to the poor adhesion of the electrode on the GDC electrolyte limiting the ionic transfer.

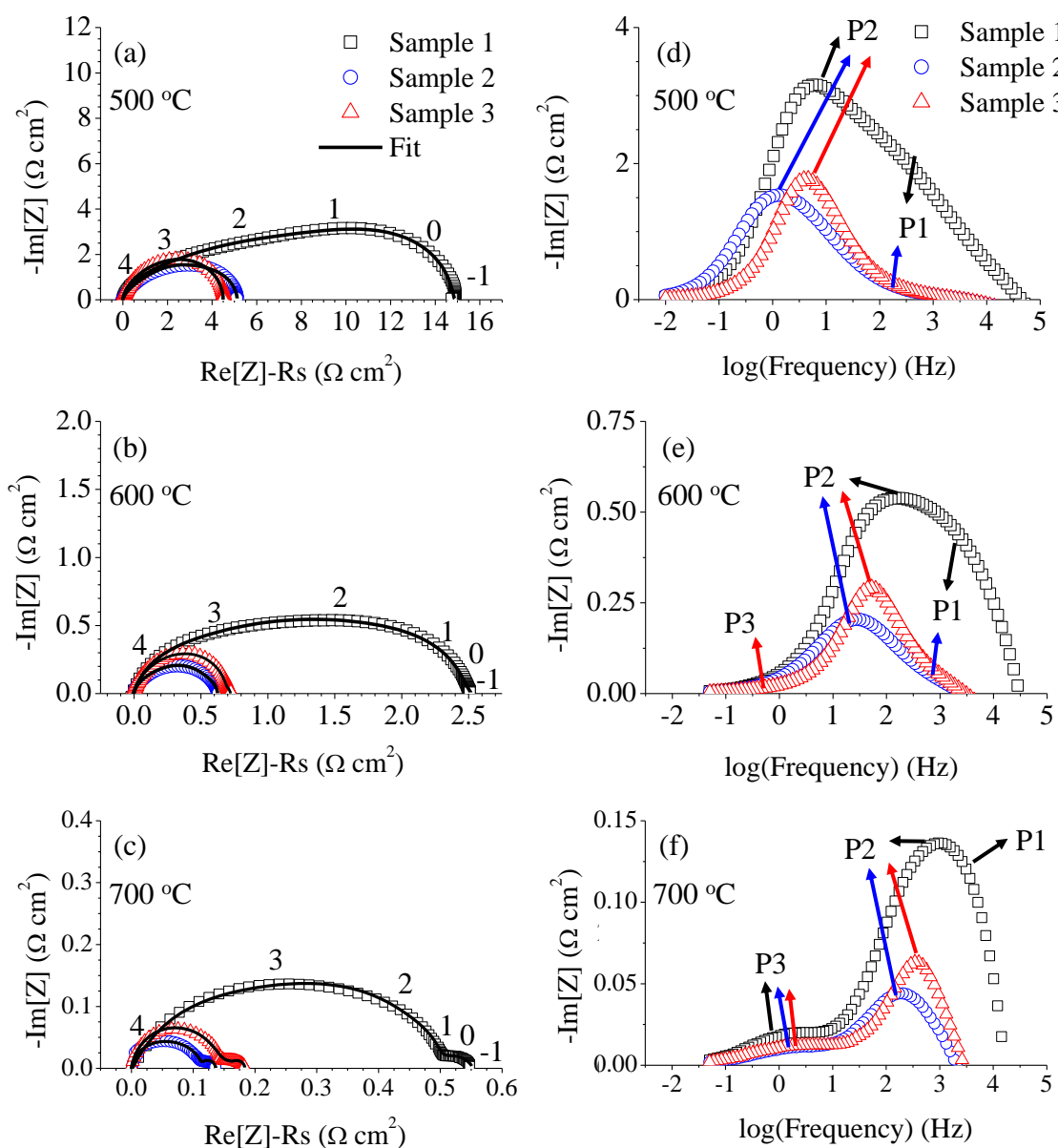


**Fig. 3. 12** (a)-(c) Nyquist plots and (d)-(f) Bode plots of samples 1, 2, and 3 at 500, 600, and 700 °C, respectively. The Nyquist plots are plotted by subtracting the contribution of the series resistance and the numbers on the Nyquist plots indicate the logarithmic of the frequencies.

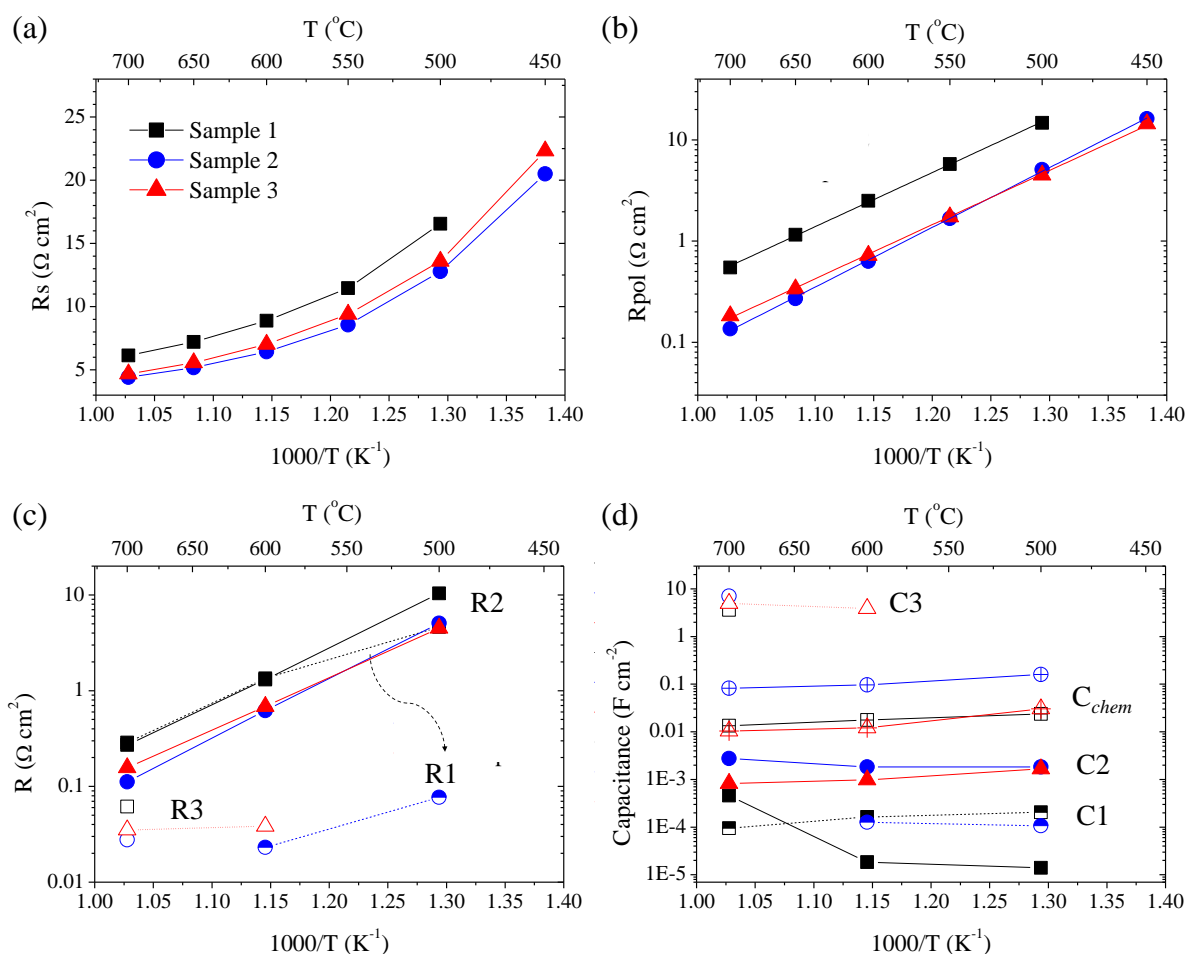


**Fig. 3.13** The Arrhenius plots of (a) series resistance ( $R_s$ ) and (b) polarization resistance ( $R_{pol}$ ). The deconvolution of (c) resistance ( $R$ ) and (d) capacitance ( $C$ ) associated with P1 (half-filled markers), P2 (filled markers), and P3 (empty markers) processes, as well as chemical capacitance ( $C_{chem}$ , empty with plus sign markers). All plots are for sample 1 (black square), 2 (blue circle), and 3 (triangle red).

A crossing of Arrhenius plots of  $R_{pol}$  between sample 2 and sample 3 (**Fig. 3.13b**) can be observed at 550 °C. Indeed, at a temperature lower than 550 °C, the ESD layer (sample 3) performs slightly better than the one of the SP layer (sample 2). Above 550 °C, a reverse behavior is detected. It is primordial to consider key parameters such as the microstructure (particle size, porosity, etc.), the purity, and the interfaces (the electrode/electrolyte one and the electrode surface) to compare electrochemical properties of both samples. The reasons why the ESD film is performing better at low temperature are certainly triple. First, ESD films are characterized by particles at the nanometer-length scale (**Fig. 3.10c** in §3.3) which are much

more electrochemically active than in the case of sample 2. Second, both samples also present a good electrode/electrolyte interface as no delamination is observed on either sample. However, unlike for sample 2, the process at higher frequency (P1) is unnoticeable for sample 3 at all temperatures which implies that the electrode/electrolyte interface is even better for the electrode deposited by ESD in consequence of the continuous contact formed at the interface as seen by SEM observation in **Fig. 3.10**. Thus, it appears that better adherence is reached for LPNO ESD layer and GDC electrolyte even after sintering at only 960 °C than after sintering at 1100 °C for the SP layer. Thirdly, another point to consider is the secondary phase of (LP)3N2, which is present in a larger content in sample 3 than in sample 2 (**Fig. 3.8b** (iii) and **Fig. 3.9** in §3.3). This secondary phase is also electrochemically active and can help to improve the performance, especially at a higher temperature, as explained in more detail in §3.6. If one refers to a temperature above 550 °C, sample 2 is performing better than sample 3. In this case, at a higher temperature, a much better contact is reached between the electrode and the gold grid of the measurement setup and especially for sample 2. Indeed, sample 2 is characterized by a flatter surface than the one of sample 3 which presents a rough electrode surface due to the coral-like microstructure of the layer deposited by ESD. Thus, at a lower temperature, the smaller particle size, higher amount of the secondary phase, and the better electrode/electrolyte interface of the ESD layer with comparison to the SP one play key a role in the performance of the electrode. Meanwhile, at a higher temperature, it seems that the better electrode surface of the SP layer becomes more important.

To confirm that each process is correctly assigned, the deconvolution of the capacitance is given in **Fig. 3.13d**. As has been explained in §3.4, the values of C1, C<sub>chem</sub>, and C3 are indeed in agreement with the values of capacitance for interfacial, chemical, and gas diffusion capacitance, respectively. The values of C2, which comes from the capacitor in parallel to the fractal Gerischer element, is lower than the values of C<sub>chem</sub>. However, in the case of sample 2 and 3, its values are larger than the interfacial capacitance. Meanwhile, the values are in the range of the interfacial capacitance for sample 1, especially at a lower temperature. It has been explained in §3.4 that while this additional capacitor helps to improve the fitting, the physical meaning of it is still not clear. It can be suspected that for sample 1 it is related to the charge transfer since the electrode kinetic is largely limited by this process, while for sample 2 and 3 it is related to something else.

### 3.6 Influence of the secondary higher-order phase on the electrochemical performance of the ESD layer

In §3.3, it has been shown that a secondary phase, which is identified as  $(\text{La,Pr})_3\text{Ni}_2\text{O}_{7-\delta}$  or abbreviated as  $(\text{LP})_3\text{N}_2$ , co-exists in a small amount with LPNO phase in the ESD layer after sintering at 960 °C for 6 h in air. In order to investigate the effect of this secondary phase, three double-layer (DL) electrodes with different heat-treatment temperatures have been prepared (samples 4-6, **Table 3.1**). The manufacturing of the DL electrodes starts with the deposition of an AFL of LPNO by ESD which is then followed by the coating of a CCL LPNO by SP. A heat-treatment step is required after each deposition step. The sintering after ESD has been carried out at 960 °C for 6 h in air and is referred to as the first heat-treatment, while the one after SP is referred to as the second heat-treatment. It is of great importance to characterize the nature of phases present in the ESD layer after the second heat-treatment. For that, the ESD layers have been annealed at three different temperatures after the first heat-treatment and then characterized by XRD. **Fig. 3.14** shows the XRD patterns of the ESD layer after first heat-treatment (i) and after second heat-treatment in air at 450 °C for 2 h + 800 °C for 2 h (ii), 450 °C for 2 h + 900 °C for 2 h (iii), and 450 °C for 2 h + 1050 °C for 2 h + 1100 °C for 0.5 h (iv). By comparing to the XRD patterns after only first heat-treatment (i) and second heat-treatment at 800 °C (ii) confirms that there is no change in the composition of the phase. However, second heat-treatment at a temperature higher than 800 °C (iii and iv) leads to a larger amount of the secondary phase  $(\text{LP})_3\text{N}_2$ . However, after 900 °C, the content of the secondary phase is reaching a maximum. From the literature, the higher-order nickelates of Ruddlesden-Popper with  $n = 2$  and 3 have been reported to be also active materials with higher electrical conductivity compared to the lower order nickelates [19], [40], [41]. A study shows that the composite based on a mixture of  $\text{La}_2\text{NiO}_{4+\delta}$  and  $\text{La}_4\text{Ni}_3\text{O}_{10-\delta}$  (another Ruddlesden-Popper phase with  $n = 3$ ) presents a lower polarization resistance than the one of each individual single-phase, especially at a temperature higher than 600 °C [92]. In another work, composite of  $\text{La}_2\text{NiO}_{4+\delta}$ – $\text{La}_3\text{Ni}_2\text{O}_{7-\delta}$ – $\text{Ce}_{0.55}\text{La}_{0.45}\text{O}_{2-\delta}$  (an ionic conductor) also shows a good performance with  $R_{\text{pol}}$  of 1.11  $\Omega \text{ cm}^2$  at 600 °C [90]. Thus, the presence of a high-order nickelate as a secondary phase may improve the electrode performance. Therefore, the impact of the different amounts of the higher-order nickelates  $(\text{LP})_3\text{N}_2$  in the ESD layer for the DL electrodes on the electrochemical performance has been investigated by EIS. For this purpose, three double-layer symmetrical cells have been prepared which are called sample 4 (second final heat-treatment at 800 °C),

sample 5 (second final heat-treatment at 900 °C), and sample 6 (second final heat-treatment at 1100 °C).

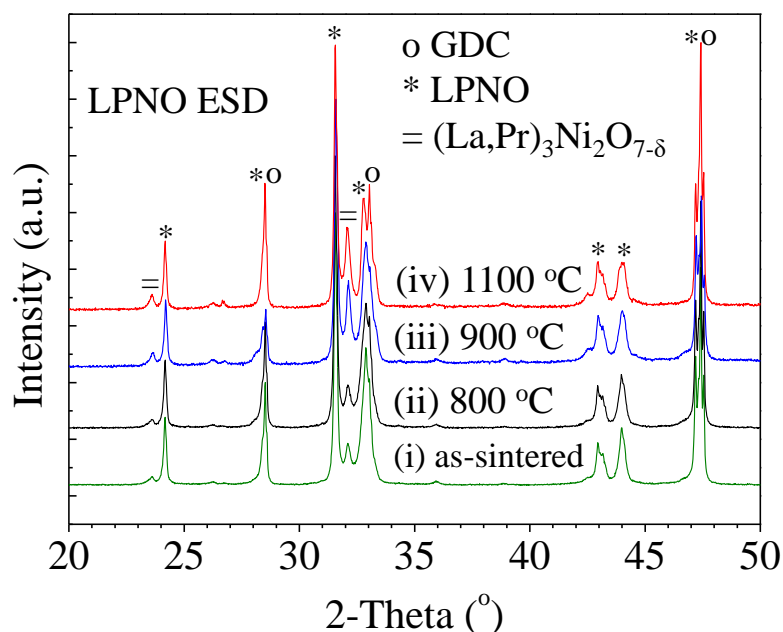


**Fig. 3. 14** XRD patterns of the ESD layer (i) as-sintered at 960 °C for 6 h in air and after second heat-treatment in air at (ii) 450 °C/2 h + 800 °C/2 h, (iii) 450 °C/2 h + 900 °C/2 h, and (iv) 450 °C/2 h + 1050 °C/2 h + 1100 °C/0.5 h.

From the Nyquist plots of the three samples taken at measurement temperatures of 500, 600, and 700 °C in **Fig. 3.15a-c**, the shape of the plots are quite similar for all samples even though the size varies. The Bode representations in **Fig 3.15d-f** further show that the frequency distributions are alike for all samples at all temperatures. The peaks correspond to P2 are strongly present at all temperatures while P3 contribution starts to be more important at 600 °C. There is no contribution of P1 detected for all samples at all temperatures as seen in sample 3 in the previous section which indicates a good electrode/electrolyte interface in such a way the ionic transfer at the electrode/electrolyte interface is not limiting. As in sample 3, the first layers of the electrode for samples 4-6 were deposited by ESD. **Fig. 3.16a** shows that the  $R_s$  values of the three samples are comparable and still within the error range (the deviation is less than 10%) which further indicates the similar electrode/electrolyte quality (without partial delaminations).

However, the three electrodes show different electrochemical behavior depending on the temperature as shown by the  $R_{pol}$  values in **Fig. 3.16b**. Firstly, sample 5 presents lower  $R_{pol}$

compared to sample 4 for all the temperature range and the difference is enhanced when the temperature is increased. From the cross-section image obtained by SEM shown in **Fig. 3.17a-b**, the ESD layer of sample 5 is only 20  $\mu\text{m}$ -thick and shows an average particle size of 150 nm, which means that the layer is more densified and has slightly bigger particle size than the ESD layer after the first sintering (**Fig. 3.10c-d** in §3.3). There are no SEM images for the ESD layer of sample 4, but it can be expected that there is less densification and grain growth compared to the ESD layer of sample 5 due to the lower second heat-treatment temperature. Thus, despite its unfavorable microstructural coarsening, it can be concluded that the improvement of the performance of sample 5 is mainly due to the presence of a higher amount of the (LP)3N2 secondary phase. Secondly, sample 6 exhibits a different thermal behavior as sample 5 even though both of them have a similar amount of the secondary phase in the ESD layer. Sample 6 has the highest  $R_{\text{pol}}$  between the three samples at low temperature, then the  $R_{\text{pol}}$  becomes smaller than sample 4 at a temperature higher than 600 °C, while its value is similar to sample 5 at 700 °C. From the cross-section images by SEM in **Fig. 3.17c-d**, the ESD layer of sample 6 has a thickness of 10  $\mu\text{m}$  and an average particle size of 200 nm, indicating quite a severe densification and grain growth. Thus, the electrode is less performing at low temperature due to the low specific surface area which reduces the number of sites where the reaction of oxygen incorporation can take place. However, as the temperature increases, the presence of the higher-order secondary phase in this electrode helps to significantly improve the electrode performance. It can be safely inferred from these results that the impact of the higher-order phase on the electrode performance is sufficiently thermally activated to overcome the effect of the microstructure densification. The different behavior of the three samples is also evident from the activation energy values which are 0.95, 1.08, 1.21 eV for samples 4, 5, and 6, respectively.

The deconvolution of the polarization resistance in **Fig. 3.16c** shows that the electrode resistance is majorly contributed by R2 with the same trendline as the polarization resistance. The P3 starts to minorly contribute at 600 °C. The contribution of R3 to the total polarization resistance is less than 6% at 600 °C and less than 30% at 700 °C for all samples. By analyzing the capacitance values related to each process shown in **Fig. 3.16d**, the values of  $C_{\text{chem}}$  are within the theoretical value for chemical capacitance and the large values of C3 are related to the capacitance for gas diffusion. Meanwhile, the C2 values are smaller than those of  $C_{\text{chem}}$ , but they are larger than the capacitance related to interfacial capacitance.

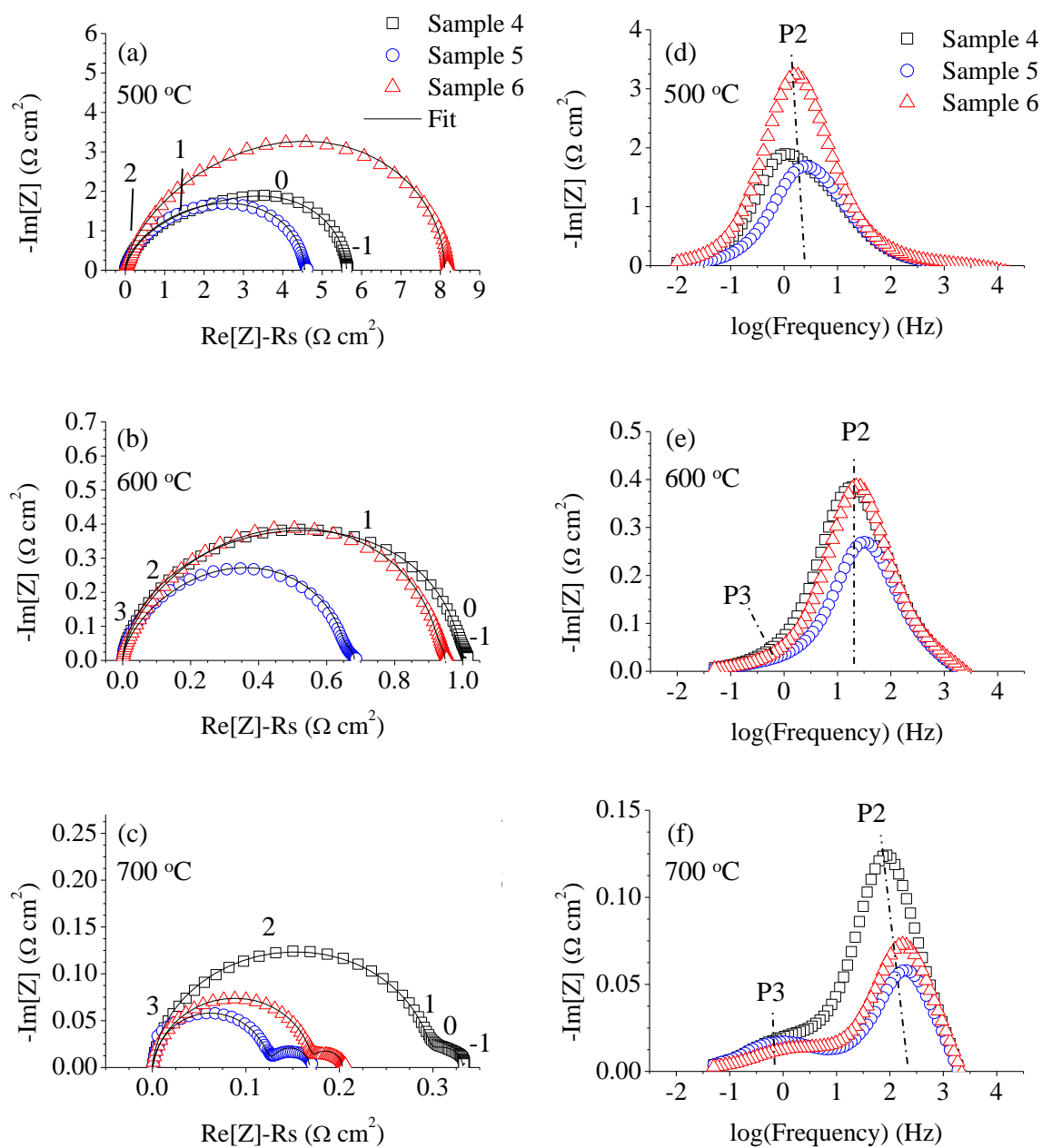


**Fig. 3. 15** (a)-(c) Nyquist plots and (d)-(f) Bode plots of samples 4, 5, and 6 at 500, 600, and 700 °C, respectively. The Nyquist plots are plotted by subtracting the contribution of the series resistance and the numbers on the Nyquist plots indicate the logarithmic of the frequencies.

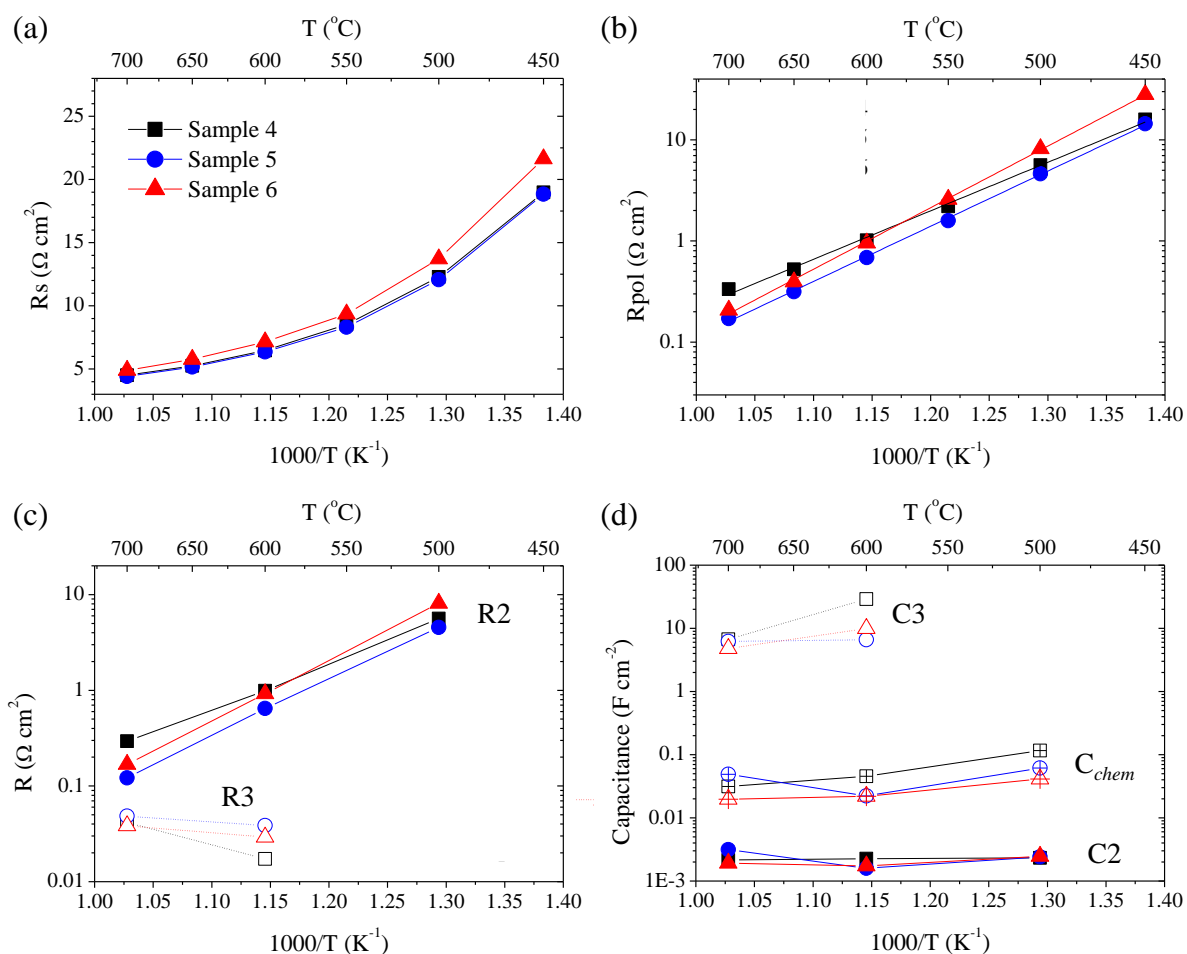


**Fig. 3. 16** The Arrhenius plots of (a) series resistance ( $R_s$ ) and (b) polarization resistance ( $R_{pol}$ ). The deconvolution of (c) resistance ( $R$ ) and (d) capacitance ( $C$ ) associated with P2 (filled markers) and P3 (empty markers) processes, as well as chemical capacitance ( $C_{chem}$ , empty with plus sign markers). All plots are for sample 4 (black square), 5 (blue circle), and 6 (triangle red).

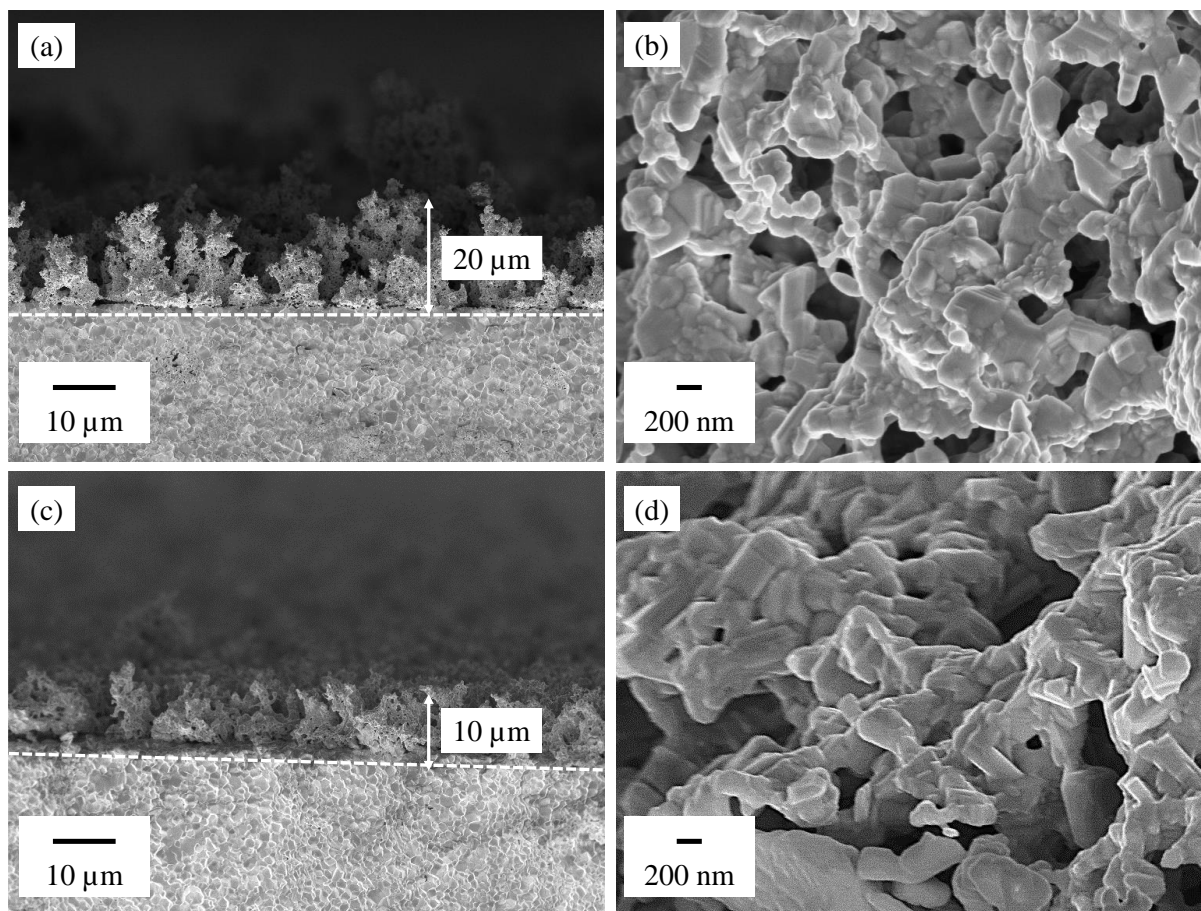


**Fig. 3. 17** The cross-section images of (a), (b) ESD layer after second heat-treatment at 450 °C/2 h + 900 °C/2 h and (c), (d) ESD layer after second heat-treatment at 450 °C/2 h + 1050 °C/2 h + 1100 °C/0.5 h at two different magnifications. The dashed white line indicates the electrode/electrolyte interface.

### 3.7 Influence of the CCL microstructure on the performance of the electrode

In both double (DL) and triple (TL) layer electrode configurations, a CCL of LPNO was deposited by SP. As discussed in §3.3, the cross-section of the single SP layer (**Fig. 3.10a-b**) shows that the LPNO particles form big agglomerates which are detrimental especially for the DL and TL electrodes. Indeed, these agglomerates may compress the AFL deposited by ESD beneath and, consequently, deteriorate its fine microstructure. Therefore, a part of the LPNO powder for SP was previously ball-milled in a planetary ball mill for 2 h to reduce the particle size and then used in the preparation of the ink for screen-printing of the CCL. The microstructure, as well as the electrochemical performance, were then compared to the

electrode prepared by using powder without ball-milling for the CCL. The SEM images of the LPNO powder before and after ball-milling are shown in **Fig. 3.18a-b** and **3.18c-d**, respectively. Qualitatively, it is clear to see that the particles of the ball-milled powder are significantly well-separated rather than clumped together in agglomerates as in the non-ball-milled powder. The average agglomerate size of the non-ball-milled powder is 13.75  $\mu\text{m}$  with an average particle size of 300 nm. After ball-milling, the average particle size is decreased to 160 nm. The effect of the smaller and well-separated particles of the LPNO powder is also clearly evident in the final microstructure of the DL electrode. In **Fig. 3.18e**, non-ball-milled powder is used as the CCL. The big agglomerates are clearly compressing the ‘coral-like’ microstructure of the ESD layer beneath which makes it difficult to distinguish both layers. On the other hand, the much smaller particle size of the ball-milled powder preserves the microstructure of the ESD layer as shown in **Fig. 3.18f**.

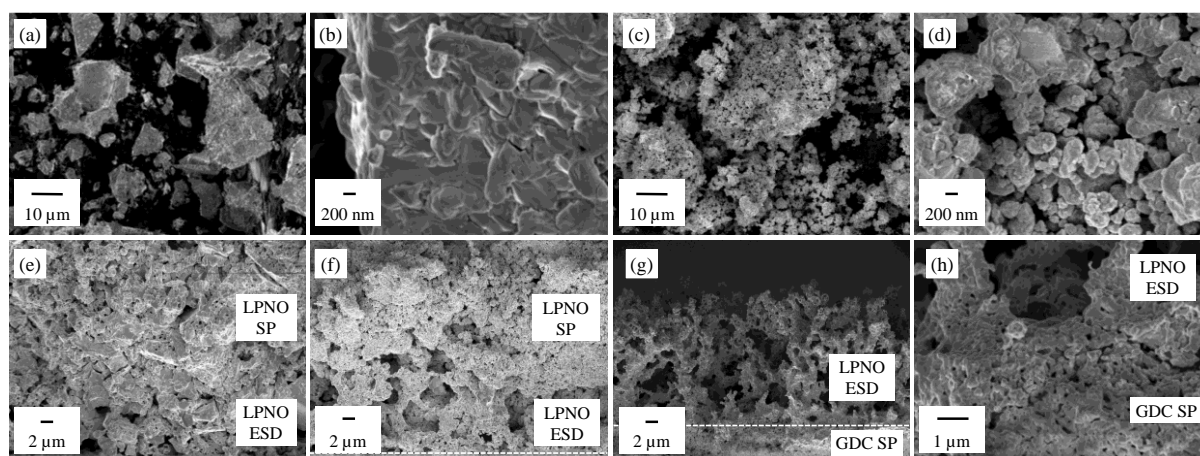


**Fig. 3. 18** SEM images of (a), (b) LPNO powder before ball-milling; (c), (d) LPNO powder after ball-milling; the cross-section of the double-layer electrodes (e) with non-ball-milled LPNO powder and (f) with ball-milled LPNO powder as the CCL; and (g), (h) the cross-section of the triple-layer electrode at two different magnifications. The dashed white line indicates the interfaces.

To understand the influence of the CCL microstructure on the electrochemical performance of the electrode, the EIS study for the DL electrode was carried out by comparing sample 4 to sample 7 (**Table 3.1**). Both electrodes were prepared following the same manufacturing protocol except that the ball-milled powder was used for the CCL deposit of sample 7. The same EIS study was also performed for the TL electrode. The cross-section of the AFL of a TL electrode, which comprises of GDC deposited by SP and LPNO deposited by ESD, is presented

in **Fig. 3.18g-h**. The thickness of the GDC SP layer is 6  $\mu\text{m}$  with an average particle size of 150 nm. Since this SP layer is porous and the particle size is slightly larger than the LPNO ESD layer, it was expected that the particle of LPNO would penetrate the SP layer to form a composite of LPNO and GDC. This proposition is confirmed by the EDX analysis carried out across the thickness of the GDC SP layer shown in **Fig. 3.19**, in which the LPNO particles penetrate the GDC SP layer as deep as 3  $\mu\text{m}$  from the LPNO ESD/GDC SP interface. As in the study of DL electrodes previously mentioned, two TL symmetrical cells were prepared. Sample 8 was prepared with the non-ball-milled powder and sample 9 with the ball-milled powder.

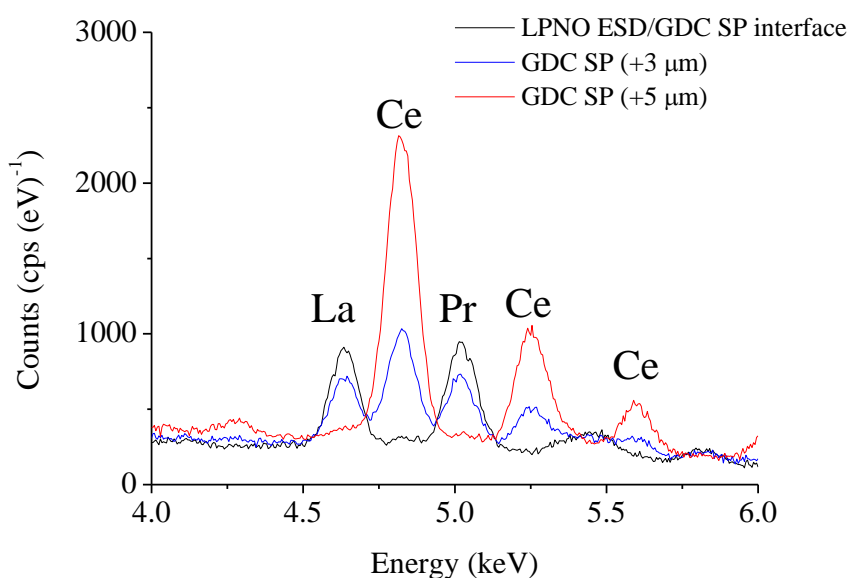


**Fig. 3. 19** The elements distribution observed at three different regions across the screen-printed GDC: at the LPNO ESD/GDC SP interface (black), at 3  $\mu\text{m}$  from this interface (blue), and at 5  $\mu\text{m}$  from this interface (red).

The EIS results further validate that the ball-milled powder does not only improve the quality of the microstructure but also the electrochemical performance of the electrode. The Nyquist plots presented in **Fig. 3.20a-c** show that the shape of the plots is similar but the size decreases from sample 4 to sample 7 as well as from sample 8 to sample 9. The Bode plots in **Fig. 3.20d-f** show that the frequency distribution is slightly shifted to a higher frequency when the ball-milled powder is used. However, the apparent processes are similar between the two DL electrodes and the two TL electrodes. For DL electrodes, the contribution of P3 starts to appear at 600  $^{\circ}\text{C}$  and there is no contribution of P1 at all temperatures, which is in agreement with the

results of the electrodes with the same DL configuration mentioned in the previous section. The TL electrodes, however, show that the contribution of P1 is apparent up to 600 °C. Since P1 is related to the charge transfer, it can be suspected that in the case of TL configuration, the GDC SP plays a role to limit the kinetics of this process. It will be explained further in the next section.

The Arrhenius plots of  $R_s$  versus temperature in **Fig. 3.21a** show that the values for the four samples are within the error range. The slightly higher series resistances for the TL cells than those of DL can be attributed to the additional thickness from the GDC SP layer. Based on the plots of  $R_{pol}$  in **Fig. 3.21b**, the polarization resistance of sample 7 is smaller than sample 4 whatever the operating temperature. Likewise, the  $R_{pol}$  of sample 9 is also smaller than sample 8 at all temperatures. These results show an improvement in the electrochemical performance of both DL and TL electrodes by optimizing the microstructure of the CCL.

The deconvolution of the resistance in **Fig. 3.21c** shows that R2 is the major contributor to the total electrode resistance for all samples. The trendline of R2 is also similar to the trendline of  $R_{pol}$ . The significant decrease in the contribution of P2, along with the previously mentioned frequency shift shown by the Bode plots, when the ball-milled powder is used indicating the improvement on the oxygen incorporation with a faster oxygen exchange on the surface. These improvements must be attributed to the combination of smaller particle size of the CCL layer and the preserved microstructure of the AFL layer prepared by ESD. Both factors ensure the large specific surface area as well as the porosity to promote a more efficient reaction to take place. As in the explanations in §3.5 and §3.6, the capacitance values for C1,  $C_{chem}$ , and C3, shown in **Fig. 3.21d**, are in the range of capacitance related to interfacial, chemical, and gas diffusion capacitance, respectively. Besides, the C2 values are smaller than  $C_{chem}$ , but it is higher than the usual interfacial capacitance.

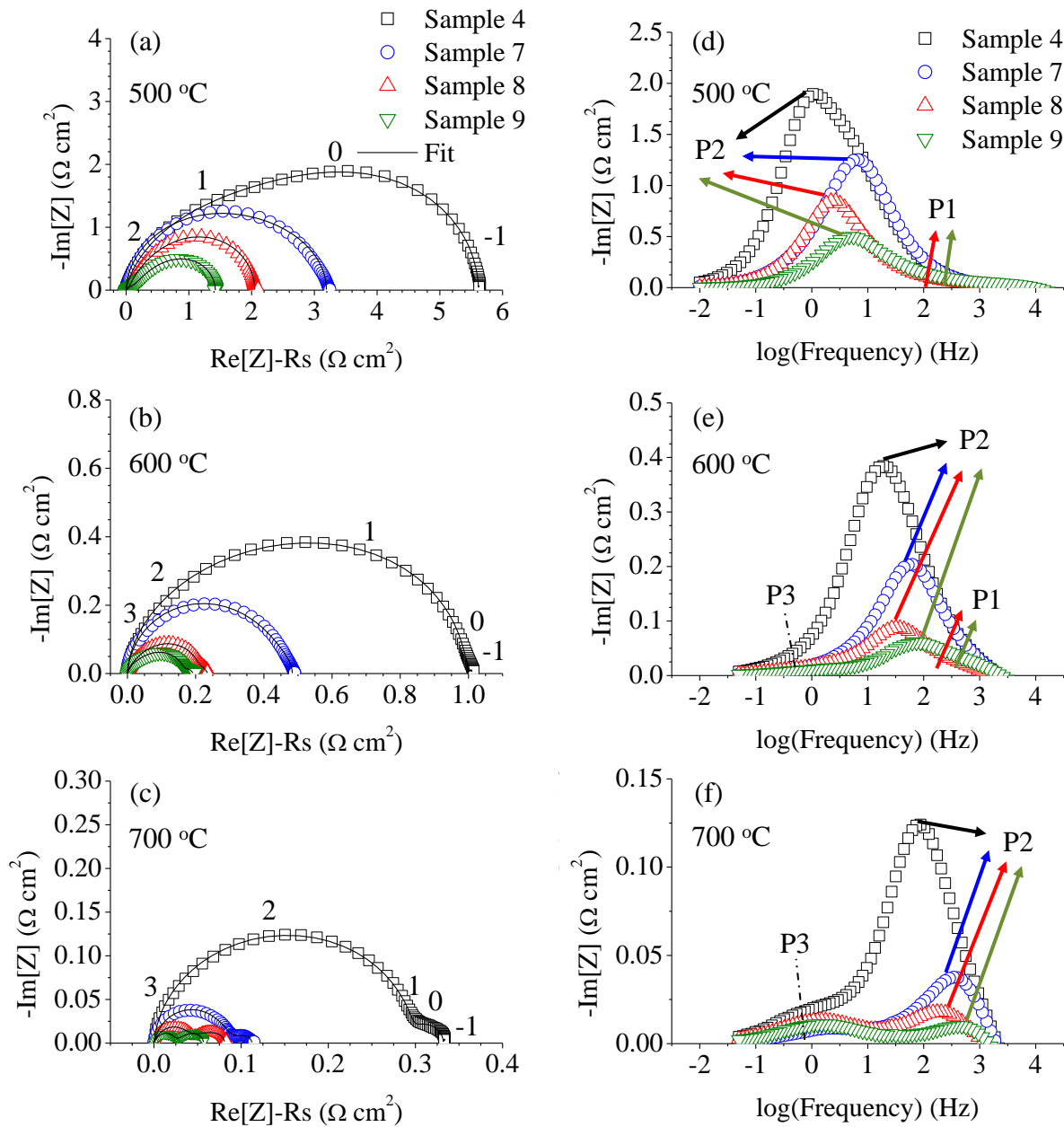


**Fig. 3. 20** (a)-(c) Nyquist plots and (d)-(f) Bode plots of samples 4, 7, 8, and 9 at 500, 600, and 700 °C, respectively. The Nyquist plots are plotted by subtracting the contribution of the series resistance and the numbers on the Nyquist plots indicate the logarithmic of the frequencies.

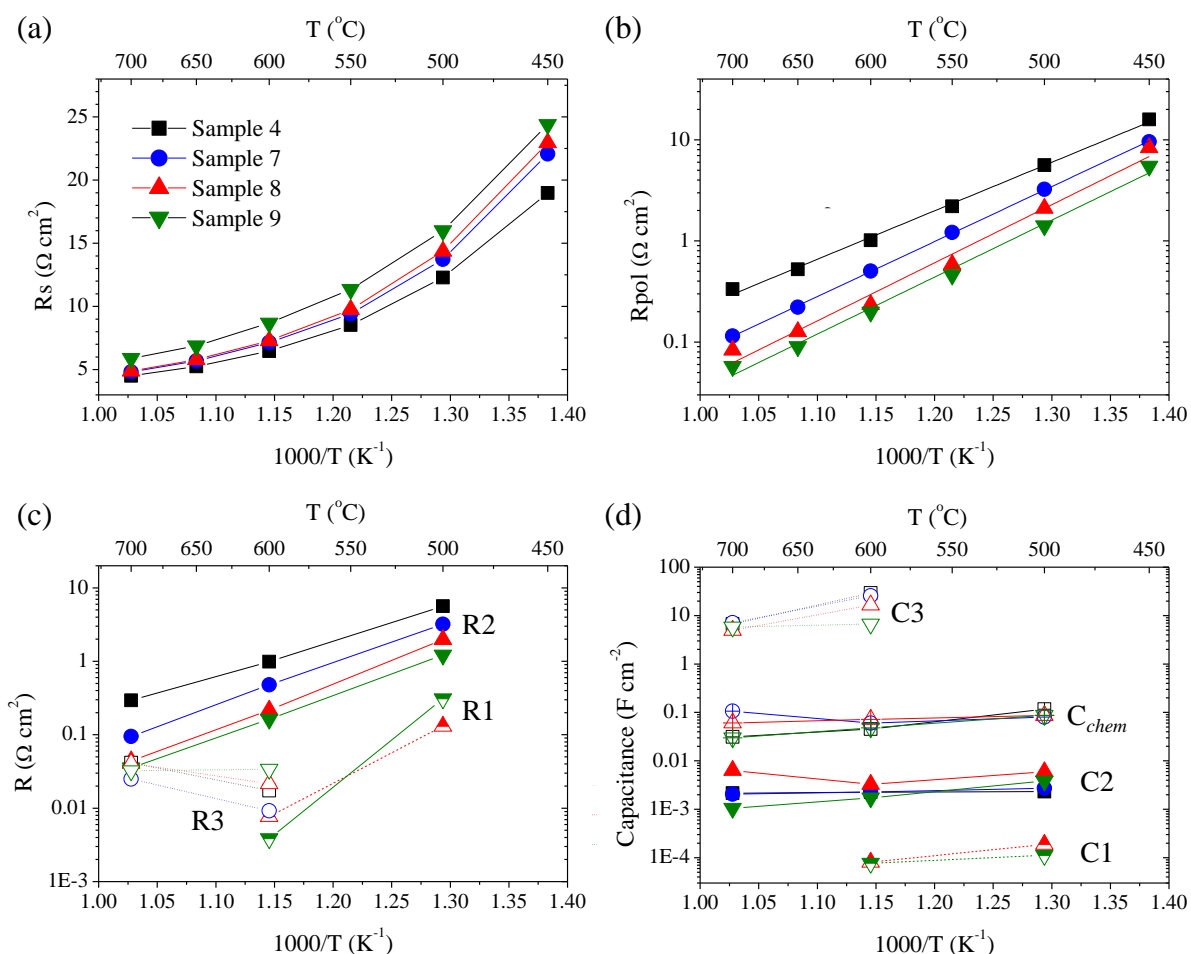


**Fig. 3. 21** The Arrhenius plots of (a) series resistance ( $R_s$ ) and (b) polarization resistance ( $R_{pol}$ ). The deconvolution of (c) resistance ( $R$ ) and (d) capacitance ( $C$ ) associated with P1 (half-filled markers), P2 (filled markers), and P3 (empty markers) processes, as well as chemical capacitance ( $C_{chem}$ , empty with plus sign markers). All plots are for sample 4 (black square), 7 (blue circle), 8 (triangle red), and 9 (inverted-triangle olive).

### 3.8 Influence of the various architectural designs on the performance of the electrode

Three LPNO electrodes which have been discussed separately in §3.5-3.7 are selected for comparison in order to study the influence of various architectural designs on the electrochemical performance. The samples are the SL ESD (sample 3), DL (sample 7), and TL (sample 9), all sintered at a maximum temperature of 960  $^{\circ}C$ . The SL SP was excluded from this study since the electrode/electrolyte interface was discontinuous.

The Nyquist and Bode plots for the three electrodes are provided in **Fig. 3.22**. The frequency distribution of the three samples is similar and the P3 becomes important at temperature  $\geq 600$  °C. The contribution of P1 associated with the GDC/LPNO interface, which was not noticeable on both SL ESD and DL electrodes, becomes detectable for TL electrode at the intermediate and low operating temperatures ( $T \leq 600$  °C). Even if the explanation is still unclear, the detection of P1 for the TL electrodes could come from a co-limitation arising at low temperatures for the oxygen bulk solid-state diffusion and the ionic transfer in the thickness of the composite (knowing that, in the same time, the process P2 is improved for this electrode architecture due the extension of the reaction zone as discussed in the next paragraph). Moreover, a contribution of triple-phase boundary lines according to a surface path could not be excluded for this kind of LPNO/GDC composite electrode. Nevertheless, further investigations are still needed to better understand the precise reaction pathway for this kind of electrodes.

The series resistance presented in **Fig. 3.23a** shows that all values are within the error range. Slightly higher values are observed for TL electrode which is most likely caused by the additional thickness from the GDC SP layer as mentioned in the previous section. The Arrhenius plots of  $R_{pol}$  for the three electrodes is presented in **Fig. 3.23b**. The  $R_{pol}$  of sample 7 is lower than sample 3 whereas the best performances are achieved with sample 9. Compared to the single-layer (sample 3), the improvement of the performance for the DL electrode (sample 7) could be attributed to a better electrode surface. Indeed, although the ESD layer has a good electrode/electrolyte interface, its surface is very rough (as mentioned in §3.3). Thus, by depositing an SP coating on top of the ESD layer, the electrode surface is flatter promoting better contact and current collection with the gold grid of the measurement setup.

The performance is then further improved on the TL electrode (sample 9). As mentioned in the previous section, this configuration results in the formation of an LPNO-GDC composite interlayer. The composite is expected to improve the mechanical contact between the LPNO and the GDC. Moreover, the oxygen solid-state diffusion must be favored thanks to the GDC backbone leading to the extension of the reaction in the electrode thickness and hence increasing the performances. This mechanism has been already proven in a previous study dedicated to TL electrode configuration with  $\text{La}_2\text{NiO}_{4+\delta}$  and  $\text{Pr}_2\text{NiO}_{4+\delta}$  nickelates [12]. Thus, it can be reasonably proposed here that the same phenomenon could explain the better performances of the TL electrode with LPNO. As shown in the Bode plots, as well as on the

deconvolution of the polarization resistance in **Fig. 3.23c**, this proposition is in good agreement with the smaller contribution of P2 for the TL electrodes as compared to the DL configurations. It is worth to note that the TL electrode is very well-performing in such a way that the contribution of P2 is very small and comparable to the contribution of P3.

The  $R_{pol}$  values obtained from this work are in agreement with the ones in literature as shown in **Fig. 3.23b**. Even though it is not the best performing LPNO electrode, the performance of the prepared electrode is still very good. The difference in the performance of SL and DL electrodes between the ones prepared in this work and the works of Sharma can be attributed to the difference in the deposition and sintering parameters (i.e. deposition time, solution composition, sintering temperature, powder preparation for SP) [35].

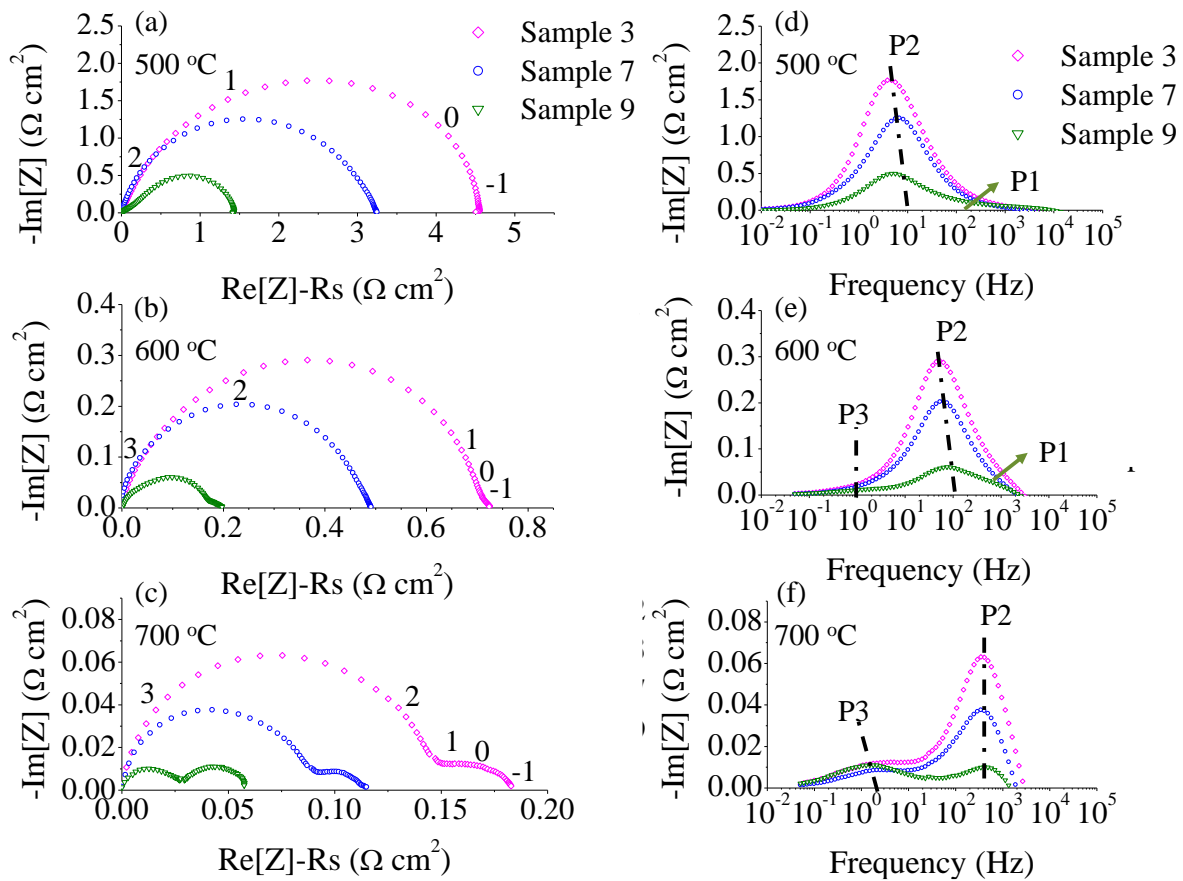


**Fig. 3. 22** (a)-(c) Nyquist plots and (d)-(f) Bode plots of samples 3, 7, and 9 at 500, 600, and 700 °C, respectively. The Nyquist plots are plotted by subtracting the contribution of the series resistance and the numbers on the Nyquist plots indicate the logarithmic of the frequency.

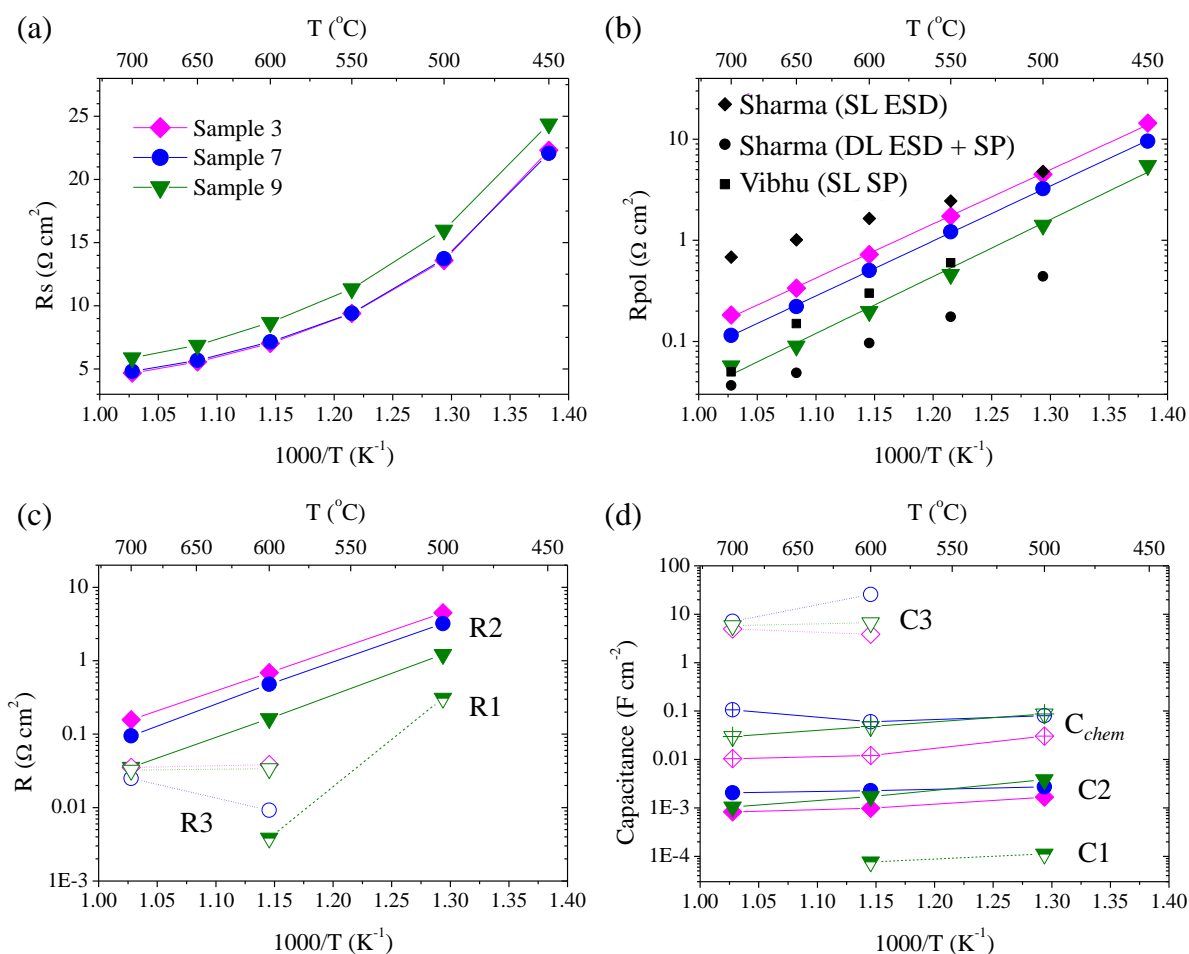


**Fig. 3. 23** The Arrhenius plots of (a) series resistance ( $R_s$ ) and (b) polarization resistance ( $R_{pol}$ ). Several  $R_{pol}$  values of LPNO with similar configuration are also given for comparison [22], [35]. The deconvolution of (c) resistance ( $R$ ) and (d) capacitance ( $C$ ) associated with P1 (half-filled markers), P2 (filled markers), and P3 (empty markers) processes, as well as chemical capacitance ( $C_{chem}$ , empty with plus sign markers). All plots are for sample 3 (magenta diamond), 7 (blue circle), and 9 (inverted-triangle olive).

### 3.9 Summary and conclusions

This chapter reports first some preliminary data on the optimization of the LPNO electrode fabrication by using SP and ESD. It can be concluded that to obtain a homogeneous SP ink, polyvinyl butyral (PVB) is preferred as the binder rather than polyvinylpyrrolidone (PVP). In the case of the ESD process, the addition of 8 drops of  $HNO_3$  in every 30 mL of precursor solution is required for solution stabilization when the mixture of ethanol and water is used as

the solvent. ESD deposition time of 4 h 30' allows obtaining a porous functional layer with coral-type morphology, 27  $\mu\text{m}$ -thick with good percolation for the application. An LPNO hierarchical morphology has been prepared for the first time by ESD, even if the adhesion at the electrode/electrolyte interface must be improved in the future for this particular microstructure. The electrochemical performance of the double-layered  $\text{La}_{2-x}\text{Pr}_x\text{NiO}_{4+\delta}$  electrode was found to increase for a larger praseodymium content, as expected from the literature. Last but not the least, the electrode fabrication by SP and ESD is proven to be reproducible.

In the second part of this chapter, the influence of microstructure and architectural design on the electrochemical performance of LPNO has also been studied on nine different samples (detailed in **Table 3.1**). Firstly, it has been shown that the good adhesion between the electrode and the electrolyte plays a key role in the global performances. This property can be achieved by optimizing the sintering condition for the SP electrode or by using alternative manufacturing processes, such as ESD, which are well-suited to make a continuous electrode/electrolyte interface. For the LPNO electrode, it has been found that a sintering temperature as high as 1100 °C is required to obtain good adhesion for the SL SP layer while a sintering temperature at only 960 °C is sufficient for SL ESD. Secondly, it has been highlighted that the quality of the CCL is also crucial since it can affect the final microstructure of the active functional electrode for the multi-layer configurations. A ball-milling step on the LPNO powder for SP prepared by auto-combustion is proven to improve the final microstructure as well as the performance of the electrode. Thirdly, the performance of the electrode can be also further improved by improving the electrode/electrolyte interface and electrode surface as indicated by the decrease of  $R_{\text{pol}}$  from 0.72, 0.50, and down to 0.20  $\Omega \text{ cm}^2$  at 600 °C for SL ESD, DL, and TL electrodes, respectively. Lastly, the presence of secondary higher-order phase nickelate, (LP)3N2, evidently helps to improve the performance especially at a higher temperature. The characteristics of the nine samples are listed in the following **Table 3.2**. A summary of the electrochemical data at 500, 600, and 700 °C for all samples mentioned in this chapter is recorded in **Table 3.3**.

**Table 3. 2** Architectural design, thickness, and particle size for all the samples mentioned in this chapter.

Sample #	Architectural design	Thickness ( $\mu\text{m}$ )	Particle size (nm)
Sample 1	SL LPNO SP	N/A	N/A
Sample 2	SL LPNO SP	38	500
Sample 3	SL LPNO ESD	27	130
Sample 4	DL LPNO (ESD + SP)	50 (total ESD+SP)	N/A
Sample 5	DL LPNO (ESD + SP)	20 (ESD layer only)	150 (ESD layer)
Sample 6	DL LPNO (ESD + SP)	10 (ESD layer only)	200 (ESD layer)
Sample 7	DL (LPNO ESD + LPNO SP)	38 (total ESD+SP)	N/A
Sample 8	TL (GDC SP + LPNO ESD + LPNO SP)	6 (GDC SP), 25 (GDC SP+LPNO ESD)	150 (GDC SP)
Sample 9	TL (GDC SP + LPNO ESD + LPNO SP)	6 (GDC SP), 25 (GDC SP+LPNO ESD)	150 (GDC SP)

**Table 3. 3** The summary of the electrochemical data at 500, 600, and 700 °C for all samples mentioned in this chapter.

	Sample 1			Sample 2			Sample 3			
Ea (eV)	1.06			1.17			1.06			
Temperature	500 °C	600 °C	700 °C	500 °C	600 °C	700 °C	500 °C	600 °C	700 °C	
R <sub>s</sub> (Ω cm <sup>2</sup> )	16.4	8.62	6.01	12.7	6.39	4.40	13.7	7.02	4.66	
P1	R1 (Ω cm <sup>2</sup> )	4.62	1.35	0.29	0.08	0.02				
	C1 (x 10 <sup>-3</sup> F cm <sup>-2</sup> )	0.21	0.16	0.05	0.11	0.13				
P2	R2 (Ω cm <sup>2</sup> )	10.40	1.31	0.27	5.05	0.62	0.11	4.50	0.69	0.16
	C <sub>chem</sub> (x 10 <sup>-3</sup> F cm <sup>-2</sup> )	23.7	17.6	13.5	159	96.8	82.5	30.3	12.11	10.4
	C2 (x 10 <sup>-3</sup> F cm <sup>-2</sup> )	0.01	0.02	0.46	1.84	1.84	2.76	1.67	0.98	0.83
P3	R3 (Ω cm <sup>2</sup> )			0.06			0.03		0.04	0.04
	C3 (F cm <sup>-2</sup> )			3.62			7.01		3.87	4.95
R <sub>pol</sub> (Ω cm <sup>2</sup> )	15.02	2.66	0.62	5.13	0.64	0.14	4.50	0.73	0.20	
	Sample 4			Sample 5			Sample 6			
Ea (eV)	0.95			1.08			1.21			
Temperature	500 °C	600 °C	700 °C	500 °C	600 °C	700 °C	500 °C	600 °C	700 °C	
R <sub>s</sub> (Ω cm <sup>2</sup> )	12.3	6.46	4.50	12.1	6.33	4.40	13.8	7.14	4.89	
P1	R1 (Ω cm <sup>2</sup> )									
	C1 (x 10 <sup>-3</sup> F cm <sup>-2</sup> )									
P2	R2 (Ω cm <sup>2</sup> )	5.62	0.99	0.29	4.55	0.65	0.12	8.11	0.92	0.17
	C <sub>chem</sub> (x 10 <sup>-3</sup> F cm <sup>-2</sup> )	116	45.7	31.4	61.3	22.2	49.0	41.2	21.9	19.7
	C2 (x 10 <sup>-3</sup> F cm <sup>-2</sup> )	2.32	2.26	2.15	2.41	1.59	3.14	2.46	1.73	1.92
P3	R3 (Ω cm <sup>2</sup> )		0.02	0.04		0.04	0.05		0.03	0.04
	C3 (F cm <sup>-2</sup> )		29.1	6.70		6.63	6.19		9.93	4.80
R <sub>pol</sub> (Ω cm <sup>2</sup> )	5.62	1.01	0.33	4.55	0.69	0.17	8.11	0.95	0.21	
	Sample 7			Sample 8			Sample 9			
Ea (eV)	1.08			1.14			1.12			
Temperature	500 °C	600 °C	700 °C	500 °C	600 °C	700 °C	500 °C	600 °C	700 °C	
R <sub>s</sub> (Ω cm <sup>2</sup> )	13.8	7.30	4.79	14.2	7.27	4.88	15.8	8.67	5.86	
P1	R1 (Ω cm <sup>2</sup> )			0.13	0.008		0.31	0.004		
	C1 (x 10 <sup>-3</sup> F cm <sup>-2</sup> )			0.19	0.08		0.11	0.08		
P2	R2 (Ω cm <sup>2</sup> )	3.19	0.48	0.09	1.98	0.22	0.04	1.22	0.16	0.04
	C <sub>chem</sub> (x 10 <sup>-3</sup> F cm <sup>-2</sup> )	80.6	60.3	106	86.3	72.0	61.0	87.5	48.2	30.0
	C2 (x 10 <sup>-3</sup> F cm <sup>-2</sup> )	2.71	2.28	2.06	5.96	3.28	6.33	3.85	1.72	1.05
P3	R3 (Ω cm <sup>2</sup> )		0.01	0.03		0.02	0.04		0.03	0.03
	C3 (F cm <sup>-2</sup> )		25.5	7.16		16.5	4.96		6.71	5.81
R <sub>pol</sub> (Ω cm <sup>2</sup> )	3.19	0.49	0.12	2.11	0.248	0.08	1.53	0.194	0.07	

---

# **CHAPTER 4: DURABILITY**

## **STUDY ON THE SYMMETRICAL**

### **AND COMPLETE CELLS**

In this chapter, the results of a long-term durability test in fuel cell and electrolysis modes in a symmetrical configuration are presented. A preliminary study of the durability of the LPNO electrode in two complete cells using different GDC barrier layers operating in electrolysis mode is described afterwards. Parts of this chapter have been published in the Journal of Power Sources (<https://doi.org/10.1016/j.jpowsour.2020.227724>).

## 4.1 Introduction

In Chapter 3, the microstructure and design of the LPNO electrode have been optimized. One of the important results is the presence of a higher-order nickelate  $(\text{La,Pr})_3\text{Ni}_2\text{O}_{7-\delta}$ ,  $(\text{LP})_3\text{N}_2$ , only detected in the AFL deposited by ESD and not in the CCL deposited by SP. It is suggested that the formation of the secondary phase on the ESD layer can be attributed to its finer particle size and more open microstructure as compared to the SP layer, yielding to a more reactive microstructure. The results in §3.6, supported also with data in the literature, show that  $(\text{LP})_3\text{N}_2$  is an electrochemically active material and is beneficial for the electrochemical activity of the oxygen electrode. However, the stability of this compound and its impact on the electrode response during long-term operation (both in electrolysis and fuel cell modes) need to be addressed. At the same time, one can wonder if the stability of LPNO is related to the microstructure of the electrode which is different according to the method of preparation. As a general matter, the amount of literature dedicated to the durability of the LPNO electrode under operation is still limited as explained in §1.4. Based on all aforementioned reasons, a long-term test was carried out on a symmetrical cell in both electrolysis and fuel cell modes with a procedure described in §2.6.1.

Aside from tests on a symmetrical cell, preliminary long-term experiments were also carried out on two different complete cells in the electrolysis mode. To the best of our knowledge, the durability test of LPNO as an oxygen electrode in a complete cell configuration is very limited, especially in its application in the electrolysis mode. Therefore, the study detailed in this chapter is relevant especially to better understand the durability behavior of the LPNO electrode in the symmetrical cell and the closer-to-real-application complete cell.

The double-layer LPNO electrode, which consists of the AFL deposited by ESD topped by a CCL deposited by SP, was selected for this study. The sample preparation procedures by both deposition techniques have been detailed in §2.2.3 and §2.2.2, respectively. The heat treatment temperatures were 960 °C for 6 h after ESD and 450 °C for 2 h followed by 800 °C for 2 h after SP; all carried out in the air. The samples are called SCell, CCell 1, and CCell 2 for the symmetrical cell, complete cell with screen-printed GDC barrier layer, and complete cell with sputtered GDC barrier layer, respectively. The summary of the sample information, as well as the test parameters, are given in **Table 4.1**. This chapter is focused on the electrochemical characterization results of the tested cells, while the post-mortem analyses are given in Chapter 5.

**Table 4. 1** The list of samples and the detailed long-term test parameters for each.

	Long-term test in symmetrical cell	Long-term test in complete cell	
<b>Sample name</b>	SCell	CCell 1	CCell 2
<b>Configuration</b>	DL on GDC electrolyte	DL on half-cell GDC/YSZ/Ni-YSZ	
<b>GDC barrier layer</b>	N/A	Deposited by SP, 4 $\mu\text{m}$ -thick	Deposited by RF magnetron sputtering, 400 nm-thick
Test parameters			
<b>Temperature</b>	700 °C		
<b>Environment</b>	Air	90/10 H <sub>2</sub> O/H <sub>2</sub> (20% steam conversion rate)	
<b>Time</b>	960 h	900 h	-
<b>Applied current</b>	Cathodic current density of 300 mA cm <sup>-2</sup> on the working electrode (bottom electrode) → anodic current on the counter electrode (top electrode)	Current density of 200 mA cm <sup>-2</sup> (anodic current for the air electrode)	

## 4.2 Durability study on the symmetrical cell

### 4.2.1 Pre-test measurements

Before the long-term test, EIS measurements were conducted on the symmetrical cell, SCell. The measurements were taken under OCP ( $i_{dc} = 0 \text{ mA cm}^{-2}$ ) at a temperature between 550 and 700 °C. Thanks to the 3-electrode configuration, the top and bottom electrodes can be measured independently. The Nyquist and Bode plots are presented in **Fig. 4.1a-b** for the bottom electrode and **Fig. 4.1c-d** for the top electrode. The series and polarization resistances, which are normalized by multiplying the measured values with the surface area of the electrode, are shown in Arrhenius plots in **Fig. 4.2a-b**. As expected, a similar frequency distribution is observed at all temperatures indicating that similar processes take place on both electrodes. However, it can be noticed from the Arrhenius plots that the response of the electrodes is not perfectly symmetric despite the identical material and microstructure. The small difference in the  $R_{pol}$  values, especially at a higher temperature, can be attributed to artifacts leading to small distortion on the measurement. They are in general related to the positioning of the Ag-wire reference electrode, which should be perfectly placed in the middle of the electrolyte side, and the alignment of the two LPNO electrodes on the electrolyte [93]. Nevertheless, the difference in the  $R_{pol}$  values is not so significant (less than 12% at all temperatures). On the other hand, a quite significant difference is apparent in the series resistance, in which the values are larger by about 50% for the top electrode as compared to the bottom electrode. Since the electrochemical responses of both electrodes are almost identical, the difference in  $R_s$  should not be due to a problem in the reference electrode positioning. Therefore, the higher  $R_s$  values

could indicate a worse contact between the top electrode and the gold grid due to insufficient load, yielding to higher contact resistance.

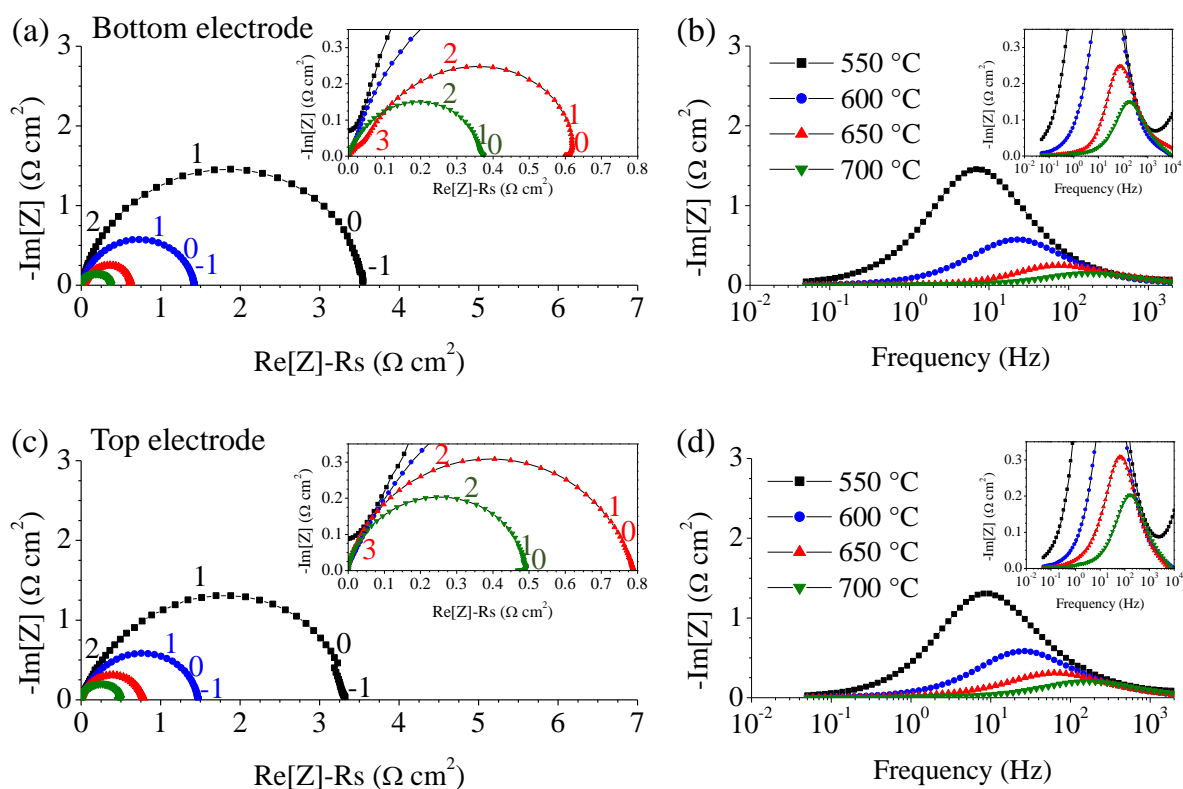


**Fig. 4. 1** (a),(c) Nyquist plots and (b),(d) Bode plots of SCell at 550-700 °C taken at OCP for the bottom and top electrodes, respectively. The Nyquist plots are plotted by subtracting the contribution of the series resistance and the numbers on the Nyquist plots indicate the logarithmic of the frequency. The inset graphs indicating the magnification of the plots taken at 650 and 700 °C for clarity.

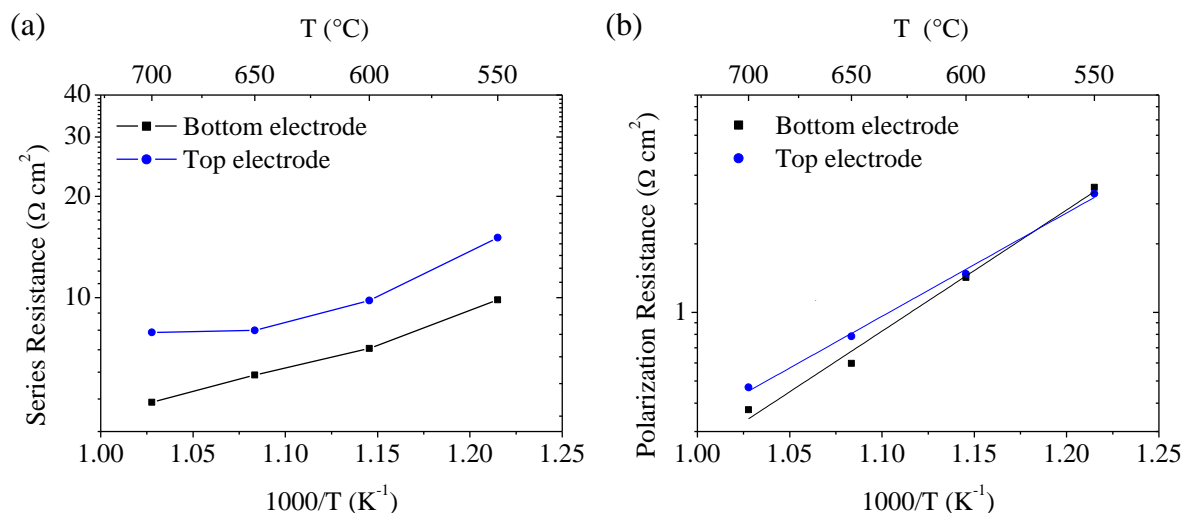


**Fig. 4. 2** The Arrhenius plots of (a) series resistance ( $R_s$ ) and (b) polarization resistance ( $R_{pol}$ ) for the bottom (black square) and top (blue circle) electrodes of SCell.

#### 4.2.2 Long-term measurement in electrolysis and fuel cell modes ( $i_{dc} = \pm 300 \text{ mA cm}^{-2}$ )

The long-term test was carried out by applying a cathodic current of  $-300 \text{ mA cm}^{-2}$  to the bottom electrode which was chosen as the working electrode. It means that the bottom electrode operated in fuel cell mode (cathodic side) while the top electrode operated in electrolysis mode (anodic side). The test was carried out in air at  $700 \text{ }^{\circ}\text{C}$  for 960 h. During this period, the voltage measured between the working and reference electrodes was recorded upon the operation and then plotted as a function of time as shown in **Fig. 4.3**. Since the working electrode is the cathodic side, this graph shows the evolution of the electrode response under fuel cell operation. The initial measured voltage is  $-1.41 \text{ V}$  and includes a part of the ohmic losses in the electrolyte. The absolute value of the voltage increases a little bit in the first 50 hours and it steadily decreases afterwards, indicating slightly better performance at the beginning followed by cell degradation. The measured voltage is the sum of all the contributions between the working and the reference electrodes, thus, any deviation on from its initial value must directly be related to changes on the interfaces and/or the bulk electrodes or/and the electrolyte. Indeed, the operating condition might induce some changes such as the new phase formation, microstructural evolution, changes on the electrode/electrolyte or electrode/Au-grid interfaces yielding to either activation (improvement) or passivation (degradation) of the cell [94]. By the end of the test, the calculated electrode degradation rate in fuel cell mode is  $219 \text{ mV kh}^{-1}$  ( $15.5 \text{ V\% kh}^{-1}$ ).

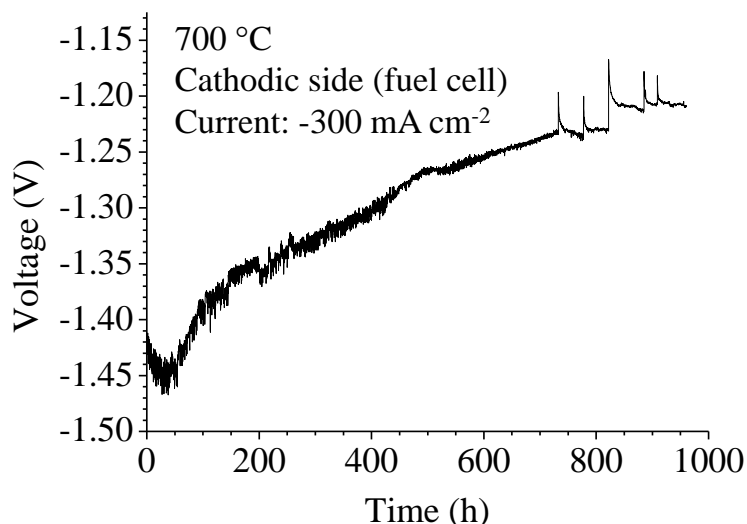


**Fig. 4. 3** Voltage between the working and the reference electrodes as a function of time for SCell operating in fuel cell mode.

To observe any changes in the two electrodes responses after the long-term test, each side of the cell is subjected to EIS measurements at OCP. The comparison of Nyquist and Bode plots taken before and after the long-term test are shown in **Fig. 4.4a-b** and **Fig. 4.4c-d** for the cathodic and anodic sides, respectively. From the Nyquist plots, the series and polarization resistances are extracted and shown in **Fig. 4.5a-b**. It is observed that both electrodes have different behavior over time in either electrolysis or fuel cell modes. The response of the anodic side (operated in electrolysis mode) is almost similar before and after the test for 960 h. Conversely, the  $R_{pol}$  value of the cathodic side significantly increases to triple the initial value before the test. This result is consistent with a previous study on the lanthanum-praseodymium nickelates in which a significant increase (between 4 times for  $\text{La}_{1.5}\text{Pr}_{0.5}\text{NiO}_{4+\delta}$  up to 35 times for  $\text{Pr}_2\text{NiO}_{4+\delta}$ ) of  $R_{pol}$  was observed on the electrode operated in fuel cell mode whereas the performance was quite stable in electrolysis mode [36]. The different behavior under electrolysis and fuel cell modes might be caused by different reaction and decomposition processes of LPNO under either anodic or cathodic polarization [44]. The decomposition products under cathodic polarization might be more detrimental to the electrochemical performance of the electrode (e.g. decomposition products that were insulators or could cause delamination), thus the  $R_{pol}$  value significantly increases after the aging. This argument is also supported by the deconvolution of the impedance spectra. A shift of frequency distribution towards lower frequency is observed within the frequency range that is related to P2 for both sides as seen from the Bode plots (see §3.4 for the equivalent electrical circuit and the

assignment of the processes involved in the electrode). It can be suspected that the frequency shift is caused by new phase formation or changes on the electrode microstructure resulting in changes on the oxygen surface exchange and/or solid-state diffusion in the bulk electrode [95]. However, while the amplitude of P2 does not change after the operation in the electrolysis mode, a significant increase is observed on the cathodic side. This observation further indicates that different changes happen in both operation modes. Moreover, a small contribution of P1 appears at high frequency for the electrode operated in fuel cell mode suggesting possible delamination at electrode/electrolyte interface. Indeed, delamination has been clearly observed on the cathodic side after the cell is removed from the measurement setup. Some post-mortem characterizations have been carried out to corroborate these propositions, which will be detailed in Chapter 5. From the polarization resistance values before and after the long-term test, the calculated cell degradation rate in fuel cell mode is  $607 \text{ m}\Omega \text{ cm}^2 \text{ kh}^{-1}$  ( $162.49 \text{ }\Omega\% \text{ kh}^{-1}$ ) while in the electrolysis mode it is only  $7.28 \text{ m}\Omega \text{ cm}^2 \text{ kh}^{-1}$  ( $1.55 \text{ }\Omega\% \text{ kh}^{-1}$ ).

In parallel, a decrease in series resistance is observed for both electrodes. The origin of this decrease is most likely caused by the improvement in the contact between the electrode and the gold grid over time (cf. discussion in §4.2.1).

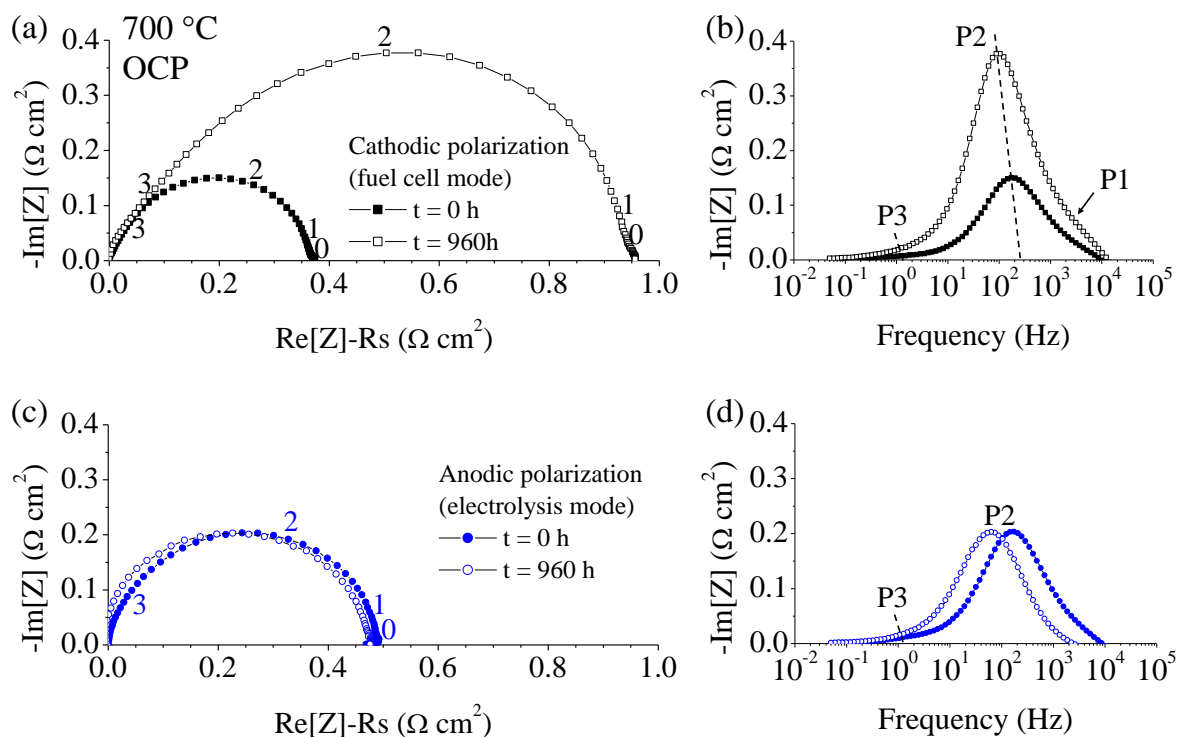


**Fig. 4. 4** (a),(c) Nyquist plots and (b),(d) Bode plots of SCell at 700 °C which are taken before and after a long-term test for cathodic and anodic sides, respectively. The Nyquist plots are plotted by subtracting the contribution of the series resistance and the numbers on the Nyquist plots indicate the logarithmic of the frequency.

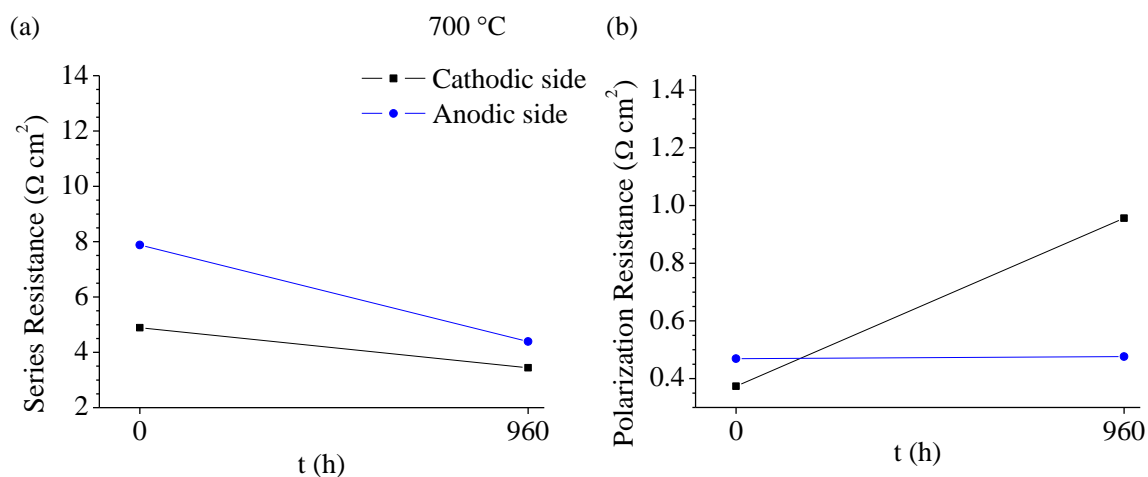


**Fig. 4. 5** (a) The series resistance ( $R_s$ ) and (b) the polarization resistance ( $R_{pol}$ ) before and after a long-term test for the cathodic (black square) and anodic (blue circle) sides of SCell.

### 4.3 Preliminary durability study on the complete cell

Based on the previously discussed durability test on a symmetrical cell, one can conclude that the LPNO electrode is electrochemically stable after an operation in electrolysis mode for 960 h. In this sub-chapter, subsequent tests on two complete cells (CCell 1 and CCell 2) in electrolysis mode are discussed to investigate and compare the behavior of the LPNO electrode as it is upscaled from symmetrical cell level to complete cell level. It is important to note that the results explained here are considered as a preliminary study on the application of the LPNO electrode for complete cell and therefore, deeper investigations will be still necessary in the future. The details on the mounting procedures of the cell to the test bench (test configuration, applied load, glass sealing, NiO reduction) as well as the long-term test procedures in electrolysis mode have been given in §2.6.2. It is reminded that during the long-term test, the O<sub>2</sub> electrode was fed by air (O<sub>2</sub>/N<sub>2</sub> = 0.21/0.79) while the H<sub>2</sub> electrode was supplied by a mixture of steam (H<sub>2</sub>O) and hydrogen (H<sub>2</sub>) with a ratio of 90/10. The total flow rate of gases on both sides is 8.9 NI h<sup>-1</sup>, and in this chapter it will be referred to as D<sub>tot,SOEC</sub> 9.

In addition to this applied flow rate, other conditions of gas supply were also used for the purpose of several pre-test and post-test measurements. A first one was chosen for measurements in electrolysis mode but with a higher flow rate called D<sub>tot,SOEC</sub> 20 (i.e. for a total flow rate of 20 NI h<sup>-1</sup> by keeping a ratio of H<sub>2</sub>O/H<sub>2</sub> of 90/10 and air at the O<sub>2</sub> side). The second one was defined to characterize the cell in fuel cell mode called D<sub>tot,SOFC</sub> 9. In this case, H<sub>2</sub> was supplied to the hydrogen electrode side while O<sub>2</sub> was passed through the oxygen electrode side. The details on the gas composition and flow rate are given in **Table 4.2**.

**Table 4. 2** The details on the gas composition and flow rates of each gas for measurements of complete cell in both fuel cell and electrolysis modes. The steam conversion rates (SC) are given for a current density of 0.2 A cm<sup>-2</sup>.

		O <sub>2</sub> electrode side		H <sub>2</sub> electrode side		
		Air flow rate (NI h <sup>-1</sup> )	Total flow rate (NI h <sup>-1</sup> )	Gas composition	SC (%)	
D <sub>tot,SOFC</sub> (NI h <sup>-1</sup> )	9	6.78	2.26	100% H <sub>2</sub>	-	
D <sub>tot,SOEC</sub> (NI h <sup>-1</sup> )	9	6.78	2.12	H <sub>2</sub> O/H <sub>2</sub> = 90/10	20.05	
	20	13.56	6.55	H <sub>2</sub> O/H <sub>2</sub> = 90/10	6.47	

It can be noticed that the sign convention of the applied current for a complete cell is the opposite of the one used for a symmetrical cell, i.e. negative sign is used for the applied anodic current on complete cell.

#### 4.3.1 Preliminary durability test on CCell 1: GDC barrier layer by screen printing

As described in **Table 4.1**, CCell 1 is prepared by using a commercial half-cell in which the GDC barrier layer with a thickness of 4  $\mu\text{m}$  is deposited by screen printing. The GDC barrier layer is important to prevent reactivity between the LPNO electrode and the YSZ electrolyte.

Before the long-term test ( $t = 0$  h), pre-test measurements at 700  $^{\circ}\text{C}$  were carried out to obtain the iV curves in both fuel cell and electrolysis modes, as well as impedance spectra at OCV. The iV curves measured in fuel cell mode with  $D_{\text{tot,SOFC}}$  9 is shown in **Fig. 4.6a** while the one taken in electrolysis mode with  $D_{\text{tot,SOEC}}$  9 is shown in **Fig. 4.6b**. The OCV can be calculated from the Nernst equation (Eq. 1.3-1.5 in §1.2.2). Based on the literature, the standard voltage of the cell,  $E_0^{\text{cell}}$ , is 1.01 V at 700  $^{\circ}\text{C}$  [96]. By considering the partial pressure of the gases involved, the calculated OCV is around 1.12 V and 0.90 V for fuel cell and electrolysis conditions, respectively. Thus, from the iV curves, the cell voltage at OCV is close to the theoretical value indicating that the gas tightness of both electrode compartments is ensured. The current density in fuel cell mode is 0.22  $\text{A cm}^{-2}$  at 0.6 V, whereas it is -0.24  $\text{A cm}^{-2}$  at 1.3 V in the electrolysis mode. These obtained values show a rather poor performance since the current density is normally found between 3-4 times larger than these values [44], [97].

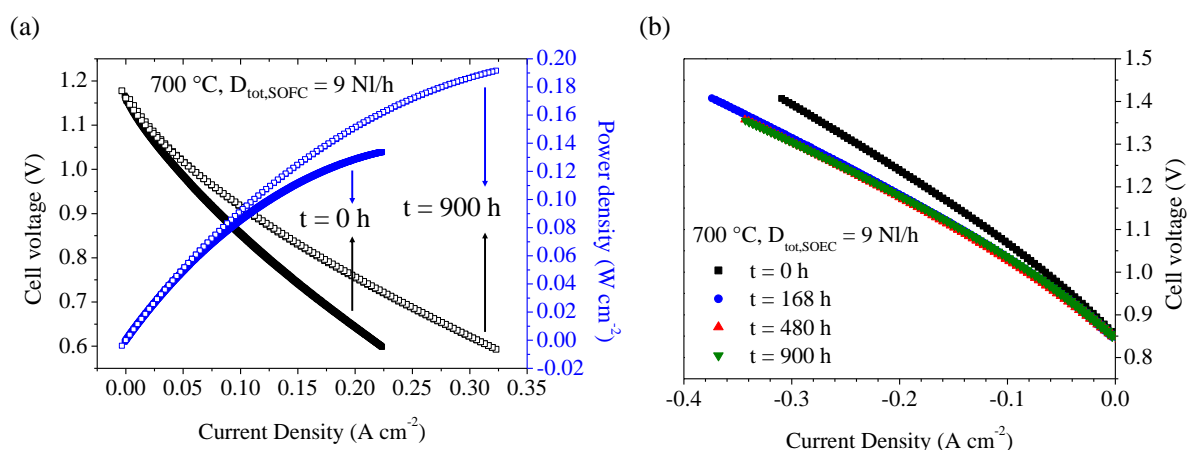


**Fig. 4. 6** The iV curve of CCell 1 at 700  $^{\circ}\text{C}$  taken at various times during the test for (a) fuel cell operation with  $D_{\text{tot,SOFC}}$  9 and (b) electrolysis operation with  $D_{\text{tot,SOEC}}$  9.

The initial EIS measurements on the pristine cell before aging are given in **Fig. 4.7a-b**. The deconvolution shows that the impedance spectra for a complete cell consist of several contributions that overlap with each other, thus the analysis is rather complicated. The contribution of the hydrogen electrode can be separated into three processes: gas conversion along the cell length and gas diffusion at low frequency, and charge transfer process at TPB spreading from medium to high frequency [98]. In addition to the gas conversion and diffusion (which are limited in this case due to the high air flow rate and the thin electrode), the main contributions for the oxygen electrode consist of the reactions on the bulk electrode arising at low to medium frequency and ionic transfer at LPNO electrode/GDC barrier layer interface at medium to high frequency. The EIS measurements were carried out with two different total gas flow rates:  $D_{\text{tot,SOEC}} 9$  and  $D_{\text{tot,SOEC}} 20$ . The responses are found to be identical at high to medium frequency, but the contribution of the low-frequency process(es) diminish(es) for the higher gas flux. As mentioned previously, the low frequency is mainly assigned to process-related especially to gas conversion and diffusion on the hydrogen electrode side. Since the same current density is applied to both measurements, it can be concluded that the higher flow rate at  $D_{\text{tot,SOEC}} 20$  allows decreasing the electrode gas supply overpotentials which are rather significant at a lower flow rate ( $D_{\text{tot,SOEC}} 9$ ).

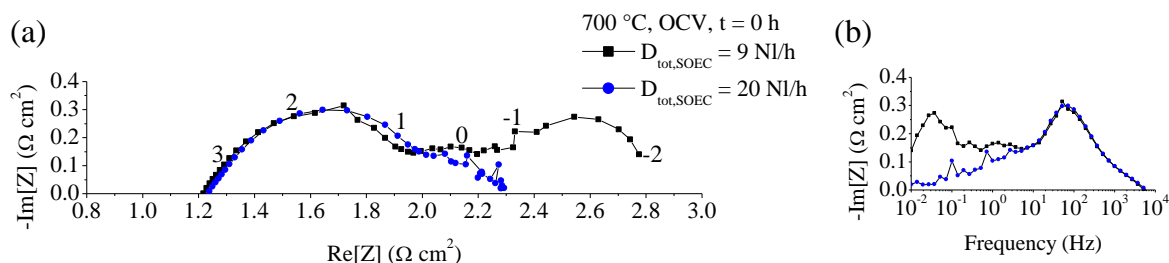


**Fig. 4. 7** The Nyquist and Bode plots of CCell 1 at 700 °C taken at OCV before the long-term test ( $t = 0$  h) for  $D_{\text{tot,SOEC}} 9$  and  $D_{\text{tot,SOEC}} 20$ . The numbers indicate the logarithm of the measuring frequency.

The long-term test was then carried out to the cell at 700 °C for 900 h in electrolysis mode by applying an anodic current of  $-0.2 \text{ A cm}^{-2}$ . The gas flux during operation is  $D_{\text{tot,SOEC}} 9$ . The evolution of cell voltage over time is shown in **Fig. 4.8**. The initial cell voltage is 1.25 V. As seen on the symmetrical cell operated as fuel cell (**Fig. 4.3**), there is also a significant decrease in the cell voltage in the first 50 hours of the test indicating an improvement on the cell

performance. However, in good consistency with the measurement in electrolysis mode for symmetrical cell, the cell voltage is then quite stable until the end of the test.

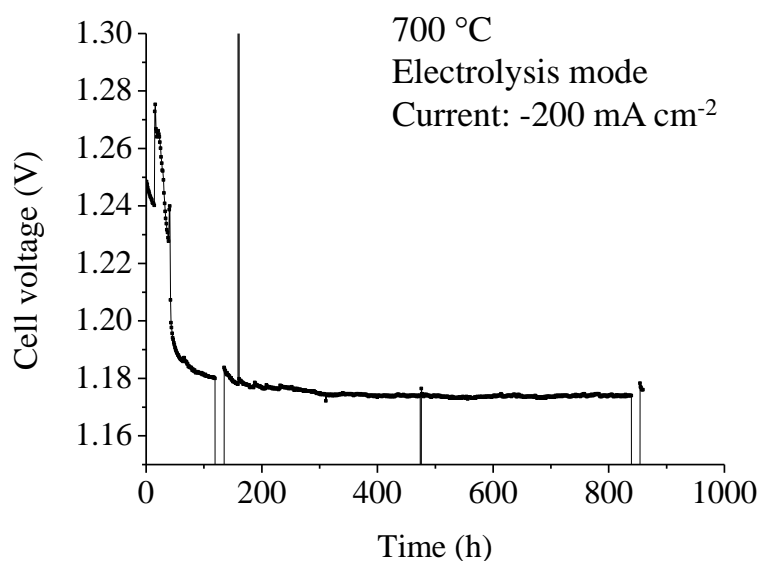


**Fig. 4. 8** Cell voltage as a function of time for CCell 1 operating in the electrolysis mode. The spikes show the timestamps when the applied current is stopped for either system check or measuring the *iV* curve and impedance of the cell.

The improvement of the cell is also observed from the *iV* curves (**Fig. 4.6a-b**) and EIS measurements (**Fig. 4.9** and **4.10**) taken during and after the test. As in the evolution of cell voltage over time previously mentioned, the improvement is especially observed at the beginning of the test. The *iV* curve measured in electrolysis mode (**Fig. 4.6b**) shows an increase of the current density at 1.3 V from  $-0.24 \text{ A cm}^{-2}$  at  $t = 0 \text{ h}$  to  $-0.28 \text{ A cm}^{-2}$  at  $t = 168 \text{ h}$ , and afterwards the *iV* curves do not change. A sharp decrease of series resistance is observed between  $t = 0 \text{ h}$  and  $t = 168 \text{ h}$ . The series resistance continues to decrease at a slower rate afterwards. As in the symmetrical cell, this decrease can be attributed to the improvement of the contact between the electrode and the gold grid over time. Meanwhile, the polarization resistance decreases at the beginning of the measurement by 10% of its initial value, and then it increases steadily at a slow rate.

From the Bode plot, there is an obvious change in the medium to high-frequency processes in which the amplitude is initially decreased before it starts to increase. The processes within this frequency interval are mainly related to the interfacial processes at the oxygen electrode side (i.e. GDC/YSZ, LPNO/GDC, LPNO/Au-grid). Thus, the initial decrease might be mainly related also to the better contact between LPNO and the Au-grid and afterwards, there are some

changes in the other interfaces which induce the slight increase of this contribution. Nevertheless, the processes on the bulk electrodes seem to not be affected by the operation in the electrolysis mode. For example, the polarization resistance and all the contributions in the Nyquist plot (**Fig. 4.9**) remain almost unchanged from 168 h to 960 h. This observation indicates that the response of the cell component including the oxygen electrode is not significantly impacted by the operation in the electrolysis mode. This statement is in perfect line with the stability of the electrode of the symmetrical cell when operated under anodic current.

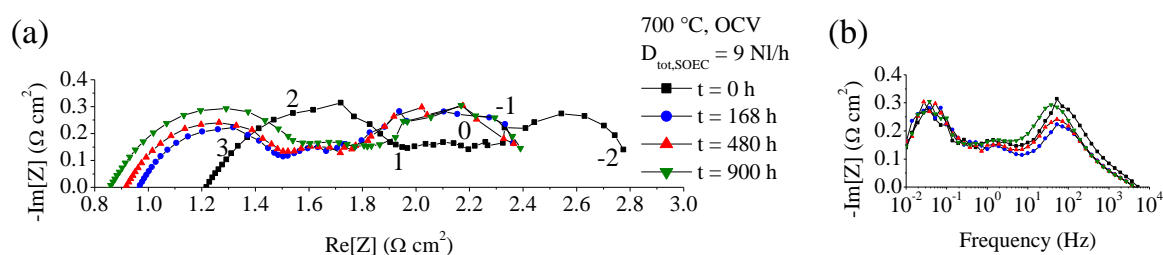


**Fig. 4. 9** The Nyquist and Bode plots of CCell 1 at 700 °C taken at OCV before, during, and after the long-term test for  $D_{\text{tot,SOEC}} = 9$ . The numbers indicate the logarithm of the measuring frequency.

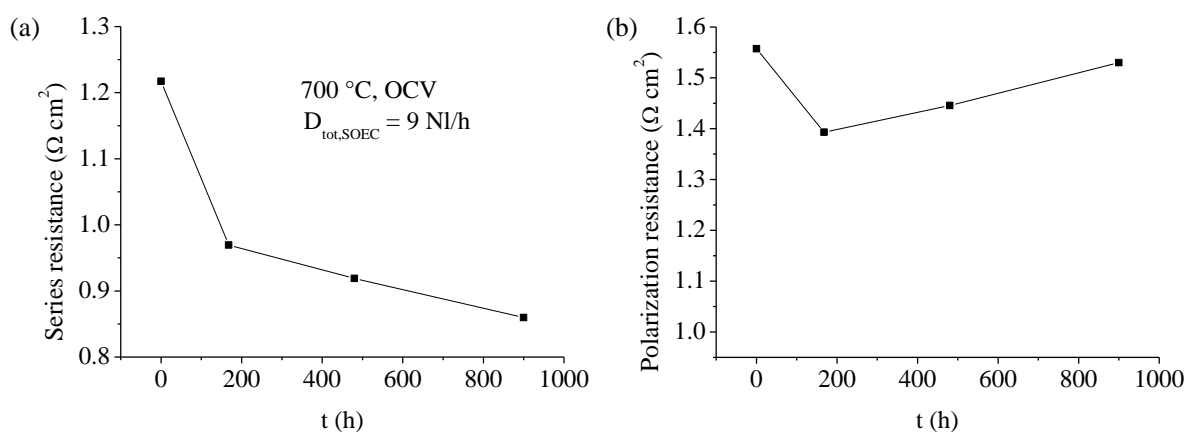


**Fig. 4. 10** (a) The series resistance ( $R_s$ ) and (b) the polarization resistance ( $R_{\text{pol}}$ ) measured at various times during the long-term test of CCell 1.

#### 4.3.2 Preliminary test on CCell 2: GDC barrier layer by RF magnetron sputtering

The pre-test measurements of CCell 1 detailed in §4.3.1 show rather poor performance. Since the oxygen electrode performance has been found to be quite interesting in the symmetrical

cell, it is suspected that the origin of the poor initial performance of CCell 1 comes from the quality of the GDC barrier layer. Indeed, the GDC layer deposited by screen printing is quite thick (4  $\mu\text{m}$ -thick) and porous which may induce a large ohmic resistance. More importantly, the contact between the porous and coarse microstructure of the barrier layer and the fine microstructure of the ESD LPNO electrode could be very poor. This non-optimal interface could thus induce a limitation on the ionic transfer at the GDC/LPNO interface (that was not present for the symmetrical cell as the electrode was layered on a fully dense GDC electrolyte). Thus, to check this assumption and overcome this difficulty, a second complete cell, CCell 2, is prepared, in which the barrier layer is deposited by RF magnetron sputtering. The layer is found to be dense and very thin (400 nm) [49].

The comparison of the initial measurements between CCell 1 and CCell 2 is presented in the iV curves (**Fig. 4.11a-b**) and the impedance spectra (**Fig. 4.12a-b**). The OCV of CCell 2 is found to be close to the theoretical values indicating gas tightness of the test setup. It is clear to see also that the current density of CCell 2 in both fuel cell and electrolysis modes is improved by the factor of two as compared to CCell 1. From the Nyquist plots, the series resistance of CCell 2 is lower than CCell 1. Since the load applied on both cells are the same, it can be said that the contact between LPNO and the grid is similar, thus this smaller value might be attributed to the thinner GDC barrier layer of CCell 2. The impedance response between the two cells is also quite different, especially at the medium frequency range. Indeed, the contribution at medium frequency has been drastically reduced for the CCell 2 compared to CCell1. This observation tends to validate our assumption of poor contact between LPNO and GDC for CCell 1. However, further investigations are still needed to fully validate this hypothesis.

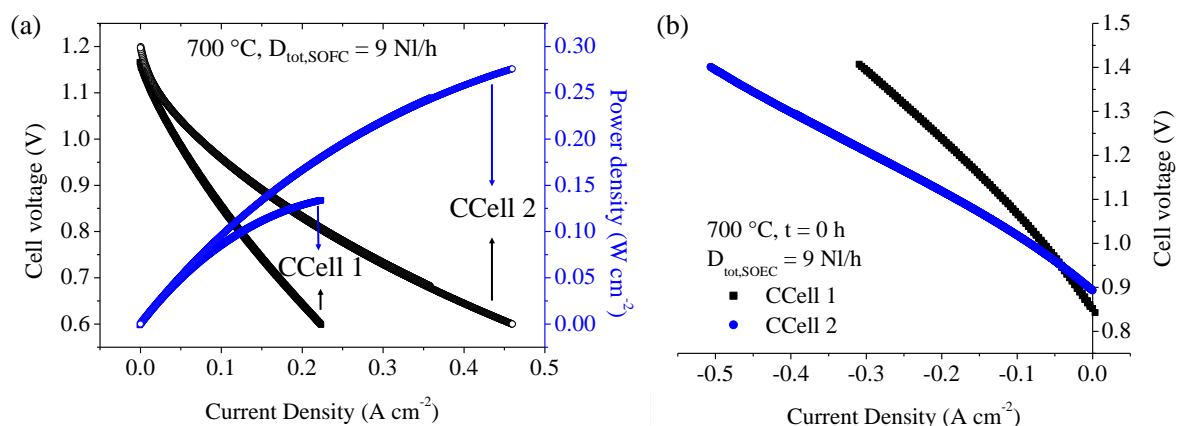


**Fig. 4. 11** The iV curve of CCell 1 and CCell 2 at 700 °C taken before the long-term test for (a) fuel cell operation with  $D_{\text{tot,SOFC}} = 9$  and (b) electrolysis operation with  $D_{\text{tot,SOEC}} = 9$ .

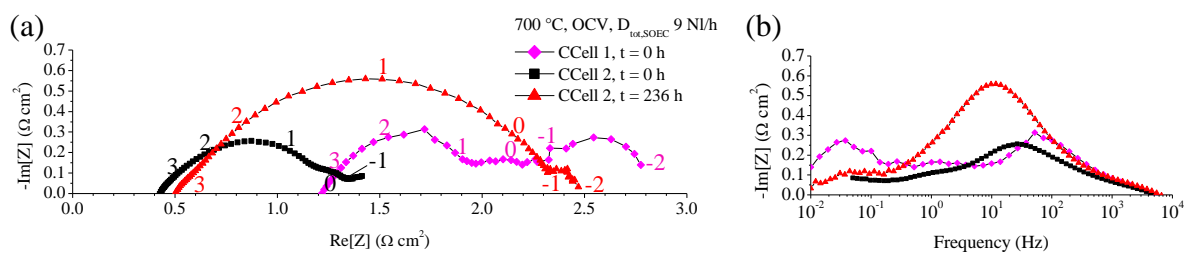


**Fig. 4. 12** The Nyquist and Bode plots of CCell 1 and CCell 2 at 700 °C taken at OCV before, and during the long-term test for  $D_{\text{tot,SOEC}} = 9$ . The numbers indicate the logarithm of the measuring frequency.

#### 4.4 Summary and conclusions

In this chapter, the durability behavior of the LPNO double-layer electrode has been investigated. For this purpose, a long-term test has been carried out in galvanostatic mode at  $\pm 300 \text{ mA cm}^{-2}$  using a symmetrical cell with a three-electrode setup configuration. This experiment was complemented by a preliminary work at the complete cell level with a first long term test performed in electrolysis mode at  $-200 \text{ mA cm}^{-2}$ .

The test on symmetrical cell, SCell, was carried out at 700 °C for 960 h on both fuel cell and electrolysis modes. The pre-test measurements confirmed the good symmetry between the two electrodes and the reference. The post-test measurements after the durability experiment have shown that the polarization resistance ( $R_{\text{pol}}$ ) of the electrode did not change after the test in

electrolysis mode while a significant increase was observed under fuel cell mode. The degradation rate in fuel cell mode was  $219 \text{ mV kh}^{-1}$  ( $15.5 \text{ V\% kh}^{-1}$ ) or  $607 \text{ m}\Omega \text{ cm}^2 \text{ kh}^{-1}$  ( $162.49 \text{ }\Omega\% \text{ kh}^{-1}$ ) while in electrolysis mode was  $7.28 \text{ m}\Omega \text{ cm}^2 \text{ kh}^{-1}$  ( $1.55 \text{ }\Omega\% \text{ kh}^{-1}$ ).

Following the test on the symmetrical cell, preliminary long-term test on a complete cell was carried out at  $700 \text{ }^\circ\text{C}$  in electrolysis mode by applying an anodic current of  $-200 \text{ mA cm}^{-2}$ . The complete cell, CCell 1, was prepared by depositing the  $\text{O}_2$  electrode on a  $4 \text{ }\mu\text{m}$ -thick and porous screen-printed GDC barrier layer. The pre-test measurements have shown a rather poor performance of the cell. However, CCell 1 was found to be quite electrochemically stable after operation for 900 h as indicated by an improvement at the beginning of the test followed by a stable performance which is in agreement with the results on the symmetrical cell operated in the electrolysis mode.

The initial poor performance measured on CCell 1 was suspected to be caused by the thick and porous GDC barrier layer. As a preliminary work to investigate this issue, a second complete cell, CCell 2, was prepared in which the dense,  $400 \text{ nm}$ -thick GDC barrier layer was deposited by RF magnetron sputtering. The iV curves taken before the long-term test have shown that the current densities of CCell 2 on both fuel cell and electrolysis modes doubled the values obtained for CCell 1 indicating a better cell performance.

A deeper investigation to explain the behaviors of the two selected cells (SCell and CCell 1) will be given in Chapter 5.

---

# **CHAPTER 5: POST-MORTEM STRUCTURAL AND MICROSTRUCTURAL CHARACTERIZATIONS**

This last chapter is dedicated to the post-mortem analysis of the samples after durability tests. The chapter is divided into two sub-chapters: (i) microstructural characterizations by SEM and FIB-SEM and (ii) structural characterizations by XRD,  $\mu$ -XRD, and  $\mu$ -XRF. A comparison between the aged samples and the pristine electrode is also performed here. Large parts of this chapter have been published in the Journal of Power Sources (<https://doi.org/10.1016/j.jpowsour.2020.227724>).

## 5.1 Introduction

In Chapter 4, durability experiments have been carried out on symmetrical and complete cells to investigate the degradation of LPNO as an oxygen electrode for both SOFC and SOEC operating modes. Several hypotheses have also been proposed to explain the results. To go further in the analysis, several post-mortem microstructural and structural characterizations, which are described in this chapter, have been conducted on the pristine and aged LPNO electrodes.

The microstructure was characterized by SEM (§2.3.1) and FIB-SEM tomography (§2.3.2). The latter technique allows obtaining the 3D reconstruction of the analyzed electrode from which various microstructural properties can be obtained from numerical modeling. For structural characterization, laboratory XRD (§2.4.1) and synchrotron-based  $\mu$ -XRD and  $\mu$ -XRF (§2.4.2) were used. The synchrotron-based X-ray was carried out in a beamline in Swiss Light Source (SLS), Paul Scherrer Institut (PSI), Switzerland. This technique enables a depth profiling of elements and phases in the prepared lamella. It is a very useful technique especially for multi-layer samples such as the double-layer electrode used in this study. Thanks to the fine resolution, the elements and phases distribution can be observed separately between the ESD and SP layers, thus enable an analysis of the effect of the microstructure to the destabilization of the LPNO electrode in operation.

In complementarity with the cells that have been mentioned in Chapter 4 (SCell and CCell 1), two other cells are also characterized for comparison purposes. The two samples are a pristine double-layer electrode deposited on GDC electrolyte and a thermally-aged single-layer ESD which is also deposited on GDC electrolyte. No further treatments or tests are carried out on the pristine cell after the fabrication, and this cell will be used as a reference for the other results. The thermally-aged cell was subjected to a heat treatment in air at 700 °C for 1000h.

The list of the samples, their treatments, and the summary of the results are given in **Table 5.1**. Six samples are listed: sample 1 is the pristine cell, sample 2 is the thermally-aged cell, sample 3 is the anodic side of the symmetrical cell (SCell-anodic from Chapter 4), sample 4 is the anodically-aged complete cell with screen-printed GDC barrier layer (CCell 1 from Chapter 4), and sample 5 is the cathodic side of the symmetrical cell (SCell-cathodic from Chapter 4). All samples were observed by SEM, but only samples 1 and 3 were characterized by FIB-SEM

tomography. Only samples 1-4 were characterized in PSI. The structural characterization of sample 5 was carried out by laboratory XRD.

**Table 5. 1** The list of samples and the summary of the characterization results.

		Pristine electrode (reference)	Thermally-aged electrode	Long-term test in electrolysis mode		Long-term test in fuel cell mode
Samples		Sample 1	Sample 2	Sample 3 (SCell-anodic)	Sample 4 (CCell 1)	Sample 5 (SCell-cathodic)
Configuration		DL on GDC electrolyte	SL ESD on GDC electrolyte	DL on GDC electrolyte	DL on half-cell GDC/YSZ/Ni-YSZ	DL on GDC electrolyte
GDC barrier layer		N/A	N/A	N/A	Deposited by SP, 4 $\mu\text{m}$ -thick	N/A
Treatment		N/A (as-prepared sample)	700 °C, 1000 h in air	700 °C, 960 h in air, at +300 mA cm <sup>-2</sup>	700 °C, 900 h in 90/10 H <sub>2</sub> O/H <sub>2</sub> , at +200 mA cm <sup>-2</sup>	700 °C, 960 h in air, at -300 mA cm <sup>-2</sup>
Microstructures		No delamination	No delamination	No delamination	No delamination	Delamination of LPNO electrode from GDC electrolyte
Lab XRD	ESD layer	LPNO + (LP)3N2	Not available (N/A)	N/A	N/A	Bulk electrode: LPNO + (LP)3N2 + Pr <sub>6</sub> O <sub>11</sub> + (LP)4N3
	SP layer	LPNO	N/A	N/A	N/A	
$\mu$ -XRD and $\mu$ -XRF	ESD layer	LPNO + (LP)3N2 + Pr <sub>6</sub> O <sub>11</sub>	LPNO + (LP)3N2 + Pr <sub>6</sub> O <sub>11</sub>	LPNO + (LP)3N2 + Pr <sub>6</sub> O <sub>11</sub> + (LP)4N3	LPNO + (LP)3N2 + Pr <sub>6</sub> O <sub>11</sub> + (LP)4N3	N/A
	SP layer	LPNO + Pr <sub>6</sub> O <sub>11</sub>	N/A	LPNO + (LP)3N2 + Pr <sub>6</sub> O <sub>11</sub> + (LP)4N3	LPNO + (LP)3N2 + Pr <sub>6</sub> O <sub>11</sub> + (LP)4N3	N/A

## 5.2 Post-mortem microstructural characterization: SEM and 3D reconstruction by FIB-SEM

### 5.2.1 Characterization of the samples operated in the electrolysis mode

The SEM images of the pristine electrode (sample 1), as well as the anodically-aged electrodes in the symmetrical and complete cell configurations (sample 3 or SCell-anodic and sample 4 or CCell 1), can be viewed in **Fig. 5.1a-c**, respectively. The 3D rendering volumes for the reconstructions of the pristine cell (sample 1) and anodic side of the symmetrical cell (sample 3) are shown in **Fig. 5.2a-b**.

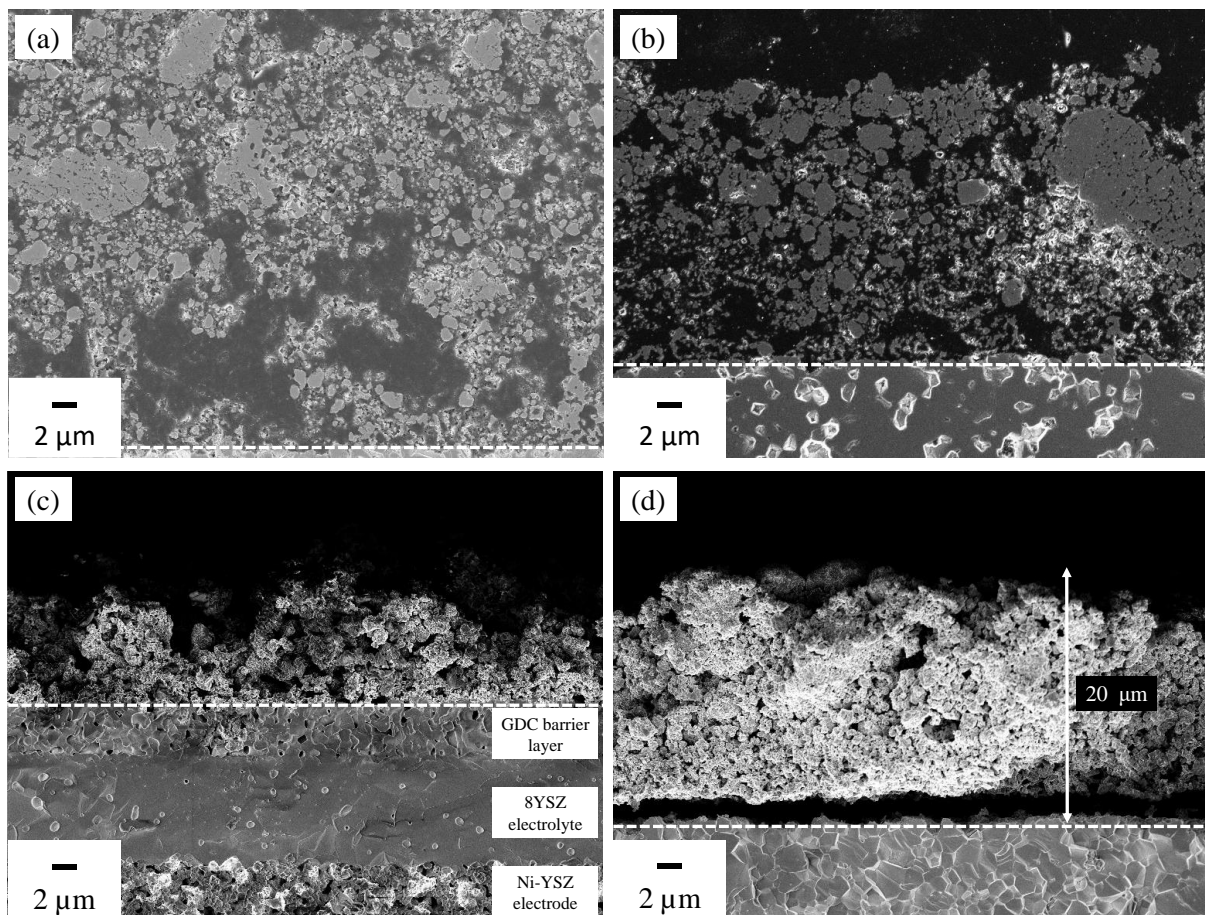


**Fig. 5. 1** The cross-section SEM images of (a) pristine cell (sample 1), (b) anodically-aged symmetrical cell (sample 3 or SCell-anodic), (c) anodically-aged complete cell (sample 4 or CCell 1), and (d) cathodically-aged symmetrical cell (sample 5 or SCell-cathodic). The dashed white line indicates the LPNO electrode/electrolyte interface. The surface of sample 4 is slightly damaged during the removal of the cells from the test bench after electrolysis operation by sandblasting.

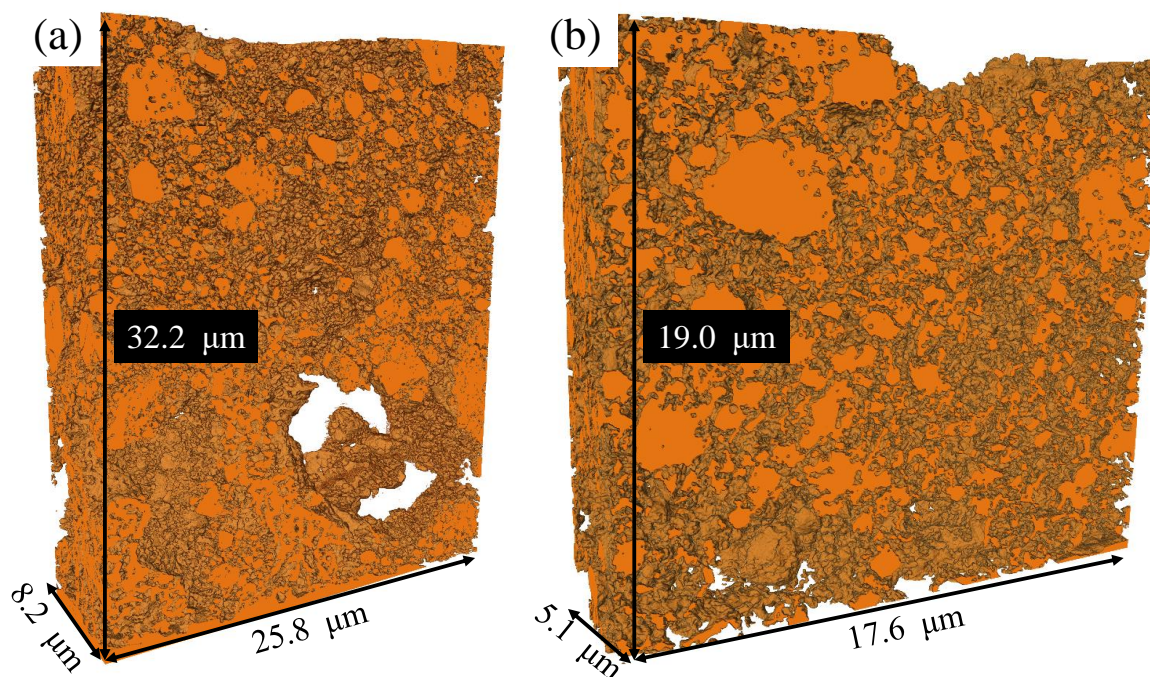


**Fig. 5. 2** The 3D reconstruction visualization of (a) pristine cell (sample 1) and (b) anodically-aged symmetrical cell (sample 3 or SCell-anodic).

From the visual inspection of the SEM images and the 3D reconstructions, no striking microstructure changes can be detected before and after the long-term testing for samples 1, 3, and 4. In addition, good adhesion of the LPNO electrode on the GDC electrolyte is preserved after the anodic aging for both the symmetrical cell (**Fig. 5.1b**) and complete cell (**Fig. 5.1c**) configuration. To go further in the analysis and to validate these preliminary observations, the microstructural properties of both sample 1 and sample 3, are then computed from the 3D reconstructions. The data in terms of volume fraction, mean particle diameter of the LPNO phase, specific surface area, and tortuosity factor of the gas phase are given in **Table 5.2**. After the long-term test in the electrolysis mode, the porosity in the electrode is almost identical with the fresh sample and there is no obvious particle growth. These statements mean that there is no sign of layer densification. Only a minor decrease in the specific surface area is found. This evolution can be explained by the first stage of the material sintering that occurs at a very low rate. Finally, it can be mentioned that the tortuosity factor is not affected by the operation. All these results indicate that the microstructure is not significantly changed upon operation, which is consistent with the stability of the electrode performance in the electrolysis mode (see §4.2 and §4.3.1).

**Table 5. 2** The values of several microstructural properties of the pristine cell and anodic side of the symmetrical cell calculated based on the 3D reconstruction by FIB-SEM.

	Porosity (%)	Mean particle diameter ( $\mu\text{m}$ )	Specific surface area ( $\mu\text{m}^2/\mu\text{m}^3$ )	Tortuosity factor (-)
Sample 1	59.02	0.22	1.86	1.69
Sample 3	63.06	0.18	1.70	1.49

### 5.2.2 Characterization of the sample operated in fuel cell mode

In contrast to the sample operated in the electrolysis mode, severe delamination of the LPNO electrode appears at the GDC interface after the operation in fuel cell mode (sample 6 or SCell-cathodic) as shown in **Fig. 5.1d**. It can be mentioned that this electrode detachment cannot be due to an artifact coming from the sample preparation for the SEM observations. Indeed, using the same protocol, no delamination was observed for the electrode operated in the electrolysis mode. Moreover, the cross-section has been also milled in sample 5 using the plasma-FIB and the observations have also revealed interfacial cracks along the electrode/electrolyte interface.

The electrode detachment for operation in fuel cell mode could be caused by the formation of phase(s) close to the electrolyte interface with expansion/contraction that could trigger the debonding. To justify this hypothesis, further structural characterization of the cathodic side will be discussed in §5.3.4. Nevertheless, it can be pointed out that the significant increase of the  $R_{\text{pol}}$  for the sample aged in fuel cell mode must be largely attributed to the electrode delamination.

### 5.3 Post-mortem structural characterization: synchrotron-based $\mu$ -XRD and $\mu$ -XRF

As explained in §2.4.2, characterization by synchrotron-based X-ray required a very thin sample or lamella. The SEM micrographs of the prepared lamella for samples 1-4 are shown in **Fig. 5.3a-d**. It is reminded here that the lamella preparations have been performed in collaboration with Federico Monaco (a PhD student at the laboratory).

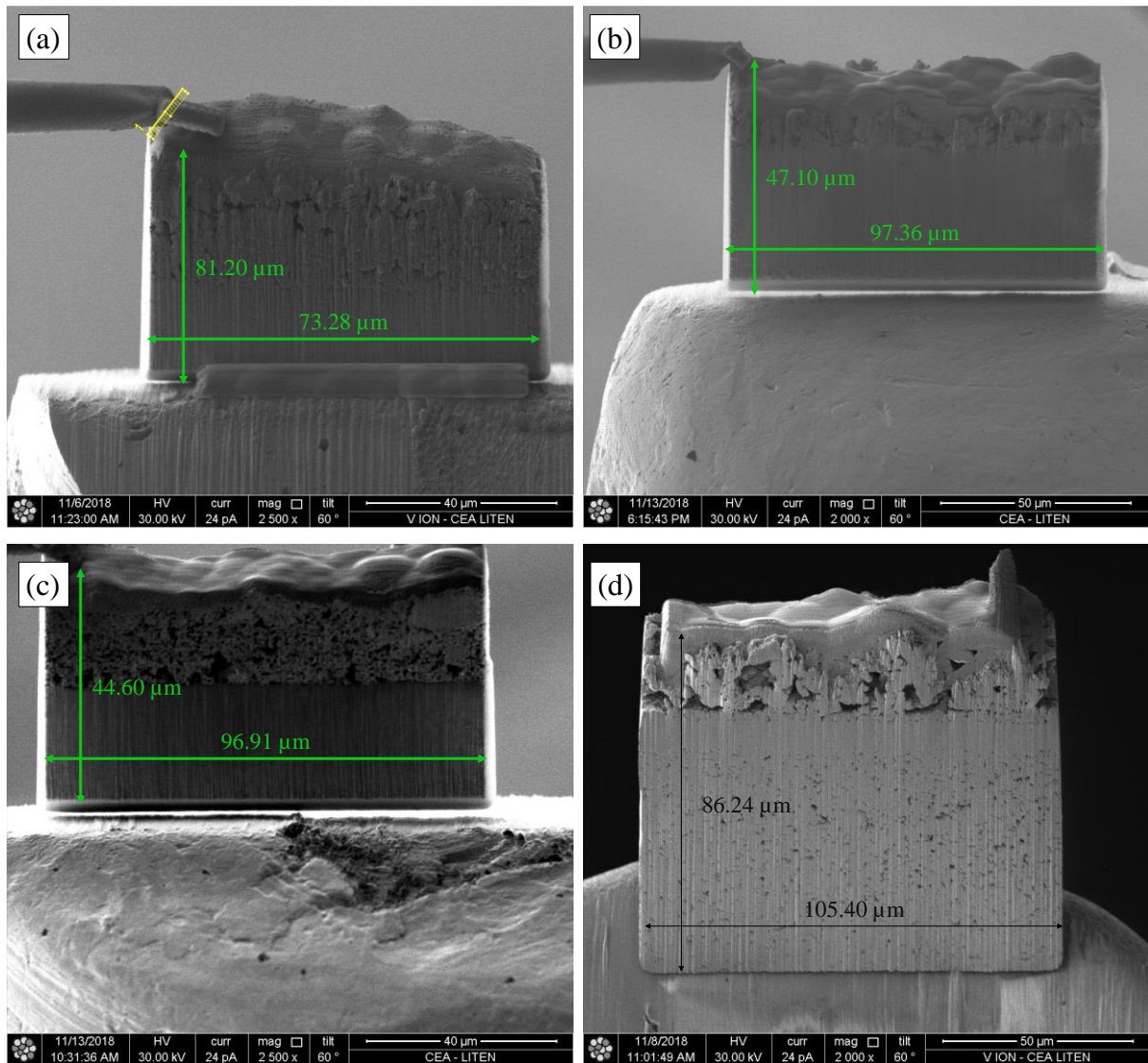


**Fig. 5. 3** SEM micrographs of the lamella of (a) pristine cell (sample 1), (b) thermally-aged cell (sample 2), (c) anodically-aged symmetrical cell (sample 3 or SCell-anodic), and (d) anodically-aged complete cell (sample 4 or CCell 1).

### 5.3.1 Pristine cell

The pristine cell (sample 1) is characterized by both laboratory XRD and synchrotron  $\mu$ -XRD –  $\mu$ -XRF. The purpose is to check the LPNO purity in the fresh electrode and to analyze the distribution of any secondary phases in the thickness of the deposit. Since the electrode was in a double-layer configuration, the laboratory XRD characterization is performed separately for

both ESD (**Fig. 3.9** in §3.3) and SP layers (**Fig. 3.8b(i)** in §3.3). Indeed, X-ray diffraction data obtained in the typical Bragg-Brentano geometry gives a spectral signature throughout the electrode thickness. Thus, it is not possible to differentiate between diffraction patterns from the ESD and SP layers.

#### 5.3.1.1 Laboratory XRD characterizations for ESD and SP layers

As already mentioned in §3.3, a large quantity of the LPNO phase is detected in the ESD single-layer. The phase is indexed to an orthorhombic unit cell with the  $Bmab$  space group (No. 64). The cell lattice parameters deduced from the Rietveld refinement ( $a = 5.432(2) \text{ \AA}$ ,  $b = 5.475(8) \text{ \AA}$ , and  $c = 12.586(9) \text{ \AA}$ ) are found to be in a good agreement with literature data [22]. X-ray diffraction from the GDC electrolyte shows distinct and sharp peaks belonging to the cubic unit cell ( $Fm\bar{3}m$ , No. 225) with a lattice parameter of  $5.419(1) \text{ \AA}$ . This result is also fully consistent with the reported GDC structure (PDF card no 04-002-6160). Apart from LPNO and GDC, there is an apparent presence of a secondary phase which is identified as the higher-order Ruddlesden-Popper phase  $(La,Pr)_3Ni_2O_{7-\delta}$ , (LP)3N2. The formation of this secondary phase is caused by the decomposition of the LPNO structure which might be due to the small particle size in the ESD layer (130 nm on average) with a coral-like microstructure exhibiting large porosity and large specific surface area (see **Fig. 3.10c** in §3.3).

In contrast to the ESD film, only the unique LPNO phase without secondary phases is detected in the SP layer. The denser and coarser microstructure of the SP layer (**Fig. 3.18f** in §3.7) should explain the higher stability of the LPNO phase compared to the very fine microstructure deposited by ESD.

#### 5.3.1.2 Synchrotron-based $\mu$ -XRD and $\mu$ -XRF characterizations for ESD-SP double-layer electrode

A double-layer pristine electrode is also characterized by  $\mu$ -XRD and  $\mu$ -XRF in order to have information on the distribution of the phases in the electrode thickness. **Fig. 5.4a** shows the averaged X-ray diffraction patterns for several vertical positions in the sample (Y-direction) starting from the LPNO/GDC interface. In addition to LPNO, the high-order (LP)3N2 phase is clearly detected at few micrometers above the LPNO/GDC interface (**Fig. 5.4c**) which corresponds to the ESD layer. Meanwhile, this phase is not observed in the upper region of the electrode related to the SP layer (**Fig. 5.4b**). These local characterizations are in a good

agreement with the result from the laboratory XRD described previously. However, the presence of a supplementary phase, which is not detected by the laboratory XRD, is observed all over the electrode thickness. From the peak refinement (**Fig. 5.4b-c**), this phase is identified as  $\text{Pr}_6\text{O}_{11}$ . There are two main possibilities to explain the detection of this phase only in the synchrotron  $\mu$ -XRD pattern. The presence of this new phase could be due to a decomposition of the electrode material during the preparation of the lamella. However, this explanation is rather unlikely since there was no clear evidence that the lamella preparation could induce the decomposition of LPNO (from previous experiments in our group [71]). Alternatively, it is worth noting that the peak intensities corresponding to this phase are very small in such a way that they could be concealed by the peaks of another phase(s) in the laboratory XRD pattern. Indeed, the main  $\text{Pr}_6\text{O}_{11}$  peak ( $2\theta$  angle of  $12.98^\circ$  by synchrotron beam or  $27.98^\circ$  by  $\text{Cu-K}\alpha$  beam) is located very close to GDC peak ( $2\theta$  angle of  $13.22^\circ$  by synchrotron beam or  $28.51^\circ$  by  $\text{Cu-K}\alpha$  beam). Therefore, with the laboratory XRD, the  $\text{Pr}_6\text{O}_{11}$  peak could be completely convoluted by the strong peak intensity coming from the GDC electrolyte.

It can be noticed that  $\text{Pr}_6\text{O}_{11}$  is also an MIEC compound with a very high electronic and ionic conductivity through the electron hopping between the mixed metal oxidation state and high oxygen mobility due to the large concentration of ordered oxygen vacancies [99]–[101]. A previous study has also shown that this material exhibits a very high electrochemical activity for oxygen oxidation/reduction [62]. Thus, albeit unexpected, the presence of  $\text{Pr}_6\text{O}_{11}$  in the two layers of the electrode must promote the electrochemical processes. Therefore, the electrode performances could be improved or at least not impacted by the formation of this secondary phase.

The 2D XRD and XRF maps show the distribution of both crystallographic phases and chemical elements in the whole electrode cross-section (**Fig. 5.5a** and **5.6a**). The visualization inspection confirms that the formation of high order phase (LP)3N2 is restricted to the ESD layer whereas the praseodymium oxide  $\text{Pr}_6\text{O}_{11}$  is found on both layers of the electrode. Finally, the observation all along the electrode/electrolyte interface reveals no sign of reactivity between LPNO and GDC.

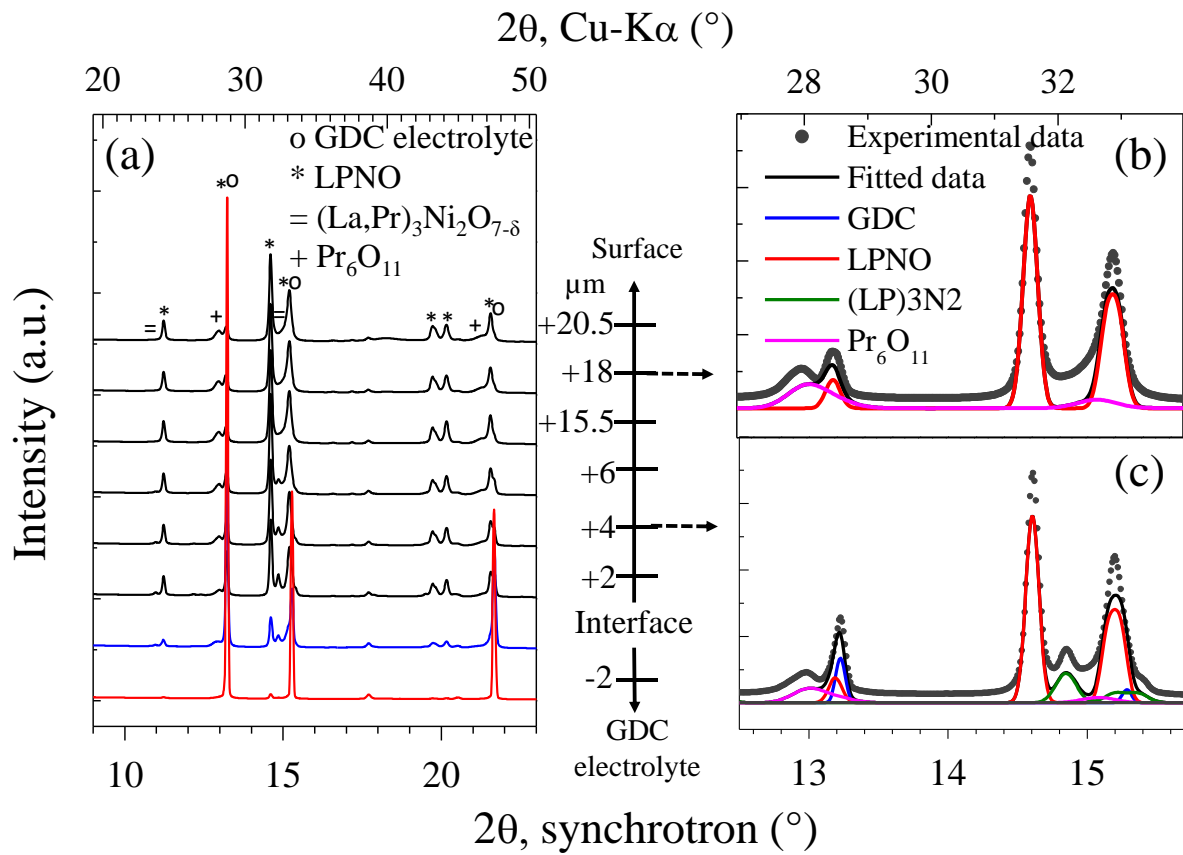


**Fig. 5. 4** (a) The average XRD patterns on several Y-positions and (b)-(c) refinement of the peaks at two different Y-positions, i. e. 18 and 4  $\mu\text{m}$  above the electrode/GDC, respectively, for the pristine cell (sample 1).

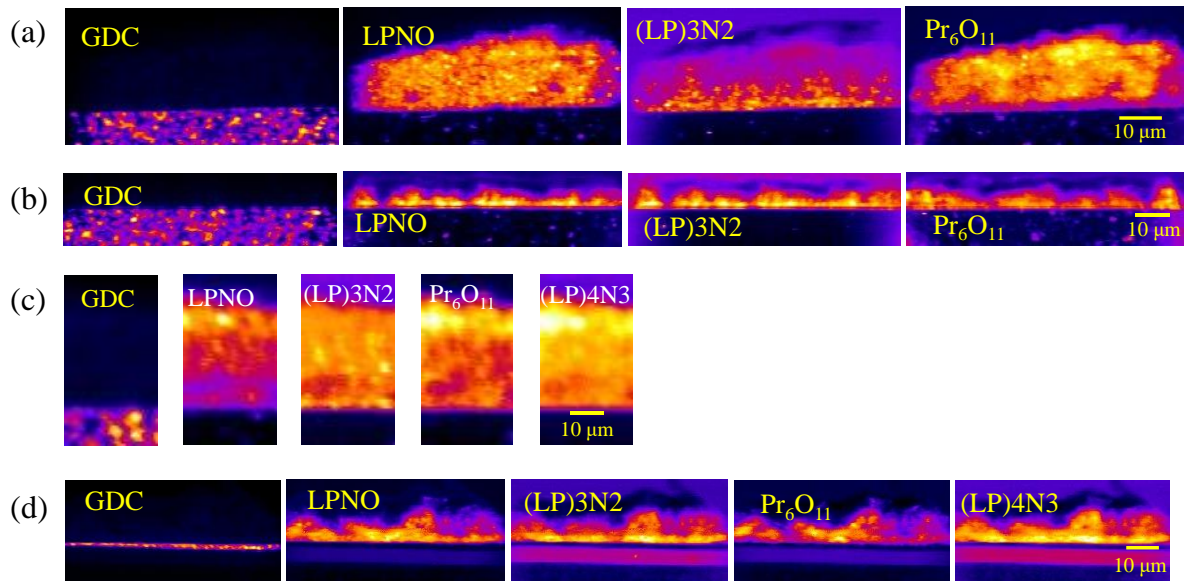


**Fig. 5.5** 2D maps of the XRD which shows the distribution of the phases, namely GDC, LPNO, (LP)3N2, Pr<sub>6</sub>O<sub>11</sub>, and (LP)4N3, in (a) pristine cell (sample 1), (b) thermally-aged cell (sample 2), (c) anodically-aged symmetrical cell (sample 3 or SCell-anodic), and (d) anodically-aged complete cell (sample 4 or CCell 1). The brighter color indicates the higher local intensity of the corresponding compound.

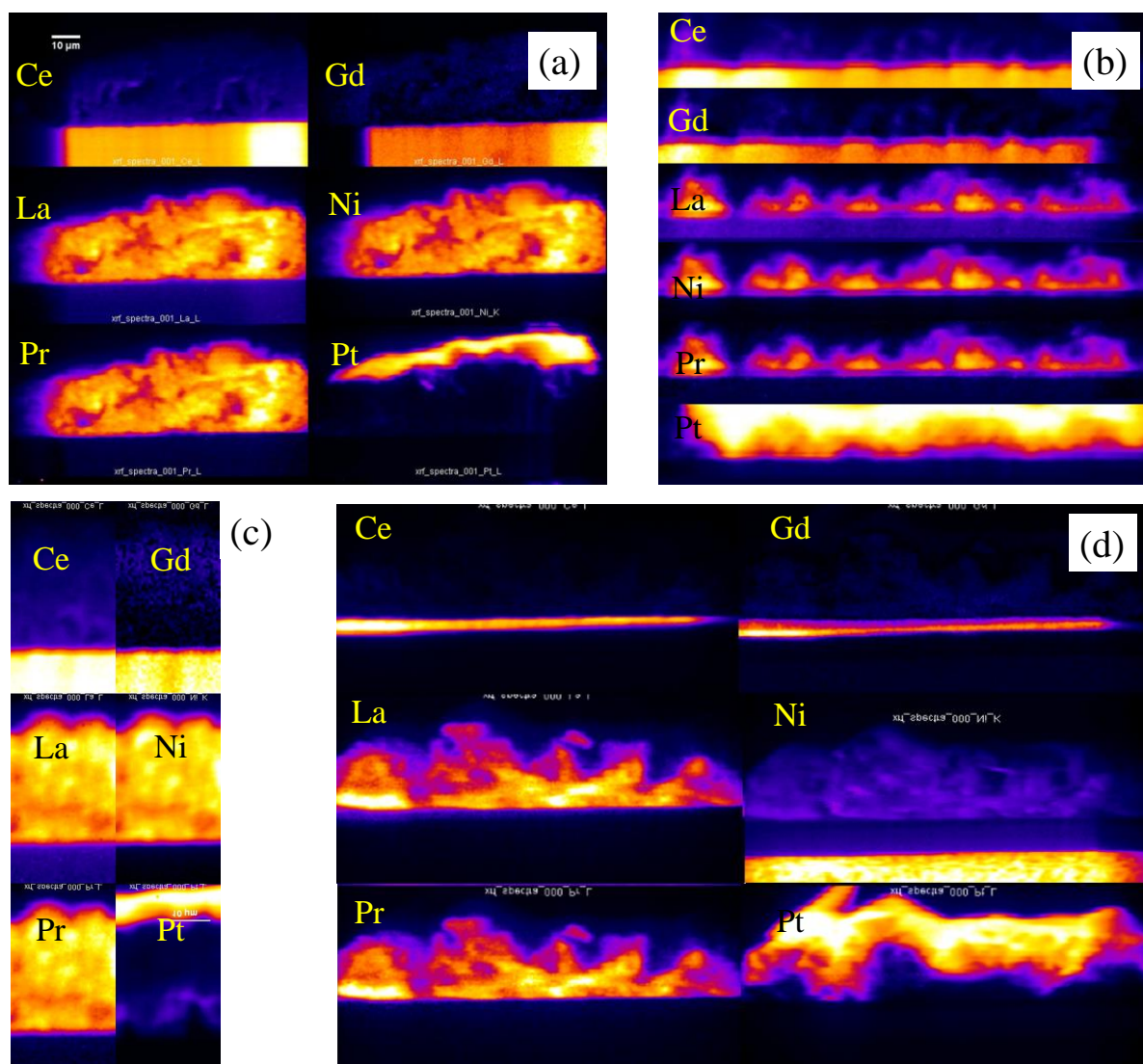


**Fig. 5. 6** 2D maps of the XRF which shows the distribution of the elements, namely Ce, Gd, La, Ni, Pr, and Pt, in (a) pristine cell (sample 1), (b) thermally-aged cell (sample 2), (c) anodically-aged symmetrical cell (sample 3 or SCell-anodic), and (d) anodically-aged complete cell (sample 4 or CCell 1). The brighter color indicates the higher local intensity of the corresponding element.

### 5.3.2 Thermally-aged cell

The thermally-aged cell (sample 2) composed of a single ESD layer deposited on the GDC electrolyte is annealed at 700 °C for 1000 h in air. This experiment is conducted only on the ESD layer to check whether the small amount of secondary phases in the fresh material could

evolve and would have any impact on the thermal stability of the electrode. The synchrotron  $\mu$ -XRD characterizations (**Fig. 5.7**) reveal that the thermal aging does not induce the formation of new phases as compared to the ESD layer of the pristine cell. As in the pristine cell, there is also no indication of reactivity between the LPNO electrode and GDC electrolyte as evidently shown in the 2D maps (**Fig. 5.5b** and **5.6b**). However, from the phase quantification from the  $\mu$ -XRD fitting shown in **Fig. 5.8a-b**, it seems that the amount of both (LP)3N2 and, especially,  $\text{Pr}_6\text{O}_{11}$  slightly increases after the thermal aging. Therefore, although there are no new decomposition products, the LPNO might slightly decompose into (LP)3N2 and  $\text{Pr}_6\text{O}_{11}$  at  $700^\circ\text{C}$  under air.

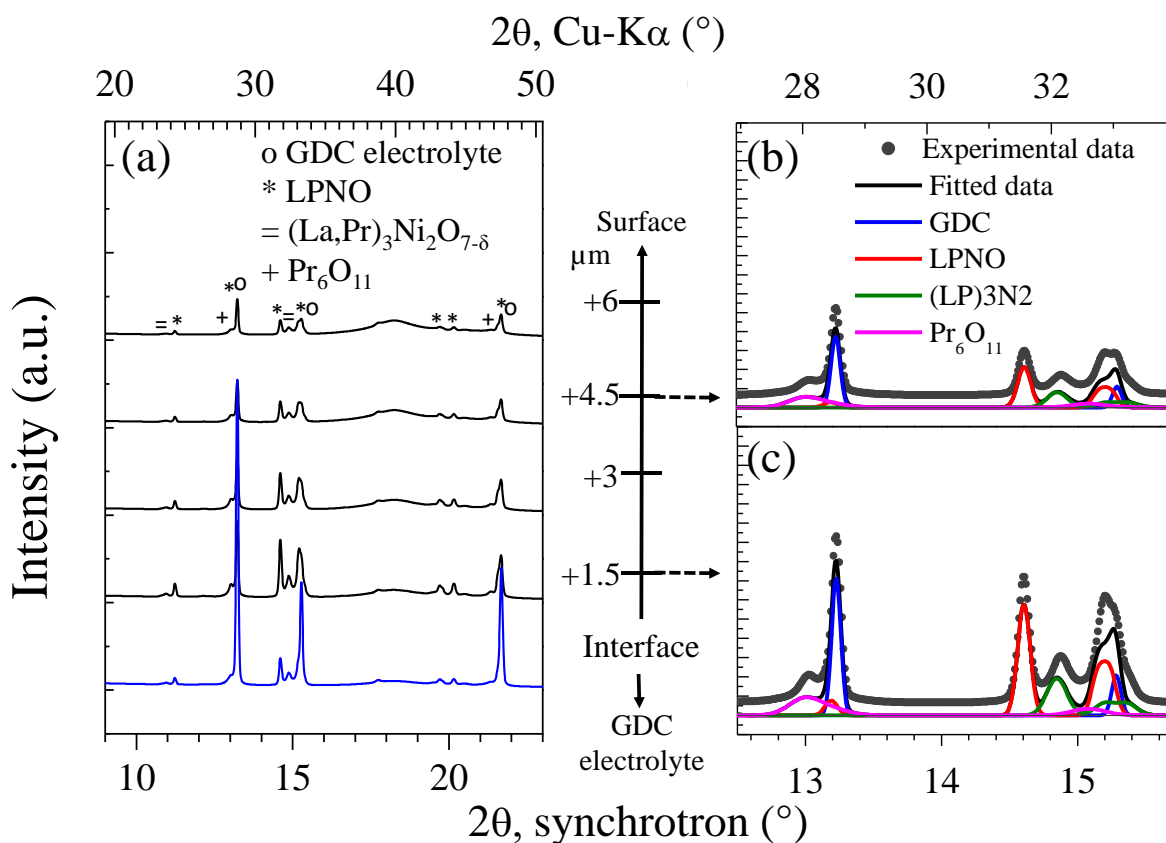


**Fig. 5.7** (a) The average XRD patterns on several Y-positions and (b)-(c) refinement of the peaks at two different Y-positions, i. e. 4.5 and 1.5  $\mu\text{m}$  above the electrode/GDC interface, respectively, for the thermally-aged cell (sample 2).

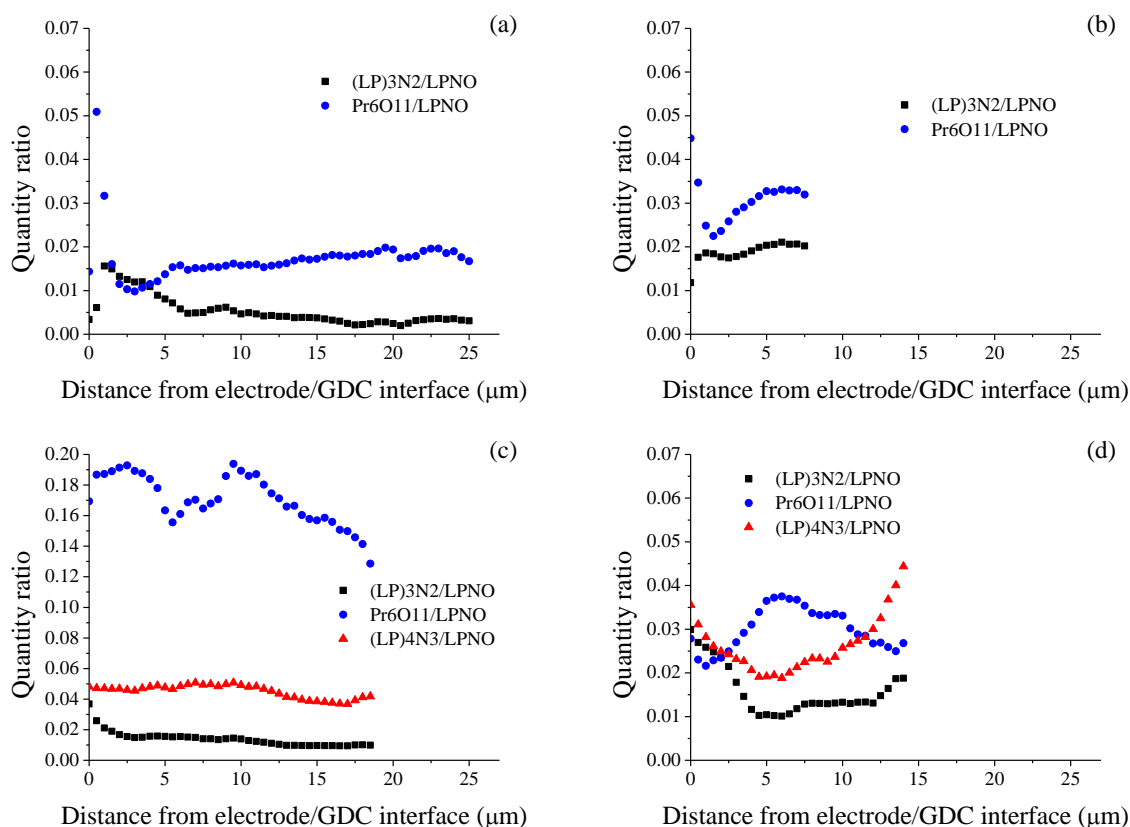


**Fig. 5. 8** The quantitative comparison of (LP)3N2, Pr6O11, and (LP)4N3 to LPNO in the LPNO electrode as the function of distance from electrode/GDC interface for (a) pristine cell (sample 1), (b) thermally-aged cell (sample 2), (c) anodically-aged symmetrical cell (sample 3 or SCell-anodic), and (d) anodically-aged complete cell (sample 4 or CCell 1).

### 5.3.3 Long-term test in electrolysis mode (anodic polarization): symmetrical and complete cells

#### 5.3.3.1 Anodic side of the symmetrical cell (sample 3 or SCell-anodic)

Thanks to the  $\mu$ -XRD characterizations, a new phase is detected on the anodic side of the symmetrical cell (sample 3 or SCell-anodic) after the durability experiment. As shown in **Fig. 5.5c** and **5.9a-c**, this new phase is found to appear on both ESD and SP layers. The peak refinement (**Fig. 5.9b-c**) has allowed identifying this compound as another higher-order Ruddlesden-Popper phase  $(\text{La,Pr})_4\text{Ni}_3\text{O}_{10-\delta}$ , abbreviated as (LP)4N3. Moreover, the phase of (LP)3N2 was also found in the SP layer which previously was not present in the SP layer of the pristine cell. Additionally, the phase quantification unambiguously shows that the amount

of  $\text{Pr}_6\text{O}_{11}$  is significantly higher after aging (**Fig. 5.8c**). From all these results, it can be concluded that the operation in electrolysis mode accelerates the decomposition of LPNO compared to simple thermal aging. Nevertheless, all these phases including (LP)4N3 are known to be electrochemically active [19], [42]. Besides, according to the 2D maps of crystalline phases and chemical elements (**Fig. 5.5c** and **5.6c**), no reactivity is detected after operation between LPNO electrode and GDC electrolyte. For these reasons, the electrode response should not be affected by the aging, which is consistent with the electrode performance stability measured in electrolysis mode (see §4.2).

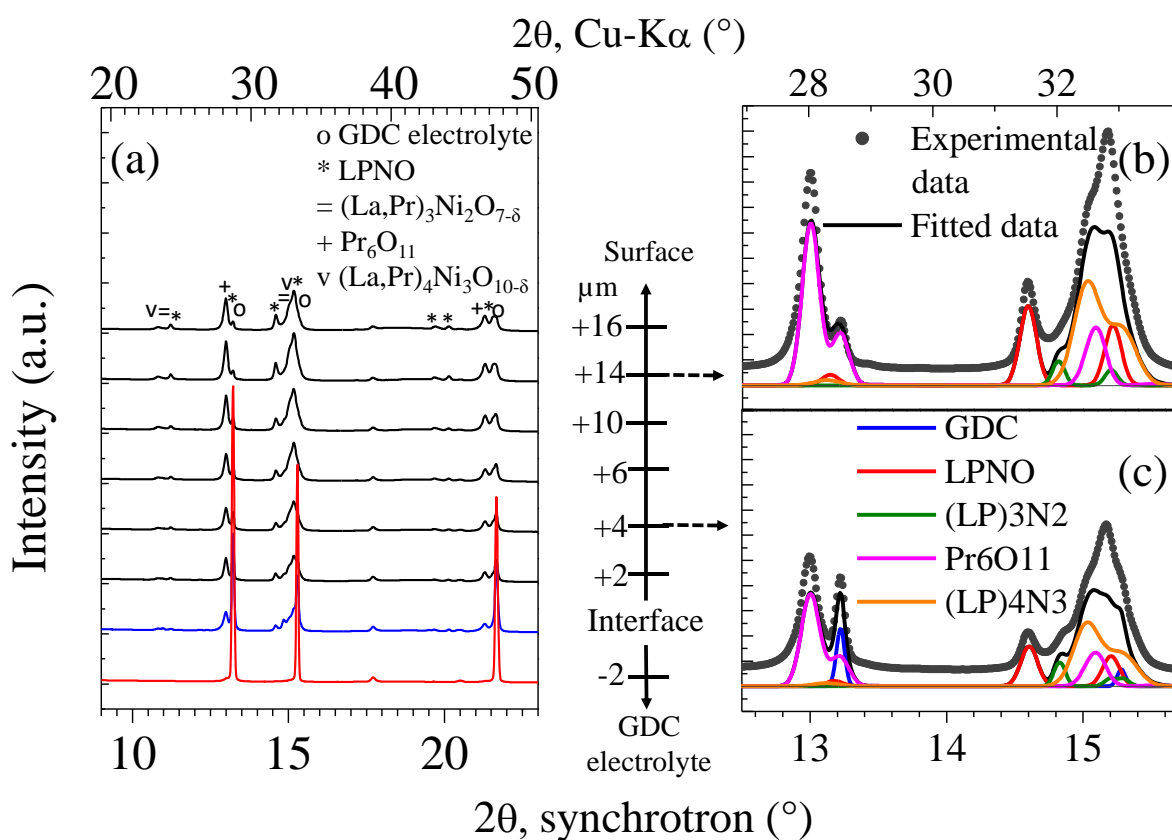


**Fig. 5.9** (a) The average XRD patterns on several Y-positions and (b)-(c) refinement of the peaks at two different Y-positions, i. e. 14 and 4  $\mu\text{m}$  above the electrode/GDC interface, respectively, for the anodically-aged symmetrical cell (sample 3 or SCell-anodic).

## 5.3.3.2 Anodically-aged oxygen electrode of the complete cell (sample 4 or CCell 1)

The  $\mu$ -XRD characterization data on the LPNO electrode of the complete cell (sample 4 or CCell 1) after long-term test in electrolysis mode shows that the final phases are similar to the anodic side of the symmetrical cell (sample 3). Indeed, (LP)4N3 is also formed in both ESD and SP layer while the decomposition in (LP)3N2 extends in the SP layer (**Fig. 5.5d** and **5.10a-c**). These observations reinforce the statement that the operation in electrolysis mode favors the LPNO destabilization. However, conversely to the symmetrical cell, the quantifications have shown that the amount of  $\text{Pr}_6\text{O}_{11}$  seems to be not significantly increased after the operation. This apparent discrepancy between the two samples can be explained by the difference in aging condition. Indeed, the durability test with the symmetrical cell was performed at higher current than for the complete cell (anodic current of  $300 \text{ mA cm}^{-2}$  vs  $200 \text{ mA cm}^{-2}$ ). From this point of view, the underlying mechanisms accelerating the material destabilization under electrolysis mode should be related to the current or the electrode overpotential. In this frame, it could be suggested that the change of the LPNO oxygen stoichiometry under electrolysis current could favor the decomposition.

Finally, the 2D maps for the complete cell show that there is no indication of reaction between LPNO and GDC. However, a composition gradient of Ce and Gd is detected in the GDC barrier layer (**Fig. 5.6d**). The area close to the LPNO electrode is richer in Ce while the area close to the 8YSZ electrolyte is richer in Gd. However, it is still not clear whether the origin of this gradient of composition was induced by the manufacturing of the half-cell itself (i.e. interdiffusion during the barrier layer sintering) or related to evolution during the durability test.

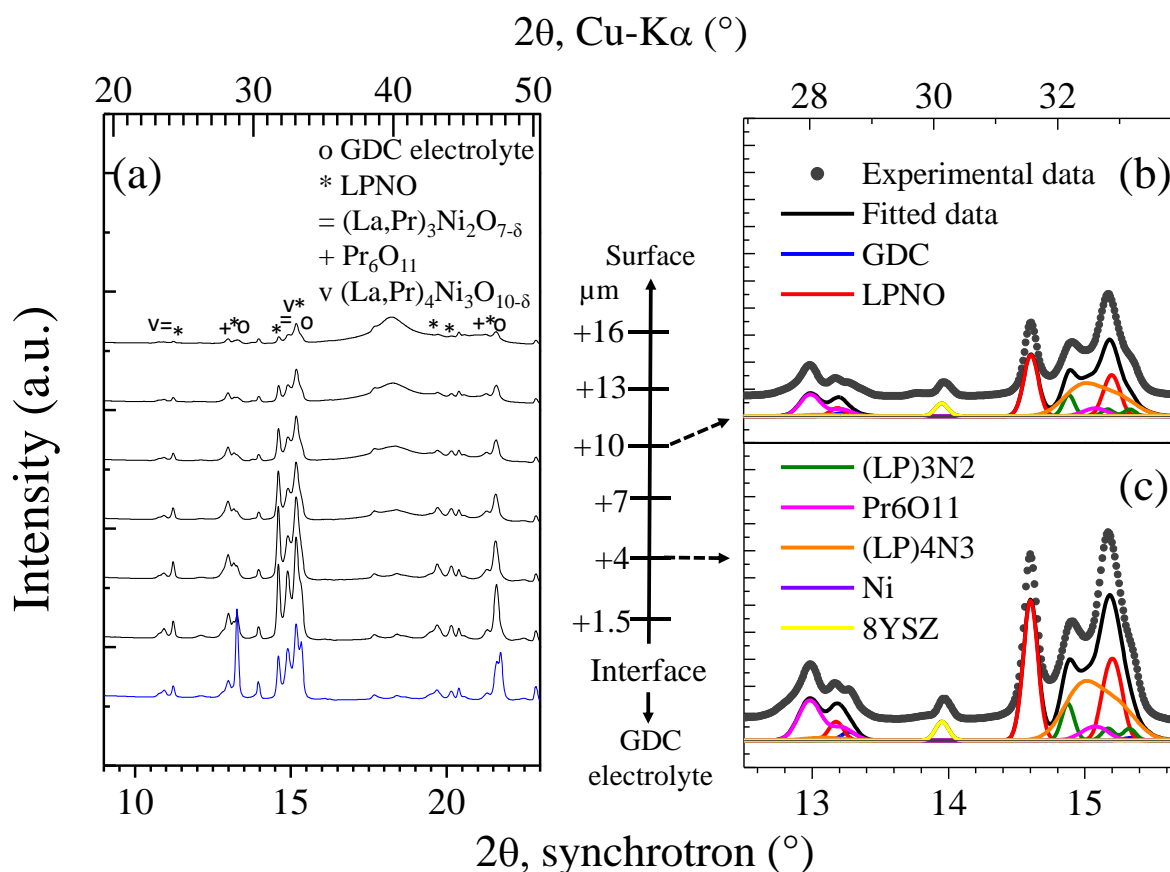


**Fig. 5.10** (a) The average XRD patterns on several Y-positions and (b)-(c) refinement of the peaks at two different Y-positions, i. e. 10 and 4  $\mu\text{m}$  above the electrode/GDC interface, respectively, for the anodically-aged complete cell (sample 4 or CCell 1).

#### 5.3.4 Long-term test in fuel cell mode (cathodic polarization): symmetrical cell

Because of difficulties in the specimen preparation due to the poor electrode attachment onto the electrolyte after aging in fuel cell mode, only laboratory XRD characterizations are carried out on sample 5 (cathodic side of the symmetrical cell). Indeed, the electrode aged under cathodic polarization was delaminated in such a way that the thin lamella was lost during the last stage of its preparation. Even if the laboratory XRD technique cannot provide information within the thickness of the electrode, the presence or appearance of secondary phases after the long-term operation can be compared to the pristine cell. As for the electrode aged in the electrolysis mode, the secondary phases (LP)3N2,  $\text{Pr}_6\text{O}_{11}$ , and (LP)4N3 have also been detected in sample 6 (**Fig. 5.11b**). Conversely to the pristine electrode (**Fig. 5.11a**), it can be noticed that the possibility to detect the  $\text{Pr}_6\text{O}_{11}$  phase with laboratory equipment for the aged sample proves that its quantity has been significantly increased. These results suggest that the cathodic

current also accelerates the LPNO destabilization. However, at this stage, it is still unclear whether the decomposition is more pronounced when the electrode is operated in fuel cell or electrolysis mode. Nevertheless, this structural characterization does not reveal a strong reactivity at the electrode/GDC interface that could explain the delamination. Therefore, it can be speculated that the amount of the secondary phases formed under fuel cell current is higher so that they could destabilize the interface. In this view, one could consider the origin of LPNO degradation coming from the mechanism of the oxygen reduction reaction that occurs at the cathodic side in fuel cell mode. Indeed, in these reducing conditions under cathodic polarization, the oxygen over-stoichiometry in  $\text{LaPrNiO}_{4+\delta}$  material is decreased since a flux of oxide ions are transported from the oxygen electrode to the hydrogen electrode through the electrolyte. The LPNO is consequently losing some interstitial oxygen ions and this evolution should not be in favour of its structural stability. On the contrary, when LPNO is working as an anode material in oxidizing conditions in the electrolysis mode, LPNO is fed by oxygen ions that could occupy interstitial sites of the structure. Therefore, the increase of the oxygen over-stoichiometry under anodic current could be less impacting and could limit the LPNO structural instability compared to operation under cathodic current. In contrast for materials exhibiting oxygen under-stoichiometry such as the state-of-the-art LSCF, it is interesting to note that the performance degradation caused by either delamination or cation diffusion and the formation of secondary phase had been observed during the practical operation in electrolysis mode [45], [102], [103]. Moreover, in a present review work [44], the authors focus on providing an understanding of SOEC degradation in which the role of oxygen chemical activity appears as a major factor governing various degradation phenomena including cation diffusion, secondary phase formation, and delamination of the electrode. Finally, in the specific case of the LPNO electrode, the delamination could also be related to the behavior of  $\text{Pr}_6\text{O}_{11}$  in different  $p\text{O}_2$ . As mentioned in the literature [104], [105], a phase transition of praseodymium oxide ( $\text{PrO}_x$ ) from  $\text{Pr}_6\text{O}_{11}$  ( $=\text{PrO}_{1.83}$ ) to  $\text{Pr}_7\text{O}_{12}$  ( $=\text{PrO}_{1.71}$ ) appears at either  $\sim 700$  °C in the air or in a slightly low  $p\text{O}_2$  environment or at  $\sim 800$  °C in high  $p\text{O}_2$ . Since the test in SOFC mode is carried out at 700 °C, this structural transition could take place in the vicinity of the interface where low  $p\text{O}_2$  is induced by the reaction of oxygen reduction.

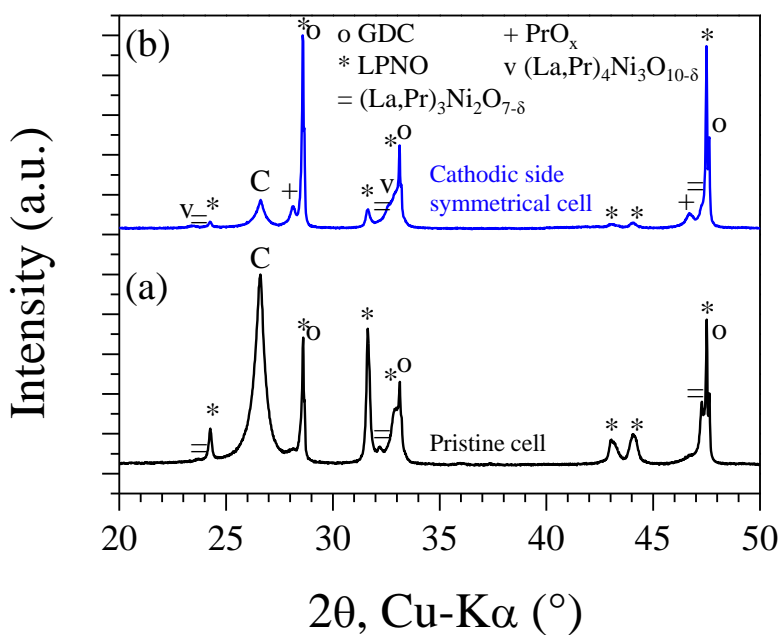


**Fig. 5. 11** The lab XRD of (a) pristine cell (sample 1) and (b) cathodically-aged symmetrical cell (sample 5 or SCell-cathodic). The symbol ‘C’ indicated the carbon phase which is originating from the carbon tape used for sample preparation by p-FIB.

#### 5.4 Summary and conclusions

Several microstructural and structural characterizations have been carried out to investigate the behavior of the LPNO electrode under polarization. SEM observations and FIB-SEM reconstructions have shown that the microstructure is not affected by the operation in the electrolysis mode. However, the sample aged in fuel cell mode exhibits severe delamination at the electrode/electrolyte interface which is not observed for the electrode operating in the electrolysis mode. This delamination at the LPNO/GDC interface must explain the higher degradation rate induced by the fuel cell operation.

In complementarity of the microstructural analysis, structural characterizations by laboratory XRD and synchrotron  $\mu$ -XRD and  $\mu$ -XRF have been performed. For the pristine electrode analyzed just after the manufacturing process, it has been found that the fine microstructure of the ESD layer induces a minor decomposition into the (La,Pr)<sub>3</sub>Ni<sub>2</sub>O<sub>7-δ</sub> and Pr<sub>6</sub>O<sub>11</sub> secondary phases while the coarse microstructure of the SP layer is more stable with only the presence of

$\text{Pr}_6\text{O}_{11}$ . It can be noticed that the amount of this phase is very limited in the pristine samples in such a way that it can be only detected in the  $\mu$ -XRD pattern.

The structural observation for the thermally-aged electrode has not revealed the formation of any additional secondary phases. However, a slight increase in the amount of  $(\text{La,Pr})_3\text{Ni}_2\text{O}_{7-\delta}$  and, especially  $\text{Pr}_6\text{O}_{11}$ , has been detected indicating that LPNO in the ESD layer is decomposed at a very slow rate in temperature.

Compared to the thermal aging, it has been found that the LPNO decomposition is much more pronounced for the electrodes operated in an anodic or cathodic polarization. Indeed, for the samples aged in the electrolysis mode, the  $\mu$ -XRD maps have shown that a new secondary phase  $(\text{La,Pr})_4\text{Ni}_3\text{O}_{10-\delta}$  appears in both the ESD and SP layers. Moreover, the quantity of  $\text{Pr}_6\text{O}_{11}$  is strongly increased especially at high current density, while the formation of  $(\text{La,Pr})_3\text{Ni}_2\text{O}_{7-\delta}$  extends in the SP layer. These results mean that the operation under electrolysis current accelerates the decomposition of LPNO compared to simple thermal aging. With the XRD laboratory characterizations, the same conclusions have been drawn for the electrode operated in fuel cell modes. However, the difference in the material stability between the two operating modes is still unclear and further investigations are required. Nevertheless, two main hypotheses have been proposed to account for the electrode delamination only observed in fuel cell mode. Firstly, since the oxygen over-stoichiometry decreases under cathodic current, especially at the electrolyte interface where the depletion in interstitial oxygen should be the highest, the rate of the LPNO destabilization could be accelerated compared to the anodic operation. Secondly, the behavior of  $\text{Pr}_6\text{O}_{11}$  under reducing atmosphere at the electrolyte interface in fuel cell conditions could also participate or explain the delamination.

To conclude, the suitability of  $\text{LaPrNiO}_{4+\delta}$  (LPNO) as a durable oxygen electrode for electrolysis cell has been proved to be promising. Indeed, the electrode polarization resistances of the complete cell remain unchanged after the durability test carried out under electrolysis current thanks to the presence of electrochemically active secondary phases coming from the decomposition of the LPNO phases. Moreover, the destabilization of the electrode seems to not be affected by the microstructure as indicated by the same destabilization behavior on both ESD and SP layers.

---

# **GLOBAL CONCLUSIONS AND PERSPECTIVES**

## Conclusions

The evaluation of lanthanum-praseodymium nickelate,  $\text{LaPrNiO}_{4+\delta}$  or LPNO, as a suitable material for the oxygen electrode of Solid Oxide Cells (SOCs) has been carried out and discussed in this work. The manufacturing parameters have been optimized for electrodes deposited either by electrostatic spray deposition (ESD) with a coral-like microstructure or by screen printing (SP). One of the most important results is the presence of secondary phase higher-order nickelate,  $(\text{La,Pr})_3\text{Ni}_2\text{O}_{7-\delta}$  or  $(\text{LP})_3\text{N}_2$ , in the prepared ESD layer which is suspected to be caused by the fine particle size.

The electrode response has been characterized by electrochemical impedance spectroscopy (EIS). A single equivalent electrical circuit has been proposed to fit all measurement data. The circuit takes into account the contribution of the pure ohmic resistance or the series resistance  $R_s$  (with a resistor), the ionic transfer at the electrode/electrolyte interface (with a resistor in parallel with a constant phase element,  $R//\text{CPE}$ ), the bulk electrode processes (with a fractal Gerischer in parallel with a pure capacitor,  $G_f//C$ ), and the gas diffusion (with a finite-length Warburg element, FLW).

Besides the choice of materials with suitable intrinsic properties, the microstructure and architecture of the electrode also play an important role in the performance. Hence, the electrochemical performance of the LPNO electrode has been optimized by improving the microstructure and electrode design. Several symmetrical cells consisting of the LPNO electrode deposited on gadolinium-doped ceria,  $\text{Ce}_{0.9}\text{Gd}_{0.1}\text{O}_{2-\delta}$  or GDC, have been prepared and characterized, yielding to four main results. Firstly, the quality of the electrode/electrolyte interface is a key factor that can be optimized with sufficient sintering temperature to enhance the electrode/electrolyte adhesion. In this frame, it has been shown that an even better electrode adhesion of the ESD layer can be obtained at a lower sintering temperature (960 °C) as compared to the SP layer (1100 °C). However, the coral-like microstructure of the ESD layer leads to a rougher surface than the SP layer, which is not favorable for good current collecting. Thus, various electrode designs have been manufactured and tested in order to combine the advantage of the two processes. For this purpose, a double-layer (DL) configuration which consists of the ESD layer as the active functional layer (AFL) and topped by the SP layer as the current collector layer (CCL) has been thoroughly investigated. It has been shown that this architecture allows improving substantially the performance because of a better electrode/electrolyte interface of the ESD layer and flatter surface of the SP layer; the latter

favoring the current collecting. Even better performance has been obtained for a triple-layer (TL) electrode, which consists of a thin GDC layer deposited by SP, followed by an LPNO layer by ESD, and lastly LPNO layer by SP. The LPNO ESD is found to penetrate the GDC SP and forming a composite of LPNO-GDC. It is suggested that the formation of this composite is beneficial to improve the mechanical contact and the oxygen solid-state diffusion. Moreover, it is also suspected that the increase in the density of triple-phase boundary lines in the composite could also participate in the electrode performances by activating the so-called surface path. The third result shows that the quality of the CCL (LPNO deposited by SP) also plays an important role in the DL and TL electrodes. It is shown that when the LPNO powder used for SP ink preparation is not ball-milled, large agglomerates present in the CCL resulting in the damage of the ESD layer beneath. Since the porous ESD layer is favorable for the reactions, the damage reduces its porosity and, in consequence, the electrode performance is decreased. Thus, a well-distributed and small particle size of the CCL is required. Lastly, it has been shown that the sintering temperature after CCL deposition by SP for double and triple-layer should not exceed 800 °C to prevent the increase of (LP)<sub>3</sub>N<sub>2</sub> amount in the ESD layer. Notwithstanding this phase is electrochemically active and could even help to improve the electrochemical performance of the electrode, the initial presence of this phase should not be detrimental regarding the electrode durability. From all these results, the best electrode performance is a TL electrode whose area-specific polarization resistance value at 700 °C and open circuit potential (OCP) is 0.20 Ω cm<sup>2</sup>.

The durability of SOCs is one of the most important issues for this high-temperature technology. For this particular electrode, the degradation studies are quite challenging because of the different microstructure between the ESD and SP layer and the presence of a secondary phase in the pristine ESD layer. Moreover, the number of studies dedicated to the degradation of LPNO are in general very limited. To address this difficulty, long-term tests at 700 °C have been carried out on both DL symmetrical and complete cells to investigate the degradation of the LPNO electrode in operation. A current of ±300 mA cm<sup>-2</sup> was applied on either side of a symmetrical cell, SCell, allowing one side of the electrode to operate in fuel cell mode (cathodic current) while the other in electrolysis mode (anodic current). After 960 h, it is found that the performance of LPNO strongly decreases in fuel cell operation while it remains quite stable in the electrolysis mode. The calculated cell degradation rate in fuel cell mode was 219 mV kh<sup>-1</sup> (15.5 V% kh<sup>-1</sup>) or 607 mΩ cm<sup>2</sup> kh<sup>-1</sup> (162.49 Ω% kh<sup>-1</sup>) while in electrolysis mode was

7.28 m $\Omega$  cm<sup>2</sup> kh<sup>-1</sup> (1.55  $\Omega$ % kh<sup>-1</sup>), which means that the degradation in electrolysis operation was around 100 times lower.

Following the test on the symmetrical cell, a preliminary long-term test on a complete cell was carried out in electrolysis mode by applying an anodic current of -200 mA cm<sup>-2</sup>. The cell, CCell 1, was prepared by depositing the 4  $\mu$ m-thick GDC barrier layer by screen printing. The pre-test measurements have shown a rather poor performance of the cell. However, CCell 1 was found to be quite electrochemically stable after operation for 900 h as indicated by a slight improvement at the beginning of the test followed by a stable performance, which is in agreement with the results on the symmetrical cell operated in the electrolysis mode.

The initial poor performance measured on CCell 1 was suspected to be caused by the quite thick and porous GDC barrier layer. As an effort to investigate this issue, a second complete cell, CCell 2, was prepared in which the dense, 400 nm-thick GDC barrier layer was deposited by RF magnetron sputtering. The iV curves have shown that the current densities of CCell 2 on both fuel cell and electrolysis modes doubled the values obtained for CCell 1 indicating a better cell performance.

For a deeper understanding of the LPNO durability behavior of the three cells mentioned above, post-mortem microstructural and structural characterizations have been carried out. The results have been compared to a pristine DL LPNO electrode on GDC and to a thermally aged single-layer (SL) ESD electrode on GDC (after heat treatment at 700 °C for 1000 h in the air) to investigate the effect of polarization on the LPNO degradation. SEM observations on the cross-sections of cells operated in electrolysis mode (SCell-anodic and CCell 1) show that there is no delamination of the LPNO electrode. The comparison of the microstructural properties between the pristine cell and SCell-anodic shows that the microstructure does not change as indicated by similar porosity, mean particle diameter of the LPNO phase, specific surface area, and tortuosity factor of the gas phase. These microstructural properties are extracted from the 3D reconstructions of the electrodes by FIB-SEM tomography. Hence, it can be concluded that operation in electrolysis mode does not change the microstructure of the LPNO electrode, which is in good agreement with the electrochemical characterizations. On the contrary, severe delamination of the LPNO electrode is observed from the SEM image of SCell-cathodic explaining the strong degradation on the electrode performance obtained in this fuel cell operating mode.

---

The structural characterizations by synchrotron-based  $\mu$ -XRD and  $\mu$ -XRF have also been conducted on the pristine cell, thermally-aged cell, SCell-anodic, and CCell 1. This technique enables the depth profiling on the distribution of elements and phases, thus it is useful for a multi-layer sample such as the double-layer electrode. In agreement with the laboratory XRD results, the characterizations on the pristine double-layer electrode have revealed the presence of LPNO on both ESD and SP layers, while (LP)3N2 was found only in the ESD layer. However, another phase, praseodymium oxide  $\text{Pr}_6\text{O}_{11}$ , was also observed on both layers. This phase was never detected in laboratory XRD due to its small quantity and its peak position that is very close to the strong peak of GDC. After thermal aging, the phases present in the ESD layer are the same as in a pristine cell (LPNO, (LP)3N2,  $\text{Pr}_6\text{O}_{11}$ ). However, the quantity of the secondary phases slightly increases indicating a slow destabilization of LPNO solely under temperature. The characterizations on both SCell-anodic and CCell 1 have shown that a new higher-order nickelate phase,  $(\text{La,Pr})_4\text{Ni}_3\text{O}_{10-\delta}$  or (LP)4N3, was formed after an operation in the electrolysis mode, indicating a strong destabilization of LPNO under current. Besides, the amount of (LP)3N2 and  $\text{Pr}_6\text{O}_{11}$  secondary phases after electrochemical aging are also significantly increased. Nevertheless, since all these phases are electrochemically active, they should not affect the electrode performances despite of the LPNO chemical destabilization. Finally, no reactivity between LPNO and GDC or YSZ was observed. To conclude, all these results are consistent and explain the electrode stability in performances upon electrolysis operation.

Since lamella of SCell-cathodic is difficult to prepare due to the delamination, the structural characterization of this sample has been only carried out by laboratory XRD. Surprisingly, the same compounds as in the SCell-anodic and CCell 1 were present. However, since delamination was observed in this SCell-cathodic sample, it can be proposed that the amount of the secondary phases is larger and more concentrated close to the LPNO/GDC interface. This behavior could be explained by the nature of LPNO which contains oxygen over-stoichiometry in its lattice; thus, in reducing atmosphere such as in fuel cell operation, the number of interstitial oxygens in the electrode is expected to decrease. Consequently, that could accelerate the structure destabilization (and vice versa in electrolysis operation). The second possible origin of the phase delamination could be the structural transition from  $\text{Pr}_6\text{O}_{11}$  to  $\text{Pr}_7\text{O}_{12}$  that could take place in the vicinity of the interface in reducing atmosphere during the oxygen reduction reaction. To conclude, the suitability of  $\text{LaPrNiO}_{4+\delta}$  (LPNO) as a durable oxygen electrode for electrolysis cell has been proved to be promising.

---

## Perspectives

In this PhD thesis, architecturally designed  $\text{La}_{2-x}\text{Pr}_x\text{NiO}_{4+\delta}$  ( $x = 1$ , LPNO) oxygen electrodes deposited by ESD and SP on  $\text{Ce}_{0.9}\text{Gd}_{0.1}\text{O}_{2-\delta}$  (GDC) electrolyte have been selected as innovative solutions for the next generation of solid oxide electrolysis cells (SOECs). The preparation of LPNO electrode by ESD with specific deposition parameters resulting in porous, nanostructured active functional layer (AFL) with a coral-like microstructure and good adhesion on GDC. Low polarization resistances have been reported thanks to this microstructure, facilitating the oxygen surface exchange and ions diffusion which are fundamental in the oxygen electrode design. However, there are various other types of microstructures that can be prepared by ESD for which promising results have been obtained for the solid oxide cells application. In this work, an attempt to prepare a columnar hierarchical microstructure has been carried out following the excellent electrochemical performances of hierarchically nanostructured LSCF developed by Özden Çelikkilek in her PhD thesis in 2016 in our group. The space between columns would serve as gas channels distributing oxygen to the active zones. This preliminary experiment was not conclusive due to the adhesion issue of the columnar LPNO electrode on the electrolyte. Hence, a more careful study of ESD parameters and the subsequent sintering might be performed to improve the adhesion of the columnar-type LPNO AFL by ESD on GDC electrolyte.

In this work, long-term tests have been performed on cells with a double-layer LPNO oxygen electrode. From the optimization of the electrode design, it is found out that the best electrochemical performance of LPNO is obtained for a triple-layer electrode characterized by a GDC/LPNO composite interface where screen-printed large grains of the ionic conductor GDC are in intimate contact with electrostatically-sprayed nanostructured grains of LPNO. For future works, long-term tests on the triple-layer electrode are suggested to investigate the influence of the electrode/electrolyte interface design on the durability.

A possible extension of this work could be to consider the durability study versus Pr substitution in the  $\text{La}_{2-x}\text{Pr}_x\text{NiO}_{4+\delta}$  ( $0 \leq x \leq 1$ ) solid solution system benefiting from the best chemical stability properties of La.

Since the final chemical phases detected in post-mortem characterizations of LPNO aged in electrolysis and fuel cell modes are found to be  $(\text{La,Pr})_4\text{Ni}_3\text{O}_{10-\delta}$  and  $\text{Pr}_6\text{O}_{11}$ , it would be worth to investigate the durability of SOCs incorporating these MIEC phases as oxygen electrodes.

As discussed in this work, the long-term test on the complete cell level is still on a preliminary stage, it is especially important to address the poor performance of the cell as indicated by a rather low current density which is not expected due to the excellent performance of the LPNO electrode in symmetrical cell level.

Unlike the widely studied under-stoichiometric LSCF, the behavior of the over-stoichiometric LPNO electrode in operation is different as indicated by a slow degradation in electrolysis operation and fast degradation in fuel cell operation as opposed to LSCF. Moreover, the LPNO electrode is shown to chemically destabilize into the same compounds in both electrolysis and fuel cell operations. One can propose to study and understand the underlying mechanisms of the LPNO electrode durability (in terms of delamination and chemical stability) in a *complete fuel cell* configuration. It would be of great interest to conduct a comparative study of the mechanism of phases formation, their distribution in the electrode, and their effect on the cell performance with this work on the LPNO durability in an electrolysis mode. Finally, a physically-based electrode model could be developed at the microscopic length scale and simulations could be conducted as a guide to analyze the role of microstructure, structure and the relationship between electrode reaction mechanisms and the degradation phenomena. This facet will thus aim at proposing practical solutions for SOC technology.

---

**REFERENCES**

- [1] C. W. Team, R. K. Pachauri, and L. A. Meyer, Eds., *Climate Change 2014: Synthesis Report. Contribution of Working Groups I, II and III to the Fifth Assessment Report of the Intergovernmental Panel on Climate Change*. Geneva, Switzerland: IPCC, 2014.
- [2] D. P. van Vuuren *et al.*, “The representative concentration pathways: An overview,” *Clim. Change*, vol. 109, pp. 5–31, 2011, doi: 10.1007/s10584-011-0148-z.
- [3] F. Orecchini, “The era of energy vectors,” *Int. J. Hydrogen Energy*, vol. 31, no. 14, pp. 1951–1954, 2006, doi: 10.1016/j.ijhydene.2006.01.015.
- [4] I. Dincer and C. Acar, “Review and evaluation of hydrogen production methods for better sustainability,” *Int. J. Hydrogen Energy*, vol. 40, no. 34, pp. 11094–11111, 2015, doi: 10.1016/j.ijhydene.2014.12.035.
- [5] O. Bičáková and P. Straka, “Production of hydrogen from renewable resources and its effectiveness,” *Int. J. Hydrogen Energy*, vol. 37, no. 16, pp. 11563–11578, 2012, doi: 10.1016/j.ijhydene.2012.05.047.
- [6] I. Dincer, “Green methods for hydrogen production,” *Int. J. Hydrogen Energy*, vol. 37, no. 2, pp. 1954–1971, 2012, doi: 10.1016/j.ijhydene.2011.03.173.
- [7] S. Mekhilef, R. Saidur, and A. Safari, “Comparative study of different fuel cell technologies,” *Renew. Sustain. Energy Rev.*, vol. 16, no. 1, pp. 981–989, 2012, doi: 10.1016/j.rser.2011.09.020.
- [8] N. Mahato, A. Banerjee, A. Gupta, S. Omar, and K. Balani, “Progress in material selection for solid oxide fuel cell technology: A review,” *Prog. Mater. Sci.*, vol. 72, pp. 141–337, 2015, doi: 10.1016/j.pmatsci.2015.01.001.
- [9] A. J. Appleby, “Fuel cell technology: Status and future prospects,” *Energy*, vol. 21, no. 7/8, pp. 521–653, 1996, doi: 10.1016/0360-5442(96)00030-8.
- [10] A. B. Stambouli, “Fuel cells : The expectations for an environmental-friendly and sustainable source of energy,” *Renew. Sustain. Energy Rev.*, vol. 15, no. 9, pp. 4507–4520, 2011, doi: 10.1016/j.rser.2011.07.100.
- [11] S. P. S. Badwal, S. Giddey, C. Munnings, and A. Kulkarni, “Review of progress in high temperature solid oxide fuel cells,” *J. Aust. Ceram. Soc.*, vol. 50, no. 1, pp. 23–37, 2014.
- [12] P. E. Dodds *et al.*, “Hydrogen and fuel cell technologies for heating: A review,” *Int. J.*

- Hydrogen Energy*, vol. 40, no. 5, pp. 2065–2083, 2015, doi: 10.1016/j.ijhydene.2014.11.059.
- [13] N. Q. Minh, “Solid oxide fuel cell technology - features and applications,” *Solid State Ionics*, vol. 174, no. 1–4, pp. 271–277, 2004, doi: 10.1016/j.ssi.2004.07.042.
- [14] Y. Zhao *et al.*, “Recent progress on solid oxide fuel cell: Lowering temperature and utilizing non-hydrogen fuels,” *Int. J. Hydrogen Energy*, vol. 38, no. 36, pp. 16498–16517, 2013, doi: 10.1016/j.ijhydene.2013.07.077.
- [15] E. D. Wachsman and K. T. Lee, “Lowering the temperature of solid oxide fuel cells,” *Sci.*, vol. 334, no. 6058, pp. 935–939, 2011, doi: 10.1126/science.1204090.
- [16] B. C. H. Steele, “Appraisal of Ce<sub>1-y</sub>Gd<sub>y</sub>O<sub>2-y/2</sub> electrolytes for IT-SOFC operation at 500°C,” *Solid State Ionics*, vol. 129, no. 1–4, pp. 95–110, 2000, doi: 10.1016/S0167-2738(99)00319-7.
- [17] L. J. Gauckler *et al.*, “Solid oxide fuel cells: Systems and materials,” *Chim.*, vol. 58, no. 12, pp. 837–850, 2004.
- [18] G. Constantin, C. Rossignol, J. P. Barnes, and E. Djurado, “Interface stability of thin, dense CGO film coating on YSZ for solid oxide fuel cells,” *Solid State Ionics*, vol. 235, pp. 36–41, 2013, doi: 10.1016/j.ssi.2013.01.015.
- [19] S. Takahashi, S. Nishimoto, M. Matsuda, and M. Miyake, “Electrode properties of the Ruddlesden-Popper series, Lan+1NinO3n+1 (n = 1, 2, and 3), as intermediate-temperature solid oxide fuel cells,” *J. Am. Ceram. Soc.*, vol. 93, no. 8, pp. 2329–2333, 2010, doi: 10.1111/j.1551-2916.2010.03743.x.
- [20] H. Zhao, F. Mauvy, C. Lalanne, J. M. Bassat, S. Fourcade, and J. C. Grenier, “New cathode materials for ITSOFC: Phase stability, oxygen exchange and cathode properties of La<sub>2-x</sub>NiO<sub>4+δ</sub>,” *Solid State Ionics*, vol. 179, no. 35–36, pp. 2000–2005, 2008, doi: 10.1016/j.ssi.2008.06.019.
- [21] G. Amow and S. J. Skinner, “Recent developments in Ruddlesden-Popper nickelate systems for solid oxide fuel cell cathodes,” *J. Solid State Electrochem.*, vol. 10, pp. 538–546, 2006, doi: 10.1007/s10008-006-0127-x.
- [22] V. Vibhu, A. Rougier, C. Nicollet, A. Flura, J. C. Grenier, and J. M. Bassat, “La<sub>2-x</sub>Pr<sub>x</sub>NiO<sub>4+δ</sub> as suitable cathodes for metal supported SOFCs,” *Solid State Ionics*, vol. 278, pp. 32–37, 2015, doi: 10.1016/j.ssi.2015.05.005.

- 
- [23] S. B. Adler, “Factors governing oxygen reduction in solid oxide fuel cell cathodes,” *Chem. Rev.*, vol. 104, no. 10, pp. 4791–4843, 2004, doi: 10.1021/cr020724o.
- [24] Y. Takeda, R. Kanno, M. Noda, Y. Tomida, and O. Yamamoto, “Cathodic polarization phenomena of perovskite oxide electrodes with stabilized zirconia,” *J. Electrochem. Soc.*, vol. 134, no. 11, pp. 2656–2661, 1987.
- [25] J. Laurencin and J. Mougin, “High Temperature Steam Electrolysis,” in *Hydrogen Production by Electrolysis*, Wiley-VCH, 2015, pp. 191–272.
- [26] C. Lefrou, P. Fabry, and J.-C. Poignet, *Electrochemistry: The Basics, with Examples*. Berlin Heidelberg: Springer-Verlag, 2012.
- [27] V. S. Bagotsky, *Fundamentals of Electrochemistry*, Second Edi. Hoboken, New Jersey: John Wiley & Sons, Inc., 2006.
- [28] V. Ramani, “Fuel Cells,” *Electrochem. Soc. Interface*, pp. 41–44, 2006.
- [29] S. B. Adler, J. A. Lane, and B. C. H. Steele, “Electrode kinetics of porous mixed-conducting oxygen electrodes,” *J. Electrochem. Soc.*, vol. 143, no. 11, pp. 3554–3564, 1996, doi: 10.1149/1.1837252.
- [30] S. N. Ruddlesden and P. Popper, “The compound  $\text{Sr}_3\text{Ti}_2\text{O}_7$  and its structure,” *Acta Crystallogr.*, vol. 11, no. 1, pp. 54–55, 1958, doi: 10.1107/s0365110x58000128.
- [31] M. Greenblatt, “Ruddlesden-Popper  $\text{Ln}_{n+1}\text{Ni}_n\text{O}_{3n+1}$  nickelates: Structure and properties,” *Curr. Opin. Solid State Mater. Sci.*, vol. 2, no. 2, pp. 174–183, 1997, doi: 10.1016/s1359-0286(97)80062-9.
- [32] A. Tarancón, M. Burriel, J. Santiso, S. J. Skinner, and J. A. Kilner, “Advances in layered oxide cathodes for intermediate temperature solid oxide fuel cells,” *J. Mater. Chem.*, vol. 20, pp. 3799–3813, 2010, doi: 10.1039/b922430k.
- [33] K. Yakal-Kremiski, L. V. Mogni, A. Montenegro-Hernández, A. Caneiro, and S. A. Barnett, “Determination of electrode oxygen transport kinetics using electrochemical impedance spectroscopy combined with three-dimensional microstructure measurement: Application to  $\text{Nd}_2\text{NiO}_{4+\delta}$ ,” *J. Electrochem. Soc.*, vol. 161, no. 14, pp. F1366–F1374, 2014, doi: 10.1149/2.0521414jes.
- [34] G. Amow, I. J. Davidson, and S. J. Skinner, “A comparative study of the Ruddlesden-Popper series,  $\text{La}_{n+1}\text{Ni}_n\text{O}_{3n+1}$  ( $n = 1, 2$  and  $3$ ), for solid-oxide fuel-cell cathode
-

- applications,” *Solid State Ionics*, vol. 177, no. 13–14, pp. 1205–1210, 2006, doi: 10.1016/j.ssi.2006.05.005.
- [35] R. K. Sharma, S. K. Cheah, M. Burriel, L. Dessemond, J. M. Bassat, and E. Djurado, “Design of  $\text{La}_{2-x}\text{Pr}_x\text{NiO}_{4+\delta}$  SOFC cathodes: A compromise between electrochemical performance and thermodynamic stability,” *J. Mater. Chem. A*, vol. 5, pp. 1120–1132, 2017, doi: 10.1039/c6ta08011a.
- [36] V. Vibhu, J.-M. Bassat, A. Flura, C. Nicollet, J.-C. Grenier, and A. Rougier, “Influence of La/Pr ratio on the ageing properties of  $\text{La}_{2-x}\text{Pr}_x\text{NiO}_{4+}$  as cathodes in IT-SOFCs,” *ECS Trans.*, vol. 68, no. 1, pp. 825–835, 2015, doi: 10.1149/06801.0825ecst.
- [37] A. Montenegro-Hernández, J. Vega-Castillo, L. Moggi, and A. Caneiro, “Thermal stability of  $\text{Ln}_2\text{NiO}_{4+\delta}$  (Ln: La, Pr, Nd) and their chemical compatibility with YSZ and CGO solid electrolytes,” *Int. J. Hydrogen Energy*, vol. 36, no. 24, pp. 15704–15714, 2011, doi: 10.1016/j.ijhydene.2011.08.105.
- [38] S. Nishimoto, S. Takahashi, Y. Kameshima, M. Matsuda, and M. Miyake, “Properties of  $\text{La}_{2-x}\text{Pr}_x\text{NiO}_4$  cathode for intermediate-temperature solid oxide fuel cells,” *J. Ceram. Soc. Japan*, vol. 119, no. 1387, pp. 246–250, 2011, doi: 10.2109/jcersj2.119.246.
- [39] A. J. Jacobson, “New Cathode Materials for Intermediate Temperature Solid Oxide Fuel Cells,” University of Houston, 2004.
- [40] J. C. Park, D. K. Kim, S. H. Byeon, and D. Kim, “XANES study on Ruddlesden-Popper phase,  $\text{La}_{n+1}\text{Ni}_n\text{O}_{3n+1}$  ( $n = 1, 2$  and  $\infty$ ),” *J. Synchrotron Radiat.*, vol. 8, no. 2, pp. 704–706, 2001, doi: 10.1107/S0909049500015983.
- [41] Z. Lou *et al.*, “High performance  $\text{La}_3\text{Ni}_2\text{O}_7$  cathode prepared by a facile sol-gel method for intermediate temperature solid oxide fuel cells,” *Electrochem. commun.*, vol. 22, pp. 97–100, 2012, doi: 10.1016/j.elecom.2012.06.004.
- [42] R. K. Sharma, M. Burriel, and E. Djurado, “ $\text{La}_4\text{Ni}_3\text{O}_{10-\delta}$  as an efficient solid oxide fuel cell cathode: Electrochemical properties versus microstructure,” *J. Mater. Chem. A*, vol. 3, pp. 23833–23843, 2015, doi: 10.1039/C5TA07862H.
- [43] R. K. Sharma, M. Burriel, L. Dessemond, J.-M. Bassat, and E. Djurado, “ $\text{La}_{n+1}\text{Ni}_n\text{O}_{3n+1}$  ( $n = 2$  and  $3$ ) phases and composites for solid oxide fuel cell cathodes: Facile synthesis and electrochemical properties,” *J. Power Sources*, vol. 325, pp. 337–345, 2016, doi: 10.1016/j.jpowsour.2016.06.047.

- 
- [44] Y. Wang, W. Li, L. Ma, W. Li, and X. Liu, “Degradation of solid oxide electrolysis cells: phenomena, mechanisms, and emerging mitigation strategies – a review,” *J. Mater. Sci. Technol.*, 2019, doi: 10.1016/j.jmst.2019.07.026.
- [45] J. Laurencin *et al.*, “Degradation mechanism of  $\text{La}_{0.6}\text{Sr}_{0.4}\text{Co}_{0.2}\text{Fe}_{0.8}\text{O}_{3-\delta}/\text{Gd}_{0.1}\text{Ce}_{0.9}\text{O}_{2-\delta}$  composite electrode operated under solid oxide electrolysis and fuel cell conditions,” *Electrochim. Acta*, vol. 241, pp. 459–476, 2017, doi: 10.1016/j.electacta.2017.05.011.
- [46] T. L. Skafte, J. Hjelm, P. Blennow, and C. R. Graves, “Quantitative review of degradation and lifetime of solid oxide cells and stacks,” in *Proceedings of 12th European SOFC & SOE Forum 2016*, 2016, no. B0501, pp. 8–27.
- [47] Q. Fang, L. Blum, and D. Stolten, “Electrochemical performance and degradation analysis of an SOFC short stack for operation of more than 100,000 hours,” *ECS Trans.*, vol. 91, no. 1, pp. 687–696, 2019, doi: 10.1149/09101.0687ecst.
- [48] S. J. Kim, K. J. Kim, A. M. Dayaghi, and G. M. Choi, “Polarization and stability of  $\text{La}_2\text{NiO}_{4+\delta}$  in comparison with  $\text{La}_{0.6}\text{Sr}_{0.4}\text{Co}_{0.2}\text{Fe}_{0.8}\text{O}_{3-\delta}$  as air electrode of solid oxide electrolysis cell,” *Int. J. Hydrogen Energy*, vol. 41, no. 33, pp. 14498–14506, 2016, doi: 10.1016/j.ijhydene.2016.05.284.
- [49] N. Coppola *et al.*, “Structural and electrical characterization of sputter-deposited  $\text{Gd}_{0.1}\text{Ce}_{0.9}\text{O}_{2-\delta}$  thin buffer layers at the Y-stabilized zirconia electrolyte interface for IT-solid oxide cells,” *Catalysts*, vol. 8, no. 12, 2018, doi: 10.3390/catal8120571.
- [50] A. Shutka, G. Mezinskis, and A. Pludons, “Preparation of dissimilarly structured ferrite compounds by sol-gel auto-combustion method,” *Chemine Technol.*, vol. 54, no. 1, pp. 41–46, 2010.
- [51] L. Shi, C. Zeng, Y. Jin, T. Wang, and N. Tsubaki, “A sol-gel auto-combustion method to prepare Cu/ZnO catalysts for low-temperature methanol synthesis,” *Catal. Sci. Technol.*, vol. 2, pp. 2569–2577, 2012, doi: 10.1039/c2cy20423a.
- [52] C. Chen, “Thin-Film Components for Lithium-Ion Batteries,” Delft University of Technology, 1998.
- [53] C. H. Chen, E. M. Kelder, M. J. G. Jak, and J. Schoonman, “Electrostatic spray deposition of thin layers of cathode materials for lithium battery,” *Solid State Ionics*, vol. 86–88, no. Part 2, pp. 1301–1306, 1996, doi: 10.1016/0167-2738(96)00305-0.
-

- [54] A. M. Gañán-Calvo, J. M. López-Herrera, M. A. Herrada, A. Ramos, and J. M. Montanero, “Review on the physics of electrospray: From electrokinetics to the operating conditions of single and coaxial Taylor cone-jets, and AC electrospray,” *J. Aerosol Sci.*, vol. 125, pp. 32–56, 2018, doi: 10.1016/j.jaerosci.2018.05.002.
- [55] G. I. Taylor, “Disintegration of water drops in an electric field,” *Proc. R. Soc. Lond. A. Math. Phys. Sci.*, vol. 280, no. 1382, pp. 383–397, 1964, [Online]. Available: <http://rspa.royalsocietypublishing.org/content/royprsa/280/1382/383.full.pdf>.
- [56] J. Russell, “Biosurfactants in electrospinning,” 2015.
- [57] A. M. Gañán-Calvo, J. Davila, and A. Barrero, “Current and droplet size in the electrospraying of liquids. Scaling laws,” *J. Aerosol Sci.*, vol. 28, no. 2, pp. 249–275, 1997.
- [58] D. Marinha, C. Rossignol, and E. Djurado, “Influence of electrospraying parameters on the microstructure of La<sub>0.6</sub>Sr<sub>0.4</sub>Co<sub>0.2</sub>Fe<sub>0.8</sub>O<sub>3-δ</sub> films for SOFCs,” *J. Solid State Chem.*, vol. 182, no. 7, pp. 1742–1748, 2009, doi: 10.1016/j.jssc.2009.04.018.
- [59] T. Nguyen and E. Djurado, “Deposition and characterization of nanocrystalline tetragonal zirconia films using electrostatic spray deposition,” *Solid State Ionics*, vol. 138, no. 3–4, pp. 191–197, 2001, doi: 10.1016/S0167-2738(00)00795-5.
- [60] Özden Çelikkilek, L. Dessemond, and E. Djurado, “State-of-the-art La<sub>0.6</sub>Sr<sub>0.4</sub>Co<sub>0.2</sub>Fe<sub>0.8</sub>O<sub>3-δ</sub> cathode for SOFC: Microstructural and electrochemical properties,” *ECS Trans.*, vol. 78, no. 1, pp. 747–758, 2017, doi: 10.1149/07801.0747ecst.
- [61] R. K. Sharma, M. Burriel, L. Dessemond, J. M. Bassat, and E. Djurado, “Design of interfaces in efficient Ln<sub>2</sub>NiO<sub>4+δ</sub> (Ln = La, Pr) cathodes for SOFC applications,” *J. Mater. Chem. A*, vol. 4, pp. 12451–12462, 2016, doi: 10.1039/c6ta04845e.
- [62] R. K. Sharma *et al.*, “Highly efficient architected Pr<sub>6</sub>O<sub>11</sub> oxygen electrode for solid oxide fuel cell,” *J. Power Sources*, vol. 419, pp. 171–180, 2019, doi: 10.1016/j.jpowsour.2019.02.077.
- [63] R. K. Sharma, M. Burriel, L. Dessemond, V. Martin, J.-M. Bassat, and E. Djurado, “An innovative architectural design to enhance the electrochemical performance of La<sub>2</sub>NiO<sub>4+δ</sub> cathodes for solid oxide fuel cell applications,” *J. Power Sources*, vol. 316, pp. 17–28, 2016, doi: 10.1016/j.jpowsour.2016.03.067.
- [64] L. A. Giannuzzi and F. A. Stevie, “A review of focused ion beam milling techniques for

- TEM specimen preparation,” *Micron*, vol. 30, no. 3, pp. 197–204, 1999, doi: 10.1016/S0968-4328(99)00005-0.
- [65] J. Gierak, “Focused ion beam nano-patterning from traditional applications to single ion implantation perspectives,” *Nanofabrication*, vol. 1, pp. 35–52, 2014, doi: 10.2478/nanofab-2014-0004.
- [66] H. Moussaoui *et al.*, “Stochastic geometrical modeling of solid oxide cells electrodes validated on 3D reconstructions,” *Comput. Mater. Sci.*, vol. 143, pp. 262–276, 2018, doi: 10.1016/j.commatsci.2017.11.015.
- [67] F. Usseglio-Viretta, J. Laurencin, G. Delette, J. Villanova, P. Cloetens, and D. Leguillon, “Quantitative microstructure characterization of a Ni-YSZ bi-layer coupled with simulated electrode polarisation,” *J. Power Sources*, vol. 256, pp. 394–403, 2014, doi: 10.1016/j.jpowsour.2014.01.094.
- [68] J. Laurencin, R. Quey, G. Delette, H. Suhonen, P. Cloetens, and P. Bleuet, “Characterisation of Solid Oxide Fuel Cell Ni-8YSZ substrate by synchrotron X-ray nano-tomography: From 3D reconstruction to microstructure quantification,” *J. Power Sources*, vol. 198, pp. 182–189, 2012, doi: 10.1016/j.jpowsour.2011.09.105.
- [69] O. M. Pecho *et al.*, “3D microstructure effects in Ni-YSZ anodes: Prediction of effective transport properties and optimization of redox stability,” *Materials (Basel)*, vol. 8, no. 9, pp. 5554–5585, 2015, doi: 10.3390/ma8095265.
- [70] J. Rodríguez-Carvajal, “Recent advances in magnetic structure determination by neutron powder diffraction,” *Phys. B*, vol. 192, no. 1–2, pp. 55–69, 1993, doi: 10.1016/0921-4526(93)90108-I.
- [71] M. Hubert *et al.*, “Role of microstructure on electrode operating mechanisms for mixed ionic electronic conductors: From synchrotron-based 3D reconstruction to electrochemical modeling,” *Solid State Ionics*, vol. 294, pp. 90–107, 2016, doi: 10.1016/j.ssi.2016.07.001.
- [72] T. Tao, J. S. Ro, J. Melngailis, Z. Xue, and H. D. Kaesz, “Focused ion beam induced deposition of platinum,” *J. Vac. Sci. Technol. B*, vol. 8, no. 6, p. 1826, 1990, doi: 10.1116/1.585167.
- [73] G. Ashiotis *et al.*, “The fast azimuthal integration Python library: pyFAI,” *J. Appl. Crystallogr.*, vol. 48, pp. 510–519, 2015, doi: 10.1107/S1600576715004306.

- 
- [74] W. De Nolf and K. Janssens, "Micro X-ray diffraction and fluorescence tomography for the study of multilayered automotive paints," *Surf. Interface Anal.*, vol. 42, no. 5, pp. 411–418, 2010, doi: 10.1002/sia.3125.
- [75] W. De Nolf, F. Vanmeert, and K. Janssens, "XRDUa: Crystalline phase distribution maps by two-dimensional scanning and tomographic (micro) X-ray powder diffraction," *J. Appl. Crystallogr.*, vol. 47, no. 3, pp. 1107–1117, 2014, doi: 10.1107/S1600576714008218.
- [76] E. Barsoukov and J. R. Macdonald, Eds., *Impedance Spectroscopy: Theory, Experiment, and Applications*, Second Edi. Hoboken, New Jersey: John Wiley & Sons, Inc., 2005.
- [77] D. Vladikova, "The technique of the differential impedance analysis part I: Basics of the impedance spectroscopy," in *Proceedings of the International Workshop "Advanced Techniques for Energy Sources Investigation and Testing,"* 2004, pp. L8-1-L8-28, [Online]. Available: <https://pdfs.semanticscholar.org/b6ac/e8d1aba6e3e917b590045eacdc6352746b38.pdf>.
- [78] M. R. Somalu, A. Muchtar, W. R. W. Daud, and N. P. Brandon, "Screen-printing inks for the fabrication of solid oxide fuel cell films: A review," *Renew. Sustain. Energy Rev.*, vol. 75, pp. 426–439, 2017, doi: 10.1016/j.rser.2016.11.008.
- [79] M. Wegener, M. Kato, K. Kakimoto, S. Spallek, E. Spiecker, and A. Roosen, "PVP a binder for the manufacture of ultrathin ITO/polymer nanocomposite films with improved electrical conductivity," *J. Mater. Sci.*, vol. 50, pp. 6124–6133, 2015, doi: 10.1007/s10853-015-9168-9.
- [80] D. Marinha, L. Dessemond, and E. Djurado, "Electrochemical investigation of oxygen reduction reaction on  $\text{La}_{0.6}\text{Sr}_{0.4}\text{Co}_{0.2}\text{Fe}_{0.8}\text{O}_{3-\delta}$  cathodes deposited by electrostatic spray deposition," *J. Power Sources*, vol. 197, pp. 80–87, 2012, doi: 10.1016/j.jpowsour.2011.09.049.
- [81] Özden Çelikbilek, "Optimisation de la cathode pour pile à oxyde électrolyte solide: approches expérimentale et numérique," Université Grenoble Alpes, 2016.
- [82] D. Marinha, J. Hayd, L. Dessemond, E. Ivers-Tiffée, and E. Djurado, "Performance of  $(\text{La,Sr})(\text{Co,Fe})\text{O}_{3-x}$  double-layer cathode films for intermediate temperature solid oxide fuel cell," *J. Power Sources*, vol. 196, no. 11, pp. 5084–5090, 2011, doi: 10.1016/j.jpowsour.2011.01.063.
-

- 
- [83] F. Ciucci, “Modeling electrochemical impedance spectroscopy,” *Curr. Opin. Electrochem.*, vol. 13, pp. 132–139, 2019, doi: 10.1016/j.coelec.2018.12.003.
- [84] W. Lai and S. M. Haile, “Impedance spectroscopy as a tool for chemical and electrochemical analysis of mixed conductors: A case study of ceria,” *J. Am. Ceram. Soc.*, vol. 88, no. 11, pp. 2979–2997, 2005, doi: 10.1111/j.1551-2916.2005.00740.x.
- [85] Özden Çelikbilek, E. Siebert, D. Jauffrès, C. L. Martin, and E. Djurado, “Influence of sintering temperature on morphology and electrochemical performance of LSCF/GDC composite films as efficient cathode for SOFC,” *Electrochim. Acta*, vol. 246, pp. 1248–1258, 2017, doi: 10.1016/j.electacta.2017.06.070.
- [86] J. Fleig, “On the current-voltage characteristics of charge transfer reactions at mixed conducting electrodes on solid electrolytes,” *Phys. Chem. Chem. Phys.*, vol. 7, no. 9, pp. 2027–2037, 2005, doi: 10.1039/b501086a.
- [87] B. A. Boukamp, “Electrochemical impedance spectroscopy in solid state ionics: Recent advances,” *Solid State Ionics*, vol. 169, no. 1–4, pp. 65–73, 2004, doi: 10.1016/j.ssi.2003.07.002.
- [88] T. Jacobsen, P. V. Hendriksen, and S. Koch, “Diffusion and conversion impedance in solid oxide fuel cells,” *Electrochim. Acta*, vol. 53, no. 25, pp. 7500–7508, 2008, doi: 10.1016/j.electacta.2008.02.019.
- [89] C. Chen, E. M. Kelder, P. J. J. M. van der Put, and J. Schoonman, “Morphology control of thin LiCoO<sub>2</sub> films fabricated using the electrostatic spray deposition (ESD) technique,” *J. Mater. Chem.*, vol. 6, no. 5, pp. 765–771, 1996, doi: 10.1039/JM9960600765.
- [90] P. Li *et al.*, “A novel La<sub>2</sub>NiO<sub>4+δ</sub>-La<sub>3</sub>Ni<sub>2</sub>O<sub>7-δ</sub>-Ce<sub>0.55</sub>La<sub>0.45</sub>O<sub>2-δ</sub> ternary composite cathode prepared by the co-synthesis method for IT-SOFCs,” *Int. J. Hydrogen Energy*, vol. 42, no. 27, pp. 17202–17210, 2017, doi: 10.1016/j.ijhydene.2017.05.202.
- [91] F. Zurlo *et al.*, “La<sub>0.8</sub>Sr<sub>0.2</sub>Fe<sub>0.8</sub>Cu<sub>0.2</sub>O<sub>3-δ</sub> as ‘cobalt-free’ cathode for La<sub>0.8</sub>Sr<sub>0.2</sub>Ga<sub>0.8</sub>Mg<sub>0.2</sub>O<sub>3-δ</sub> electrolyte,” *J. Power Sources*, vol. 271, pp. 187–194, 2014, doi: 10.1016/j.jpowsour.2014.07.183.
- [92] R. J. Woolley and S. J. Skinner, “Novel La<sub>2</sub>NiO<sub>4+δ</sub> and La<sub>4</sub>Ni<sub>3</sub>O<sub>10-δ</sub> composites for solid oxide fuel cell cathodes,” *J. Power Sources*, vol. 243, pp. 790–795, 2013, doi: 10.1016/j.jpowsour.2013.06.106.
-

- 
- [93] M. Cimenti, A. C. Co, V. I. Birss, and J. M. Hill, “Distortions in electrochemical impedance spectroscopy measurements using 3-electrode methods in SOFC. I-effect of cell geometry,” *Fuel Cells*, vol. 7, no. 5, pp. 364–376, 2007, doi: 10.1002/fuce.200700019.
- [94] A. Hauch, S. H. Jensen, S. Ramousse, and M. B. Mogensen, “Performance and durability of solid oxide electrolysis cells,” *J. Electrochem. Soc.*, vol. 153, no. 9, pp. A1741–A1747, 2006, doi: 10.1149/1.2216562.
- [95] J. Hjelm, M. Søggaard, M. Wandel, M. Menon, M. B. Mogensen, and A. Hagen, “Electrochemical impedance studies of SOFC cathodes,” *ECS Trans.*, vol. 7, no. 1, pp. 1261–1270, 2007, doi: 10.1149/1.2729227.
- [96] G. Chiodelli and L. Malavasi, “Electrochemical open circuit voltage (OCV) characterization of SOFC materials,” *Ionics (Kiel)*, vol. 19, pp. 1135–1144, 2013, doi: 10.1007/s11581-013-0843-z.
- [97] M. A. Laguna-Bercero, “Recent advances in high temperature electrolysis using solid oxide fuel cells: A review,” *J. Power Sources*, vol. 203, pp. 4–16, 2012, doi: 10.1016/j.jpowsour.2011.12.019.
- [98] A. Bertei, G. Arcolini, J. P. Ouweltjes, Z. Wuillemin, P. Piccardo, and C. Nicolella, “Physically-based deconvolution of impedance spectra: Interpretation, fitting and validation of a numerical model for lanthanum strontium cobalt ferrite-based solid oxide fuel cells,” *Electrochim. Acta*, vol. 208, pp. 129–141, 2016, doi: 10.1016/j.electacta.2016.04.181.
- [99] V. Thangadurai, R. A. Huggins, and W. Weppner, “Mixed ionic-electronic conductivity in phases in the praseodymium oxide system,” *J. Solid State Electrochem.*, vol. 5, pp. 531–537, 2001, doi: 10.1007/s100080000187.
- [100] B. M. Abu-Zied, Y. A. Mohamed, and A. M. Asiri, “Fabrication, characterization, and electrical conductivity properties of Pr<sub>6</sub>O<sub>11</sub> nanoparticles,” *J. Rare Earths*, vol. 31, no. 7, pp. 701–708, 2013, doi: 10.1016/S1002-0721(12)60345-7.
- [101] S. Shrestha, C. M. Y. Yeung, C. Nunnerley, and S. C. Tsang, “Comparison of morphology and electrical conductivity of various thin films containing nano-crystalline praseodymium oxide particles,” *Sensors Actuators A*, vol. 136, no. 1, pp. 191–198, 2007, doi: 10.1016/j.sna.2006.11.019.
-

- 
- [102] J. Schefold, A. Brisse, and H. Poepke, “23,000 h steam electrolysis with an electrolyte supported solid oxide cell,” *Int. J. Hydrogen Energy*, vol. 42, no. 19, pp. 13415–13426, 2017, doi: 10.1016/j.ijhydene.2017.01.072.
- [103] F. Tietz, D. Sebold, A. Brisse, and J. Schefold, “Degradation phenomena in a solid oxide electrolysis cell after 9000 h of operation,” *J. Power Sources*, vol. 223, pp. 129–135, 2013, doi: 10.1016/j.jpowsour.2012.09.061.
- [104] V. Vibhu, “Stability and ageing studies of Praseodymium-based nickelates as cathodes for Solid Oxide Fuel Cells,” Université de Bordeaux, 2016.
- [105] B. G. Hyde, D. J. M. Bevan, and L. Eyring, “On the praseodymium+oxygen system,” *Philos. Trans. R. Soc. A*, vol. 259, no. 1106, pp. 583–614, 1966, doi: 10.1098/rsta.1966.0025.
- [106] B. J. Inkson, “Scanning electron microscopy (SEM) and transmission electron microscopy (TEM) for materials characterization,” in *Materials Characterization Using Nondestructive Evaluation (NDE) Methods*, Elsevier Ltd, 2016, pp. 17–43.
- [107] B. D. Cullity, *Elements Of X-Ray Diffraction*. Addison-Wesley Publishing Company, Inc., 1956.
- [108] S. T. Misture, “In situ X-ray diffraction studies of electroceramics,” *J. Electroceramics*, vol. 16, pp. 167–178, 2006, doi: 10.1007/s10832-006-6202-y.

**APPENDIX A: Scanning electron microscopy**

Scanning electron microscopy (SEM) has become in 50 years an indispensable tool in the exploration of the "infinitely small". It is a technique that produces images of a sample by scanning the surface with a focused beam of electrons. The interaction of the electron beam with the atoms in the sample produces various signals which give information on the topography and composition of the analyzed sample. The schematic illustration of SEM set-up is shown in **Fig. A.1a**. The electron beam is produced by an electron gun located on the topmost part of the set-up. There are several types of an electron gun, namely thermionic gun in which thermal energy is applied on a filament made of materials with high melting point (e.g. tungsten) to emit electrons and field emission gun (FEG) where the electrons are extracted by a strong electric field. There are two kinds of FEG SEM; the first one called the cold cathode which works at room temperature with an extremely fine tungsten (W) tip and the second one called Schottky cathode in which the tungsten tip is thermally activated and covered by ZrO<sub>2</sub> coating. The emitted electron beam is then focused by utilizing condenser and objective lenses. These lenses produce a magnetic field to focus the beam at the surface of the sample at a certain focal distance with the smallest spot size if the resolution is expected. Following the development on the resolution of SEM, the resolution of a FEG is now around 1 nm and can be decreased until 0.5 nm. The beam scans the surface of the sample by a deflection of the electron paths using a series of scanning coils present in the column and mostly inside the objective lens. The focused electron beam with energy in the range of 0.2 to 40 keV is then entered the sample chamber. The sample chamber is under a secondary vacuum to prevent interaction between the electron beam and the air molecules. In the sample chamber, several detectors are placed to record the signals coming from the interactions between the electron beam and the atoms in the sample.

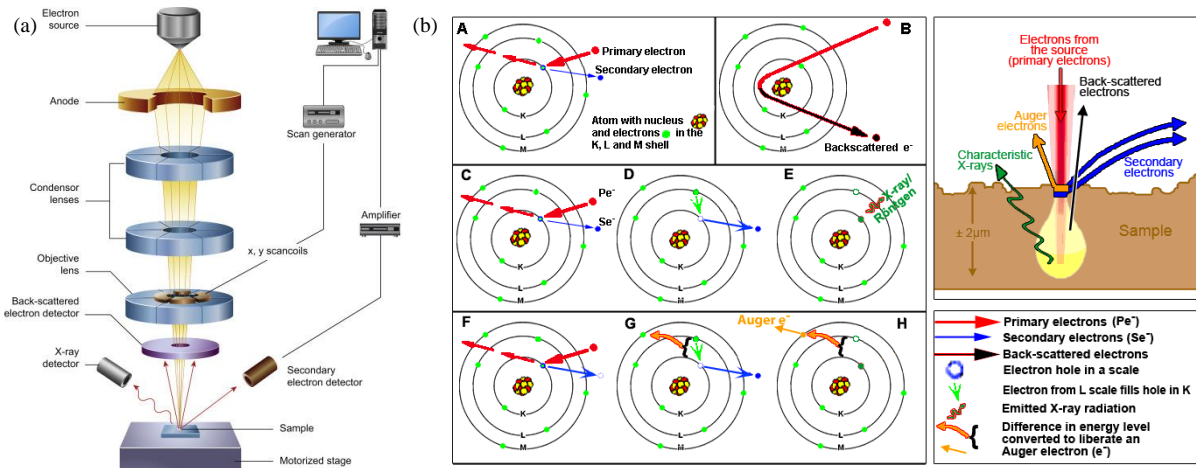


**Fig. A.1** (a) The schematic illustration of SEM set-up (Inkson, 2016) [106] and (b) the various interactions between the electron beams and the atoms in the sample (from <https://www.vcbio.science.ru.nl/en/fesem/eds/>).

**Fig. A.1b** shows the various interactions between the electron beam and the sample. Panel A shows the penetration of the electron beam (referred to as the primary electrons) in the electron shell of the atoms. The energy of these primary electrons is able to eject the electrons due to an inelastic interaction from the shell close to the surface of the analyzed sample. These emitted electrons are called secondary electrons (SE). The number of emitted secondary electrons is directly related to the topography of the sample because the escape distance is less than 10 nm from the surface, thus the secondary electron detection is used to reconstruct the topographical image of the sample surface. In panel B, back-scattered electrons (BSE) from the elastic scattering of the primary electrons are shown. This scattering happens at deeper locations, around 10-100 nm depth, from the sample surface. Elastic scattering occurs when the kinetic energy of the electrons is conserved upon interaction, but the propagation direction is modified. The resolution of BSE images is not as good as SE images because the emission area of BSE is larger than SE. However, BSE is directly correlated to the atomic number of the sample. Thus, BSE images can be used to observe the distribution of different elements or phases present in the sample. However, the identity of the elements cannot be concluded from BSE images. Panels C, D, E show that when the electrons inner electron shells are ejected by the primary electrons, electrons at higher energy levels can fill the electron holes on that inner shells and release energy. The released energy can be in the form of either light or X-ray and called characteristic light (cathodoluminescence, CL) and X-ray, respectively. CL can be used for high-resolution optical imaging of the sample. The energy of characteristic X-ray is specific

for each chemical element; thus it can be used to identify and quantify the elements present in the sample by coupling SEM with energy-dispersive X-ray spectroscopy (EDX). Lastly, panels F, G, H show the energy release due to the emission of Auger electrons which occurs very close to the sample surface. Auger electrons are ejected from the outer electron shells due to the energy from the filling of electron holes described previously. The released energy is also characteristic of each atom.

**APPENDIX B: Laboratory X-ray diffraction (XRD): room temperature and *in-situ* XRD**

X-ray diffraction (XRD) is an analytical and non-destructive technique to identify the atomic and molecular structure of a crystalline phase. It provides information on the identity and quantity of phases in the sample. The structural parameters such as crystallite size, crystallinity, strain, and crystal defects can also be obtained. XRD can also be used to observe the preferred texture (crystal orientation).

The principle of XRD is based on the diffraction of an incident beam upon interaction with well-ordered atoms in a crystal to many specific directions. X-rays are waves of electromagnetic radiation and thus, it is scattered upon interaction with atoms through elastic scattering. It means that the waves are scattered in all directions as secondary waves which have the same kinetic energy, thus, the same wavelength, as the incident X-ray waves. The scattered waves cancel each other out in most directions due to the destructive interference, except in a few specific directions where they interfere constructively and increase the intensity. These specific directions are determined by the so-called Bragg's Law:

$$2d_{hkl} \sin \theta = n\lambda \quad (\text{Eq. B.1})$$

In this equation,  $d_{hkl}$  is the interplanar distance,  $\theta$  is the angle of the incident beam with respect to the  $hkl$  lattice planes or also called diffraction angle,  $n$  is an integer number, and  $\lambda$  is the wavelength of the X-ray beam. The graphical illustration behind the explanation of this equation is presented in **Fig. B.1a**. To begin the explanation, it is important to first understand about the crystal itself. Crystal is defined as a solid composed of three-dimensional periodic patterns of atoms [107]. In crystallography, crystal is built up on a framework consisting of a set of imaginary points that has a fixed relation in space to the actual atoms in the crystal. Each point has identical surroundings and is called as point lattice. These points are arranged in three-dimensional arrays and form three sets of lattice planes as indicated by the yellow arrow in **Fig. B.1b**. The planes in each set are parallel and equally spaced. The smallest repeating group of point lattices which has the symmetry of the crystal structure is called a unit cell as highlighted in red in **Fig. B.1b**. The unit cell has various possible shapes depending on the way the three lattice planes are arranged with respect to each other. The size and shape of the unit cell are defined by three vectors (**a**, **b**, **c**) taken from a reference point (indicated in bold in **Fig. B.1c**). These vectors are called the crystallographic axes. The crystal is built from the repetitive translation of the unit cell along these axes. The lengths of the vectors ( $a$ ,  $b$ ,  $c$ ) and the angles

---

between them ( $\alpha, \beta, \gamma$ ) are called the lattice parameters or lattice constants or cell parameters. The orientation of the planes in a lattice is usually indicated by Miller indices which are the integers  $h, k$ , and  $l$ . The miller indices are determined from the intercepts of the plane with the crystallographic axes at  $a/h, b/k$ , and  $c/l$ .

Back to the diffraction mechanism of X-ray diffraction, constructive interference occurs when the X-ray beam is scattered at the same angle as the incident beam (specular angle) and the scattered beams should remain in phase. Since the interplanar distance in a crystal is equal for each  $hkl$ -plane, the difference in the path length of the scattered beam from different  $hkl$ -planes should be equal to the integer multiple  $n$  of the wavelength (**Fig. B.1a**). By applying a simple trigonometric function based on these conditions, Bragg's equation (Eq. B.1) is obtained. The diffraction condition can be determined from this equation. For a specific wavelength of the X-ray beam, the diffraction angle  $\theta$  depends only on the interplanar distance  $d_{hkl}$ . Since every crystalline compound has different  $d_{hkl}$ , the diffraction angles provide precise information on the identity of the phases in the sample. Besides, the quantity of the phases can be calculated from the intensity.

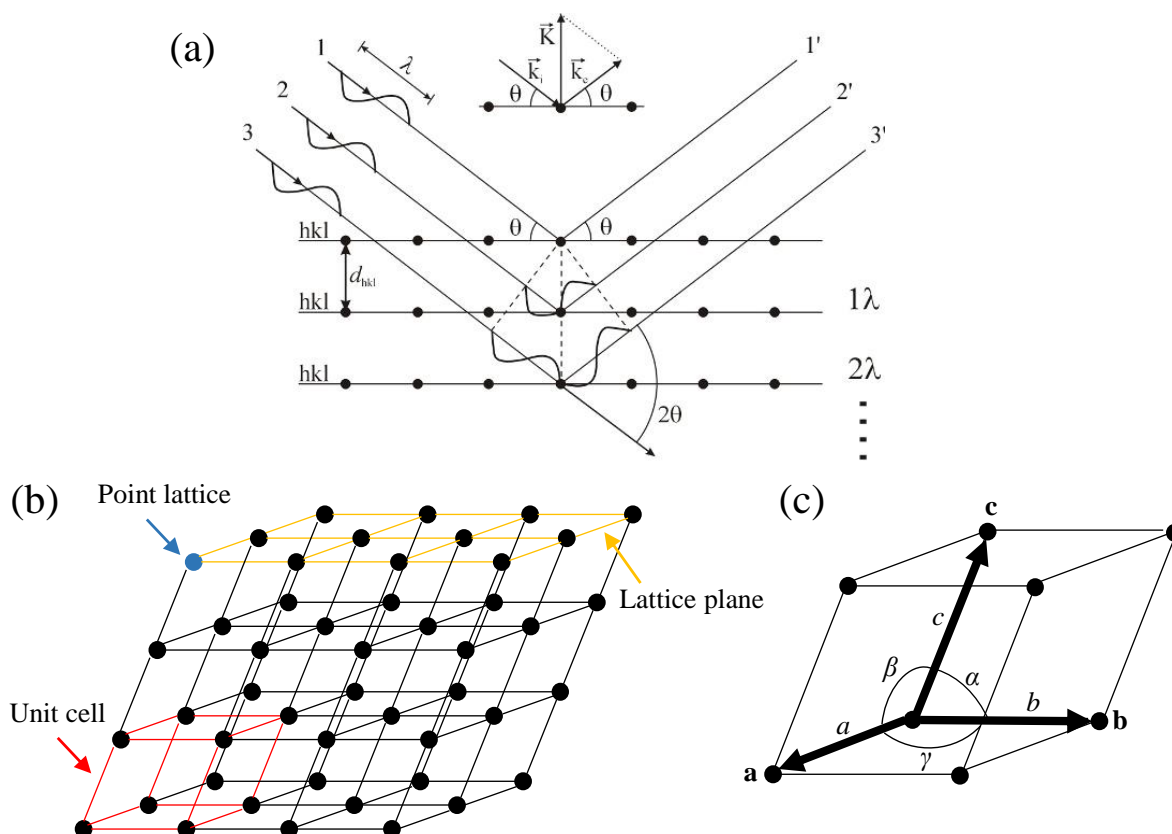


**Fig. B.1** (a) The graphical illustration of the X-ray beam scattering in constructive interference (taken from <https://fys.kuleuven.be/iks/nvsf/experimental-facilities/x-ray-diffraction-2013-bruker-d8-discover>), (b) the representation of lattice, and (c) a unit cell.

In the laboratory set-up, the incident X-ray beam is produced from an X-ray tube source. It consists of a cathode and a metal plate (copper is the widely used one) as the anode. The electrons in the cathode are accelerated by a high electric field and collide with the metal plate anode at high velocity releasing X-ray. Since the X-ray is generated in various wavelength, a monochromator is used to single out a wavelength. Afterwards, it is collimated in a single direction before it is used for the characterization. A 1D, point detector is used to record the intensity of the diffracted beams.

The laboratory XRD characterization is normally carried out in Bragg-Brentano geometry or also called reflective geometry. There are two possible configurations: either the X-ray tube source is fixed while the sample and the detector is rotated by  $\theta$  and  $2\theta$ , respectively, or both X-ray tube and the detector is rotated from  $-\theta$  to  $\theta$ . In either setup the detector records the intensity of the diffracted beams on every  $2\theta$  angle, resulting in the diffraction pattern called diffractogram which shows the diffraction peaks of phases present in the sample. To use the

obtained pattern for structural analysis, one of the vastly used technique is Rietveld refinement. This technique used the least square approach to fit the measured patterns with the theoretical ones. The refinement resulting in the information on the position, amplitude, and width of the diffraction peaks and can be used for various structural analyses.

Besides measurement at ambient condition, XRD can also be performed in non-ambient conditions such as under temperature, pressure, electric field, etc. As explained by Misture [108], this *in-situ* characterization provides information on the dynamic of the materials under external variables. To do *in-situ* XRD, a specific chamber is required depending on the type of environmental control that is planned.

**APPENDIX C: Electrochemical characterization technique: Electrochemical impedance spectroscopy (EIS)**

The equivalent electrical elements:

- (i) Lumped element: resistance  $R$ .

As has been previously mentioned, there is no phase difference ( $\theta = 0$ ) between the voltage and current for a pure resistance. Consequently, from Eq. 2.4, the impedance (which, in this case, equals the resistance) only consists of the real part with the magnitude of  $|Z|$ , as shown in Eq. 2.6. Thus, resistance for each frequency is plotted along the  $x$ -axis in the Nyquist plot (**Fig. C.1a**). The resistance value explains the energy losses in the system, for example the ohmic losses due to the electrolyte resistance.

$$Z_R(\omega) = |Z| = R \quad (\text{Eq. C.1})$$

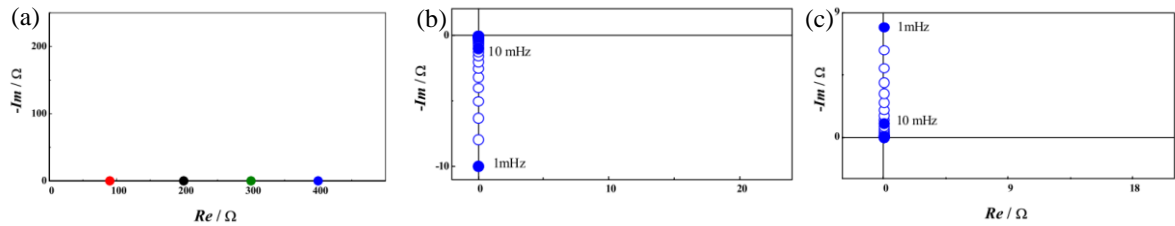


**Fig. C.1** The Nyquist representation of (a) resistance ( $R$ ), (b) inductance ( $L$ ), and (c) capacitance ( $C$ ) (Vladikova, 2004) [77].

- (ii) Lumped element: inductance  $L$ .

The inductance is characterized by a  $+90^\circ$  phase shift ( $\theta$ ) between current and voltage. From the Fourier transform of the Faraday's law of induction, the impedance related to inductance is given by Eq. C.2. Thus, inductance only has an imaginary part. The impedance has a positive value for positive inductance which means that it is plotted in a Nyquist plot as a vertical line below the  $x$ -axis (**Fig. C.1b**). Inductance element is used to model the contribution due to the accumulation of magnetic energy and movement of the charge carrier, thus it normally used to attribute the contribution from the connecting wires.

$$Z_L(\omega) = j\omega L \quad (\text{Eq. C.2})$$

(iii) Lumped element: capacitance  $C$ .

The current and voltage in capacitance is  $-90^\circ$  out of phase. The impedance related to capacitance is obtained from the Fourier transform of current-capacitance relation, resulting in Eq. C.3. As in an inductance, a capacitance also only consists of the imaginary part. However, contrary to an inductance, it has a negative value for positive capacitance. In a Nyquist plot, it is plotted as a vertical line above the  $x$ -axis (**Fig. C.1c**). Capacitance can be related to the contribution coming from the accumulation of electrostatic energy and charge carriers.

$$Z_C(\omega) = \frac{1}{j\omega C} = \frac{-j}{\omega C} \quad (\text{Eq. C.3})$$

(iv) Frequency-dependent element: constant-phase element  $CPE$ .

Constant-phase element (CPE) is a circuit element that takes into account various factors on a real electrode such as surface roughness and thickness variations. The impedance equation is given by Eq. C.4. In this equation,  $Q$  is called the factor of proportionality which is the value of the admittance ( $1/|Z|$ ) at  $\omega = 1$  rad/s and  $\alpha$  is the exponent of CPE with the value between 0 and 1. CPE has a constant, independent of frequency, phase angle ( $\theta$ ) of  $-(\alpha \times 90)^\circ$ , as indicated by the Nyquist plot in **Fig. C.2**. The impedance of CPE resembles capacitance when the value of  $\alpha$  is close to 1. CPE can be used to fit many experimental data which can be fitted by other elements. However, since the exact nature of CPE itself is not clear, especially at very high or very low frequency, data fitting using this element should be used only as a basis for the modelling.

$$Z_{CPE}(\omega) = \frac{1}{Q(j\omega)^\alpha} \quad (\text{Eq. C.4})$$

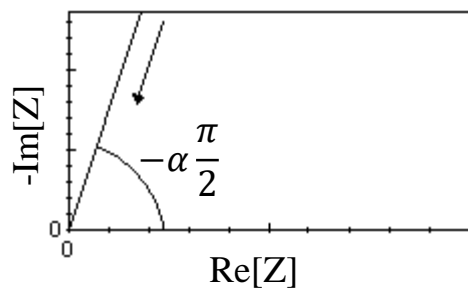


**Fig. C.2** The Nyquist plot of a constant-phase element ( $CPE$ ). The arrow indicates the increasing frequency.

- (v) Frequency-dependent element: Warburg  $W$  and finite-length Warburg  $FLW$ .

Warburg element is used to describe a semi-infinite linear diffusion process. It is derived from the second Fick's law of diffusion, yielding on impedance equation indicated by Eq. C.5. The real and imaginary parts of the impedance are equal; thus the phase angle is  $45^\circ$  and independent of the frequency as shown in **Fig. C.3a**.

$$Z_W(\omega) = \frac{\sqrt{2}\sigma}{\sqrt{j\omega}} \quad (\text{Eq. C.5})$$

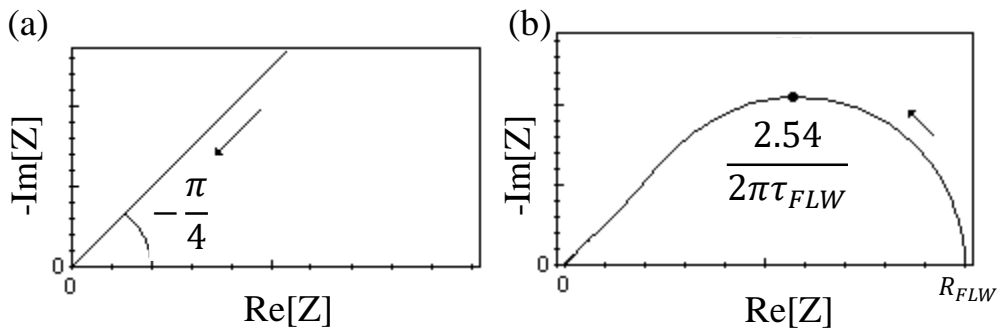


**Fig. C.3** The Nyquist plot of (a) Warburg ( $W$ ) and (b) finite-length Warburg ( $FLW$ ). The arrow indicates the increasing frequency.

Finite-length Warburg ( $FLW$ ) element is used for linear diffusion on a finite electrode thickness since no real system has an electrode with infinite thickness as described by the Warburg element. The equations related to this element are given by Eq. C.6-C.8 and the Nyquist plot is presented in **Fig. C.3b**.

$$Z_{FLW}(\omega) = R_{FLW} \frac{\tanh(\sqrt{j\omega\tau_{FLW}})}{\sqrt{j\omega\tau_{FLW}}} \quad (\text{Eq. C.6})$$

$$\omega_p \tau_{FLW} = 2.54 \rightarrow f_p = \frac{2.54}{2\pi\tau_{FLW}} \quad (\text{Eq. C.7})$$

$$\tau_{FLW} = 3R_{FLW}C_{FLW} \quad (\text{Eq. C.8})$$

- (vi) Frequency-dependent element: Gerischer  $G$  and fractal (modified) Gerischer  $G_f$ .

Gerischer element was initially used to explain the homogeneous electrochemical reactions in aqueous electrolytes. However, Adler, *et.al.* [29] show that the mathematical

expression of the Gerischer element can also be used to explain the processes on a porous MIEC electrode, as explained by the Adler-Lane-Steele (ALS) model (§1.2.2). Gerischer element provides the physical explanation for a non-charge-transfer process such as oxygen surface exchange (chemical reaction) combined with the solid-state diffusion (with the electrochemical reaction is taken at equilibrium). Eq. C.9-C.10 show the impedance equation and the relation between the frequency at the peak of the impedance arc with  $R_G$  and  $C_G$  for this element. The plot of Gerischer element has a characteristic of linear line with an angle of  $45^\circ$  from  $x$ -axis at high frequency, resembling the Warburg element (**Fig. C.4a**).

$$Z_G(\omega) = \frac{R_G}{\sqrt{1 + j\omega\tau_G}} \quad (\text{Eq. C.9})$$

$$\omega_p\tau_G = \omega_p R_G C_G = \sqrt{3} \rightarrow f_p = \frac{\sqrt{3}}{2\pi R_G C_G} \quad (\text{Eq. C.10})$$

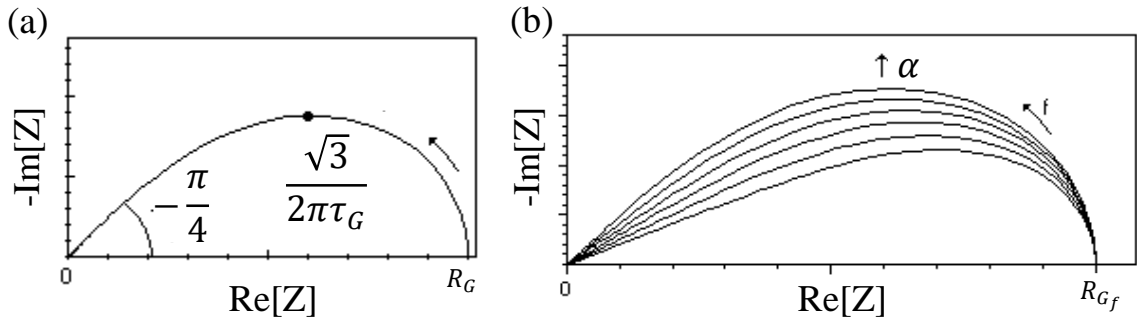


**Fig. C.4** The Nyquist plot of (a) Gerischer ( $G$ ) and (b) fractal Gerischer ( $G_f$ ). The arrow indicates the increasing frequency.

Several deviations from the ideal Gerischer might take place in the electrode resulting in the deformation of the shape of the response by a factor called  $\alpha$  ( $0 < \alpha < 1$ ). This deviation resulting in an element called fractal Gerischer ( $G_f$ ) with the impedance equation shown in Eq. C.11. As indicated by **Fig. C.4b**, the shape of the fractal Gerischer is more depressed as the value of  $\alpha$  is closer to 0.

$$Z_{G_f}(\omega) = \frac{R_{G_f}}{(1 + j\omega\tau_{G_f})^{\alpha/2}} \quad (\text{Eq. C.11})$$

The Gerischer element derived from ALS model can be used under several assumptions: (i) the electrode should have a thickness larger than the theoretical diffusion length (i.e. the active layer where the reactions take place), (ii) the diffusion length should be larger than the average particle size, and (iii) the limiting step of the electrode kinetics should be the O<sub>2</sub> exchange at electrode/gas interface and transport of O<sup>2-</sup> across the electrode through solid-state diffusion. Deviation from one of these assumptions leads to the response related to fractal Gerischer.

(vii) Examples of common complex elements: resistance in parallel with capacitance  $R//C$  and constant phase element  $R//CPE$ .

One of the most common equivalent circuit used to model the impedance response is  $R//C$  element. It describes the response of a simple charge-transfer electrode with an assumption that it is not limited by a diffusion process. The capacitance shows the double-layer charging while the resistance corresponds to the Faradaic impedance. The impedance equation is given by Eq. C.12. In the Nyquist plot, it is represented as a half-circle with a diameter of  $R$  (**Fig. C.5a**). The relation between the frequency at the peak of the half-circle with  $R$  and  $C$  is given on Eq. C.13.

$$Z_{RC}(\omega) = \frac{R}{1 + j\omega\tau_{RC}} = \frac{R}{1 + j\omega RC} \quad (\text{Eq. C.12})$$

$$\omega_p\tau_{RC} = \omega_p RC = 1 \rightarrow f_p = \frac{1}{2\pi RC} \quad (\text{Eq. C.13})$$

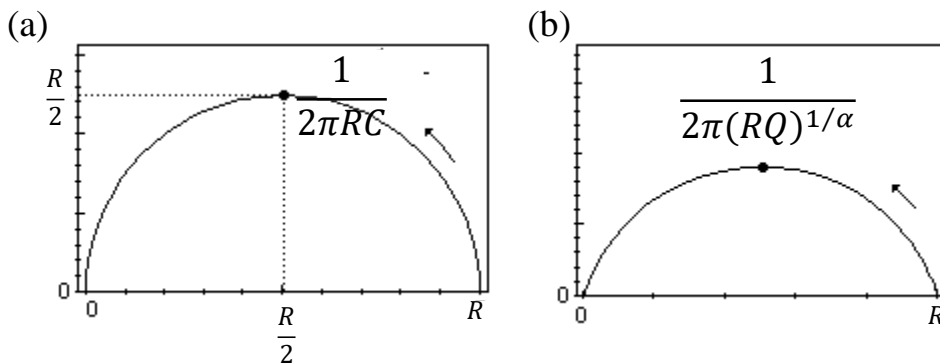


**Fig. C.5** The Nyquist plot of (a)  $R//C$  and (b)  $R//CPE$ . The arrow indicates the increasing frequency.

Another common complex element is  $R//CPE$  which is adapted due to the appearance of a depressed semi-circle instead of half-circle on the Nyquist plot of some systems (**Fig. C.5b**). The impedance equation and the relation between the frequency at the peak of the semi-circle with  $R$  and  $Q$  for this element are given by Eq. C.14-C.15. When the value of  $\alpha$  is close to 1, it resembles the equations for an  $R//C$  element. The ‘true’ capacitance can be calculated based on Eq. C.16.

$$Z_{R//CPE}(\omega) = \frac{R}{1 + RQ(j\omega)^\alpha} \quad (\text{Eq. C.14})$$

$$f_p = \frac{1}{2\pi(RQ)^{1/\alpha}} \quad (\text{Eq. C.15})$$

$$C = \frac{(RQ)^{1/\alpha}}{R} \quad (\text{Eq. C.16})$$